Advancement of closed gas loop photobioreactor for production of ^{13}C-labeled starch and related studies of metabolic and light kinetics

Zur Erlangung des akademischen Grades einer

DOKTORIN DER INGENIEURWISSENSCHAFTEN (DR.-ING.)

von der KIT-Fakultät für Chemieingenieurwesen und Verfahrenstechnik des Karlsruher Instituts für Technologie (KIT)

genehmigte

DISSERTATION

von

M. Sc. Kira Schediwy, geb. Wieneke
aus Minden

Tag der mündlichen Prüfung:	28.04.2026
Erstgutachter:	Prof. Dr.- Ing. Clemens Posten
Zweitgutachter:	Prof. Dr.- Ing. Thomas Meurer

“Efficiency is doing things right;

Effectiveness is doing the right things.”

(Peter F. Drucker)

Acknowledgements

This work was carried out at the Institute of Process Engineering in Life Sciences at KIT. Countless nerves, almost ten years, three relocations, two children, and one house purchase later, I now sit here deeply grateful that so many people have enabled, supported, enriched, and uniquely shaped my path.

First of all, I thank Prof. Dr.-Ing. Clemens Posten for the opportunity to eventually work in his group and for his patience throughout the completion of this dissertation. Thank you especially for continuously encouraging me to question assumptions, make deliberate decisions, and recognize the simplicity underlying the (complex) bigger picture – and for your essential theoretical support in (re)teaching Lotte how to ride a bike.

Thank you, Prof. Dr.-Ing. Thomas Meurer, for serving as my second reviewer.

Another thank you goes to Prof. Dr.-Ing. Alexander Grünberger for his patience and support throughout all necessary administrative processes.

I am very grateful for the support and scientific exchange within my project cooperations: the Lattice Boltzmann Research Group (LBRG) at KIT for conducting the gassing simulations; Silantes GmbH for cooperation in reactor development; and the Institute of Microbiology of the Institute of Botany of the Academy of Sciences of the Czech Republic for kindly providing the strain *Chlorella vulgaris* H14.

Thank you to the colleagues along my way for valuable discussions and support. Special thanks go to Christian Steinweg for laboratory assistance and, in particular, for adjusting the LabVIEW controllers until I was finally able to run the cultivation fully automated as intended; to Rosa, Matthias, and Andi for initial advice to get things started; to my first real office mate Nikolas, for making me fall in love with 3D printing and giving me the confidence that I would easily master it; to my follow-up office mate Franzi, for making the office more comfy together and positively influencing my work-life balance, footprint, appreciation, and self-compassion; to Inga, for catching up and making me laugh even on the darkest lab days; to Artem, for the critical questions that inspired me to look more deeply into every scientific problem; and finally to Johanna, for companionship and loyalty far beyond the call of duty.

To my students, who helped both me and this project grow: thank you for your contributions. Holger, for the essential early-stage work. Alex and Paulius, for the tremendous amount and precision of measurements and calibrations. Manuel, who was truly indispensable – from early

installation adjustments to the final measurements – and great company until the very end of the lab work. Julia, for her contributions to automation and micro-feeding.

Thanks to my friends, whom I can always count on: Trishi, thank you so much for continuous mental support, for sharing the highs and the lows throughout the years despite distance. Svenja, for believing more in me than I ever believed in myself. Luana, for tirelessly fighting against my health issues some years ago when I no longer believed I would ever again be in the condition to finish this project. Anika, for your substantial contribution to bringing my language skills to the level required for writing this dissertation and for your helpful feedback. Kati, for encouraging me to finish one project in life after the other with priority given to the dissertation. Annika, for your feedback of immeasurable value and so much more.

Thank you, Kernbohrkevin, for keeping the full renovation on track and giving me the freedom to finish this project.

My deep thanks go to heaven to my uncle Konrad, who opened the door to science for me when I was little and set the very beginning of my bio(techno)logical path, and to my aunt Hanna, who kept on supporting me emotionally and financially throughout my internship, Master's degree, and the first years of this project until she joined him in heaven.

Thank you to my parents and my sister, for their frequent visits to take care of the children and for allowing me to maintain some progress and stay connected to the project over the years. And to my twin brother, who probably has no idea how much strength and motivation I gained from his visits and calls.

Last but not least, my family: my husband Till, who has stood by me through everything; who moved to Karlsruhe for this project; who put many of his own priorities aside; who held together everything at home and provided dinner after long lab days, for wiping the green floor with me at night, and for supporting me in the final night shifts of writing either by food supply or time to rest the next day. Lotte and Finja, my heart and my sunshine, you are at once the greatest slowdown of this dissertation and the greatest joy of my life, showing me every single day how easy, wonderful, and complicated life can be – sometimes all within a single second. Thank you for your patience and your sacrifices in the final phase of this dissertation. Bolle, our dog, for his patience while waiting for the next walk whenever I "just needed to finish that thought."

I gratefully acknowledge the financial support of the German Federal Ministry of Education and Research (BMBF) and the German Research Foundation (DFG), which made this work possible.

Zusammenfassung

Im Rahmen dieser Dissertation wurde ein kompakter, intern beleuchteter Photobioreaktor (cptPBR) für die Produktion isotopenmarkierter Biomasse entwickelt, charakterisiert und optimiert. Der entscheidendste Schritt der Optimierung war der Anschluss eines geschlossenen Gaskreislaufes mit einer Protonenaustauschmembran-Brennstoffzelle (PEM). Die PEM reicherte den photosynthetisch gebildeten Sauerstoff selektiv ab, während alle anderen Gase in den cptPBR zurückgeführt wurden. Die vollständig quantitative Rückführung von CO_2 ermöglichte die stabil-isotopenmarkierte Biomasseproduktion mit ^{13}C durch Verwendung von $^{13}CO_2$ ohne Verluste dieses hochpreisigen Substrats. Zusätzlich zur Isotopenmarkierung konnte der Abreicherungsmechanismus für das Monitoring der photosynthetischen Aktivität während kinetischer Untersuchungen eingesetzt werden. Ziel der Untersuchungen war die Erhöhung der Stärkeausbeute, da Stärke zu hochpreisigem ^{13}C-Glukose hydrolysiert werden kann und eine Steigerung der Wirtschaftlichkeit ermöglicht.

Die Beleuchtung des cptPBR erfolgte über 37 horizontale Glasrohre mit einer Gesamtoberfläche von 0,909 m², entsprechend einer spezifischen Beleuchtungsfläche von 33,7 m^{-1}, die mit anderen *State-of-the-Art* Systemen vergleichbar ist. Die multidirektionale, helikale Anordnung der LEDs verringerte den Abstand zwischen den LEDs von geradlinig 19,5 mm auf effektiv 2,2 mm entlang der Längsachse. Unter diesen Lichtbedingungen hing die Produktivität des cptPBR maßgeblich von der Verteilung der zur Durchmischung dienenden Begasungsrohre ab. Die Begasungsgeometrie wurde daher mithilfe von kombinierter experimenteller und simulationsgestützter Durchmischungsanalyse optimiert. Eine Begasungsporengröße von 0,5 mm in Verbindung mit einem verbreiterten Begasungsprofil führte zu pH-Sprung-basierten Mischzeiten von 1393 ± 226 s entlang der Längsachse und 882 ± 22 s im Reaktorquerschnitt. Die optische Traceranalyse ergab Mischzeiten von unter 50 s im Reaktorquerschnitt und bestätigte somit einen schnellen Transfer von Zellen zwischen verschiedenen Lichtzonen im Verhältnis zu der vollständigen Homogenisierung des cptPBRs.

Zur produktiven photoautotrophen Kultivierung im cptPBR mit geschlossenem Gaskreislauf wurde eine PEM zur selektiven Sauerstoffabreicherung in den Kreislauf integriert. Die PEM ermöglichte eine streng stöchiometrische Reaktion von Sauerstoff zu Wasser unter Nutzung von extern zugeführtem Wasserstoff. Der Wasserstofffluss zur PEM diente aufgrund der Stöchiometrie mit dem netto produzierten Sauerstoff als Messsignal für die Berechnung der Photosyntheserate. Der theoretische biomassenspezifische Korrelationsfaktor ($\alpha_{k,H2}$ = 0,38-0,42 $g_X \cdot L_{H2}^{-1}$) und der photosynthetische Quotient (PQ = 1,22) wurden für aktiv wachsende

Chlorella vulgaris H14 experimentell bestätigt. Unter automatisiertem Betrieb mit den genannten Parametern konnte eine spezifische Wachstumsrate von 2,0-2,8 Tag^{-1} – bis zum Erreichen der maximalen Abreicherungskapazität der PEM bei einer volumetrischen Produktivität von 1,15 $g \cdot L^{-1} \cdot Tag^{-1}$ – aufrechterhalten werden. Die wasserstoffbasierte Biomassenabschätzung zeigte unter stabilen Betriebsbedingungen der PEM eine sehr gute Korrelation mit den Biotrockenmassekonzentrationen ($r = 0{,}998$). Bei Überhydratation der Membran sank der Korrelationsfaktor jedoch ($r = 0{,}735$), sodass der Feuchtegehalt der Membran als kritische Betriebsgröße identifiziert wurde.

Der automatisierte Betrieb und das quasi-kontinuierliche Monitoring des cptPBR ermöglichten die Anwendung und kinetische Untersuchung einer neu entwickelten Nährstofffütterungsstrategie. Zur mechanistischen Entkopplung der Licht- und Nährstoffdynamik wurden mithilfe einer Ulbrichtkugel die Absorptionskoeffizienten sowie mit einer eigens konstruierten, winkelauflösenden Messzelle und einem Photometer Streukoeffizienten bestimmt. Die Anpassung der Henyey-Greenstein-Funktion an die gemessene winkelspezifische Streuverteilung zeigte eine dominierende Vorwärtsstreuung ($g = 0{,}88$) bei einem geringen Anteil an Rückstreuung ($\leq 7{,}2$ % in Einzelmessungen). Die ermittelten Koeffizienten wurden für Lichtsimulationen mittels Monte-Carlo-Ray-Tracing verwendet. Das 3D-simulierte Lichtfeld für eine Einzel-LED stimmte sehr gut mit den Messwerten überein, wie für verschiedene Biomassekonzentrationen gezeigt werden konnte (Steigung = 0,829-1,078; R^2 = 0,957-0,991). Die Vervielfältigung der Einzel-LED im Reaktorquerschnitt ergab volumenelementspezifische Verteilungen von Lichtintensität und Absorptionsraten, wodurch die Lichtkinetik direkt auf die jeweilige Nährstofflimitierung bezogen und die Wachstumsreaktion kausal mit den Nährstoffbedingungen verknüpft werden konnte.

Eine als *Micro-Feeding* bezeichnete Stickstofffütterungsstrategie wurde entwickelt, um gezielt Stärkeakkumulation zu induzieren, während die metabolische Aktivität der Zellen aufrechterhalten und die Bildung aktiver Biomasse vermieden wird. Die Stickstoffzufuhr wurde auf 0,8-11,7 % im Vergleich zu wachstumsangepassten Bedingungen mit einer spezifischen Wachstumsrate von 3 Tag^{-1} reduziert. Unterschiedliche Reduktionsstufen der Fütterung führten zu einer vergleichbaren Abnahme des Stickstoffgehalts der Biomasse um 0,6 $\%\cdot h^{-1}$. Die maximale Photokonversionseffizienz betrug 7,6 % bei 6,3 % der wachstumsangepassten Nährstoffzufuhr. Dabei wurden 47-49 % der photosynthetisch fixierten Energie in Form von Stärke gespeichert, im vergleichbaren Stickstoff-Runout-Experiment hingegen nur 32 %. Der

Vergleich zwischen Micro-Feeding und klassischem Stickstoff-Runout zeigte zudem eine um 0,5 Tag^{-1} höhere spezifische Wachstumsrate im besten Micro-Feeding-Ansatz bei gleichem Stickstoffgehalt der Biomasse ($e_{N,X}$). Diese Steigerung des Wachstums im Micro-Feeding deutet auf eine Entkopplung der von Droop beschriebenen Abhängigkeit von $e_{N,X}$ durch die unmittelbare Verfügbarkeit des zugeführten NH_4^+ hin. Die im Kultivierungsverlauf abnehmende spezifische Zufütterung infolge der Biomasseakkumulation sowie eine aktive, plötzliche Reduktion der Fütterung führten jeweils zu vorübergehend geringerer Photokonversionseffizienz. Eine graduelle Anpassung der Stickstoffzufuhr ist daher erforderlich, um eine stabile Produktivität und Effizienz zu gewährleisten, wenn die Bildung aktiver Biomasse nicht vollständig unterdrückt werden kann.

Zusammenfassend kombiniert der cptPBR eine kompakte, intern beleuchtete Geometrie mit selektiver Sauerstoffabreicherung und damit eine stabile Plattform für ^{13}C-markierte Biomasseproduktion mit Prozessmonitoring und Automatisierung innerhalb klar definierter Betriebsgrenzen. Die Anwendung der *Micro-Feeding*-Strategie erhöhte die Stärkeproduktivität und die Effizienz der Produktion im Vergleich zu einem Nährstoff-Runout-Experiment. Ein geeigneter Bereich der Nährstofffütterungsreduktion wurde identifiziert, der die Effizienz der Stärkeproduktion erhöht. Dieser Bereich kann bereits die Wirtschaftlichkeit der ^{13}C-markierten Stärkeproduktion verbessern, sollte aber genauer eingegrenzt und durch Fütterungsgradienten proportional zum aktiven Biomassezuwachs angepasst werden, um das Potenzial der *Micro-Feeding*-Strategie weiter auszuschöpfen. Die Kohlenstofffixierung in verschiedenen Biomassebestandteile kann damit genauer geregelt werden. Zusätzlich sollte die Prozessrobustheit des cptPBR mit geschlossenem Gaskreislauf durch ein automatisiertes Feuchtemanagement der PEM erhöht werden. Weitere Optimierungen können höhere Sauerstoffabreicherungskapazität und homogenere Beleuchtung umfassen. Diese Anpassungen würden zudem höhere Biomassenkonzentrationen ermöglichen und unterstützen die Etablierung des cptPBR als Produktionsplattform für hochpreisige photobiotechnologische Anwendungen wie der ^{13}C-markierten Biomasse.

Abstract

This dissertation presents the development, characterization, and optimization of a compact, internally illuminated photobioreactor (cptPBR) for isotopically labeled biomass production. The decisive step in the optimization was the integration of a closed gas loop comprising a proton exchange membrane fuel cell (PEM). The PEM selectively removed photosynthetically produced oxygen while all other gases were returned to the cptPBR. Complete CO_2 retention enabled cost-efficient isotopic labeling of photosynthetically produced biomass using expensive $^{13}CO_2$. Beyond photoautotrophic biomass production without $^{13}CO_2$ loss, the cptPBR system proved suitable for metabolic monitoring in kinetic studies with microalgae. The studies aimed to investigate the potential of increasing the starch yield based on $^{13}CO_2$, as starch can be hydrolyzed to ^{13}C-glucose and maximizes profitability of the process.

The reactor utilized 37 horizontal glass tubes providing 0.909 m² of illuminated surface (33.7 m^{-1}), comparable to other state-of-the-art systems. A multi-sided helical LED arrangement with 2.2 mm effective longitudinal spacing generated a spatially structured light field. Process performance depended strongly on gas-driven mixing, and thus on the gassing tube distribution. The initial gassing system was therefore optimized through combined experimental and simulation-based mixing analysis. A pore diameter of 0.5 mm with broadened tube distribution yielded longitudinal and radial mixing times of 1393 ± 226 s and 882 ± 22 s, respectively, while optical tracers showed cross-sectional mixing in < 50 s, confirming rapid light-dark cycling relative to full homogenization.

To enable photosynthetic cultivations at high productivity within the cptPBR using a closed gas loop, a PEM was integrated for selective O_2 removal. Unlike stripping-based aeration, the PEM achieved stoichiometric O_2-to-water conversion using hydrogen. The hydrogen feed to the PEM provided a measurable signal correlated with net photosynthetic O_2 formation. The theoretically estimated biomass-specific conversion factor ($\alpha_{k,H2}$ = 0.38-0.42 $g_X \cdot L_{H2}^{-1}$) and photosynthetic quotient (PQ = 1.22) were confirmed for actively growing *Chlorella vulgaris* H14. Automated operation sustained specific growth rates of 2.0-2.8 day^{-1} until the design limit of O_2 removal at 1.15 $g \cdot L^{-1} \cdot day^{-1}$. PEM-derived biomass estimation showed excellent correlation to dry weight (r = 0.998) under stable hydration but declined (r = 0.735) during transient overhydration, identifying membrane moisture control as a critical operational boundary.

Automated operation and monitoring of the cptPBR enabled kinetic investigation of a newly designed nitrogen feeding strategy. To mechanistically decouple light and nutrient dynamics, scattering and absorption coefficients were measured using integrating sphere photometry and

a custom-built angular scattering cell. Henyey-Greenstein fits to the measured angular scattering distribution across four wavelengths (404-659 nm) yielded forward-dominated scattering ($g = 0.88$) with low backscattering (≤ 7.2 % in single measurements). Monte Carlo ray-tracing simulations with these parameters reproduced experimental single-LED 3D intensity patterns with high slope agreement across biomass concentrations (slope = 0.829-1.078, $R^2 = 0.957$-0.991). Replicating LEDs across the cptPBR cross-section generated voxel-resolved light and absorbance rate distributions, enabling alignment of light kinetics and nutrient limitations and allowing causal attribution of observed effects to nutrient conditions.

A feeding strategy termed micro-feeding was developed to induce starch accumulation while maintaining metabolic activity and suppressing active biomass formation. Nitrogen supply was reduced to 0.8-11.7 % of the balanced feed rate required for $\mu = 3$ day^{-1}, producing uniform intracellular decline of the nitrogen quota (0.6 %·h^{-1}). Photoconversion efficiency peaked at 7.6 % at 6.3 % feed, allocating 47-49 % of photosynthetically fixed energy to starch compared to maximum 32 % in a comparable nitrogen runout. At identical intracellular nitrogen quota ($e_{N,X}$), growth remained about 0.5 day^{-1} higher under the best-performing micro-feeding condition than in the classical nitrogen runout, indicating decoupling from Droop dependency through immediate use of supplied NH_4^+. However, when the specific feed declined due to biomass growth over time or sudden feed reductions to 0.8 % of balanced feed were applied transient efficiency loss was observed. Gradual feed adjustment is therefore required for stable performance when active biomass formation was only partly suppressed.

Overall, the cptPBR integrated compact geometry, internal illumination, and selective oxygen removal, providing a production system for ^{13}C-labeled biomass equipped with process monitoring and automation within clearly defined operational boundaries. The micro-feeding strategy enabled higher starch productivity and more efficient production than a comparable nutrient runout experiment. A suitable feed reduction range was identified and can already increase profitability of the ^{13}C-labeled starch production but should be further refined using feed gradients proportional to residual active biomass formation. Further investigations and adaptations of the micro-feeding strategy may improve controllability of carbon allocation and process robustness. Future developments of the cptPBR should target automated PEM hydration management, higher oxygen removal capacity, and more homogeneous LED emission. These adaptations would also support higher-density operation and strengthen the cptPBR as a production platform for photo-bioprocess engineering applications such as ^{13}C-labeled biomass production.

Table of Contents

List of Figures

List of Tables

List of abbreviations and symbols

	Definition	Unit
abs	Wavelength-dependent absorption (photometry)	
actX	Active biomass	
$A_{glass\ tube}$	Surface area of one glass tube	m^2
A_{PBR}	Illuminated area of the cptPBR	m^2
A_{sensor}	Area of sensor	
ATP	Adenosine triphosphate	-
A_{voxel}	Cross-sectional area of one voxel	m^2
C. vulgaris	*Chlorella vulgaris*	-
c_{actX}	Active biomass	$g \cdot L^{-1}$
c_{CO2}	Concentration of dissolved CO_2	$mol \cdot m^{-3}$
c_{Glc}	Glucose concentration in starch assay	$mg \cdot mL^{-1}$
CH_2O	Carbohydrates / simple sugars	-
$c_{N(,j)}$	NH_4^+ concentration, j = 0: initial, j > 0: longitudinal section j	$g_N \cdot L^{-1}$ or $mg_N \cdot L^{-1}$
$c_{N,eff,j}$	Effective ammonium concentration along cptPBR	$mg_N \cdot L^{-1}$
$c_{N,min,theo}$	Theoretical minimum NH_4^+ concentration for high uptake rates	$g_{N\text{-}NH4+} \cdot L^{-1}$
$c_{N\text{-}feed}$	Concentration of ammonium feed	$g_N \cdot L^{-1}$
cptPBR	Compact photobioreactor (developed system)	-
CTR	Carbon dioxide transfer rate	$mol \cdot m^{-3} \cdot s^{-1}$
c_X / $c_{X,sample}$	Biomass concentration in the PBR / in the sample)	$g \cdot m^{-3}$ $g \cdot L^{-1}$
d	Diameter	mm
D_{CO2}	Diffusion coefficient of carbon dioxide	
$d_{lateral}$	Distance on horizontal axis of cross section	mm
DNA	Deoxyribonucleic acid	-
D_{O2}	Diffusion coefficient of oxygen	$m^2 \cdot s^{-1}$
DOM	Discrete ordinate method	-
DoR	Degree of reduction	-
DW	Dry weight concentration	$g \cdot L^{-1}$
$E_{(510nm)}$	Extinction (at 510 nm)	-
$e_{N,X(,max)}$	(Maximum) nitrogen quota in biomass	% (w/w)
E_{photon}	Light energy per photons	$kJ \cdot mol^{-1}$
$f_{2xpore\ diameter}$	Empirical factor of mixing time at doubling pore diameter	-
$f_{broadening}$	Empirical factor of mixing time at broadened gassing configuration	-
$f_{V,replete}$	Cumulative volume fraction of NH_4^+-replete zones	%
g	Asymmetry parameter of the Henyey-Greenstein function	-
G1.4.6.8.11	Gassing tube configuration, 5 tubes, positions 1, 4, 6, 8, and 11	-

	Definition	Unit
G1.4.8.11	Gassing tube configuration, 4 tubes, positions: 1, 4, 8, and 11	-
G1.5.7.11	Gassing tube configuration, 4 tubes, positions: 1, 5, 7, and 11	-
G1-11	Gassing tube configuration, 11 tubes, positions: 1-11	-
G3P	Glyceraldehyde-3-phosphate	-
GC	Gas chromatography	-
$H_{CO2,H2O}$	Henry coefficient	$g \cdot L^{-1} \cdot bar^{-1}$
HEX	Hexadecimal version of RGB (00-FF each)	-
$H_{O2,H2O}$	Henry coefficient of oxygen in water	$g \cdot L^{-1} \cdot bar^{-1}$
$I_{hv}(x,y,z)$	Light intensity at position (x,y,z)	$\mu mol \cdot m^{-2} \cdot s^{-1}$
$I_{hv,abs}(x,y,z)$	Intensity of absorbed light at position (x,y,z)	$\mu mol \cdot m^{-2} \cdot s^{-1}$
I_{LED}	Current of light supply in cptPBR	A
$j_{deplete}$	Index of first depleted longitudinal section in the mixing model	-
k	Compound / biomass constituent	
k_{Ihv}	Calibration factor of I_{LED} to average I_{hv} on glass tube of cptPBR	$A\ m^2 \cdot \mu mol^{-1} \cdot s^{-1}$
KIT	Karlsruhe Institute of Technology	-
k_La	Volumetric gas transfer coefficient	s^{-1}
k_La_{CO2}	Volumetric mass transfer coefficient of carbon dioxide	
k_La_{O2}	Volumetric mass transfer coefficient of oxygen	
k_{laser}	Calibration factor from N_{ray} to $I_{hv}(x,y,z)$ using a laser	$\mu mol \cdot s^{-1} \cdot ray^{-1}$
k_{LED}	Calibration factor from N_{ray} to $I_{hv}(x,y,z)$ using LED(s)	$\mu mol \cdot s^{-1} \cdot ray^{-1}$
L	Length of cptPBR (or unit: liter)	mm
LBM	Lattice Boltzmann method	-
LBRG	*Lattice Boltzmann Research Group*	
LED	Light-emitting diode	-
Lim#	Names of micro-feeding cultivations, #: percentage of feed	-
LoS	Line-of-sight (LoS) shading	-
LPM	Liters per minute	$L \cdot min^{-1}$
m_0	Slope of simulated against experimental $I_{hv}(x,y,z)$	-
MC	Monte Carlo	-
M_{CH2O}	Molar mass of carbohydrates / simple sugars	$g_{CH2O} \cdot mol_C^{-1}$
M_{Glc}	Molar mass of glucose	$g_{Glc} \cdot mol_C^{-1}$
MS	Mass spectroscopy	-
m_{sample}	Mass of starch sample	mg
M_{STA}	Molar mass of starch	$g_{STA} \cdot mol_C^{-1}$
MVM	Mechanical Process Engineering and Mechanics	
M_X	Molar mass of active biomass	$g_X \cdot mol_C^{-1}$
N_2	Nitrogen	
NAD(P)H	Nicotinamide adenine dinucleotide (phosphate), reduced	-
n_{CH2O}, n_{O2}	Amounts of CH_2O and O_2, respectively	mol
NH_4^+	Ammonium(-ion)	-
NMR	Nuclear magnetic resonance spectroscopy	-
n_{quartz}	Refractive index of quartz glass	-
$N_{ray(,abs)}$	Number of (absorbed) light rays	-
$N\text{-}spI_{hv}$	Nitrogen-specific light supply rate	$\mu mol \cdot g_N^{-1} \cdot s^{-1}$
OD_{750nm}	Optical density at 750 nm	-
OT	Online transmission measurement	–
OTR	Oxygen transfer rate	$g \cdot L^{-1} \cdot s^{-1}$

	Definition	Unit
$p(\theta,\lambda,i)$	Phase function	-
P’	New computed position in ray tracing	mm
P_{abs}	Probability of absorption	-
PAR	Photosynthetically active radiation	-
PBR(s)	Photobioreactor(s)	-
$PCE_{(k)}$	Photoconversion efficiency (of one compound k) on total incident light	%
PEM	Proton exchange membrane fuel cell	-
pH	Negative logarithm of the H^+ concentration	-
ph	Photons	-
PI-curve	Photosynthesis irradiance response curve	-
P_{inner}	Position of intersection of light ray with the inner glass tube	mm
pO_2	partial pressure of oxygen	%
PQ	Photosynthetic quotient, net ratio of evolved oxygen to fixed CO_2	$mol_{O2} \cdot mol_{CO2}^{-1}$
$P_{replete,j}$	Probability of microalgae from longitudinal section *j* being exposed to replete conditions	%
P_{sca}	Probability of scattering	-
PT	Process time	H
P_V	volumetric productivity	$g \cdot L^{-1} \cdot day^{-1}$
$q_{back,j}$	Reverse local flow in the cptPBR	$L \cdot s^{-1}$
$q_{f,N}$	Ammonium feed	$g_N \cdot h^{-1}$
$q_{feed(,Ph4)}$	(Constant) nutrient feed flow (in phase IV)	$L \cdot h^{-1}$
$q_{forward,j}$	Effective local forward flow in the cptPBR	$L \cdot s^{-1}$
q_{H2}	Hydrogen flow consumed by the PEM	$mL \cdot min^{-1}$
R^2	Coefficient of determination	-
RED	Logistic fit of R color value	-
RGB	Red, green, blue color values (0-255 each)	-
$r_{glass,inner}$	Inner radius of the glass tube	mm
$r_{hv,abs}$	Specific photon absorbance rate	$\mu mol \cdot g^{-1} \cdot s^{-1}$
$r_{N(,max)}$	(Maximum) nitrogen uptake rate	$mg_N \cdot g_X^{-1} \cdot h^{-1}$
RNA	Ribonucleic acid	-
$r_{O2,i}$	Reaction and uptake rates of oxygen	$\% \cdot h^{-1}$
r_X	Specific biomass accumulation rate / specific growth rate interpreted on modeling basis	day^{-1}
$r_{X,m}$	Specific maintenance rate	day^{-1}
S	Score in backscattering estimation, sum of deviation from ideal slope and ideal R^2	-
SA:V	Ratio of illumination area to culture volume	m^{-1}
SIL(S)	Stable isotopically labeled (substances)	-
spI_{hv}	Specific light supply rate	$\mu mol \cdot g^{-1} \cdot s^{-1}$
$spI_{hv,target}$	Targeted specific light supply rate	$\mu mol \cdot g^{-1} \cdot s^{-1}$
STA	Starch in biomass	%
t / t_{mix}	Time during cultivations or mixing experiments	s or h
T14p1	Gassing tube for customization: 14 pores, d = 1.0 mm	-
T15p0.5	Reference gassing tube: 15 pores, pore d = 0.5 mm	-
TAG	Triacylglycerol	-
$t_{mix(,j)}$	Mixing time (in section *j*)	s

	Definition	Unit
u_1 & u_2	Uniformly distributed random numbers in (0,1)	-
$V_{hyd.Glc}$	Volume of the processed sample solution containing hydrolyzed glucose	mL
V_m	molar volume of an ideal gas	$L \cdot mol^{-1}$
V_{PBR}	Volume of cptPBR	L
W	Indicator of sphericity in Mauchly test	
X	Active biomass	%
$Y_{CH2O,ph}$	Molar yield on photons normalized to one C-unit in sugars	$mol_{CH2O} \cdot mol_{ph}^{-1}$
$Y_{k,ph}$	Yield of the respective compound k on photons	
$Y_{O2,ph(,theo)}$	(Theoretical) yield of oxygen on photons	$mol_{O2} \cdot mol_{ph}^{-1}$
$Y_{X,ph}$	Photosynthetic yield of active biomass on photons (net energy efficiency of growth, under replete conditions)	$g_X \cdot mol_{ph}^{-1}$
$y_{X,ph,max}$	Maximum efficiency of growth, neglecting $r_{X,m}$	$g_X \cdot mol_{ph}^{-1}$
z	Height coordinate of cptPBR	mm
$z_{cuvette}$	Light path through sample in the cuvette	mm
$\#LED_{glass\ tube}$	Number of LEDs in one glass tube	-
$(\Delta)z_{PBR,(j)}$	Length of the (longitudinal section j of the) cptPBR	mm
$^{(13)}CO_2$	Carbon dioxide (stable C-Isotope with atom mass = 13 u)	
$\hat{n}_{rad,inner}$	Radial unit normal to apply Snell's law	-
$c_{CO2}^{(*)}$	(Saturated) CO_2 concentration	
$\hat{v}$	Direction vector of light in the culture, with index in air or glass	-
$\sigma_{X,abs,\lambda}^{norm}$	Normalized spectral shape of wavelength-specific absorption cross-section with integral = 1 for modeling	-
Δs	Free optical light path, with index in air or glass	m
$\mu_{(max)}$	(Maximum) experimental specific growth rate over PBR	day^{-1}
$\alpha_{abs,\lambda}$	Absorption coefficient	m^{-1}
$\alpha_{ext,\lambda}$	Extinction coefficient	m^{-1}
$\alpha_{k,H2}$	correlation factor of volume of H_2 consumption by PEM to formed biomass as constituent k	$g_k \cdot L_{H2}^{-1}$
$\alpha_{sca,\lambda}$	Scattering coefficient	m^{-1}
$\Delta Hc^0(k)$	Heat of combustion of compound k	$kJ \cdot g^{-1}$
η	Ratio of refractive indices	-
θ	Polar angle	°
λ	Wavelength	nm
ν_{H2}	Stoichiometric correlation factor H_2 to O_2 in PEM	-
ξ	Uniform distribution in (0,1)	-
$\sigma_{X(,\lambda)}$	(Wavelength-dependent) optical cross-section merging $\sigma_{X,abs(,\lambda)}$ and $\sigma_{X,sca(,\lambda)}$	$m^2 \cdot g^{-1}$
$\sigma_{X,abs(,\lambda)}$	(Wavelength-dependent) absorption cross-section	$m^2 \cdot g^{-1}$
$\sigma_{X,abs,\lambda,norm}$	Normalized wavelength-dependent absorption cross-section	-
$\sigma_{X,sca(,\lambda)}$	(Wavelength-dependent) scattering cross-section	$m^2 \cdot g^{-1}$
$\Phi_{X(,\lambda)}$	(Wavelength-dependent) scattering phase function	-

1 Introduction

Metabolic tracers facilitate the detailed investigation of the metabolism of organisms [1] and may assist in medical diagnostics. One future perspective for non-invasive diagnostics involves oral administration of labeled metabolites to humans. Spectroscopic tracing of these metabolites *in vivo* can reveal malfunctions of metabolic pathways or organ structures. 'Labeling' is carried out by the usage of stable isotopes instead of the atoms that are naturally more abundant. Nowadays, medical research employs stable isotopic labeling to elucidate molecular structures and identify metabolites and metabolic pathways [2–5]. Common techniques utilizing stable isotopically labeled substances (SILS) are nuclear magnetic resonance spectroscopy (NMR) and mass spectrometry (MS) [6]. Spectroscopic methods use SILS for metabolic flux analysis [7,8] and as internal standards to ensure robust and efficient quantification [9,10].

SILS enable precise quantification of any compound within both the sample and the stable isotopically labeled (SIL) standard. However, SIL standards are costly, and the available range of compounds on the market is limited [11]. These compounds range from simple organic metabolites like glucose and ethanol to amino acids and even more complex substances such as flavonoids and drugs [9,11,12]. An ideal SIL standard includes all metabolites abundant in the sample [13]. Closer origin similarity between sample and SIL standard increases metabolite coverage. SILS can be produced either chemically or enzymatically *in vitro*, or metabolically *in vivo* [14]. The highest coverage and complexity of molecules are achieved through metabolic methods. Metabolic labeling refers to growing tissues and organisms on media or feeds enriched with SILS [13,14].

The appropriate feed composition for isotopic labeling varies with the organism under investigation. Mammalian model organisms in metabolic studies commonly include rodents. Many rodents primarily consume plant matter with seeds, fruit, fungi, leaves and grass as their typical natural diet [15]. An exemplary rodent diet consists of 18.6 % proteins, 44.2 % carbohydrates and 6.2 % fats in terms of their energy contribution [16]. This composition reflects the high carbohydrate content of an ideal rodent diet. The feed profile intuitively suggests generating SIL rodents in two steps: first, stable isotopic labeling of plants, and second, feeding the SIL plants to rodents. The labeling techniques for plants include hydroponic culture, stem injection and atmospheric labeling [17]. The atmospheric technique refers to a $^{13}CO_2$-enriched cultivation chamber to fixate inorganic ^{13}C in organic matter by photosynthesis. Efficient $^{13}CO_2$ fixation by photosynthesis requires airtight chambers and control of CO_2, pressure, temperature, humidity, and pH. The plants further benefit from artificial light supply

[18]. The required installations are comparatively complex and space-consuming, and either adaptations are needed in the cultivation process or ^{13}C is lost in non-edible plant material.

Opting for microalgae instead of terrestrial plants to perform stable isotopic labeling presents several advantages in process engineering. Microalgae facilitate compact system designs, higher growth rates and higher photosynthetic efficiency compared to terrestrial plants [19,20]. Another advantage of microalgae is the homogeneous biomass, while some tissues of plants are not edible. Labeling of non-edible components with costly SILS is economically inefficient. Some plant components, e.g., leaves, allow selective isotopic labeling. This selective process demands enclosing the desired component in chambers during growth, complicating the labeling procedure [17]. Adjustment of these chambers and subsequent separation of plant components further increase the complexity of the system and the workload. This complexity underlines the need for ^{13}C labeling of completely edible organisms.

Microalgae such as *Chlorella vulgaris* are edible as dried biomass or wet slurry and provide safe and even healthy addition to the rodents' diet [21,22]. The high biodiversity of microalgae [23–25] expands the market potential of photosynthetically produced ^{13}C biomass. Next to ^{13}C feed supplements, microalgal constituents can be separated and processed to serve as ^{13}C substrates for heterotrophs. Heterotrophic yeast or bacteria cultures synthetize more complex biomolecules from ^{13}C labeled glucose, for example recombinant proteins. The glucose is obtained from starch extraction and hydrolysis from microalgal biomass. The vast biodiversity of microalgae broadens the market potential for ^{13}C labeled biomass. Microalgae can also accumulate other compounds, namely lipids and proteins, for extraction and further processing [26]. However, the production of isotopically labeled microalgal biomass possesses several engineering challenges, especially gas retention when using $^{13}CO_2$.

The objectives of this dissertation and their interconnection with the conducted studies are outlined in Figure 1. The first aim was to address challenges of ^{13}C-labeled biomass production by designing a photobioreactor for ^{13}C-labeling of microalgae with complete quantitative utilization of $^{13}CO_2$ to achieve an economically viable process. The system should offer a fully controllable environment on a compact laboratory scale due to the high substrate and product value and maximum purity requirements. Reactor compactness and short light paths in the culture to achieve high productivities are mutually exclusive in common photobioreactor geometries. However, the extraordinarily high value of ^{13}C-labeled biomass allows complex and costly designs. Internal illumination effectively bridges the trade-off between compactness and light supply, despite drawbacks in mixing patterns, cleaning effort, and limited robustness.

The light distribution predominantly imposes limitations on photoautotrophic growth, so evaluation by light modeling is mandatory as part of this dissertation to distinguish different kinetic effects, especially in the context of starch accumulation. Understanding and controlling biomass accumulation toward starch formation was of central interest in this dissertation due to the high value of ^{13}C-labeled glucose. While nutrient runout cultivations are a common procedure for inducing starch accumulation in microalgae, photosynthetic efficiency drops as nutrient limitation progresses. A promising approach to mitigate this efficiency loss was to introduce markedly sub-stoichiometric nutrient feed rates after an initial cultivation phase of biomass growth, which is further called *micro-feeding* and is investigated in this thesis.

In the following, the theoretical foundations relevant to this dissertation are summarized. The overview introduces essential aspects of microalgal metabolism, reactor design, light modeling, and kinetic considerations that form the scientific basis of the conducted work. These elements together outline the framework within which the experimental and modeling approaches of this thesis were developed and applied using the microalga *Chlorella vulgaris*.

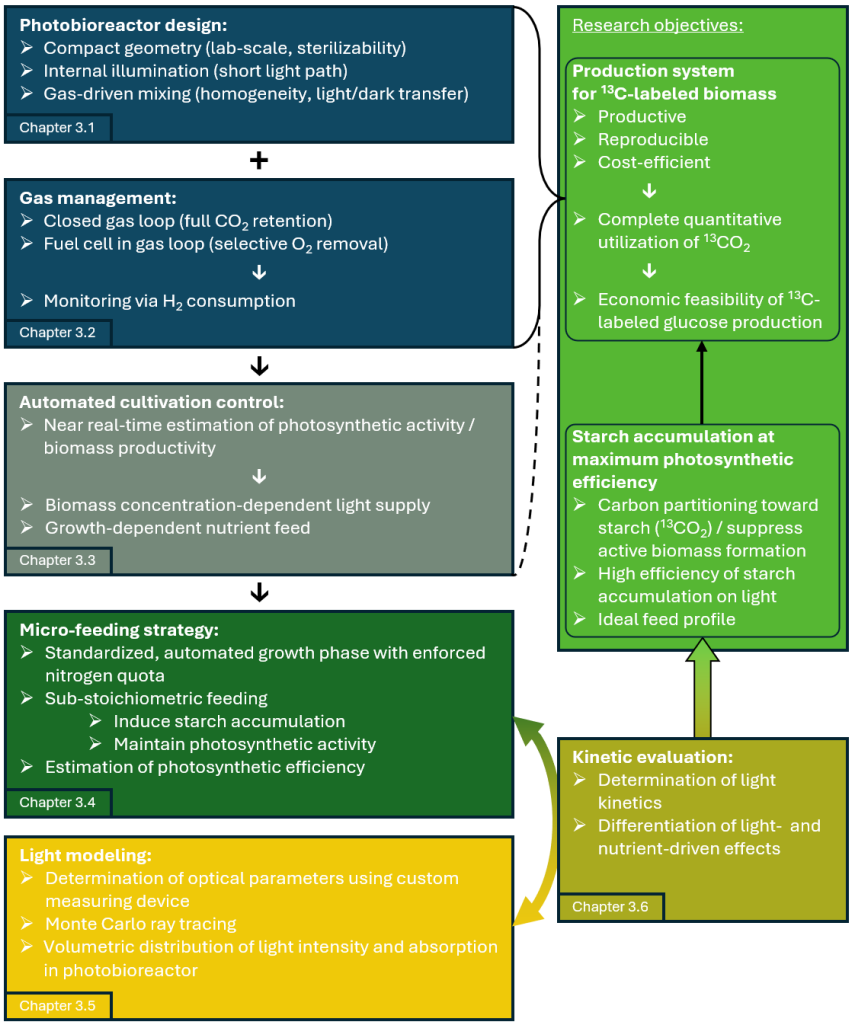

Figure 1: Logical structure and interconnection of research objectives and investigations in this dissertation.

1.1 Microalgae – the production species *Chlorella vulgaris*

The green microalga (Chlorophyta) *Chlorella vulgaris* qualifies for versatile applications due to rapid growth rates, high photosynthetic efficiency, robustness and varying biomass composition [23,25,27–29]. *C. vulgaris* is scientifically well investigated and approved for human consumption [27]. The biomass composition is customizable in response to nutrients, light, temperature and pH [23,25,30]. Depending on the growth conditions, the cells measure from 2 µm to 10 µm in spherical or ellipsoidal shape [30]. The cellular shape is solidified by a glucosamine layer (up to 21 nm) in the cell wall after maturation. After proliferation the cell wall of the four daughter cells is thinner (2 nm) and more flexible. The cell wall and the inlying membrane confine the cytoplasm with soluble proteins and minerals. The cytoplasm hosts the nucleus, the vacuoles, the Golgi body, the mitochondria and the chloroplast [23].

The chloroplast consists of two bi-layered membranes in agreement with the endosymbiosis theory. The outer membrane envelops the chloroplast and allows metabolites and ions to pass [23]. The inner membrane – stacked as thylakoids – holds proteins for the oxygenic photosynthesis, namely the complexes of the electron transport chain: the photosystems II and I, the cytochrome b6f and the adenosine triphosphate (ATP) synthase. These complexes use energy from absorbed photons to form the reducing agent Nicotinamide adenine dinucleotide phosphate (NADPH) and the energy carrier ATP [31]. NAPDH and ATP are released to the stroma of the chloroplast and used in the Calvin-Benson cycle for carbon fixation [32]. The carboxylation in the Calvin-Benson cycle generates the sugar derivative glyceraldehyde-3-phosphate (G3P).

Under favorable growth conditions G3P is converted to sugar or directly feeds the anabolism, e.g. protein synthesis [33]. The anabolism may be hindered and consequently the synthesis and accumulation of starch granules or lipid globules is promoted by the depletion of nutrients. Nutrient starvation is one strategy to customize the composition of *C. vulgaris* as a renewable feedstock [23].

The feedstock *C. vulgaris* serves for the commercial production of food supplements, dyes, pharmaceuticals, cosmetics, livestock and aquaculture feed as well as for wastewater treatment [25,28–30,34]. Industrial mass cultures are mainly grown outdoors using sunlight in photobioreactors (PBRs) or open systems, mostly ponds [33]. The choice of the cultivation system depends – besides the ambient conditions and scale – on the product value [24] and the interplay of the mode of nutrition and the required purity [35]. Contaminations threaten the product purity especially in mixotrophic or heterotrophic cultivations [36], as organic carbon

sources are easily accessible for contaminants. Contaminations can be prevented by harsh, extremophile conditions or closed systems [27].

Closed photobioreactors involve higher installation costs, which may be compensated by the value of (by)products [37]. High value products justify the expense of complex photobioreactors [24] by reducing contamination risk and increasing product purity. Recent advances in light-emitting diode (LED) technology, namely cost reduction and improved energy efficiency [38], have increased the use of artificial illumination for commercial-scale microalgal production [39]. In this dissertation, the high-priced substrate $^{13}CO_2$ was the primary reason for selecting a closed system, which was inevitably illuminated artificially to provide robust process conditions (see chapter 3.1). Furthermore, the consistent process conditions enabled metabolic studies with clear differentiation of nutrient and light supply effects.

1.2 Light distribution – the applicability of various modeling approaches

Designing a photobioreactor (PBR) for the cultivation of microalgae requires understanding of the light distribution to achieve high productivities. Flux and absorbance characteristics render ideal light distribution hardly possible. 'Ideal light distribution' refers to one identical light intensity at the position of each cell and, in other words, no light gradients [40]. Light gradients naturally occur due to light attenuation by absorption and scattering [41].

The light distribution can be predicted by light models, requiring input parameters to represent the optical characteristics of the culture. For simplicity, we consider the cells as the only active contributors to the optical characteristics of the culture. The optical characteristics are described by two coefficients: the absorption cross-section $\sigma_{X,abs}$ and the scattering cross-section $\sigma_{X,sca}$. The absorbance, defined by $\sigma_{X,abs}$, determines the light availability for photosynthesis, which also depends on the abundant light intensity. To predict the light distribution in a PBR, scattering needs to be incorporated into the light models. Scattering potentially occurs into all directions. The three-dimensional scattering coefficient is commonly expressed as the two-dimensional scattering phase function Φ_X from 0° to 180°. The angular scattering probabilities given by Φ_X translate to three-dimensional descriptions by projecting onto a spherical coordinate system. Φ_X depends on the size and the optical properties of the cells and increases the complexity of the light model [42].

The applicability of simple light modeling attempts is limited. The simple models mainly use exponential expressions. $\sigma_{X,abs}$ and $\sigma_{X,sca}$ are merged into one optical cross-section σ_X or correction factors/parameters are incorporated for the prolongation of the straight light path to the actual light path length [42–47]. Scattered photons may hit cells at other locations in the

PBR. In flat-panel PBRs, out-scattered photons from any light ray can equal the in-scattering from all the neighboring light rays in a symmetric pattern. The equilibration of neighboring scattering events may be simplified to the prolongation of the light path length for forward scatters. Based on the simplifications for parallel light rays, the exponential law approximates the light intensity along the light path through flat panels. The prolongation mathematically compensates for the non-linear way the light penetrates through the PBR, which is affected by the forward scattering of microalgal cells. Any scattering apart from 0° reduces the uniformity of the light direction with each scattering event.

Forward scattering remarkably supports light transfer into the suspension compared to other scattering distributions such as isotropic scattering. If forward scattering is not predominant, short light paths with few cell-layers lead to darkness. Only parallel light rays combined with strong forward scattering justify the prolongation of the light path length as the simplification demands symmetric scattering behavior in all neighboring sections. In other terms, the exponential modeling approaches reproduce measured light gradients along the straight light path for simple PBR geometries [45,48,49] not taking into account any boundary conditions. This simplicity limits prediction reliability and applicability to specific PBR geometries and conditions.

Complex PBR geometries do not meet the conditions that justify the simplification of prolonging the light path length. Scattering of neighboring light rays cannot equilibrate in the non-parallel setup. The distribution of the light direction changes with each scattering event and needs to be simulated and tracked. The simulation of the angular distribution of the light direction and the local light intensity require ideally the wavelength dependent absorption cross-section $\sigma_{X,abs,\lambda}$ and scattering phase function $\Phi_{X,\lambda}$ as input parameters. $\Phi_{X,\lambda}$ and $\sigma_{X,abs,\lambda}$ vary differently with the wavelength [50]. Incorporating wavelength dependency into light models gives the potential to more accurate predictions. The parameters $\Phi_{X,\lambda}$ and $\sigma_{X,abs,\lambda}$ should be measured for different physiological states to maximize the mechanistical meaning and achieve predictive character of the simulations as performed in chapter 3.5.

Accurate predictions of anisotropic scattering and absorption within a culture require respect for light intensities from all prevalent directions at each simulated position. Unlike solutions to field equations, modeling light propagation necessitates treating light rays independently, using tensor equations to represent the light direction and intensity. These tensor equations allow for the modeling and tracking of light propagation through the culture but require numerical solutions. These solutions must incorporate the angular light distribution, a characteristic

essential for calculating further light propagation. To address these complex requirements, solutions of the radiative transport equation by numerical methods such as the discrete ordinate method (DOM) [51], Monte Carlo (MC) approaches [52,53] and the lattice Boltzmann method (LBM) [54] have been described in the literature.

The strength of LBM is the parallelizability, which is achieved through discretizing the simulated volume into a three-dimensional grid. The parallelism facilitates high-performance computing of multiphysics applications. Multiphysics in the context of PBRs refers to coupling light distribution, flow dynamics, gas exchange and algal kinetics [41] as performed by the open source code available in [55]. When modeling appropriate mechanisms and feeding the model with well determined parameters, the multiphysics simulations can become a powerful tool for integrated PBR design in the future. Nevertheless, the complexity of LBM demands careful interpretation of interacting mechanisms and submodels.

For the sole simulation of light distribution, MC approaches are powerful techniques with straight forward and transparent mechanisms. A high number of 'virtual photons' is simulated and their propagation is calculated according to physical law and optical characteristics of the culture to approximate the light distribution by the total of simulated photons [52]. The MC simulations can be solely based on the most essential information: the PBR geometry, the characteristics of light sources and the culture specific parameters $\sigma_{X,abs,\lambda}$ and $\Phi_{X,\lambda}$. Higher computing efficiency can be achieved by combining MC and DOM, or, in other words, restricting the scattering of photons to discrete angles [56]. This restriction is especially reasonable, when the discretization of the ordinates meets the geometric measuring accuracy of the phase function $\Phi_{X,\lambda}$.

Mostly estimations of $\Phi_{X,\lambda}$ are based on calculations respecting the cellular characteristics [53], experimentally assisted estimations [57] or asymmetrically weighed probability distributions [58,59]. Precise measurements of the phase function are rarely available in the literature and depend on the physiological state and morphology of the cells [57]. To estimate the phase function most experimental procedures still demand mathematical analytics [60] or radiative modeling [61]. Simplified goniometers with low demand for data processing have been suggested in [62,63]. In this thesis (chapter 3.5.1-3.5.2), the same optical principles are applied using a minimalistic and low-cost design of a measurement device to allow the investigation of $\Phi_{X,\lambda}$ at different physiological states. The investigation of $\Phi_{X,\lambda}$ at varying state is essential for optimizing the PBR design and cultivation strategies regarding light installations and light supply. Models that respect $\Phi_{X,\lambda}$ help design strategies to analyze and to maximize light

utilization and, consequently, microalgal productivity, especially in internally illuminated photobioreactors.

1.3 Light kinetics – the influence of their mechanisms on PBR design

Light, as a photon flux, cannot be stored or mixed in the growth medium in contrast to other energy sources such as organic substrates. Consequently, characteristics of light kinetics differ from the kinetics of other substrates. They were addressed in the photobioreactor design in chapter 3.1.2 and reevaluated to distinguish between light- and nutrient-related effects in chapter 3.6. Pigments physically absorb photons [26], converting the light energy to electrical energy via excitation, and, finally, to chemical energy [64]. The absorption of photons by microalgal pigments causes the excitation of pigments and can be described as the specific photon absorbance rate $r_{\mathrm{h}\nu,\mathrm{abs}}$:

$$r_{\mathrm{h}\nu,\mathrm{abs}} = \sigma_{\mathrm{X,abs}} \cdot I_{\mathrm{h}\nu} \qquad \text{Equation 1}$$

with the absorption cross-section of the biomass $\sigma_{\mathrm{X,abs}}$ and the local light intensity $I_{\mathrm{h}\nu}$. The absorption step is mechanistically independent from subsequent reactions that may be summarized to a second step in the most simplified attempt of light kinetics. This second step includes the energy transfer and conversion along the electron transport chain, the CO_2 fixation in the Calvin-Benson cycle and anabolic reactions, which together results in the yield of biomass on photons. The photoautotrophic growth can then be approximated analogously to heterotrophic organisms according to Pirt's law, if no other limitations besides light are assumed:

$$r_X\left(r_{\mathrm{h}\nu,\mathrm{abs}}\right) = y_{\mathrm{X,ph}} \cdot r_{\mathrm{h}\nu,\mathrm{abs}} - r_{\mathrm{X,m}} \qquad \text{Equation 2}$$

for light limiting conditions ($r_{\mathrm{X}} \leq r_{\mathrm{X,max}}$). Metabolic processes related to maintenance shorten the net energy efficiency of growth $y_{\mathrm{X,ph}}$ by the specific maintenance rate $r_{\mathrm{X,m}}$. Figure 2 illustrates the photosynthesis irradiance response curve (PI-curve) as the light kinetics under ideal conditions (Equation 2) [26]. Many PI-curves in the literature use the light intensity instead of the light absorption. The description based on $r_{\mathrm{h}\nu,\mathrm{abs}}$ is beneficial for the investigation of the light kinetics as it directly reveals the metabolic efficiency $y_{\mathrm{X,ph}}$ in the cell. $y_{\mathrm{X,ph}}$ approaches $y_{\mathrm{X,ph,max}}$ shortly before light saturation due to the maintenance related processes decreasing relatively to the growth rate. The absolute energy requirement for maintenance increases with the photosynthetic activity, but diminishes relative to the growth rate [65]. Rounder correlation curves, such as the Michaelis-Menten shape, can result from dissipation of photons or metabolic steps subsequent to the photosynthesis.

When the growth rate approaches $r_{X,max}$, any additional absorbance of photons causes heat dissipation. For the further increase of the photon absorbance rate due to higher light intensities, light saturation changes over to light inhibition. Light inhibition causes photodamage in addition to heat dissipation. The heat dissipation, maintenance and repair mechanisms set light limiting conditions as the optimization target to yield high metabolic efficiencies of biomass on absorbed photons [26].

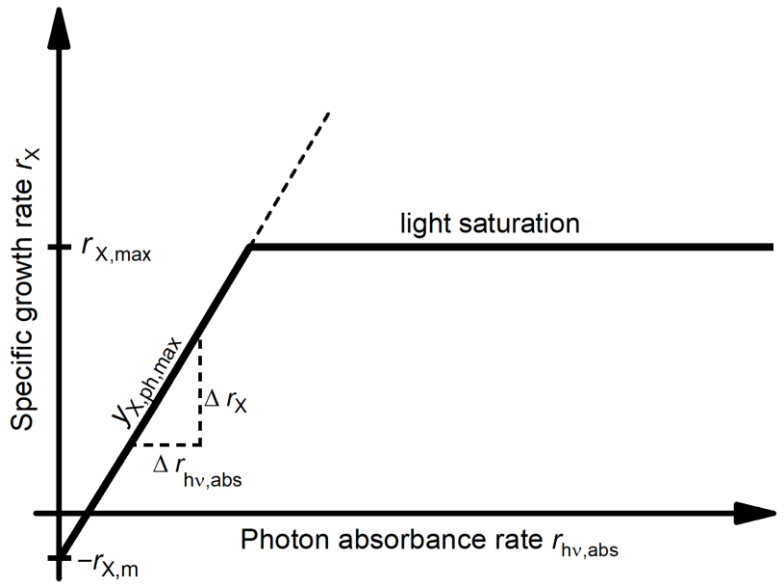

Figure 2: Photosynthesis irradiance response curve based on absorbed photons in the most simplified shape as given by Equation 2.

The intended light conditions vary according to the interplay of light kinetics, target products and other process conditions [26]. Understanding these kinetics and adjusting the PBR design accordingly can significantly enhance the efficiency of microalgal photosynthesis and biomass yields [66]. Estimation of light kinetics further supports the analysis of metabolic efficiency (chapter 3.6) across the low nutrient feeding rates applied in chapter 3.4 to enhance efficient starch accumulation.

1.4 Biomass composition – the scope of variability and limits of viability

Microalgal biomass composition depends on growth conditions, which were investigated by systematic variation of micro-feeding rates aiming for efficient starch accumulation in chapter 3.4 of this thesis. This variability in composition affects culture viability, productivity, and efficiency evaluation. Light and metabolic kinetics determine the photosynthetic performance under given growth conditions. Models require knowledge or assumptions on the light profile in the PBR, the nutrient availability and concentrations, strain specific characteristics and the metabolic state of the culture, e.g. the acclimation and the metabolic composition. Microalgae mainly consist of proteins, carbohydrates and lipids (Figure 3). Pigments, deoxyribonucleic acid (DNA), ribonucleic acid (RNA), ash, and some essential micronutrients comprise a smaller fraction of the biomass.

Minimum fractions of each biomass constituent are required for survival and to maintain the functionality of the photosynthetic and metabolic mechanisms [26], the totality of these fractions is referred to as 'active biomass' [67]. Accumulation of any constituent lowers the fractions of the functional constituents on a mass balance, while the active biomass fraction is considered to hardly change composition. Influencing the carbon partitioning to different constituents by adjusting the growth conditions can optimize biomass quality for various applications. Some cellular constituents, especially, lipids and carbohydrates, may be accumulated to 50 % and more. The high potential starch fraction demonstrates the suitability of microalgae for efficiently utilizing ^{13}C to produce isotopically labeled glucose, which was the aim of the production system designed in chapter 3.1 and 3.2.

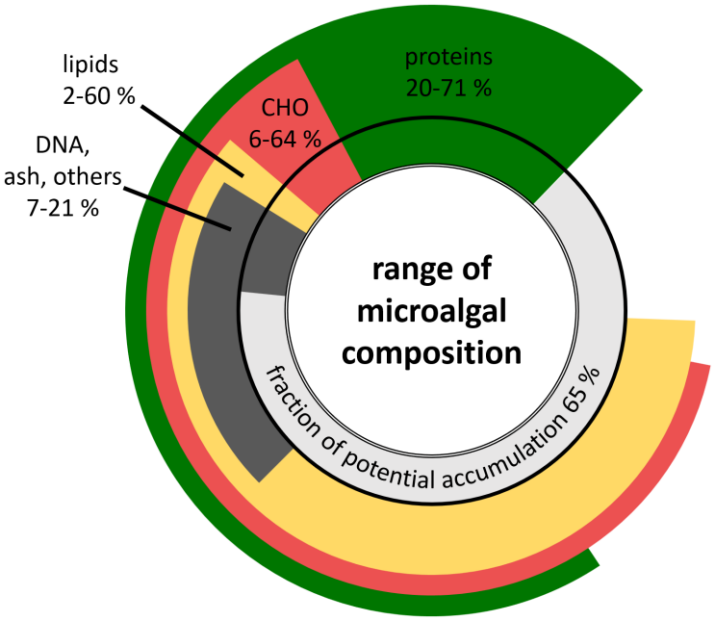

Figure 3: Variability of the cellular composition of microalgal dry mass in photoautotrophic cultivations. Active biomass typically contains ~ 40 % proteins, while lower protein fractions mainly result from mass 'dilution' by accumulated storage compounds. In the diagram, lower and upper boundaries are illustrated inside and outside the black circle, respectively. The lightest segment (fraction of potential accumulation) indicates the remaining fraction of the cell that may theoretically be filled up with any (accumulated) biomass constituent [26].

1.5 The photosynthetic yield of active biomass and storage compounds

In addition to ^{13}C utilization efficiency, microalgae also need to grow with high photosynthetic efficiency to achieve high productivities. The underlying metabolic mechanisms and intrinsic boundaries are addressed below to conceptually frame the principles of PBR control (chapter 3.2.3 and 3.2.4), the experimentally determined efficiencies of micro-feeding (chapter 3.4.5), and the kinetic reevaluation (chapter 3.6). Photosynthetic efficiency is governed by photon absorption, primary carbon fixation, and the subsequent intracellular metabolic processes derived from the primary fixed carbon. Photosynthesis is essentially the fixation of carbon in the form of simple sugar derivates (sugars). The formation of these carbohydrates (CH_2O) is stoichiometrically described in the gross photosynthetic equation as:

$$n\ CO_2 + n\ H_2O \rightarrow (CH_2O)_n + n\ O_2 \qquad \text{Equation 3}$$

Theoretically, based on energy balances, eight photons are required to evolve one oxygen molecule corresponding to the fixation of one carbon atom, or, in other terms, the theoretical yield of oxygen on photons is $Y_{O2,ph,theo}$ = 0.125 $mol_{O2} \cdot mol_{ph}^{-1}$. In reality, $Y_{O2,ph,theo}$ cannot be reached, presumably, due to intrinsic photon losses or limitations. Experimental studies revealed the minimum need of 10 photons per released molecule of oxygen giving $Y_{O2,ph}$ = 0.100 $mol_{O2} \cdot mol_{ph}^{-1}$ [68], which corresponds to the equimolar amount of fixed carbon atoms. The molar yield on photons, here, normalized to one C-unit in sugars, calculates as

$$Y_{CH2O,ph} = Y_{O_2,ph} \cdot \frac{n_{CH2O}}{n_{O2}} \qquad \text{Equation 4.}$$

This gross photosynthetic balance describes the need of 10 mol photons to deliver energy for the photosynthetic fixation of 1 mol carbon in sugars, $Y_{CH2O,ph}$ = 0.100 $mol_{CH2O} \cdot mol_{ph}^{-1}$.

Describing the biosynthesis of microalgae subsequent to photosynthesis in analogy to that of heterotrophic organisms is supported by the common evolutionary origin of prokaryotes and mitochondria according to the endosymbiosis theory. Subsequent to initial sugar formation, other cellular compounds are synthetized based on these sugars. The sugars are partially degraded in respiratory processes to gain the energy carriers ATP and NAD(P)H. The energy carriers from respiration are essential to drive anabolic reactions. Further respiration, but to a smaller extend than for biosynthesis, is needed to provide energy to maintenance related mechanisms [69,70]. The respiration reverses the photosynthetic reaction on a net elemental balance and reduces the photosynthetic yield for the formation of the active biomass to the net value below the above-mentioned values.

The molar yield of C-normalized active biomass (actX) on photons (ph) is then described as

$$Y_{actX,ph} = Y_{actX,CH2O} \cdot \frac{M_{CH2O}}{M_X} \cdot Y_{CH2O,ph} \qquad \text{Equation 5}$$

with the molar mass of sugars M_{CH2O} = 30.0 $g \cdot mol_C^{-1}$ and of actX M_{actX} = 22.9 $g \cdot mol_C^{-1}$ (q_C = 0.52 [67]), and the typical heterotrophic yield of actX on sugars $Y_{actX,CH2O} \approx 0.5$ (m/m) as recalculated from molar yields on glucose in [71]. The resulting molar photosynthetic yield of 0.066 $mol_{actX} \cdot mol_{ph}^{-1}$ corresponds to the mass yield $Y_{actX,ph}$ = 1.50 $g_{actX} \cdot mol_{ph}^{-1}$ and to the demand of 15.27 mol photons per mol carbon fixed in active biomass.

Experimental findings agree with this roughly estimated value of $Y_{actX,ph}$. For the green microalga *Scenedesmus obliquus*, $Y_{X,ph}$ = 1.4 $g \cdot mol^{-1}$ was found under nitrogen depletion and low light conditions [72]. This value corresponds to a photoconversion efficiency (PCE) of

13 to 15 % depending on the biomass composition, which is comparatively close to the theoretical maximum of 17-18 %.

This efficiency metric is essential for evaluating micro-feeding cultivations described in chapter 3.4.5 and for guiding the further optimization of light and nutrient supply to maximize productivity and achieve the desired biomass composition. The major variability of the biomass composition (Figure 3) originates from the accumulation of the storage compounds and, potentially, their subsequent respiration or conversion: lipids, or, more explicitly triacylglycerol (TAG), starch (STA), and, in some cases, proteins. Without considering protein accumulation, the total microalgal biomass can be represented by three main constituents: the active biomass plus the storage compounds TAG and STA Table 1. TAG and STA share to be composed of carbon, oxygen and hydrogen atoms only, but largely differ in energy and carbon content due to different metabolic pathways [73] in the heterotrophic part of the cell.

The efficiency of the photon use in biosynthesis may be evaluated on three levels: mass, energy and carbon (Table 2), dependent on the optimization target of the cultivation. STA biosynthesis is highly efficient on a mass balance. But the energy content of STA is comparatively low, which is also shown by the degree of reduction (DoR) being close to zero. The higher energy content of TAG is a result from roughly 40 % release of primarily fixed carbon as CO_2 during TAG biosynthesis from sugars. The CO_2 release occurs during catabolic respiration to feed the TAG synthesis but comes at the cost of less carbon being fixed in the biomass per photon. In other terms, the carbon yield is lower for TAG than for starch, but the energy content of TAG is higher. The inversely correlated effects of carbon loss and energy content result in a difference < 10 % in the efficiency of energy fixation, playing only a minor role in process design when no further metabolic conversion is intended.

The target applications play the key role in defining the objectives for process design based on the desired biomass composition. Biomass rich in lipids is particularly valuable for industries such as biofuel production and cosmetics, owing to its potential for high energy content and beneficial properties for skin care formulations. Starch-rich biomass undergoes efficient biological and chemical conversion into sugars, which is crucial for both nutritional purposes and various chemical applications. In the context of this thesis, for ^{13}C labeling the primary focus is on biological and chemical accessibility of ^{13}C and maximizing the efficiency of carbon fixation to enhance overall productivity, which both demand high starch accumulation. Increased starch accumulation enhances the utility and economic viability of the ^{13}C-biomass production process and subsequent processing steps.

Table 1: Average composition of biomass, starch (STA) and TAG. $e_{C,k}$: elemental fraction of carbon C in compound k, M molecular weight.

Compound k	**Elemental formula**	$e_{C,k}$	**M / g·mol^{-1}**
STA	$CH_{1.67}O_{0.83}$	0.45	26.95
TAG	$CH_{1.87}O_{0.11}$	0.77	15.63
Active biomass*	$CH_{2.08}O_{0.40}N_{0.15}P_{0.01}$	0.52	22.90
STA-rich biomass: 55 % active biomass + 45 % STA	$CH_{1.90}O_{0.59}N_{0.08}P_{0.01}$	0.49	24.72
TAG-rich biomass: 55 % active biomass + 45 % TAG	$CH_{1.99}O_{0.27}N_{0.08}P_{0.01}$	0.61	19.63

* elemental composition in agreement with [67,74]

Table 2: Overview of the theoretical photosynthetic yields ($Y_{k,ph}$), the degree of reduction (DoR) and the heat of combustion (ΔH_c^0) for different biomass compositions, TAG and STA.

Compound k	$Y_{k,ph}$ **/ g·mol^{-1}**	$Y_{k,ph}$ **/ mol$_C$·mol$_{ph}^{-1}$**	**DoR***	ΔH_c^0****/ kJ·mol$_C^{-1}$**	ΔH_c^0**/ kJ·g^{-1}**	$\Delta H_c^0 \cdot Y_{k,ph}$ **/ kJ·mol$_{ph}^{-1}$**
STA	2.22	0.082	0.01	[75] 469.2	17.41	38.65
TAG	0.91	0.058	1.65	[76] 617.6	39.51	35.96
Active biomass***	1.50	0.066	0.78	539.2	23.55	35.32
STA-rich biomass: 55 % active biomass + 45 % STA	1.82	0.074	0.44	507.7	20.54	37.46
TAG-rich biomass: 55 % active biomass + 45 % TAG	1.23	0.063	1.17	574.5	29.27	36.13

* DoR calculation was based on biomass composition in Table 1 with oxidation numbers H: +I, O: -II, N: -III and P: -V.

** The ΔH_c^0 of TAG was calculated based on [76] and the assumption of TAG containing equimolar amounts of C16 and C18:1 fatty acid residues due to their high abundance in microalgae [77–79] and esterification to glycerol 3-phosphate [80]. ΔH_c^0 of the biomass was linearly correlated to the DoR with starch and TAG as the boundaries ($\Delta H_c^0 = 90.488 \cdot \text{DoR} + 468.3$) in agreement of a theoretical assessment of active biomass constituents and in the range of exemplary measurements.

*** elemental composition in agreement with [67,74]

PBRs essentially create a controlled environment to promote efficient cell growth and productivity. The design and operational parameters of PBRs are crucial for optimizing microalgal growth conditions, including light distribution with respect to light kinetics, nutrient and CO_2 supply, as well as temperature and pH control. This makes the PBR a critical component in the production of stable isotopically labeled substances, as the conditions directly influence the metabolic activity and biomass compositions of the cultivated microalgae. Addressing these PBR design principles, as outlined in chapter 3.1, ensures that the cultivated cells are exposed to consistent and optimized growth conditions, thereby enhancing the overall efficiency and quality of isotopic labeling and biomass production processes in this project.

2 Materials & Methods

2.1 Microalgal strains: *Chlorella vulgaris* H 14

The *Chlorella vulgaris* production strain 1996/H 14 (H 14, Czech patent 299352) was selected by the Institute of Botany of the Academy of Sciences of the Czech Republic (ASCR, Třeboň). The Institute of Microbiology of the ASCR provided the strain H 14 under a material transfer agreement. In other studies, *C. vulgaris* H 14 was grown heterotrophically with maximum specific growth rates of 4.3 day^{-1} at 35 to 37 °C and pH 6.0 to 7.5 [81].

2.2 Cultivation medium

The cultivation medium was based on the common tris(hydroxymethyl)aminomethane (TRIS)-acetate-phosphate (TAP) medium with three stock solutions: the potassium phosphate buffer [82], Beijerinck's four-salt nutrient solution [83], and Hutner's trace element solution [84]. No acetate was used to avoid organic carbon sources and ensure photoautotrophic growth. TRIS (2.42 $g \cdot L^{-1}$) was only supplied to the systems without pH regulation. One liter of standard medium was composed of water and 3.00 mL phosphate solution (K_2HPO_4 28.8 $g \cdot L^{-1}$; KH_2PO_4 14.4 $g \cdot L^{-1}$), 25 mL salt solution (NH_4Cl 15.0 $g \cdot L^{-1}$; $MgSO_4 \cdot 7H_2O$ 4.0 $g \cdot L^{-1}$; $CaCl_2 \cdot 2H_2O$ 2.0 $g \cdot L^{-1}$), and 20 mL Hutner's trace element solution ($Na_2C_{10}H_{14}N_2O_8$ (EDTA) 2.5 $g \cdot L^{-1}$; H_3BO_3 $5.7 \cdot 10^{-1}$ $g \cdot L^{-1}$; $ZnSO_4 \cdot 7H_2O$ 1.1 $g \cdot L^{-1}$; $MnCl_2 \cdot 4H_2O$ $25.5 \cdot 10^{-2}$ $g \cdot L^{-1}$; $FeSO_4 \cdot 7H_2O$ $25.0 \cdot 10^{-2}$ $g \cdot L^{-1}$; $CoCl_2 \cdot 6H_2O$ $8.0 \cdot 10^{-2}$ $g \cdot L^{-1}$; $CuSO_4 \cdot 5H_2O$ $8.0 \cdot 10^{-2}$ $g \cdot L^{-1}$; $(NH_4)_6Mo_7O_{24} \cdot 4H_2O$ $5.5 \cdot 10^{-3}$ $g \cdot L^{-1}$). The medium was modified in agreement with the elemental balance from [74] to enable sufficient supply and simultaneous limitation of the macronutrients S, N, and P. The phosphate content was reduced by the volume of the phosphate solution (3 mL). The sulfate content was lowered in the salt solution by partly exchanging $MgSO_4 \cdot 7H_2O$ by $MgCl_2 \cdot 6H_2O$ (NH_4Cl 15.0 $g \cdot L^{-1}$; $MgSO_4 \cdot 7H_2O$ $5.3 \cdot 10^{-1}$ $g \cdot L^{-1}$; $MgCl_2 \cdot 6H_2O$ 2.86 $g \cdot L^{-1}$; $CaCl_2 \cdot 2H_2O$ 2.0 $g \cdot L^{-1}$).

2.3 Cultivation systems

Three cultivation systems were used for this dissertation: Shake flasks for growing cultures to provide inoculum for photobioreactors (PBRs) and for strain maintenance; Small flat-panel photobioreactors for preliminary testing; and the compact photobioreactor (cptPBR) for the main cultivations.

2.3.1 Shake flasks for preculture cultivation

Precultures were grown in shake flasks with a total volume of 500 mL. Gas was passively exchanged through a cellulose plug (Culture plug ROTILABO®, 45 P) in the wide neck of the flask (47 mm). Gas exchange was supported, and sedimentation was prevented by a horizontal

shaker (100 min^{-1}) equipped with flask holders on a warm white LED panel. The culture volume (200 mL) was illuminated from below with an illumination area of 65 cm^2. Light settings were adjusted in gradients over time to provide constant light supply per biomass. The shake flasks were placed in a cultivation chamber at 27 °C.

2.3.2 Flat-panel photobioreactor (0.2 L) for preliminary experiments

The culture volume (0.2 L) of flat-panel photobioreactors was illuminated at 100 mm x 100 mm with warm white LEDs and lenses. The light path was 2 cm. Gassing (0.5 vvm) and mixing were performed through a membrane with a mixture of air and 1 % (v/v) CO_2. Autoclaving the flat-panel PBR and sterile filters (ROTILABO® Polyethersulfone, 0.45 µm, 15 mm) for in and off-gas ensured axenic conditions. The flat-panel PBR were placed in a cultivation chamber at 27 °C. Due to limitations in control, monitoring and sampling volume, the flat-panel PBR were only used for preliminary experiments. The optimization of the light regime and the initial setup of for oxygen removal using a proton exchange membrane fuel cell (PEM, Horizon fuel cell technologies, 0.3 W) were conducted in this system. The PEM proof of concept included gas chromatographic tests for gas tightness. After successful PEM operation on a small scale, development continued for the compact photobioreactor.

2.3.3 Compact photobioreactor

In this section, only technical details on the compact photobioreactor will be added to the fundamental design and advancements in chapter 3.1. The core body of the cptPBR consisted of a horizontal glass tube (L = 500 mm, d = 300 mm, CE 0035, Boro 3.3, M703-1194306, SL6678, PS p_s=-1/+1.5 bar, T_s = -50/+200 °C, $\Delta\Theta$ = 180 K). The ends of the cptPBR's core body were sealed with stainless-steel plates housing the measurement instruments, gassing connectors, and light installations. The measurement instruments included a spectral sensor (Avantes, SDP-7UV200, AvaSpec), a pH sensor (Hamilton Polilyte plus 120; P/N: 242431, two-point calibrated: pH 4.01, Hanna Instruments HI 7004, and pH 7.01, Hanna Instruments HI7007), and a temperature sensor (PT100; transmitter: Mettler Toledo M 300, two-point calibrated: 0 °C and 100 °C with GMH 3710), as well as a pO_2 sensor (Hamilton, Visiferm DO 120, P/N: 242450, calibrated in nitrogen and air) for all cultivations. The cultivation temperature was controlled at 27 °C. The cooling unit (Huber Unichiller 025-MPC) cooled the cptPBR through two cooling bars (d = 22 mm, L = 500 mm) via flow regulation. The pH was controlled to 7.5 mainly by the addition of 4 M NaOH (peristaltic pump Alitea-XV) and 2 M HCl (peristaltic pump Alitea-XV). Stock solutions were fed through a 4-channel peristaltic

pump (Masterflex® Ismatec® Reglo). The pump was current controlled and calibrated with tubes for micro-feeding (ID of Pharmed® 3 stop tubing: 0.89 mm, 0.3 $mL \cdot h^{-1}$ to 296.0 $mL \cdot h^{-1}$).

Light was supplied by 2664 LED spots (Nichia, NS6L183BT) on 37 LED bars with 72 spots each. The LED bars were placed in horizontal glass tubes (Glass tubes Duran®, borosilicate glass, d = 16 mm). Cultivations were started at a volume of 28.0-28.5 L to allow for a maximum of 3 L of sampling volume, while the top layer of glass tubes with light bars stayed completely below the liquid level also during gassing. Without gassing, the liquid volume was 19 mm above the top glass tubes with the light bars and raised locally to 30 mm during gassing. The liquid level varied throughout the cultivation due to sampling and feeding (± 1.5 L), while the average working volume of the cptPBR was 27 L in most cultivations. The headspace without gassing measured 53 mm in height providing 4.2 L headspace volume.

The content of the cptPBR was mixed by gassing (≈ 1 vvm). Gassing installations inside the cptPBR were developed within this project (chapter 3.1.4). The off-gas outlet was connected to a condenser, which reduced the moisture in the off-gas to allow passage through sterile filters (0.45 µm). The gassing setup in the periphery of the cptPBR differed for the open system and closed gas loop. In the open setup the compressed air (29.7 $L \cdot min^{-1}$, MKS 1579A, calibrated by Gilian Gilibrator wet bubble cell 2 LPM - 30 LPM) was supplied and enriched with 1 % (v/v) CO_2 (0.3 $L \cdot min^{-1}$, MKS GE50A, calibrated by Gilian Gilibrator wet bubble cell 20 cc/min - 6 LPM). For the closed gas loop, the diaphragm vacuum pump (KNF, Laboport®, N816.1.2 KN.18, rated flow of 30 $L \cdot min^{-1}$) conducted the gas flow at effectively 24 to 27 $L \cdot min^{-1}$. The medium was initially in equilibrium with a 1 % (v/v) CO_2 atmosphere and during cultivation CO_2 (MKS 1179, calibrated by Gilian Gilibrator wet bubble cell 1 cc/min - 250 cc/min) was added in equimolar amounts to the calculated consumption. N_2 (MKS 1179, calibrated by Gilian Gilibrator wet bubble cell 1 cc/min - 250 cc/min) was supplied to compensate for pressure deviations originating from humidity in sterile filters in the gas loop upon demand.

For some cultivations, online transmission measurement was implemented in an external loop with a continuously circulating culture volume directly connected to the reactor. The light source (Osram SFH 4544 Infrared Emitter, 940 nm, max. 75 mW), the flow-through cuvette (d = 10 mm) and the sensor were housed in sealed enclosure to prevent interference from ambient light or stray light from the cptPBR.

2.4 Methods for the characterization of the compact photobioreactor

Mixing and gassing were evaluated through experimental and modeling approaches to advance the cptPBR design especially regarding the light/dark frequency experienced by the microalgae.

2.4.1 Experimental investigation of the flow pattern and mixing rates

After the pH stabilized ($pH_0 = 7.2 \pm 0.2$) the investigation of mixing by gassing (air, 30 $L \cdot min^{-1}$) started. The radial and longitudinal mixing were evaluated with two techniques: step response of pH (1) and pH-dependent coloring with red cabbage extractive (2). The changes in pH (1) or color and pH (2) were induced by acid (1: 0.1 M HCl, 27 mL; 2: 4 M HCl, 20 mL) or base (2: 4 M NaOH, 20 mL) injections above the liquid level. The liquid in the photobioreactor (PBR) was composed of deionized water (1: 27 L; 2: 26 L) and the red cabbage extractive (2: 1 L). The red cabbage was cut and boiled in deionized water to extract the colorant. The red cabbage extractive displayed color changes in response to varying pH values (Figure 4). These changes are attributed to anthocyanins, compounds in red cabbage known for their high pH sensitivity [85]. The color variability results from alteration in charge state and structure [86]. The color change visualized the pattern of mixing and supported quantitative analysis.

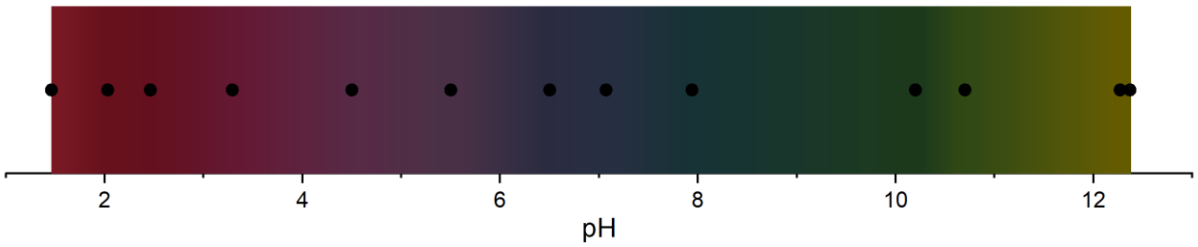

Figure 4: Color scale of red cabbage extractive (anthocyanin) diluted in deionized water. The pH was adjusted with 4 M NaOH and 4 M HCl to receive the color gradation (●) from photographs complemented with linear interpolation.

To analyze the mixing on different levels, the colorant experiments (2) were video recorded from two perspectives. The perspective from the plate or from the longitude corresponded to the injection method. The injection method caused the mixing time to result predominantly from either radial or longitudinal mixing as longitudinal mixing was slower. For the analysis of longitudinal mixing (1 and 2), acid was injected by a peristaltic pump (Alitea-XV, 99.9 %, 35.3 s) through one needle at port 2 in the left plate of the cptPBR. Base was analogously added at port 4 (Figure 5). The plate of stainless-steel was replaced by acrylic glass to investigate radial mixing. Radial investigations (1) used a tube (14 mm, pores every 5 mm) at port 3 to generate uniformly distributed acid droplets along the longitude by a peristaltic pump (Alitea, U1-MIDI-D; 1: 50 %, 10.6 s; 2: 99.99 % 26.5 s). Data acquisition (interval: 1 s) continued until the pH stabilized ($\Delta pH \leq 0.02$) for ≥ 360 s (1) or no color change was visible (2). After the termination of each acid experiment the addition of NaOH (1: 0.1 M, 27 mL; 2: 4 M NaOH,

20 mL as an additional experiment) at port 4 neutralized the acid and the resulting NaCl remained in the solution for replicates. The base injection as analogously used to the acid injection for the video recording of coloring experiments.

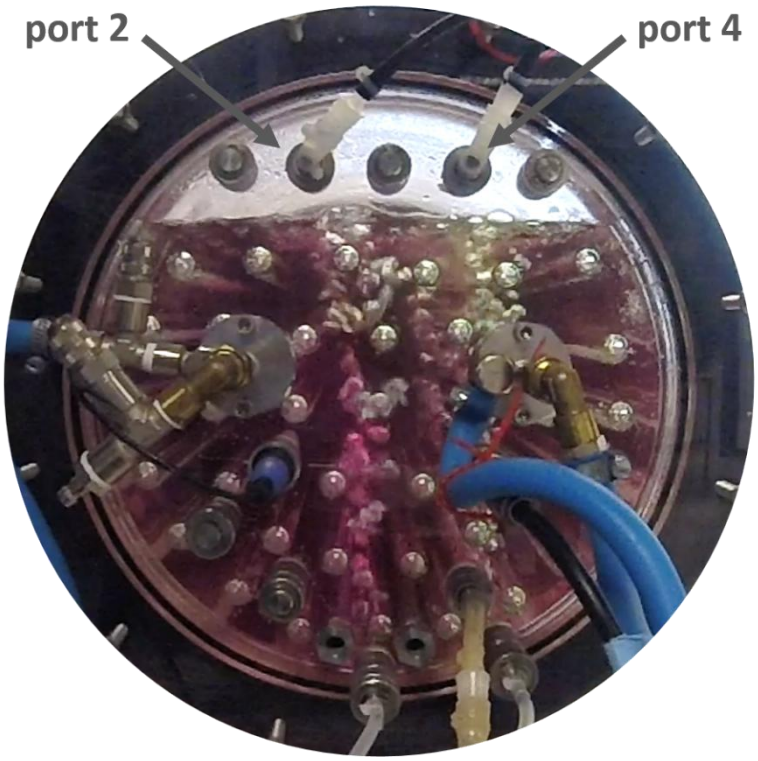

Figure 5: Acrylic plate that replaced the stainless-steel plate of the compact photobioreactor to host ports and installations during the experiments for the determination of the mixing time with method (2). The picture shows the injection of base for equilibration at port 4.

Integrated mixing times from pH measurements were analyzed as step responses with pH tolerances of 5 % (example of step response and calculation in Figure 6). This mixing time was integrated over the entire cptPBR. The differences in mixing dimensions were solely due to the injection method: (1) radial mixing: injection along the longitude, and (2) longitudinal mixing: injection at a single port in the stainless-steel plate. The predominance of longitudinal mixing as the slower process results from the inherent characteristics of this mixing dimension.

More detail on the mixing pattern in the cptPBR was revealed by the coloring experiments. Changes of the RGB color values at different positions in the cptPBR were investigated over time. The red color value was especially valuable due to its inversely proportional behavior with the pH in the range of 2 to 8 (Figure 7).

The acquisition of RGB values was performed through video recording. Average HEX color values over a 5x5 pixel area were extracted from these videos using a software tool (Just Color picker). This process was automated to the measurement interval of 1 s using Auto Keyboard

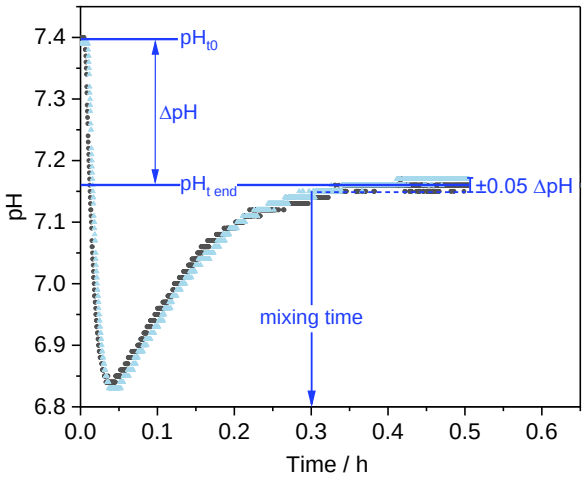

Figure 6: Graphical interpretation of the mixing time based on the step response to acid injection in the cptPBR. Calculations were based on duplicates (as shown here for one preliminary construction) or triplicates and the mixing time was defined as the time from injection to the final pH value with 5 % tolerance of the pH difference.

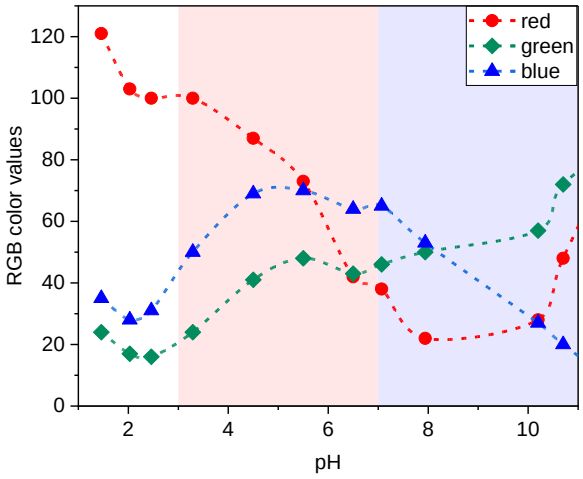

Figure 7: RGB color values were extracted from photographs of samples at different pH values. The colors referring to the RGB values in the diagram are displayed in Figure 4. The background colors highlight the color of the value used for picture analysis. Connecting lines only improve visibility.

(MurGee.com) at each measurement position. The HEX values were subsequently converted to RGB values to facilitate the numerical expression of red color differences. The color values were recorded at different positions in the cptPBR from both perspectives for longitudinal and radial mixing. The red color value over time was mimicked by a logistic fit. The data evaluation method differed for longitudinal and radial mixing.

At longitudinal positions, the distinct and directed color shift (Figure 9) was associated with the shift of inflection points of the logistic fit. Preliminary testing of appropriate spatial mixing intervals was performed at eight longitudinal positions (A1, A2, B1, B2, C1, C2, D1 and D2) with the red color values plotted in Figure 8. The distance between the measurement positions was alternately 1- and 5-fold distance of the straight distance of neighboring LEDs (~19.5 mm).

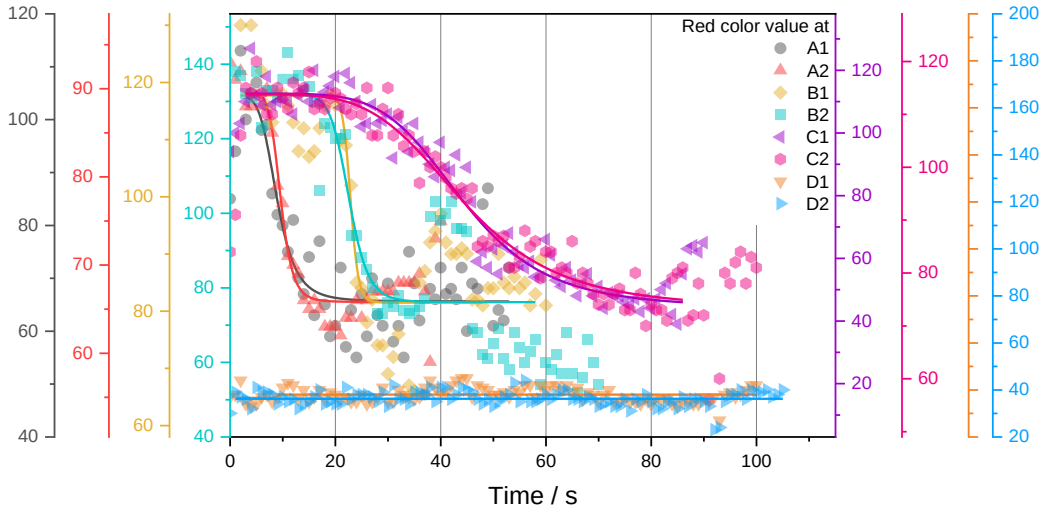

Figure 8: Red color values of preliminary longitudinal mixing experiment using the reference gassing tube after base injection with fitted curves for visibility.

Testing the different positions showed, which positions and distances were analyzable. The positions D1 and D2 were not analyzable due to shading and reflection on the cptPBR surface overlaying the visible color change. Positions labeled within the same letter (A, B, C, D) were each 19.5 mm apart. Comparing the position A1, B1 and C1 to A2, B2 and C2 being each 19.5 mm apart, the noise of the red color value exceeded the measurable difference in the color change. To obtain differentiable results, positions in the 5-fold distance of two neighboring LEDs was chosen to record color values for the final data assessment.

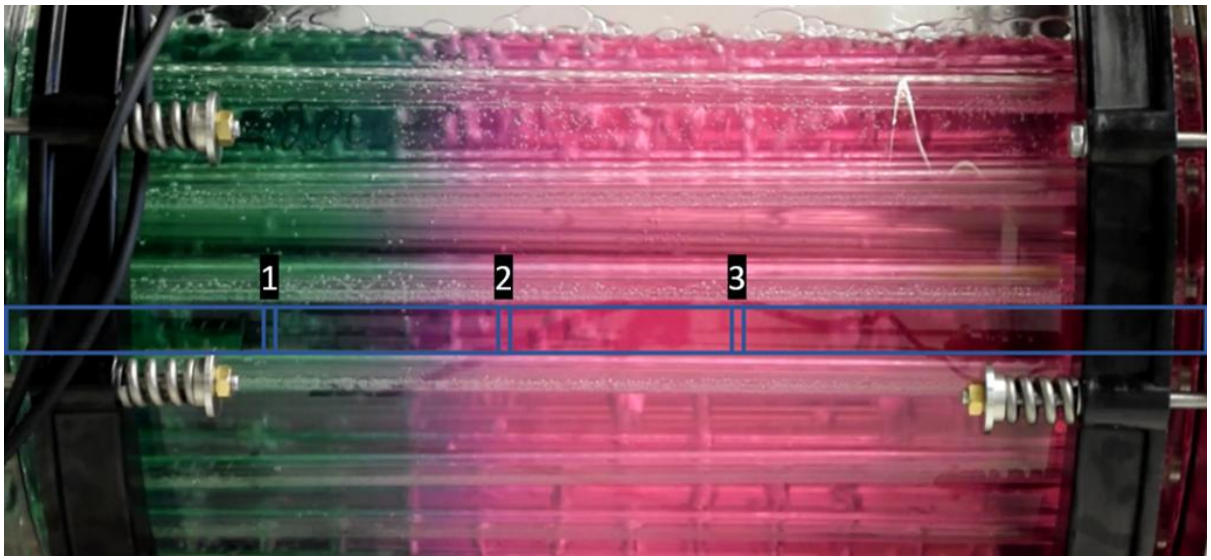

Figure 9: Final measurement positions for mixing analysis along the longitude labeled on a photograph of the cptPBR.

The positions for the final evaluation of the longitudinal mixing were 110.0 mm, 207.5 mm and 305 mm ± 2.5 mm from the injection port and varied in height within the areas 1, 2 and 3 (Figure 9). The variation in height prevented color deviations caused by reflections on the glass body of the cptPBR during the testing of different gassing tubes. The preliminary testing data set from Figure 8 was further used to exemplify the data processing method.

The logistic fit of red color values (RED, Equation 6) at three positions were used to determine the time t of longitudinal mixing

$$\mathrm{RED} = \frac{A_1 - A_2}{1 + \left(\frac{t}{t_0}\right)^p} + A_2 \qquad \text{Equation 6}$$

with the fitted parameters A_1, A_2, t_0 and p.

The fastest change in color, visualizing the pH, was recorded, when the color layer passed the measurement position as between position 1 and 2 in Figure 9. Mathematically, the fastest change is defined as the maximum slope of the function, so, the inflection point of the sigmoidal curve, which was in agreement with the optical impression.

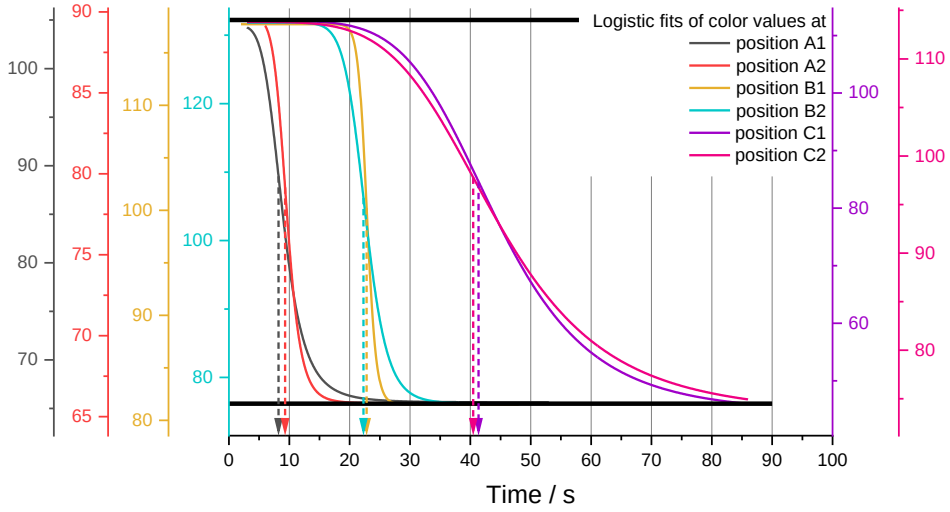

Figure 10: Logistic fits of red color values of preliminary mixing experiments using the reference gassing tube. The graphs from Figure 8 were rescaled for better visibility, and the times corresponding to the inflection points were labeled with arrows.

The necessary condition of the inflection point is defined by the second derivative of the function equaling zero, which gives:

$$t = t_0 \left(\frac{p-1}{p+1}\right)^{\frac{1}{p}} \qquad \text{Equation 7}$$

The time of inflection point for the change in red color values was compared to the time at other positions. The differences were interpreted as the mixing time for the respective distance along the longitude, further referred to as optical mixing time.

At radial positions, the use of inflection points for data evaluation was not applicable. Indistinct mixing led to blurry color development, resulting in generally flatter slopes in the logistic fits, with greater variation in slopes at different positions. This increased the potential for high errors in determining the inflection point. To account for the blurriness and reversing color development, the 80 % red color change was chosen. For the analysis of the radial flow pattern, seven positions on the cross-section were defined (Figure 11), and color values were recorded every second for the positions listed in Table 3.

The red color values of all positions on the cross-section were fitted by the same logistic fit function as the longitudinal values (Equation 6). To analyze the radial mixing pattern, the initial change induced by mixing needed to exceed the fluctuations. Fluctuations were < 20 % of the step response from A1 to A2 for the analyzed data, so completing 80 % of red color change was the target value for comparison as given by Equation 8.

$$t = t_0 \cdot 0.25^{\frac{1}{p}} \qquad \text{Equation 8}$$

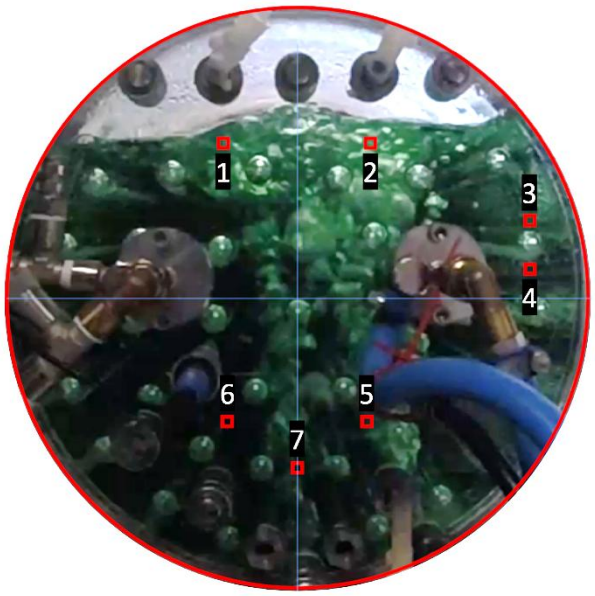

Figure 11: Measurement positions for radial mixing analysis labeled on a photograph of the cptPBR cross-section through the acrylic plate.

Table 3: Color measurement positions for radial mixing analysis.

Measurement no.	x from center / mm	y from center / mm
1	-38	80
2	38	80
3	120	40
4	120	15
5	36	-64
6	0	-88
7	-36	-64

The calculated times of 80 % color change completion were relatively interpreted to gain information on the mixing pattern, while eliminating disturbances of red cabbage extractive concentration or quality. The quality of red cabbage extraction changed due to salt concentrations from previous pH shifts and storage.

2.4.2 Simulation of gassing and mixing

High-resolution 3D simulations of gassing and mixing were conducted using a multiphase solver in OpenFOAM at the Institute of Mechanical Process Engineering and Mechanics at KIT. The process involved introducing air into the liquid volume of the photobioreactor through one or more gassing tubes, which created an air fraction within the water. This air fraction induced a liquid flow, driven by density and pressure differences. After the start-up phase, the simulation was continued until a steady state was reached. The simulation outcome provided flow velocities and directions for approximately 20,000 geometrically defined cells.

2.4.3 Determination of the volumetric gas transfer coefficient (k_La)

In respect to Henry's law the Henry coefficient ($H_{O2,H2O}$ / g·L^{-1}·bar^{-1}) correlates the oxygen transfer rate (OTR / g·L^{-1}·s^{-1}, Equation 9) to the time derivative of the partial pressure of oxygen in equilibrium with the medium (dpO_2/dt / bar·s^{-1}, Equation 10). The partial pressure of oxygen pO_2 over the time t was measured in triplicate after oxygen was stripped with N_2 to set the get pO_2(t) < 5 %. The air flow (30 L·min^{-1}) was started and the initial time t_0 and pO_2(t) was recorded until pO_2(t) > 15 %. The negative slope of ln(pO_2^* − pO_2(t)) of the recorded data gave the volumetric gas transfer coefficient of oxygen (k_La / s^{-1}, Equation 11). The saturated partial

pressure of oxygen (p^*_{O2}) was determined by gassing with air until pO_2(t) in the cptPBR stabilized. The cptPBR was filled with 1 x TP-medium (details on medium composition in 2.2, 27 L, pH 7.5).

$$OTR = k_L a \cdot (c^*_{O2} - c_{O2}) = H_{O2,H2O} \cdot \frac{dpO_2}{dt} \quad \text{Equation 9}$$

$$\frac{dpO_2}{dt} = k_L a \cdot (pO^*_2 - pO_2) \quad \text{Equation 10}$$

$$k_L a = \frac{\ln\left(\frac{pO^*_2 - pO_2(t_0)}{pO^*_2 - pO_2(t)}\right)}{t - t_0} \quad \text{Equation 11}$$

2.5 Technical specifications and safety mechanisms of the closed gas loop system

The closed gas loop (design in chapter 3.2) was realized with oxygen being selectively removed through a proton exchange membrane fuel cell (PEM). The PEM (Horizon educational, H-12 PEM fuel cell 12W, FCS-B12) was fed upon demand with H_2 from an electrolyzer (H-TEC education, Electrolyser E207 H_2O_2 230, max. 230 mL·min^{-1} at 4.4 A, 14 V, and 0 mbar to 20 mbar) after desiccation through a gas cooler (M&C Products Analysentechnik GmbH, ECP 1000) and silica gel beads (KC-Trockenperlen, orange chameleon). The H_2 flow was measured (MKS 1179B, calibrated by Gilian Gilibrator wet bubble cell 1-250 cc/min) and the measured flow was utilized to monitor and automate the cultivation in the cptPBR as further elaborated in chapter 3.2.3. The automated control was implemented in LabView 2018 with custom controllers written in a MathScript formula node at a parameter set interval of 1 s (for code see the appendix A2).

The gas tightness of the cptPBR setup including the membrane was validated regarding nitrogen, oxygen and hydrogen by gas chromatography (Figure 12) measurements. The

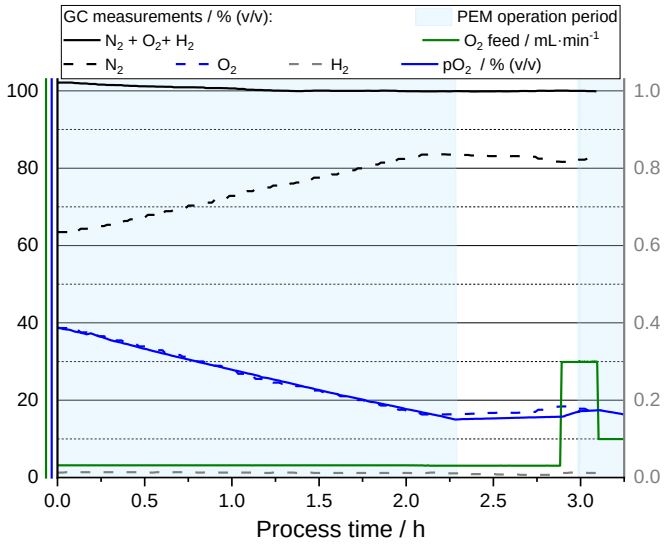

Figure 12: Gas chromatography measurements during O_2 feed for photosynthesis simulation in the cptPBR.

maximum fraction of hydrogen in the cptPBR gas cycle was 0.014 % being close to the lower measuring limit of the gas chromatography (GC), which was not significantly above the threshold. During one cultivation (3 days) GC measurements were conducted on a sample basis without any further increase in hydrogen content.

To ensure the durability of the equipment and safe operation, several measurements and mechanisms were implemented. The H_2 for the PEM was only produced upon demand to circumvent the risk of explosions. The H_2 tightness of the system was ensured through pressure holding experiments at 50 to 100 mbar over 5 to 10 min before every cultivation and covering of critical connections with specialized foam to visualize leakages by bubble formation. After completing the system design, the gas tightness was additionally ensured by GC measurements. After any adaptation to the system, the gas line was checked with an H_2 detector (Trotec, T2000). These elaborate tests were especially demanded, since the electrolyzer was operated above the pressure range given by the manufacturer's instruction due to the demand of the PEM. The ingoing pressure of 0.45 bar was required by the fuel cell to supply hydrogen instantly to all of the 13 cells in one PEM stack. The stack was removed from the original housing and placed in a gas-tight chamber, where the airflow from the cptPBR was piped through. The larger chamber prevented heat accumulation by allowing sufficient ventilation.

To protect the PEM from damage due to the change in direction of electrical current, which causes performance reductions and may cause irreversible damage the fuel cell was always operated at voltages > 6.5 V (> 0.5 V per cell) after a time offset of 10 s for voltage buildup. This voltage, including tolerance for fluctuations, was ensured by resistances of 15 Ω to 65 Ω, resulting in H_2 consumption rates of 75 mL·min^{-1} to 105 mL·min^{-1} (Figure 13) measured in the

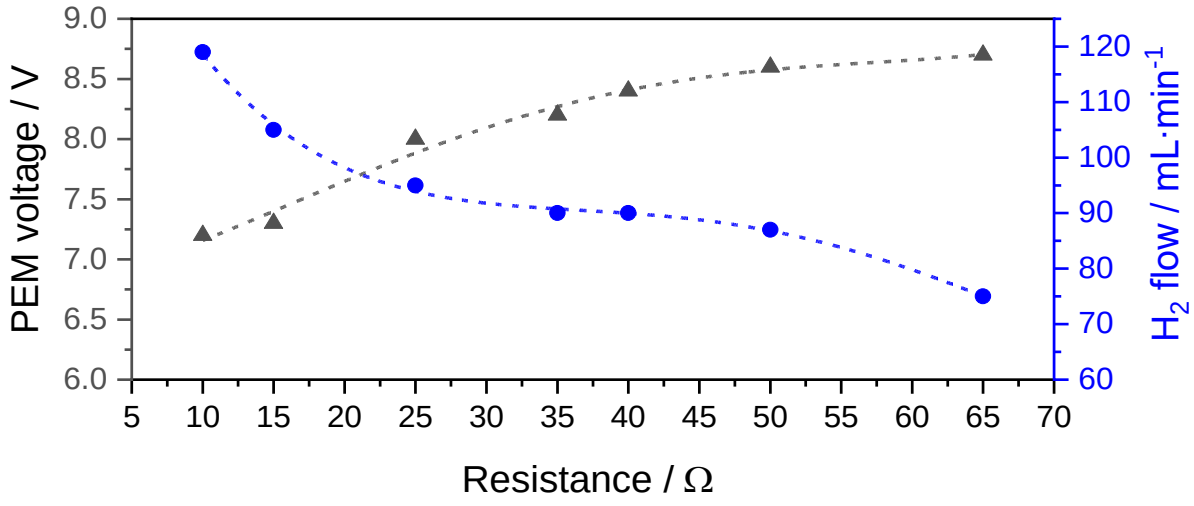

Figure 13: Hydrogen consumption and voltage of the PEM during operation at different resistances and 0.5 bar ingoing pressure of hydrogen.

H_2 gas line before the fuel cell by a mass flow control (MKS 1179B) at 0.5 bar. 10 Ω was not used due to voltage drops during pressure fluctuations at the beginning of PEM operation intervals during cultivations.

At the end of each PEM operation interval a pinch valve (Bio-Chem valve P/N 075P2NC24-10SM) behind the PEM was opened to release the pressure and flush the PEM. The flushing reduced the humidity in the anode chamber of the PEM. The humidity (B&B Thermo Technik, humidity transmitter FF-GLT-20MA-INT-TE1) and pressure (Keller, pressure transmitter, 35XHT) in the gas loop were also monitored to ensure the absence of safety risks.

2.6 Light calibration and optimization of light settings

The light measurements were performed with a planar light sensor (MQS-B Mini Quantum Sensor, Diffuser diameter: 5.5. mm) connected to the light meter (LI-COR, LI-250). For calibration, the light intensity (averaged over 10 s) was measured over the illumination surface and calibrated against the current to enable automated control during cultivations. The measurement positions were the glass bottom of empty shake flasks, the inner side of the glass plate in flat-panel PBR and the glass tube around the light bar for cptPBR. The calibration factor for the cptPBR was 0.0257 $A\cdot(\mu mol\cdot m^{-2}\cdot s^{-1})^{-1}$ with the light intensity measured in triplicate on one glass tube and on a sample bases on other tubes (Figure 14).

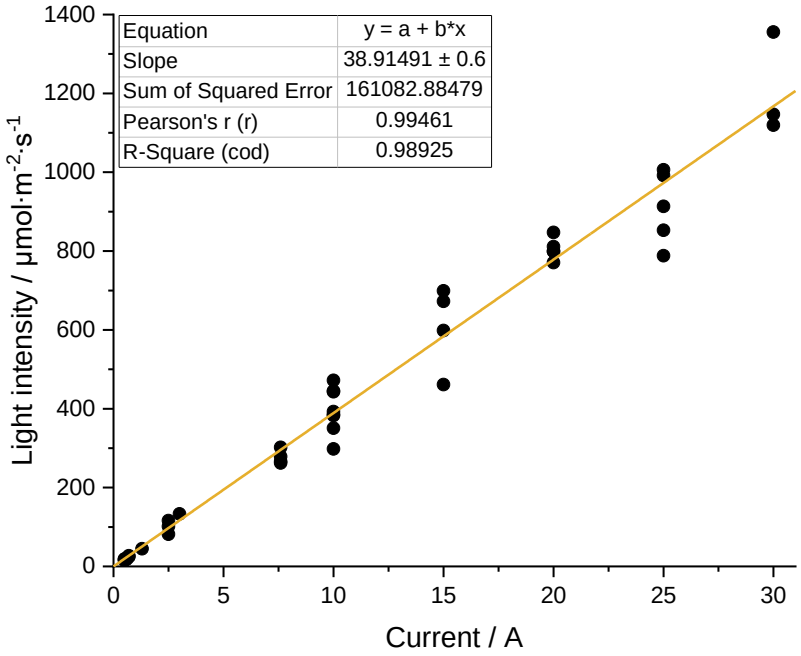

Figure 14: Calibration of the current controlled average incident light intensity in the compact photobioreactor at 20.5 ± 1.1 V. The PAR light intensity was measured on the surface of the glass tube. Each data point resulted from automatic averaging over 10 s. The reciprocal of the slope ($0.0257\ A\cdot(\mu mol\cdot m^{-2}\cdot s^{-1})^{-1}$) served as the calibration factor for the computation of the current to be set based on the required light intensity.

The light supply was set proportional to the measured or estimated biomass in the cultivation system giving the light intensity according to

$$I_{\mathrm{hv}} = spI_{\mathrm{hv}} \cdot c_{\mathrm{X}} \cdot \mathrm{SA{:}\,V}^{-1} \qquad \text{Equation 12}$$

with the area to volume ratio being $\mathrm{SA{:}\,V} = \mathrm{A_{PBR}} \cdot {\mathrm{V_{PBR}}}^{-1}$.

Mainly flat-panel PBR was used for the optimization of the specific light supply rate spI_{hv} with the optimization target of efficient growth at high growth rates. The specific growth rate (μ / day^{-1}) was continuously determined using fitted functions of the biomass concentration $c_{\mathrm{X}}(t)$ based on multiple samplings and deriving the function's time derivative $\frac{\mathrm{d}c_{\mathrm{X}}}{\mathrm{d}t}(t)$.

$$\mu = \frac{\frac{\mathrm{d}c_{\mathrm{X}}}{\mathrm{d}t}(t)}{c_{\mathrm{X}}(t)} \qquad \text{Equation 13}$$

The specific growth rates approached their maximum at $spI_{\mathrm{hv}} \geq 50$ µmol·g^{-1}·s^{-1} in the flat-panel PBRs (Figure 15). 50 to 60 µmol·g^{-1}·s^{-1} was then applied to cultivations in the cptPBR to approach maximum specific growth rates and, consequently, productivity, while maintaining light efficiency.

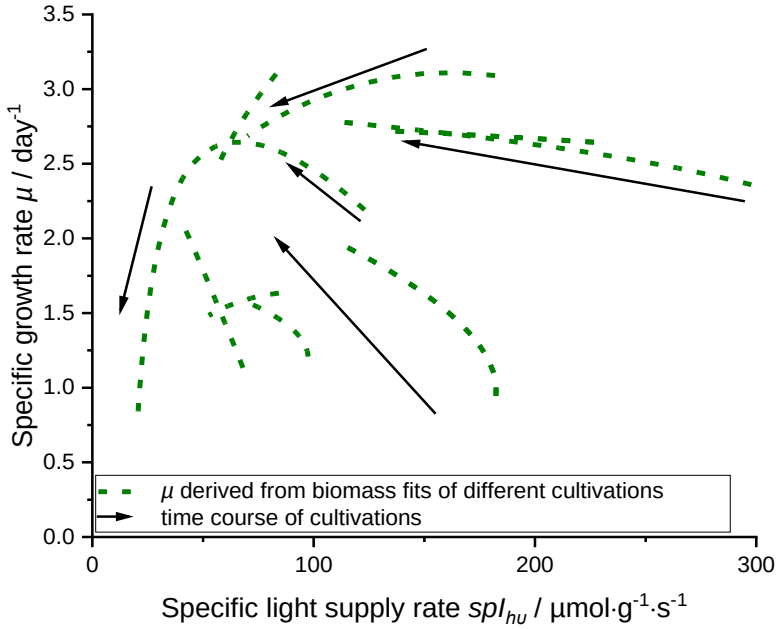

Figure 15: Investigation of light kinetics in flat-panel PBRs. The data displayed by the dashed lines was derived by fitting the biomass concentration c_X based on OD_{750nm} measurements over time according to the correlation given in 2.7.1 and. Equation 13. Each line represents one cultivation phase of 1 to 2 days with minimum three OD_{750nm} samples. The arrows indicate the course of time during the cultivations.

2.7 Offline Analytics

Offline analysis of samples detected deviations from the calculated biomass concentration from automated control based on the H_2 measurement to manually measured concentrations. The offline determined data was used to reset the biomass concentration in the controller for

automated process control and recalibrate the Biomass concentration during data analysis. Controllers were used for nutrient feed and light supply according to predefined stoichiometry or settings in advanced setups.

2.7.1 Optical density

The extinction ($E = -\lg(I/I_0)$) also referred to as optical density at 750 nm, 680 nm and 480 nm corresponded to the biomass concentration, chlorophyll content and carotenoid content, respectively. Samples of the culture were photometrically measured (Perkin Elmer; UV/VIS Spectrometer; Lambda 35) and diluted before, if needed to achieve $OD_{750nm} < 0.4$ in a polystyrene single-use cuvette (BRAND®, semi-micro cuvette, 7590 15). The biomass concentration under growth conditions correlated linearly to the OD_{750nm} with the factor 0.1716 $g \cdot L^{-1} \cdot OD_{750nm}^{-1}$.

2.7.2 Photometric measurement with integrating sphere

Measurements with the integrating sphere (labshere RSA-PE-20, d = 50 mm, integration time 0.08 s, 1 nm interval in Perkin Elmer; UV/VIS Spectrometer; Lambda 35) aimed to determine the absorption cross-section. The simplest measurement of the absorption cross-section assumes collecting all light in the integrating sphere, which is not absorbed by the sample in the transmittance port. The transmittance measurement was used to approximate the absorption cross-section ($\sigma_{X,abs,\lambda}$ / $m^2 \cdot g^{-1}$) as

$$\sigma_{X,abs,\lambda} = \frac{abs_\lambda \cdot \ln(10)}{z_{cuvette} \cdot c_{X,sample}} \qquad \text{Equation 14}$$

with the wavelength-dependent absorption abs_λ after normalization to the wavelength 740 nm to 750 nm, the light path of the cuvette $z_{cuvette}$ = 2 mm (Hellma Analytics, Macro-Cell 100-QS), and the biomass concentration in the sample ($c_{X,sample}$ / $g \cdot m^{-3}$). The measurement was blanked with centrifuged medium (21 380 rcf, 5 min) or deionized water when the sample was also analyzed using the measuring device for determination of scattering characteristics. The estimation in Equation 14 is only precise for exclusively forward scattering cells. More precise investigations of the optical characteristics of the microalgal culture were performed using the measuring device in chapter 3.5.1.

2.7.3 Dry weight measurement

The biomass concentration was determined gravimetrically on filters. The glass fiber filters (VWR, grade 698, Ø 0.45 mm, 0.7 µm) were prewashed (3x 30 mL ultrapure water) under vacuum and dried in two aluminum dishes (Memmert universal oven, 80 °C, 48 h). The filters and dishes were cooled to room temperature in a desiccator. The inner dish with the filter was

weighed on an analytical balance (Kern, ABJ 320-4). The described procedure was repeated but the sample (1 to 10 mL dependent on culture density) was diluted in ultrapure water and poured on the filter before subsequent washing steps. The difference of masses per applied volume gave the biomass concentration.

2.7.4 Starch assay

The starch content of homogenized biomass was determined using an α-amylase and amyloglucosidase-based starch assay (Megazyme, Total Starch Assay Kit (AA/AMG), K-TSTA-100A) similar to the method described by [87], as described below.

Freeze-dried biomass (approx. 5 mg; 48 h, Christ, Alpha 1-2 LDplus) was quantified gravimetrically (m_{sample} / mg; KERN, ABJ) and disrupted in 2 mL safe-lock tubes through bead milling (10 min, 30 Hz) with glass beads (Retsch, d = 0.25-0.50 mm, part no. 22.222.0002) in 125 µL 80% (v/v) ethanol. Exemplary microscopic observations showed full cell disruption. After transferring the content of the first tube to a fresh safe-lock tube by four washing steps with 450 µL 80 % (v/v) ethanol each, the suspension was incubated in a shaking heat block (5 min, 82 °C, 300 min^{-1}) to extract optically interfering compounds and free sugars. Non-dissolvable biomass constituents including starch were precipitated by centrifugation (5 min, 3000 rcf). The supernatant was discarded. The pellet was dissolved in 1.5 mL α-amylase-3-(N-morpholino)propanesulfonic acid solution and incubated (6 min, 100 °C, 300 min^{-1}; 5 min, 50 °C). 2 mL of Na-acetate buffer and amyloglucosidase solution were added in a 15 mL tube and incubated (30 min, 50 °C) to complete the hydrolyzation of starch to glucose. After centrifugation, 50 µL of the supernatant were added to 1.5 mL Glucose Oxidase-Peroxidase reagent and measured against a D-glucose calibration series at 510 nm to determine the glucose concentration. The glucose calibration series ranged from 0.0-1.0 $mg \cdot mL^{-1}$ based on dilutions from a 1 $mg \cdot mL^{-1}$ solution included in the assay. The calibration was linear for $E_{510nm} \geq 0.04$ (Equation 15) and was measured for each batch of analyzed samples against the water blank, so b = 0.

$$c_{Glc} = a \cdot E_{510nm} + b \qquad \text{Equation 15}$$

The mass fraction of starch was then calculated as

$$x_{STA} = \frac{c_{Glc} \cdot V_{hyd.Glc} \cdot M_{STA}}{m_{sample} \cdot M_{Glc}} \qquad \text{Equation 16}$$

with the volume of the processed sample solution containing hydrolyzed glucose $V_{hyd.Glc}$ = 3.55 mL and $M_{STA} \cdot M_{Glc}^{-1}$ = 0.9. For samples not analyzed directly after freeze drying,

the m_{sample} was corrected for the exemplary determined moisture fraction with three samples from each freeze-drying batch.

2.7.5 Analysis of nutrient concentrations in the culture

Samples for nutrient analysis were centrifuged (Hettich, Mikro 22, 2 min, 36220 g), using the supernatant for test procedures. Ammonium (NH_4^+) test kits verified NH_4^+ depletion in runout experiments, while photometric Spectroquant test was used for micro-feeding experiments.

The NH_4^+ concentrations were estimated using a photometric test (Merck, Spectroquant, no. 1.14752, 0.013-3.86 mg $(NH_4^+)\cdot L^{-1}$) according to the manufacturer's instructions but with one fourth of the sample volume and reagents. Samples were measured (UNICAM UV/Vis Spectrometer UV2, 690 nm) against a serial dilution of NH_4Cl (0.063-2.67 mg $(NH_4^+)\cdot L^{-1}$).

2.7.6 Light intensity measurement

The light sensors were connected to the Light Meter (LI-COR, LI-250A) for measurements during cultivations. The planar photosynthetically active radiation (PAR) sensor (Walz; MQS-B) with automatic averaging over 15 s measured the ingoing light intensity on illumination surfaces and outgoing light intensities on the cptPBR surface.

The spherical light sensor (Walz, US-SQS/L) was used to detect local light intensities in microalgal suspensions, the medium, or water, depending on the experimental setup.

2.8 Measuring device for determination of scattering phase function

A custom-built measuring device (chapter 3.5.1) was 3D-printed (Prusa MK3S, ± 0.05 mm) from dull black polyethylene terephthalate glycol-modified (PETG) filament and equipped with a cylindrical quartz cuvette (Hellma, 540-QS, outer dimensions: 75 × 10 mm, inner dimensions, 74 × 8 mm, 3.2 mL, n_{quartz} = 1.46 to 1.47 in the visible spectrum) to determine the scattering phase function of microalgal suspensions. The sensor was positioned at 10° intervals, while the light source remained fixed. Lasers of different wavelengths served as illumination sources (violet: 404 nm, blue: 446 nm, green: 522 nm, red: 659 nm). The light intensity at angular positions was measured with a planar Mini Quantum Sensor (Walz, LS-C, 350 to 750 nm, < ± 3 % at -30° to 30°) connected to the Universal Light Meter & Logger (Walz, ULM-500) for detailed assessment of optical characteristics through the program WinControl-3.

The test setup introduced in chapter 3.5.4 used a red laser (678 nm, beam diameter = 2 mm, 4.5 W, 1 A) as a monochromatic light source (incident light intensity: 1950 $\mu mol\cdot m^{-2}\cdot s^{-1}$). Measurements were performed using a submersible spherical quantum sensor (Walz, US-SQS/L, 3.7 mm) with sensitivity restricted to photosynthetically active radiation.

3 Results & Discussion

The research carried out in this dissertation aimed to design a photobioreactor (PBR) for cost-efficient production of ^{13}C-labeled microalgal biomass. Microalgae incorporate ^{13}C in biomass from $^{13}CO_2$, with starch accumulation being of special interest due to the high value of ^{13}C-labeled glucose. Efficient incorporation of the high-priced substrate $^{13}CO_2$ into biomass was essential to achieve economic feasibility, while installation and operation costs were of secondary relevance. The high value of the product and substrate demanded a lab-scale cultivation system to achieve high reproducibility and controllability of process conditions and minimized contamination risks.

The compact photobioreactor (cptPBR) was therefore developed and optimized to cultivate microalgae (chapter 3.1) under effective CO_2 retention (chapter 3.2). Compactness enabled reproducible laboratory operation including sterilization prior to cultivation. Conversely, high photoautotrophic productivity required a short light path. This contradiction was solved by internal illumination to ensure compactness and high quality and productivity [88] of the isotopically labeled biomass. Gas-driven mixing prevented sedimentation and minimized gradients of CO_2, O_2 and nutrient concentrations.

In open systems, CO_2 loss in the off-gas at the same partial pressure as in the suspension would be inevitable, because CO_2 in the suspension is required to enable photoautotrophic growth. For economic $^{13}CO_2$ usage, gas management was configured to retain all gases except photosynthetically produced oxygen. The central technical challenge was designing a closed gas loop for the cptPBR that selectively removed oxygen while retaining CO_2. Selective oxygen removal and full CO_2 retention were achieved by a proton exchange membrane fuel cell (PEM).

The cultivation system with oxygen removal by the PEM additionally enabled systematic investigation of strategies for efficient starch accumulation (chapter 3.4) supported by light modeling (chapter 3.5 and 3.6). The measured hydrogen feed to the PEM provided precise near-online monitoring of the photosynthetic oxygen evolution, allowing estimation of the biomass productivity. This monitoring was especially valuable for the automated control of the light regimes and nutrient feeds and facilitated assessment of metabolic performance at varying nutrient feed rates. Micro-feeding targeted microalgal starch production at high photosynthetic efficiency based on the incident light supply. Differentiation between light- and nutrient-driven effects on growth required knowledge of the light kinetics derived from the light distribution within the cptPBR. Scattering and absorption coefficients were measured in a custom-built device to model the light propagation in the complex geometry of the cptPBR.

3.1 Compact photobioreactor design with internal illumination

Key features of the cptPBR in this dissertation were its compactness, sterilizability and controllability of the temperature, pH, gas composition and flow, nutrient feeds and the light intensity to ensure high productivities and consistent biomass quality. The light supply as internal illumination enabled high growth rates by minimizing the light path, while retaining the compactness of the system. The light bars and other installations in the cptPBR were placed horizontally. The horizontal design required effective mixing by gassing to prevent sedimentation on the installations. The initial gassing design was improved regarding mixing by broadening the gassing profile. The gassing ensured the microalgal cells the quick passage through different light zones to support effective growth.

3.1.1 Reactor type, construction and installations

The core body of the cptPBR consisted of one horizontal glass tube (L = 500 mm, Ø 300 mm) with an average working volume of 27 L. On both sides, stainless-steel plates closed the cptPBR being sealed with O-rings. One plate contained the measurement technique (pH, pO_2, spectrometer, T) in the liquid phase (Figure 16). The other steel plate was equipped with 37

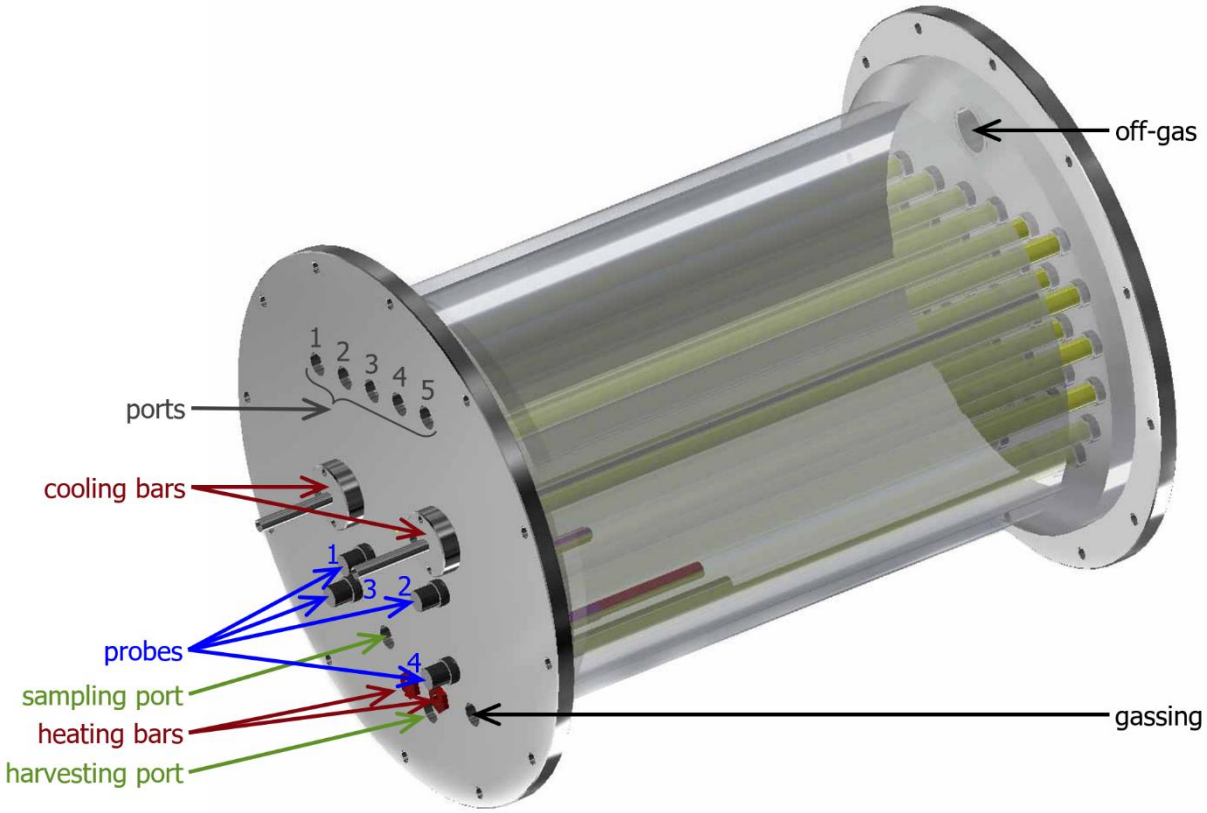

Figure 16: Engineering drawing of the cptPBR including all installations except for gassing tubes. The cptPBR was equipped with probes (blue) for pH (1), pO2 (2), light spectrum (3) and temperature (4) measurement. Cooling and heating bars were placed into the working volume and ports for nutrient feeds, pH adjustment (1-5, grey) in the head space. Sampling and harvesting ports (green) were installed close to the bottom of the cptPBR.

glass tubes embedding light bars in the liquid phase and with an off-gas connection above. During cultivation, the pH and temperature were controlled at 7.5 and 27 °C, respectively. The pO_2 was measured online, but only controlled in cultivations with closed gas loop (see 3.2.1 for details). Further ports below the liquid level were built-in for sampling and gassing, and heating and cooling bars (Figure 16). Ports above the liquid level facilitated pH adjustment and feeding.

To minimize down-time and ensure operational flexibility and product purity, the cptPBR – including all installations except for the light sources – was autoclavable and alternatively designed for the steam sterilization in place. After sterilization, the light bars were placed into the glass tubes for internal illumination.

3.1.2 Illumination of the compact photobioreactor

'Ideal illumination' refers to one location-independent light intensity in a PBR, which supports the formation of uniform biomass and product quality. Theoretically, consistent light intensity can be achieved through the complete compensation of light attenuation by a light-concentrating effect. For kinetic studies, this compensation was successfully realized by directing external illumination through the microalgal culture to a central focal point of a cylindrical PBR [40]. The larger the diameter, the higher the necessary light intensities for the same cell concentration to achieve the full compensating effect. In this project, the required compactness of the system demanded a large PBR diameter, making compensation for light attenuation through geometrical light concentration infeasible. The infeasibility for large PBR diameters arises from physiological reasons and engineering challenges, specifically light inhibition and cooling capacity.

In practice, the best illumination is achieved by a PBR with a large surface-to-volume ratio (SA:V) and short light paths. SA:V values around 600 m^{-1} have been realized through optical structures that channel light from external sources into the culture [89], for example, using glass sponges [90]. While glass sponges induce a turbulent flow pattern enhancing mixing in tubular PBRs, they also create zones of low flow that may lead to microalgae sedimentation [41]. Sedimentation results in non-uniform biomass growth and biofilm formation [91], which in turn reduces light penetration into the culture. Additionally, sedimentation increases the demand for harvesting and cleaning effort, which carries the risk of damage to the fragile optical structures. Therefore, the PBR design needs to balance the complexity of installations with their utility for light distribution to develop a practically viable and robust system.

Within the engineering boundaries of compactness and robustness of the PBR, internal light sources lead to the most uniform light pattern. In the compact PBR (cptPBR), the light sources were placed into glass tubes to be protected from the culture and to be removable and accessible for cleaning, sterilization and maintenance. The 37 glass tubes (Figure 17) were distributed in a radial pattern and passed through the stainless-steel plate of the cptPBR (Figure 18). The distribution of the glass tubes was equidistant as long as compatible with other reactor installations. The cptPBR installations, e.g. cooling bars, heating bars and probes led to distances of 23 mm to 25 mm between neighboring surfaces of glass tubes. As approximated by the outer surface area of the glass tubes, the total illumination area of the 37 light bars amounts to 0.909 m^2. This gives SA:V = 33.7 m^{-1}, which is within a common range (21.5 m^{-1} to 47.3 m^{-1}) for internally illuminated PBRs [89].

Figure 17: Side view of one light bar with 24 LED spots on each of three circuit boards in the glass tube (Duran®, borosilicate glass). The surface of the glass tube is $2.458 \cdot 10^{-2}$ m^2.

The average light intensities on the surface of the glass tubes were controllable from 4 to 1167 $\mu mol \cdot m^{-2} \cdot s^{-1}$ (0.01 to 30.0 A), with the calibrated slope in Figure 14 (chapter 2.6) of 38.91 $\mu mol \cdot m^{-2} \cdot s^{-1} \cdot A^{-1}$. The LEDs were configured in a series circuit to enable precise current-driven control proportional to the average light intensity over the glass tube surface. Each glass tube (Figure 17) contained one light bar with 72 warm white LED spots. The light bars contained three 120° shifted circuit boards with the LEDs in helical distribution. This LED distribution allowed the cptPBR illumination to be mathematically divided into 25 repetitive longitudinal sections of ~20 mm (Figure 19) for modeling purposes, disregarding the boundary conditions near each stainless-steel plate.

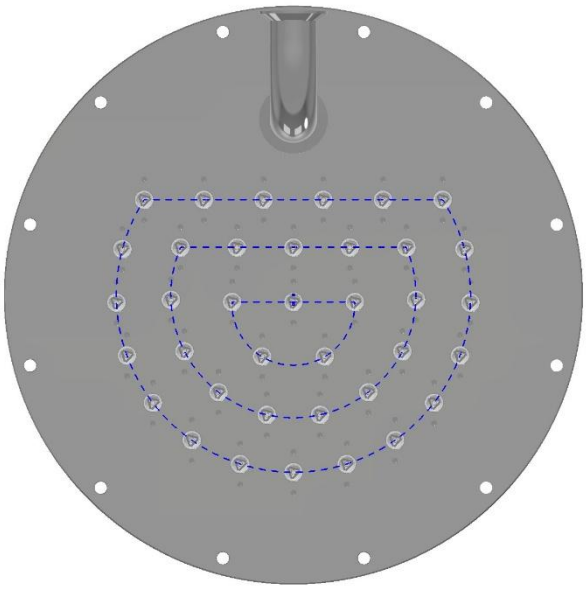

Figure 18: Engineering drawing of the stainless-steel plate of the cptPBR hosting the glass tubes for the LED bars distributed on the radii 130 mm, 90 mm and 45 mm.

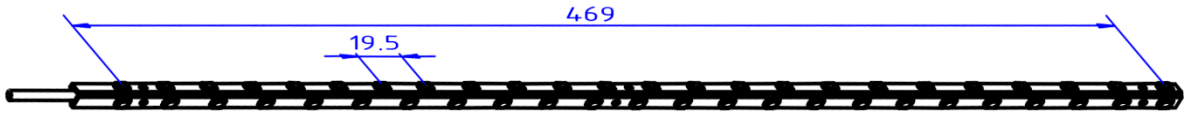

Figure 19: Engineering drawing of one light bar for the cptPBR. Measurements in millimeter.

During the cptPBR operation, heat was generated by the LEDs – directly as heat loss from the LEDs, and indirectly as partial heat dissipation of absorbed photons and by the metabolic activity of the microalgae. The generated heat was removed by cooling devices to maintain the optimum temperature of the microalgae in the culture and allow high photosynthetic performance. Two cooling bars were installed in the working volume, with the cooling water flow being temperature regulated. When only applying cooling by the cooling bars, the temperature on the LED circuit boards exceeded 70 °C at 720 $\mu mol \cdot m^{-2} \cdot s^{-1}$. To prevent this heat accumulation and unsuitable temperatures of the glass tubes, pressurized air (3 bar) was continuously supplied through the glass tubes along the LED bars at light intensities above 500 $\mu mol \cdot m^{-2} \cdot s^{-1}$. The air flow reduced the temperature from 70 °C to 35 °C. The cptPBR illumination needs to be discussed in the context of mixing, as mixing transfers the microalgae through different light zones and high light/dark frequencies may enhance growth [92–96].

3.1.3 Requirements of mixing for light distribution, gas transfer and nutrient supply

Mixing times can be categorized into three levels, each corresponding to a key requirement of photosynthetic biomass production: light supply, gas transfer, and nutrient availability. These levels were geometrically defined by the supply installations and intertwine with the photosynthetic requirements. Improvements at one level can positively or negatively impact the others. Distinguishing the effects on different levels clarifies the need for improvements in gassing design. Design strategies must account for the interactions across different mixing dimensions to simultaneously optimize the light, gas, and nutrient supply.

Light absorption and gas exchange are more time sensitive than nutrient uptake during biomass growth, since light absorption and CO_2 uptake are essential for primary photosynthetic carbon fixation. A lack of sufficient light reduces photosynthetic activity and, potentially, leads to biomass degradation to meet the maintenance related energy demand. CO_2 is required as the substrate for carboxylation. Without adequate CO_2 uptake, light exposure initially causes increased heat dissipation of photons, followed by an excess of NADPH and ATP, and consequently oxidative damage. Thus, light and CO_2 availability instantly affect the photosynthetic performance of the PBR.

In the cptPBR, light and CO_2 were supplied at multiple spots along the longitudinal axis. This longitudinal supply decouples the photosynthetic growth performance from longitudinal mixing and shifts the primary focus of mixing optimization to radial flow dynamics. Along the radial flow pattern, microalgae pass through various light zones, which can balance the effects of steep light gradients on growth. For high-frequency transfer between the light zones, the light

intensities that would cause light limitation and photoinhibition balance and let the cells physiologically respond to moderate light conditions. Growth is then mathematically described as a function of the integrated light intensity over the transferred light zones. This transfer is commonly mimicked by flashing light at a certain frequency. Light-dark frequencies of ≤ 1 Hz [95] and 10 Hz [92–94] have been shown to reach high productivity with different microalgal species, and even up to 100 Hz for *Chlamydomonas reinhardtii* [97]. In other words, microalgae should transfer between different light zones within 0.1 s to 1 s to achieve productivities comparable to those under homogeneous light conditions in the cptPBR.

For sufficient transfer between the light zones, the target flow velocity depends on the reactor geometry, particularly the light and flow patterns. The positioning and orientation of the light sources determine the distance over which cells need to transfer in < 1 s. The longitudinal distance between the centers of neighboring LEDs is ~19.5 mm, which includes 15.2 mm of straight distance, accounting for the LED spot size of 4.3 mm. The helical design of the LED bars (see chapter 3.1.2) reduces the effective longitudinal distance between the LED spots. The effective longitudinal distance is 2.2 mm, assuming the cells transfer halfway around the tube in < 1 s. Even without considering the emission pattern of the LEDs, the short effective longitudinal distance minimizes the importance of longitudinal mixing for light supply. This reduced importance of longitudinal mixing comes at the cost of higher demand for radial mixing. The radial mixing needs to ensure the transfer halfway around the light bars and between the different light bars within < 1 s.

While longitudinal mixing has minimum impact on light supply, it plays an important role for the distribution of nutrient solutions, as well as pH regulators and antifoam agent. The solutions were injected through ports located on one side of the cptPBR. The time sensitivity of nutrient supply at the metabolic level may be accessed experimentally by comparing pulsed versus continuous nutrient feeding. The time interval between pulses represents an extreme case where there is no mixing of nutrients. For instance, cultures of the microalga *Spirulina platensis*, which were fed continuously with urea as the nitrogen source, achieved similar biomass growth when the feed was provided intermittently at 24-hour intervals [98]. The low variability in growth under different feeding modes suggests that even mixing times in the order of hours are sufficient for nutrient distribution for growth. In contrast, light supply requires much shorter mixing times of < 1 s to ensure effective light/dark transfer and achieve high productivities. The demanded flow velocity depends on the flow pattern, since straight passage between light zones allows lower velocities than indirect passage to achieve the same light/dark frequency.

Therefore, precise analysis of mixing is demanded to evaluate the light distribution and potential effects on the cptPBR productivity.

3.1.4 Gassing and mixing of the culture in the compact photobioreactor

Mixing was achieved by gassing at 1 vvm ± 10 % from the bottom of the cptPBR. The gassing geometry was under development, with the initial design serving as a simple reference case, using a single gassing tube. This reference case was analyzed within both experimental and modeling frameworks. Experiments were carried out with the reference tube (T15p0.5 in Figure 20) and straight gassing tubes (T14p1 in Figure 21) and analyzed in context with simulation results. The gassing geometries were evaluated based on mixing times and mass transfer coefficients, and the resulting effects on microalgal growth.

Figure 20: Engineering drawing of the gassing tube (15 pores, Ø 0.5 mm) initially installed in the cptPBR. This tube (T15p0.5) served as the experimental reference case.

Figure 21: Engineering drawing of the gassing tube T14p1 with 14 pores (Ø 1.0 mm). The tube was used for experimental testing.

3.1.4.1 Integrated mixing time and longitudinal mixing pattern

The mixing times were measured experimentally as the pH step response with a 5 % tolerance to completion of mixing. This measurement gave mixing times integrated over the cptPBR. The longitudinal integrated mixing time is particularly relevant for the homogeneous supply of feed solutions, which were introduced from one side along the longitudinal axis. The mixing time based on pH response also reflected the temporal delay of offline samples in the case of inhomogeneities. For the experimental reference case (Figure 20), integrated longitudinal mixing time (tolerance 5 %) was 0.387 ± 0.063 h.

A more detailed view on the mixing pattern was gained by pH shifts in the cptPBR filled with red cabbage extract (see chapter 2.4.1 for details). The pH shift induced a color change that visualized mixing but did not precisely indicate the extent of homogeneity. The color change was tracked through the red color value at three longitudinal positions to calculate the optical

mixing time. This mixing time was extrapolated along the length of the cptPBR using an exponential fit function (Figure 22).

The non-linear increase in optical mixing time along the longitudinal axis was attributed to back-mixing and the configuration of the gassing system. Reverse flows are an inherent part of the flow dynamics in a closed system operating at constant liquid level. In the present setup, the influence of reverse flows could not be visually distinguished from reduced forward mixing velocities. The latter could be caused by the pressurized gas supply entering from one side of the gassing geometry. As gas was released through the pores, the internal pressure dropped along the gassing tubes, reducing the volumetric gas flow toward the end of the cptPBR. Broadening the gas profile increased the number and total area of pores and was expected to improve radial mixing but to reduce the axial momentum despite the identical gas flow.

Experimental results aligned with expectations: doubling the pore diameter from 0.5 mm (T15p0.5) to 1 mm (T14p1 in Figure 22) led to an increase in the optical mixing time of $f_{2\text{xpore diameter}}$ = 59 % along the entire cptPBR. This effect was primarily attributed to the increased pore diameter rather than to the pore area itself. Larger pores visibly promoted bubble coalescence, resulting in fewer individually rising bubbles and thereby reduced turbulence in both longitudinal and radial directions. Broadening the gassing geometry by doubling the number of 1 mm pore tubes led to an increase in longitudinal mixing time of $f_{\text{broadening}}$ = 116 % (from T14p1 to 2×T14p1 in Figure 22). Combining these two effects of broadening the gassing profile and increasing the pore size from T15p0.5 to 2×T14p1 was estimated assuming a multiplicative effect:

$$t_{\text{mix,2×T14p1}} = t_{\text{mix,T15p0.5}} \cdot (1 + f_{\text{broadening}}) \cdot (1 + f_{\text{2xpore diameter}}) \qquad \text{Equation 17}$$

The approximation from Equation 17 exactly matched the mixing time from the fit of the experimental data from the gassing geometry 2×T14p1 with a mixing time of 440 s. Moreover, the trends throughout the cptPBR matched ($r = 0.984$, $p < 0.001$, $n = 500$), strengthening the plausibility of the quantitatively distinguished effects.

The use of two tubes particularly highlighted the influence of pressure and flow drops in the latter part of the cptPBR due to more and larger pores while maintaining the same total gas flow. The exponential fit matched the data sets but potentially overpredicted the mixing time. Such overprediction was preferable to underprediction to ensure sufficient supply of light, nutrients and CO_2 to support high productivities.

The integrated and longitudinal optical mixing times for the three evaluated geometries were all below the doubling time of *C. vulgaris* even under mixotrophic conditions (2.15 h, 4.63 h)

[99,100], ensuring that metabolic effects of changes in nutrient supply occur within the cell cycle under nutrient replete conditions.

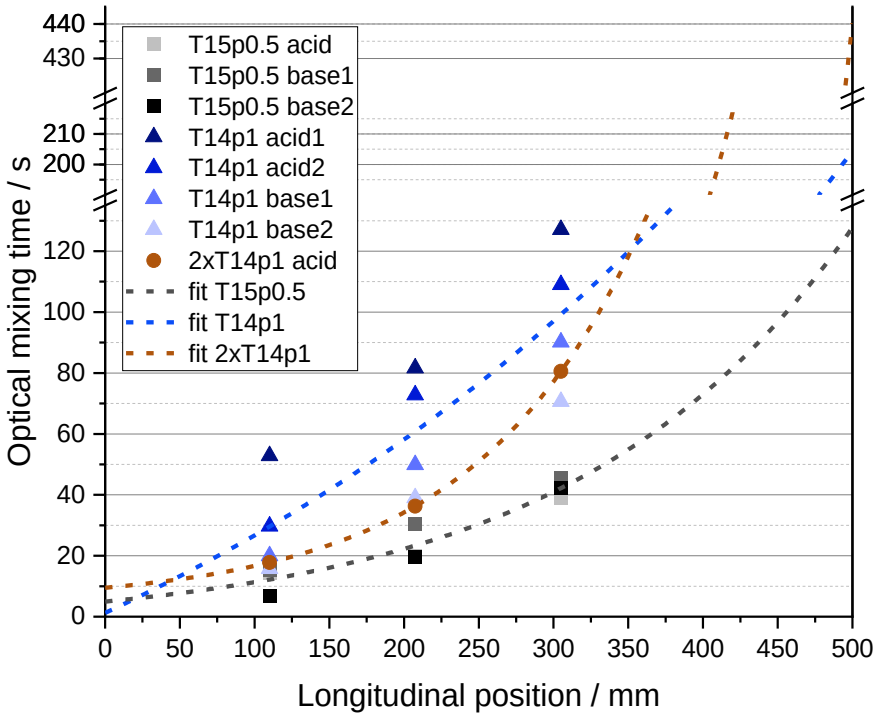

Figure 22: Measurement of the optical mixing time at three longitudinal positions (110.0 mm, 207.5 mm, and 305 mm). The data sets for each tube were exponentially fitted and extrapolated to the full longitude (500 mm).

The mixing time exceeding a cell cycle indicated that the longitudinal mixing was sufficient. However, any adjustments of gassing should maintain smaller gassing pores to allow the application of feeding strategies that require smaller timescales and to prevent the observed effect of excessive pressure drops in the latter section of the cptPBR. Smaller gassing pores further enlarge the area-to-volume ratio, which is crucial for gas exchange during photosynthesis.

3.1.4.2 Gas exchange as the limitation for carbon supply in photoautotrophic growth

The gas exchange can be assessed by the determination of the volumetric mass transfer coefficient. The experimental reference setup revealed a volumetric mass transfer coefficient for oxygen (k_La_{O2}) of $0.0045 \pm 0.0001\ s^{-1}$, which is in the typical range for airlift photobioreactors [101,102]. The correlation of k_La_{O2} to k_La_{CO2} (Equation 18) allows one to assess limitations by CO_2 mass transfer in PBRs [103], which is crucial for photoautotrophic growth.

$$k_La_{CO2} = k_La_{O2} \cdot \sqrt{D_{CO2} \cdot (D_{O2})^{-1}} \qquad \text{Equation 18}$$

The diffusion coefficients $D_{O2} = 2.4 \cdot 10^{-9}$ $m^2 \cdot s^{-1}$ [104] and $D_{CO2} = 2.2 \cdot 10^{-9}$ $m^2 \cdot s^{-1}$ in water [105] approximate the $k_L a_{CO2}$ to 0.0043 s^{-1}. The maximum carbon dioxide transfer rate (*CTR*) from the gas phase to the liquid can be found when c_{CO2} approached 0.

$$\lim_{c_{CO2} \to 0} CTR = k_L a_{CO2} \cdot (c^*_{CO2} - c_{CO2}) = k_L a_{CO2} \cdot c^*_{CO2} \qquad \text{Equation 19}$$

The calculation was based on the saturated CO_2 concentration c^*_{CO2} from the Henry coefficient $H_{CO2,H2O}$ = 34 $mol \cdot m^{-3} \cdot bar^{-1}$ and gassing with 1 % CO_2. From this maximum *CTR* ($14.62 \cdot 10^{-4}$ $mol \cdot m^{-3} \cdot s^{-1}$) the CO_2 limitation can be assessed stoichiometrically. The CO_2 supply using the initial gassing geometry supports a maximum productivity of active biomass at 2.94 $g \cdot L^{-1} \cdot day^{-1}$ (with $e_{C,X}$ = 52 %, Table 1, chapter 1.5). Doubling the number of tubes and the pore diameter (gassing geometry 2×T14p1) increased the performance by 9.6 %. The estimated CO_2 supply is not likely to limit photoautotrophic growth, as productivity typically decreases in denser cultures due to light limitation rather than CO_2 limitation is reached. Further evaluation of mixing concerning local hydrodynamics was needed to investigate potential limitations of the light/dark transfer of the cells and the homogeneity of the cptPBR.

3.1.4.3 Cross-sectional mixing characteristics of the compact photobioreactor

For light/dark transfer, the radial flow dynamics were of major interest. The integrated radial mixing time measured by pH step responses in the experimental base case was 0.245 ± 0.006 h. Integrated radial optical mixing times for all measured gassing geometries were < 0.014 h. However, due to the thickness of the liquid layer along the longitudinal axis, precise determination of the optical radial mixing time was not feasible with the given setup.

These values were sufficient for homogeneity of the biomass and nutrients, but did not reveal information to evaluate the potential photosynthetic performance in response to light. A more detailed analysis is required to optimize the flow throughout the light zones and maximize photosynthesis. The flow should ensure the passage of the culture through light zones within 1 s as elaborated in chapter 3.1.3. The flow velocity for this light/dark transfer needed to exceed 0.0125 $m \cdot s^{-1}$ for the straight passage along the light gradient and > 0.025 $m \cdot s^{-1}$ was expected to be sufficient in any direction. The exact demanded flow velocity depends on the interplay of the light distribution and the flow pattern and, ideally, needs to be reached in the entire cptPBR. The radial flow pattern was analyzed by color change experiments with pH sensitive red cabbage extract (see chapter 2.4.1 for details) and gassing simulations.

The initial experimental gassing design (T15p0.5) intended to achieve a symmetric flow pattern on the radial view (Figure 23). The central gassing aimed for one central upstream and two downstream flows at the sides of the cptPBR.

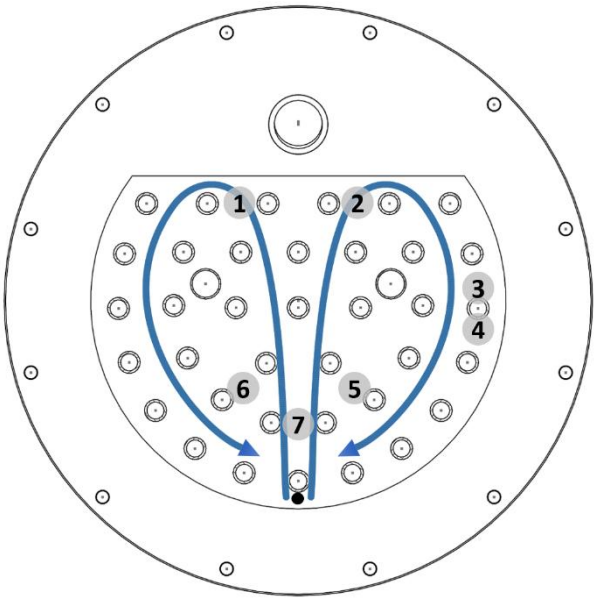

Figure 23: Schematic drawing of the intended flow pattern for the initial gassing design with measurement positions of red cabbage coloring experiments (center of grey circles) and the position of the gassing tube (black circle).

Assuming the symmetric flow pattern, the injection of acid above position 1 in Figure 23 would cause color changes of red cabbage extract in position 1 first. When only looking at the left side of the cptPBR, the color change in position 6 and subsequently 7 were expected to follow after the initial color change in position 1 as displayed in the lower line in Figure 24a. On the right side of the cptPBR, the sequence of color change would be position 2, 3, 4, 5 and 7 (upper line in Figure 24a). Whereas position 7 was expected to change color due to the left stream before the right stream reaches position 7 due to symmetric flow and shorter path of the left stream from the injection port.

The measured relative optical mixing times (Figure 24b) confirmed the intended flow pattern only for the upper central section of the cptPBR. Especially, at position 4 and 7, color changes were detected later than expected, while the color change at position 5 was earlier. The measurements indicate low flow velocities and turbulence at the outer sections of the cptPBR around position 4. The formation of the downstream flow is probably being hindered by the glass tubes for the light bars and the strong upstream of the gassing that delays the color change to reach position 7.

Changing color in position 5 before position 4 indicates flow from the left to the right half of the cptPBR to dominate over the flow in the lower cptPBR section. During cultivations, low flow rates in the outer and lower cptPBR sections reduce the light/dark transfer and increase the risk of cell sedimentation during cultivations. Both lead to non-homogeneous biomass growth and lower productivities. The findings were further investigated by high-resolution 3D-simulations using a multiphase solver to quantify the demand for improvement of the gassing installation (for details on the setup see 3.1.4.5).

According to the simulations, the central upstream of gas (Figure 25a) generates a narrow section (20 % in width) with high flow velocities (≥ 0.050 m·s^{-1}), but wide sections with low

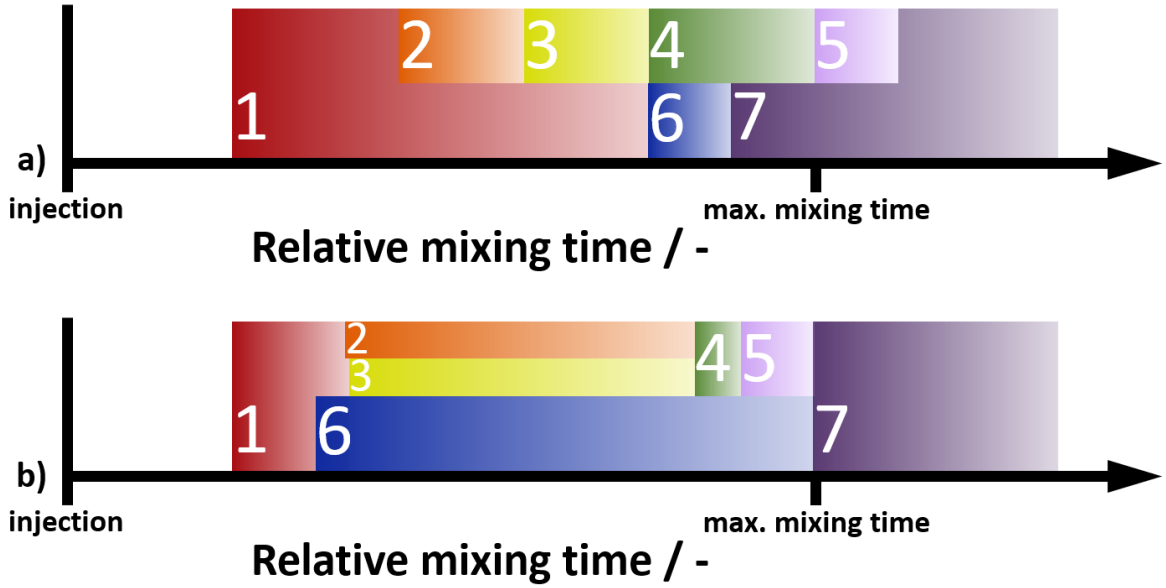

Figure 24: Expected relative mixing times for each of seven positions (Figure 23) in the experimental reference case (a) and the experimental data (b). The left sides of the boxes display, when 80 % red color change was complete during red cabbage experiments at the respective position (white number) relative to the highest time of all seven investigated positions.

flow velocities. Especially, the glass tubes at the sides of the cptPBR hinder the liquid flow causing an averaged flow velocity of 0.032 $m \cdot s^{-1}$, but flow velocities > 0.025 $m \cdot s^{-1}$ only on 47 % of the cross-section (Figure 25b).

The intended flow pattern (Figure 23) was qualitatively reached (Figure 25c), but the formation was insufficient to achieve high flow rates in the lower and outer cptPBR zones for mainly two reasons. First, the narrow upstream causes a relatively low downstream due to the disproportion of the upstream and downstream sections, which translates to the same proportion in average volumetric flows in a steady state of the flow dynamics. Second, the circulation as central upstream of the liquid volume and exterior flow downwards was hindered by the glass tubes

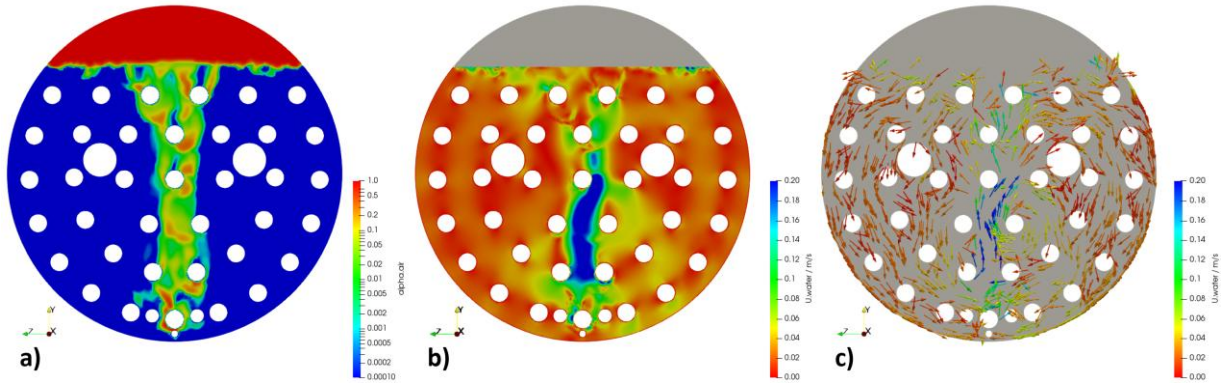

Figure 25: 2-D projections of 3D-simulation results of mixing by gassing in the cptPBR with one gassing tube in position 6 (G6) a) volumetric fraction of air in steady state / -, b) high-resolution of flow velocity / $m \cdot s^{-1}$, c) flow velocity and direction of randomly selected cells from (b) / $m \cdot s^{-1}$.

that host the illumination of the cptPBR. In certain areas on the cross-section of the cptPBR, mixing hardly occurred, thereby risking sedimentation and insufficient light/dark transfer.

Theoretically, the desired flow pattern could have been enforced by flow screens. The disadvantages of flow screens outweigh potential advantages in this case, particularly, limiting light/dark transfer, shading, reducing the cultivation volume and providing additional surface for sedimentation. The advancement of the gassing geometry itself is, thus, more reasonable.

3.1.4.4 Advancement of gassing geometries – experimental evaluation of flow pattern

The development of new gassing geometries majorly aimed to achieve faster radial mixing rates in all zones of the cross-section, and reduce sedimentation compared to the reference case. The importance of circular mixing for light/dark transfer and gas exchange demanded thorough evaluation. Both simulations and experimental testing of gassing and mixing were carried out, recognizing that such complex PBR designs might not be adequately represented by modeling alone. Modeling provided additional local information on the mixing pattern and reduced the number of required experiments. The experimental results from one and two tubes were complemented by simulations with tubes on a newly manufactured holder for multiple tubes to thoroughly investigate the mixing properties at different levels.

The lacking formation of the intended flow pattern in the experimental reference case was primarily attributed to the disproportion of upwards and downwards flow sections and the perturbation of the flow pattern by PBR installations. To support the formation of a flow pattern, the gassing should be broadened and the intended pattern should better correspond with the positions of the PBR installations than in the experimental reference case. Both points were respected in an asymmetric design with two tubes (2×T14p1). One tube was still centered at the bottom of the cptPBR (harvesting port). The second tube was side shifted (d = 65.0 mm, $d_{lateral}$ = 63.3 mm, used as gassing port for T15p0.5 before and new gassing tube holder later). The asymmetric design aimed for a circulating flow with the upstream in the right half of the cptPBR and the downstream in the left half as indicated in Figure 26.

For the gassing geometry 2×T14p1, the color change of red cabbage extract was induced above the position 1 and 2 separately. The experimental data from the acid injection above position 1 (Figure 27a) agreed with the desired flow pattern in Figure 26. The flow from the top to the outer section (position 4) in the half with gassing was more consistent compared to the experimental reference case (Figure 24b). But relatively (and absolutely, data not shown) longer mixing times were recorded to reach the bottom of the cptPBR (position 7).

More details on the mixing pattern and potential causes of the slow mixing at the cptPBR bottom were investigated by the color change experiment after base injection above position 2. In contrast to the intended pattern (Figure 26), the flow transported the base close to the liquid surface probably carried on the gassing bubbles to the outer section of the cptPBR on the right side. Furthermore, the induction of the color change in position 6 before position 1 indicates that the central gassing hinders the flow from the right side to the left in the upper cptPBR section as also visible in the photograph in Figure 28. A summary of the experimentally identified dominating flow streams is given in Figure 29.

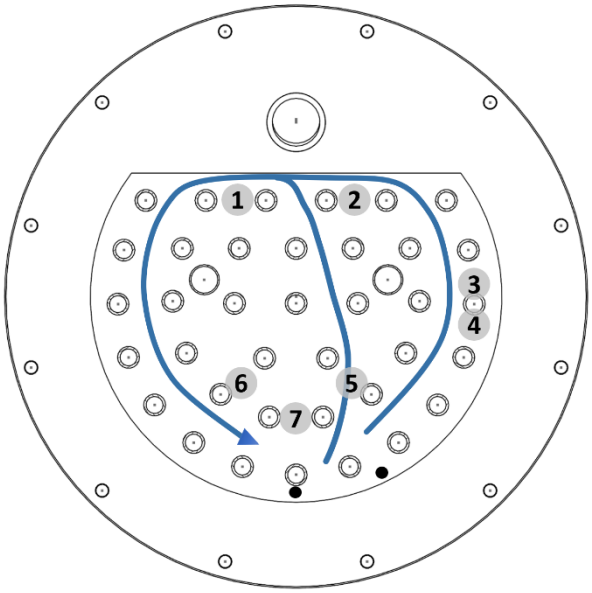

Figure 26: Schematic drawing of the intended flow pattern for the gassing geometry 2×T14p1 with measurement positions of red cabbage coloring experiments (center of grey circles) and positions of gassing tubes (black circles).

Each gassing tube supported the formation of one circulating flow. Both circulations overlapped, but the faster flow did not reach the lower section of the cptPBR. The left flow was hardly visible in video assessment and, thus, not interpreted as dominating. The experimental data clearly showed that the intended flow pattern was not achieved, but pointed out the potential of multiple smaller circulations for further gassing optimization.

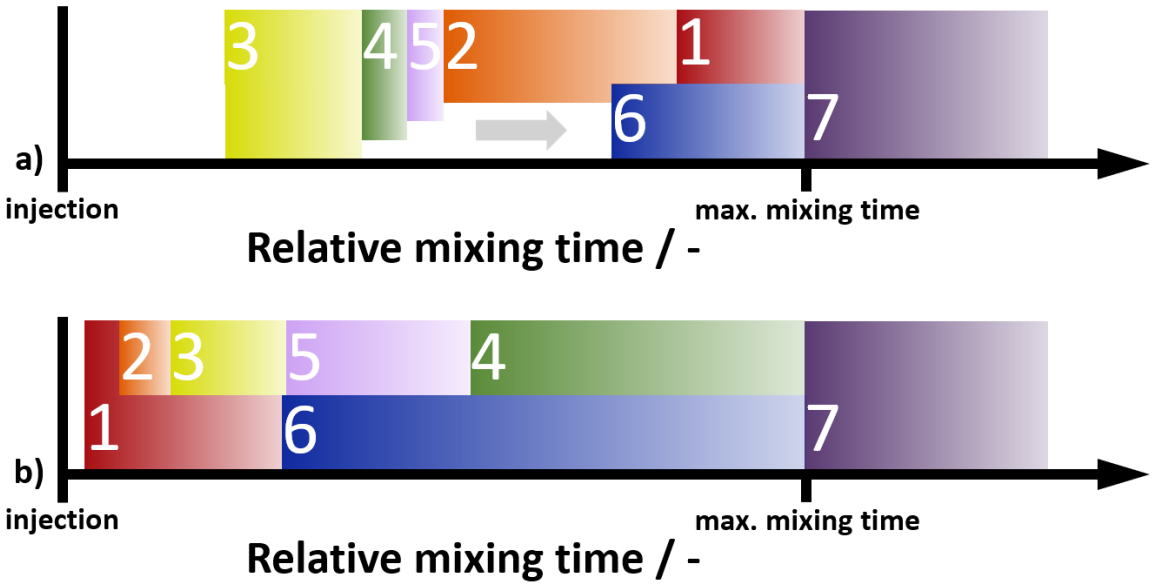

Figure 27: Relative mixing times for each position in Figure 26 for the gassing geometry 2×T14p1. The experimental data was obtained after addition of acid above position 1 (a) and base above position 2 (b). The left sides of the boxes display the 80 % red color change during red cabbage experiments at the respective position (white number) relative to the highest mixing time of all seven investigated positions.

3.1.4.5 Advancement of gassing geometries – Simulation of tube configurations

Previous results (3.1.4.3 and 3.1.4.4) demonstrated that the experimentally tested flow patterns in the cptPBR were disrupted by installations, preventing the establishment of a specific and consistent flow profile. The analysis pointed out that broadening gassing profiles with multiple tubes to create several smaller circulations increases the cross-sectional area with higher flow velocities. This higher proportion of faster flows aligns with the optimization targets: reducing mixing times, increasing light/dark frequencies, and minimizing sedimentation.

Both earlier designs revealed that the installations disrupted the flow pattern, but this disruption also generated turbulence around the light bars, which contributed to local mixing. Broader

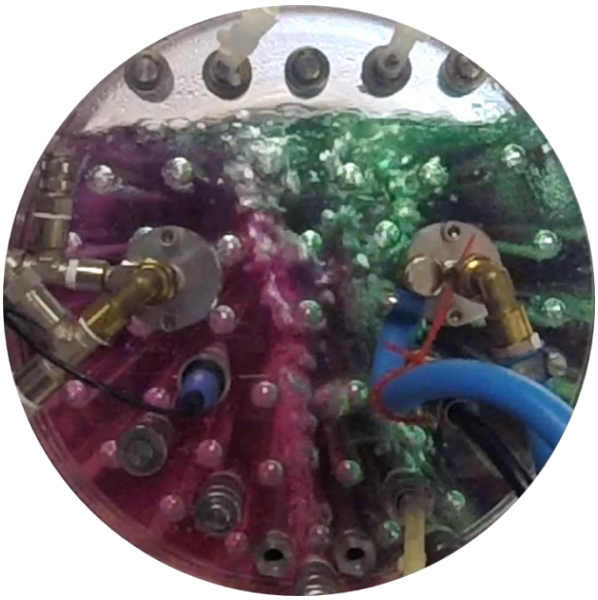

Figure 28: Photograph of the cptPBR cross-section using the gassing geometry 2×T14p1 in red cabbage coloring experiments after base injection.

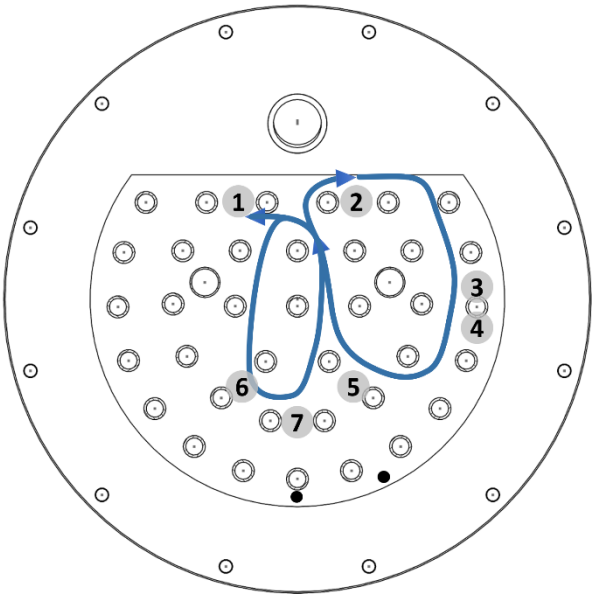

Figure 29: Schematic drawing of the dominating flows according to the experimental data of red cabbage coloring experiments in Figure 27, using the gassing geometry 2×T14p1 with measurement positions (center of grey circles) and positions of gassing tubes (black circles).

gassing profiles can induce turbulence near most light bars, facilitating the transfer of medium, including cells, between the light zones close to the light sources. As an additional advantage, the light bars, housed in glass tubes, break gas bubbles and prevent coalescence. Smaller bubbles provide a larger surface-to-volume ratio, enhancing the volumetric gas exchange within the cptPBR compared to a narrower gassing profile.

However, broadening the gassing profile also increased the number of gassing pores. The multiplication of pores reduces the volumetric flow at each individual pore, decreasing flow rates locally, especially, along the longitude. While this reduced flow through more pores can limit local mixing efficiency, it simultaneously minimizes bubble coalescence, supporting effective gas exchange and enhancing microturbulence. Therefore, the design of the gassing

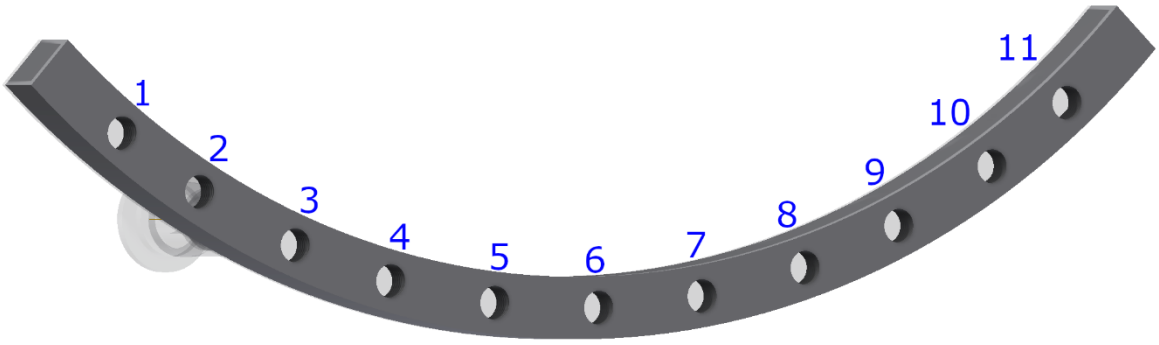

Figure 30: Holder of gassing tubes for multiple tubes T19p0.5 as shown for position 6 in Figure 31. A maximum of 11 gassing tubes can be radially positioned in a symmetric order.

unit must strike a balance between achieving adequate flow velocities and longitudinal mixing and ensuring area-covering turbulence to optimize the system. To address these challenges and optimize the overall performance of the cptPBR, the optimal number of gassing tubes and positioning were evaluated by high-resolution 3D-modeling using a multiphase solver. These gassing simulations were performed in cooperation with the *Lattice Boltzmann Research Group* (LBRG), part of Mechanical Process Engineering and Mechanics (MVM), at the *Karlsruhe Institute of Technology* (KIT).

For gassing simulation, the experimental reference case was closely mimicked using a holder for multiple gassing tubes (Figure 30) with one gassing tube in position 6 (Figure 31: G6). The gassing tube was equipped with 19 equidistant pores with a pore diameter of 0.5 mm. These parameters were chosen to circumvent declines of longitudinal mixing due to pressure drop while optimizing the mixing on the cross-sectional pattern, especially when using up to 11 tubes in parallel.

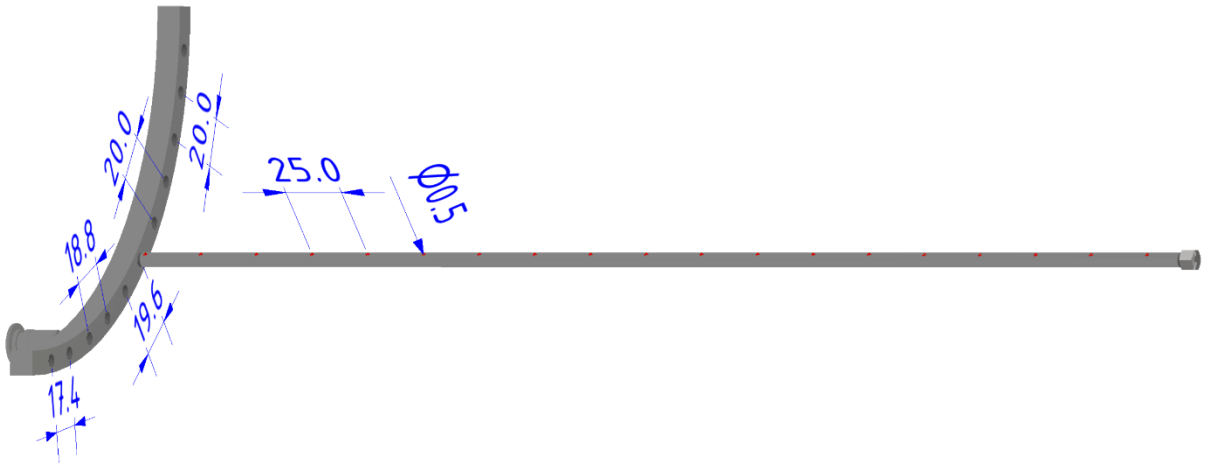

Figure 31: Engineering drawing of the gassing unit for the cptPBR with one gassing tube in position 6 (G6). The displayed geometry G6 served as the modeling reference case with one gassing tube with 19 pores (highlighted in red for visibility).

Gassing tube configurations were designed to achieve high flow velocities over the cross-section by broadening the gassing geometry. The simulated configurations ranged from the extreme case of the single reference case G6 (results shown in Figure 25, chapter 3.1.4.3) to the fully equipped gassing tube holder with 11 tubes, G1-11. Three intermediate setups were simulated to evaluate the effect of increases in tube number and variation in positioning.

The gassing geometry G1-11 generated a predominantly homogeneous distribution of flow velocities (Figure 32b). This distribution was attributed to the aeration directly covering approximately 77 % of the cross-sectional area (Figure 32a). However, 86 % of the simulated flows exhibited low velocities (< 0.0125 $m \cdot s^{-1}$). Beyond the downflows observed along the sides of the cptPBR, the flow pattern was diffuse (Figure 32c). Interactions between liquid flows and the upstreaming aeration resulted in mutual deceleration and induced turbulence. While this turbulence contributed to mixing, the resulting flow velocities remained low. These findings highlight the need for adequate space in the cross-section to ensure unobstructed downward flow and optimize hydrodynamics.

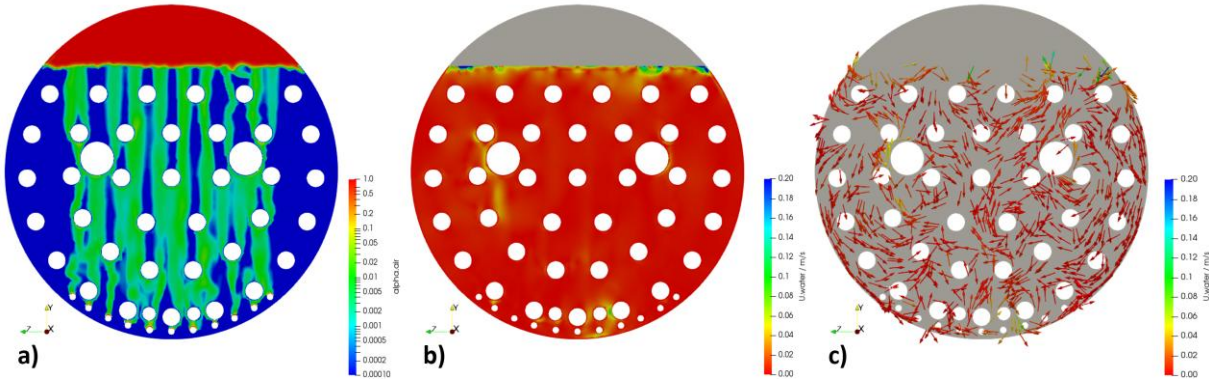

Figure 32: 2-D projections of 3D-simulation results of mixing by gassing in the cptPBR with 11 gassing tubes (G1-11) a) volumetric fraction of air in steady state / -, b) high-resolution of flow velocity / $m \cdot s^{-1}$, c) flow velocity and direction of randomly selected cells from (b) / $m \cdot s^{-1}$.

Removing six tubes from the gassing distribution provided more space for downward flow. This effect was evidenced by a reduction to 32 % of the cross-section occupied by aeration flows (Figure 33a). The primary impact was observed in localized aeration, which directly increased flow velocities at the positions of the remaining gassing tubes in G1.4.6.8.11 (Figure 33b). Upward and downward flows remained closely aligned, with limited circulation occurring around the tube positions (Figure 33c).

Configurations with fewer than five tubes appeared promising, as they provided more space for downward flows and the potential to establish a flow pattern with multiple circulations. Experimental testing (chapter 3.1.4.4) demonstrated that using two tubes resulted in two distinct

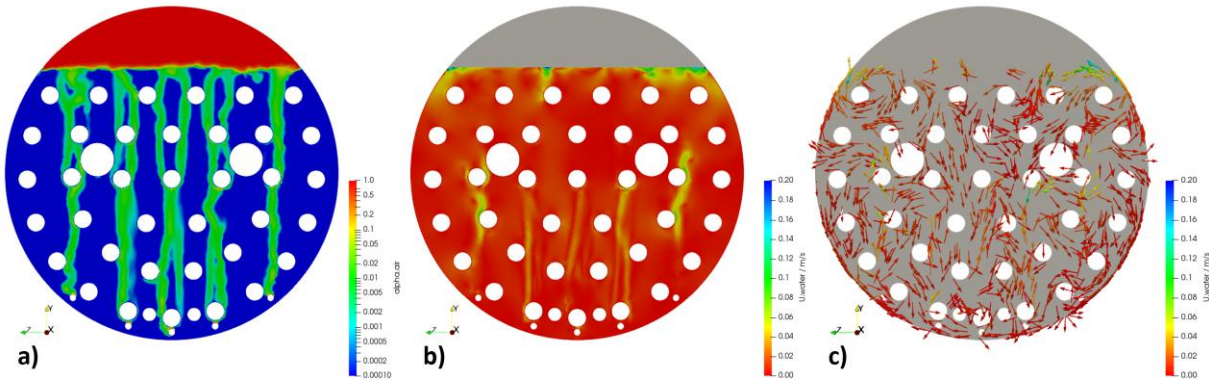

Figure 33: 2-D projections of 3D-simulation results of mixing by gassing in the cptPBR with 5 gassing tubes in the positions 1, 4, 6, 8 and 11 (G1.4.6.8.11) a) volumetric fraction of air in steady state / -, b) high-resolution of flow velocity / $m \cdot s^{-1}$, c) flow velocity and direction of randomly selected cells from (b) / $m \cdot s^{-1}$.

circulations in part of the cptPBR. To explore this further, two configurations with four symmetrically placed tubes each were evaluated. All configurations tested so far allowed for downstream at the sides of the cptPBR along the reactor shell. To maintain space for additional circulating flows in the middle section, the two outer tubes were retained in their outermost positions. A key focus of the following simulations was to assess the flow behavior in the lowest section of the cptPBR, aiming to achieve sufficient flow velocities across all sections.

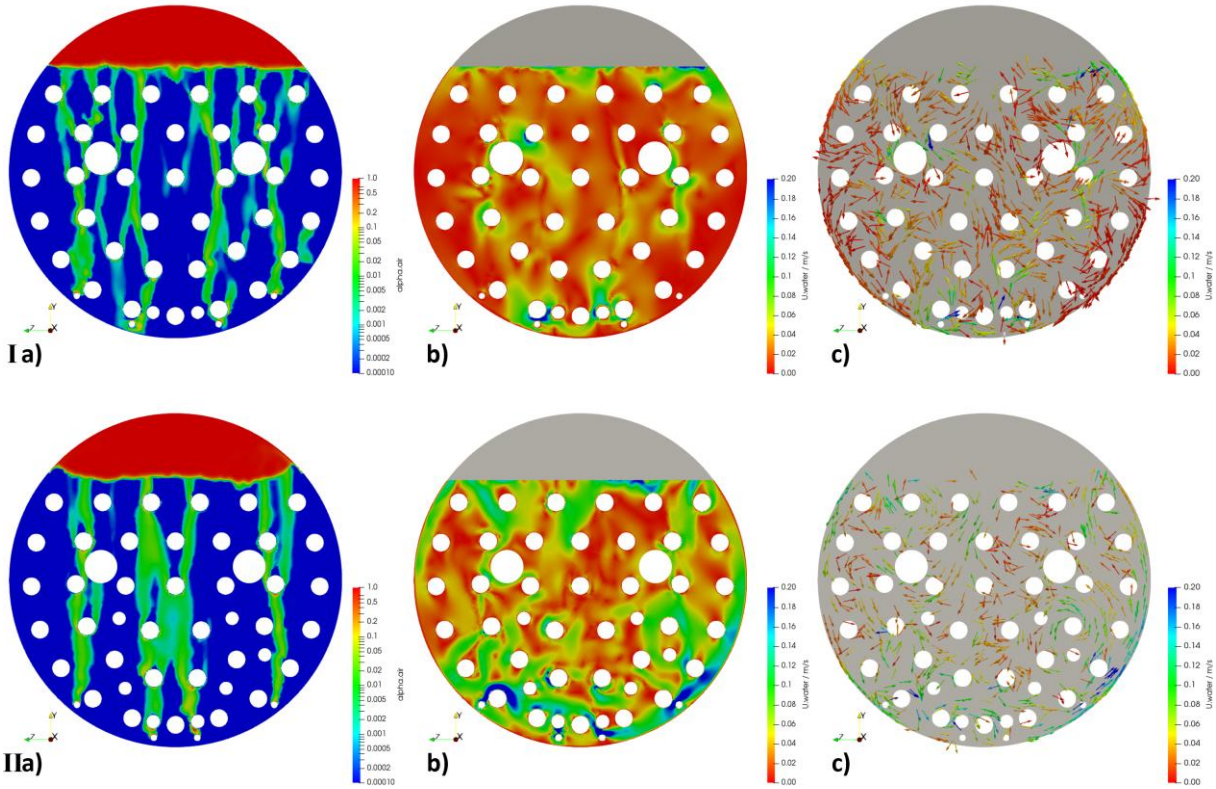

Figure 34: 2-D projections of 3D-simulation results of mixing by gassing in the cptPBR with 4 gassing tubes in the positions I: 1, 4, 8 and 11 (G1.4.8.11) and II: 1, 5, 7 and 11 (G1.5.7.11) a) volumetric fraction of air in steady state / -, b) high-resolution of flow velocity / $m \cdot s^{-1}$, c) flow velocity and direction of randomly selected cells from (b) / $m \cdot s^{-1}$.

The main difference between gassing configurations G1.5.7.11 and G1.4.8.11 lay in the placement of the deeper tubes closer to the center in G1.5.7.11. This positional change, however, interacted with the installations above, leading to substantial variations in gassing behavior (Figure 34). The heating bars primarily obstructed and slightly redirected aeration from the gassing tubes at positions 5 and 7 (Figure 34-IIa) using G1.5.7.11. For G1.4.8.11, the glass tubes housing the LED bars caused the aeration to split directly above the LEDs, with further subdivisions extending the aeration width across the entire cptPBR (Figure 34-Ia).

These variations in aeration patterns translated into distinct flow behaviors. For G1.4.8.11, the flow pattern was characterized by a central downward flow, two downward side flows in the lower section and upward side flows in the upper section. The intermediate region exhibited diffuse flow behavior (Figure 34-Ic). The average flow velocity was 0.030 $m \cdot s^{-1}$, comparable to the reference case, but only 43% of the flow exceeded 0.025 $m \cdot s^{-1}$.

G1.5.7.11 established a higher averaged flow rate of 0.057 $m \cdot s^{-1}$, being an increase of 76 % relative to the reference case. 75 % of the simulated flow velocities were > 0.025 $m \cdot s^{-1}$ and 91 % exceeded > 0.0125 $m \cdot s^{-1}$, supported by the obvious impression comparing Figure 34-Ib and IIb. The improvement in flow velocities was caused by the formation of multiple circulating streams, which made the spatial flow velocity distribution more homogeneous as indicated in Figure 35. This asymmetric simulation result represents one equilibrium and may occur mirrored in other runs.

3.1.5 Evaluation of the illumination setup with respect to mixing

Precise analysis of flow velocities and patterns in experimental pretesting and 3D-modeling identified the optimal placement of gassing tubes at positions 1, 5, 7, and 11 (G1.5.7.11). This configuration demonstrated a well-distributed flow pattern with higher average flow velocities. The higher flows also mitigated the risk of sedimentation in the lower cptPBR sections, ensuring homogeneous biomass suspension. Beyond achieving homogeneity, an adequate interplay between mixing and light distribution was essential for maximizing productivities, with ideal positioning enabling effective transfer of microalgae between light zones.

A critical factor for high photosynthetic efficiency and productivity was the light/dark frequency. Previous studies confirmed that light/dark frequencies ≥ 1 Hz can enhance biomass productivity (chapter 3.1.3). For the cptPBR, with distances of 0.0230 m to 0.0250 m between neighboring glass tube surfaces housing the light bars, up to 0.0125 m must be traversed vertical to the glass tubes to fully pass the light gradient. Rather than vertical flow, the placement of installations led to tangential flow along the glass tube surfaces. Nevertheless, tangential flow

also caused moderate light/dark transfer, as light zones were abundant due to the spot-wise illumination with 120° shifts of the circuit boards in the light bars.

Reviewing the summarized flows shown in Figure 35, the distance along the flow streams that transferred through light zones – from the directly illuminated regions to darkness or vice versa – appeared to range between half and the full straight distance (0.0125 m to 0.0250 m). To ensure optimal performance, flow volume, represented by 2D-summarized cells, should maintain flow velocities of > 0.0250 $m \cdot s^{-1}$. In this context, the G1.5.7.11 configuration outperformed other gassing installations (Figure 36).

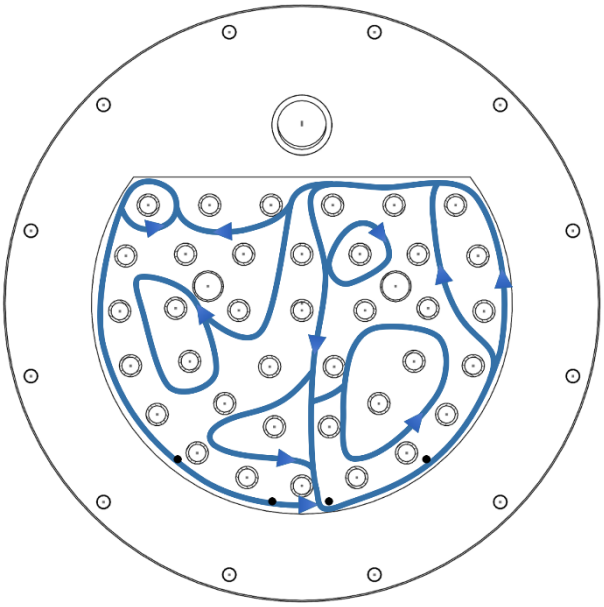

Figure 35: Schematic drawing of the summarized flows according to the simulation results in Figure 34-IIa using the gassing geometry G1.5.7.11 with positions of gassing tubes marked as black circles.

The combination of tangential flow and radially optimized velocities achieved sufficient circulation throughout all cptPBR sections using the G1.5.7.11 configuration to ensure efficient photosynthesis under nutrient replete conditions.

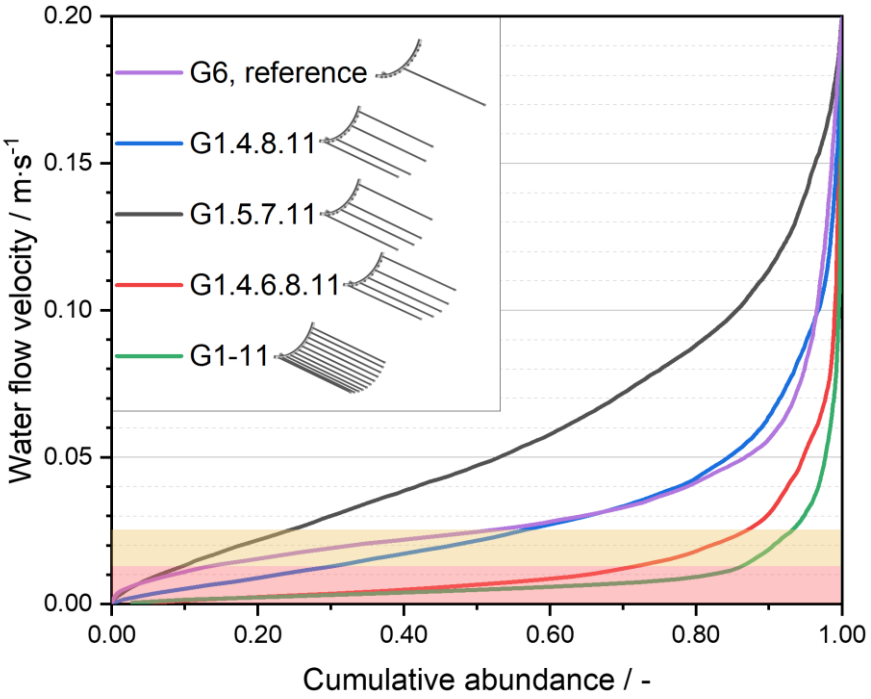

Figure 36: Cumulative abundance of flow velocities in the cptPBR according to the simulation results for different gassing geometries in chapter 3.1.4.5. The flow velocities below 0.0125 $m \cdot s^{-1}$ and 0.0250 $m \cdot s^{-1}$ were colored in red and orange, respectively.

After the successful optimization of gassing and mixing, the resulting gassing geometry was installed and tested during cultivation. Experimentally, the final assembly of gassing tubes (G1.5.7.11) demonstrated minimal sedimentation, even under nutrient depletion. The cptPBR was then ready for microalgal cultivations at high growth rates but required further advancement toward the central objective of ^{13}C-labeling with the integration of a closed gas loop and gas separation system as described in the next chapter.

3.2 Gas loop to retain $^{13}CO_2$ and monitor photosynthetic performance

The compact photobioreactor (cptPBR) was designed and, eventually, optimized in gassing and mixing to create a controlled environment and homogeneous conditions for efficient microalgal growth (chapter 3.1). Besides efficient growth, the efficiency of CO_2 utilization is critical, especially when generating stable isotopically labeled substances from $^{13}CO_2$. To ensure efficient CO_2 utilization, the cptPBR required adaptions in the gas supply and gas management systems.

In a simple setup, CO_2 can be periodically supplied to the cptPBR in a closed gas loop. During photosynthesis, oxygen accumulates in the closed system. High oxygen partial pressures limit the photosynthetic performance, necessitating the periodic removal of oxygen. By opening the gas loop and stripping with N_2 after pausing the CO_2 supply, the accumulated oxygen is removed. However, this oxygen removal also results in the loss of dissolved bicarbonate, degassing as CO_2. Additionally, stripping disrupts the cultivation due to temporary CO_2 limitation and pressure fluctuations, reducing productivity. CO_2 loss could be reduced by extending the time between stopping the CO_2 supply and stripping. However, this reduction in CO_2 losses unfortunately prolongs the period of CO_2 limitation. This interaction limits the room for improvement with this approach, prompting the need for alternative technical solutions.

More advanced systems aim to minimize or avoid CO_2 losses while maintaining PBR productivity. The two primary strategies include removing O_2 from the gas loop or recovering CO_2 from the off-gas. Various techniques were evaluated to design a suitable system for this purpose. Adsorptive processes, although capable, require labor-intensive, multistep recovery procedures with generally high energy demands, while conventional membrane systems lack sufficient selectivity for either removing O_2 or recovering CO_2 effectively. The most promising solution for optimizing the overall process was to keep the gas loop closed and selectively remove the O_2 during the cultivation process. This selective removal of O_2, while circulating all other gases, was achieved using a fuel cell.

3.2.1 Fuel cell for oxygen removal – operating principle & safety considerations

Fuel cells promote the highly selective formation of water from oxygen and hydrogen. This reaction does not literally remove the oxygen from a system, but chemically transfers the oxygen atoms from the oxygen molecules to water molecules, similar to photosynthesis, but reversed. The basic reaction equation of photosynthesis and the chemical equation show only water being formed that was split in photosynthesis before, so the overall water content in the closed system remains unaffected by the use of the fuel cell.

Safety and feasibility considerations were necessary when adapting a fuel cell strategy for O_2 removal in a PBR system. Among various types of fuel cell, the proton exchange membrane fuel cell (PEM) was identified as the most suitable for this application due to its low operating temperature (<100 °C), unlike solid oxide fuel cells which might exceed 600 °C [106]. To avoid high temperatures, a fuel cell stack operating at 65 ºC (Horizon Educational, FCS-B12) was chosen. The low temperature simplifies management and minimizes potential safety hazards.

To operate the PEM, hydrogen is required to be supplied to the anode. Handling of hydrogen generally poses the risk of flammability and explosion at concentrations of ≥ 4 % (v/v) and 15 % (v/v) in air, respectively. The chemical oxidation of hydrogen at the anode splits hydrogen molecules releasing protons that diffuse through the gas-tight membrane of the PEM and electrons that flow to the cathode (Figure 37). The generated electric flow through an external circuit to the cathode needs to be consumed by a load, such as a resistor. Disconnecting the resistor, lacking oxygen or gas flow prohibited fuel cell operation. The abundance of oxygen at the cathode was validated by a pO_2 probe and flow sensor in the gas loop. Protons and electrons,

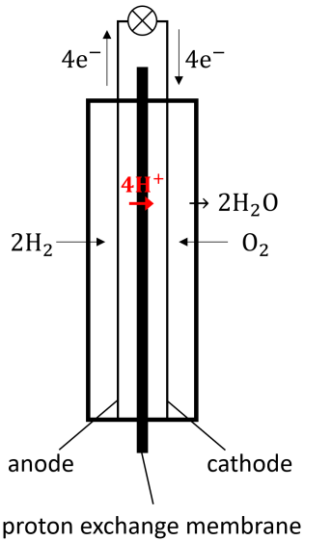

Figure 37: Operating principle of PEM fuel cell.

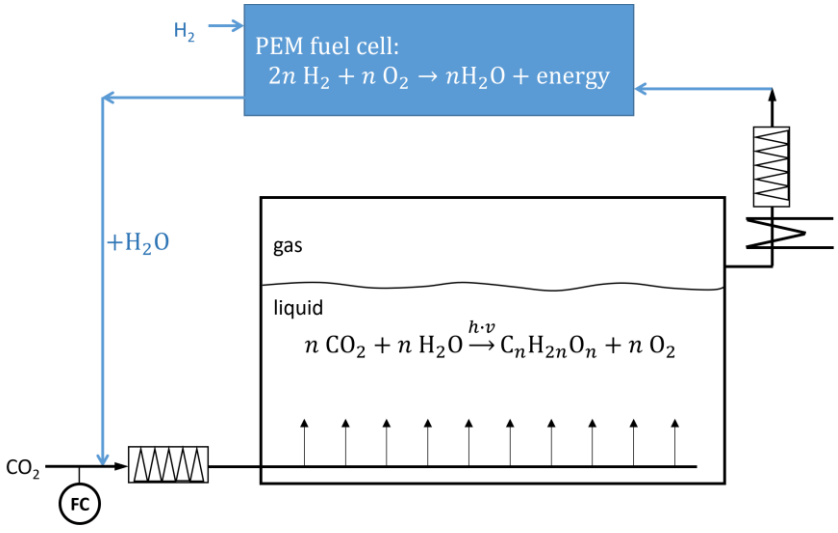

Figure 38: Operating scheme of closed gas loop with PEM fuel cell. Biomass is built by photosynthesis, releasing oxygen that is reduced by the PEM to water.

both originating from hydrogen, and oxygen from the PBR off-gas, combine to form water at the cathode. This water humidifies the gas phase and is recirculated into the PBR (Figure 38).

Humidity on both sides of the proton exchange membrane affects the long-term performance and lifespan of the PEM. Excessive humidity can cause swelling and mechanical stress to the membrane, reducing its durability. In addition to that, water can act as a physical barrier to gas flow, thus reducing gas permeability and lowering the performance of the fuel cell. Water droplets that hinder the hydrogen flow in the capillary system of a stacked fuel cell can convert single cells of the PEM stack into electrolysis cells, catalyzing the reverse reaction by using the electric potential of neighboring cells. This unintended conversion results in temporary performance reductions and induces higher voltages, which may cause localized overheating and uneven current distribution. Such conditions have the potential to degrade both the catalyst and the membrane material.

3.2.2 Experimental implementation of the PEM into a cptPBR gas loop

Safety, durability, and performance risks were associated with hydrogen flammability and explosiveness, as well as humidity in the PEM. These concerns necessitated careful consideration in the overall cptPBR design and gas management system. The implementation of the PEM into the cptPBR setup comprised three subsystems, as illustrated in the process flow diagram (Figure 39): The cptPBR with ‘PBR installations & feeds’ was directly required for cultivation. The ‘gas loop with oxygen removal’ by the PEM enabled cultivation under consistent conditions without CO_2 losses. Additionally, the PEM required dried hydrogen from the ‘H_2 synthesis & desiccation’ subsystem.

Each subsystem was equipped with separate and interlinked safety mechanisms to ensure the long-term and safe performance. As is critical for a closed system, pressure was monitored and safety valves were installed. The pressure relief valve (opening at > 0.5 bar) was placed before the sterile filters in the off-gas line of the cptPBR, whereas pressure drops would have been compensated by N_2 addition to the gas supply unit before the sterile filters. This placement of sterile filters and pressure adjustment ensured safety of equipment and axenic conditions, even when pressure adjustment in the gas line was necessary.

The off-gas of the cptPBR was highly humid, having passed through the culture and become moistened during bubbling. The humidity-related issues underscored the importance of reducing the water content in both the cathode and anode chambers of the PEM, while maintaining a moist atmosphere to ensure proton permeability of the membrane. As moisture might have damaged the fuel cell and lowered performance, the humidity in the PEM needed

to be minimized in the cptPBR off-gas and hydrogen gas stream. To manage the moisture in the off-gas, the humidity was reduced by a condenser before the stream passed through sterile filters and entered the cathode chamber of the PEM. An electrolysis cell fed the PEM with generated hydrogen. The hydrogen stream was first piped through a condenser and then through tubing filled with silica gel beads to minimize the moisture content before entering the anode chamber.

To remove moisture from the PEM capillary system after each operation period, the fuel cell was purged with hydrogen, while the electric circuit was opened to avoid additional catalytic reactions. Risks associated with handling hydrogen were minimized by producing hydrogen on demand and linking its production to safety mechanisms. Hydrogen was only generated by the electrolysis cell if the PEM was about to start operating and the pre-pressure range of hydrogen had not yet been reached. PEM operation was controlled by closing and opening the electric circuit to a resistor, restricted to the set pre-pressure range and measured voltages of the PEM with a time delay (10 s) to allow for voltage buildup. PEM activation was triggered by the partial pressure of oxygen (pO_2), measured before the PEM within the gas cycle, to remove the photosynthetically produced oxygen from the culture and the closed gas loop.

The PEM performance, in terms of oxygen consumption, and the photosynthetic oxygen production were ideally in equilibrium to maintain consistent cultivation conditions regarding the pO_2 in the gas cycle and the culture. This equilibrium required continuous adaptation of the PEM's oxygen consumption to photosynthesis. The oxygen consumption of the PEM is sensitive to several factors such as the temperature of gases, membranes, and chambers, as well as the humidity, the resistor, the run time, and the gas composition. The diversity of these influences prohibited reliable calibration of the online oxygen consumption rate with adaptable measurements on the PEM. Minor variations in any of the parameters resulted in substantial fluctuations in the oxygen consumption rate. The precise adjustment of oxygen consumption by the PEM was challenging due to the dependence of the PEM's performance on the wide range of aforementioned parameters. The issue of performance fluctuations was addressed by controlling the pO_2 within certain limits by activating and deactivating the PEM. The length of the PEM operation phases was roughly adjusted by manually switching the resistances between 15 Ω and 65 Ω. This two-phase operation mode did not allow maintaining a stationary pO_2, but it reliably maintained the pO_2 within close limits that ensured high PBR performance. This operational reliability was crucial for selective removal of oxygen for monitoring purposes as well as the production of ^{13}C-labeled biomass to avoid $^{13}CO_2$ losses.

3.2.3 Quantification of photosynthetic performance based on oxygen evolution

A stationary pO_2 and an equilibrium between photosynthetic oxygen production and PEM oxygen consumption would have been required for the online measurement of the photosynthetic oxygen production rate. This oxygen production rate could then be correlated to the biomass formation under specific PBR conditions and assumption. The discontinuous determination of the oxygen production introduces challenges in accurately approximating biomass productivity throughout the cultivation. The approximated biomass productivity is crucial for monitoring and the automated control of the developed system.

The discontinuous operation of the PEM, alternating between two phases (on/off), allowed only for near-real-time estimation by averaging the hydrogen flow over at least two phases. Hydrogen reacts stoichiometrically with oxygen in a highly reliable manner, and its flow measurement is robust. The stoichiometry of hydrogen and oxygen forming water directly indicates the oxygen removal rate. Averaging the oxygen removal rate over an even number of consecutive PEM phases, equals the photosynthetic oxygen production rate as a near-real-time measure. This measure, combined with the initial biomass concentration and assumptions regarding the physiological state of the culture and biomass composition, provides an approximation of the biomass productivity.

The algal biomass, and thus its correlation to oxygen production, is more complex than commonly suggested by the basic photosynthetic equation, which typically represents only the formation of sugars or polysaccharides and oxygen. The composition of the biomass adapts to varying conditions in the physiological range (more details discussed in chapter 1.4). Active biomass is formed under suitable conditions with regard to light profile, nutrient availability, gassing and mixing. Previous experience regarding the impact of these influences on the investigated species allows assumptions about the biomass composition at similar conditions. The approximation of the biomass composition links oxygen productivity to biomass productivity.

Correlations between biomass composition and oxygen evolution are described by the photosynthetic quotient (PQ). For *Chlorella vulgaris*, reported PQ values under light-limited conditions typically range between 1.1 and 1.5 [107]. Higher reported values around 1.8 likely resulted from the comparison of gross oxygen production to net CO_2 assimilation without accounting for respiration losses. Within the typical range, the effect of biomass composition is minor when ammonium is used as the nitrogen source [108].

The PQ expresses the molar stoichiometry of net oxygen evolution to net carbon fixation. This definition excludes the proportion of fixed carbon that is reoxidized to meet the energy demand of anabolism. Since carbon fixation and combustion are reverse reactions, their cycling reactions leave the net balance unaffected and they are omitted in the following considerations for simplicity. PQ values vary depending on the biomass composition and are influenced by both the nitrogen source and the oxygen content of the formed biomass constituents.

The approximation of the PQ can be based on simplified photosynthetic balances using the previously estimated active biomass composition (chapter 1.5, Table 1) assuming ammonium as the nitrogen source:

$$\mathrm{CO_2} + 0.80\ \mathrm{H_2O} + 0.15\ \mathrm{NH_4^+(aq)} + 0.01\ \mathrm{H_2PO_4^-(aq)} \rightarrow \mathrm{CH_{2.08}O_{0.40}N_{0.15}P_{0.01}} + \mathbf{1.22}\ \mathrm{O_2} + 0.14\mathrm{H^+} \qquad \text{Equation 20}$$

To calculate the generated biomass from the PQ value and the amount of evolved oxygen, only the molecular weight of the biomass is needed. The evolved oxygen is not directly measured, but the measured hydrogen flow correlates stoichiometrically to the oxygen flow with $\nu_{H2} = 2$ and can be converted to molar flows by the molar volume (V_m) assuming an ideal gas. The correlation factor of the biomass or biomolecule (k) to hydrogen $\alpha_{k,H2}$ (Equation 22) is then calculated using the molar mass (M_k) and the stoichiometry factor ν_{H2}:

$$\alpha_{\mathrm{k,H2}} = (V_\mathrm{m} \cdot \nu_{\mathrm{H2}} \cdot \mathrm{PQ_k})^{-1} \cdot \mathrm{M_k} \qquad \text{Equation 21}$$

$$\alpha_{\mathrm{k,H2}} = m_\mathrm{k} \cdot \left(V_{\mathrm{m,H2}}\right)^{-1} \qquad \text{Equation 22}$$

Results from this approximation method for other biomass compositions and constituents were listed in Table 4. The photosynthetically generated biomass was calculated from the oxygen evolution, after the PQ and the elemental composition were estimated for the prevalent process conditions. This estimation was performed with averaged hydrogen flows over multiple PEM operation periods and related to the initial biomass concentration and cptPBR volume to estimate productivities from near-real-time measurements. To determine the volumetric productivity P_V, Equation 23 correlates the hydrogen flow q_{H2} averaged over two consecutive phases of fuel cell operation – including the off periods – to the production of the biomass compound k using $\alpha_{k,H2}$ relative to the cptPBR volume V_{PBR}:

$$P_\mathrm{V} = \alpha_{\mathrm{k,H2}} \cdot \frac{\int_{t_{\mathrm{ON,n}}}^{t_{\mathrm{ON,n+2}}} q_{\mathrm{H2}}}{t_{\mathrm{ON,n+2}} - t_{\mathrm{ON,n}}} \cdot \frac{1}{V_{\mathrm{PBR}}} \qquad \text{Equation 23}$$

In addition to directly approximating productivities under stable conditions, the course of oxygen evolution can indicate changes in carbon partitioning to different biomass constituents

Table 4: Photosynthetic quotients (PQ) and correlation factor ($\alpha_{k,H2}$) for each composition or compound k based on simplified net photosynthetic equations, ammonium as the nitrogen source and elemental compositions from Table 1, chapter 1.5.

Compound k	**PQ** $= \frac{n_{O_2}}{n_{CO_2}}$ **/ -**	$\alpha_{k,H2}$ **/** $g_k \cdot L_{H2}^{-1}$
STA	1.00	0.60
TAG	1.41	0.25
Active biomass elemental composition in agreement with [65,72]	1.22	0.42
STA-rich biomass: 55 % active biomass + 45 % STA	1.12	0.49
TAG-rich biomass: 55 % active biomass + 45 % TAG	1.31	0.34

during cultivation. Higher oxygen evolution may result either from the biosynthesis of a compound with a higher PQ or from the biosynthesis of a compound with a comparatively lower PQ but a higher photosynthetic yield. Therefore, the interpretation of data and any automation based on the data must consider strain characteristics and the conditions to which the culture has been exposed. This approach highlights the complexity and interdependencies within the cptPBR system, emphasizing the necessity of continuous adaptation and control to maintain optimal conditions for algal growth and productivity.

3.2.4 Automation of the biomass growth in the cptPBR

The approximation of biomass productivity, derived from the quantified photosynthetic oxygen production, was crucial for advancing towards the automation of the cptPBR. This automation enabled more precise control, enhanced the efficiency of the system's operation and facilitated kinetic studies under consistent conditions. The near-real-time estimation of the generated biomass was based on assumptions regarding the abundant and synthetized biomass composition with respect to the conditions during the cultivation phase. It was assumed that primarily active biomass formed during the growth phase. During the nitrogen limitation phase, physiological changes occurred on short time scales as further synthesis of active biomass was not feasible, allowing mainly the formation of starch in *C. vulgaris* H 14.

From a process control perspective, the cultivation was segmented into four distinct phases, mainly differentiated by nutrient feed profiles. The initial batch phase allowed for acclimation of inoculum in the cptPBR. When the ammonium (NH_4^+)-concentration dropped below a certain limit according

to the calculations on biomass growth and nitrogen uptake, the feed of NH_4^+-solution started. Other nutrients were initially supplied in excess and not actively fed during the cultivation. The

aim of this control setup was to achieve high biomass productivities during the growth phase, but enable immediate switching to nitrogen limitation to support starch formation. The N-feed was, first, intentionally kept below the proportional nitrogen demand for active biomass growth to let the NH_4^+-concentration decrease further towards NH_4^+-depletion in the medium. The NH_4^+-depletion initiated proportional N-feeding to biomass growth and facilitated immediate transition to manual nutrient limitation with custom feeding in phase IV. The primary focus in this chapter was the automation of biomass growth during phase III.

During this growth phase, the novel automated control of the cptPBR aimed to maintain constant conditions to ensure high biomass productivities. The control, dependent on biomass concentration and photosynthetic activity, managed CO_2 and nitrogen supply, as well as the regulation of incident light intensity and is further described below. The essential components for this control included the photobioreactor, its installations and periphery, the gas loop for oxygen removal, and the equipment for hydrogen supply, along with information flows for measurement and control as described in chapter 3.2.2 and displayed in Figure 39.

The information on productivity, originating from fuel cell assessment and initial concentrations, was near-real-time and extrapolated to form a continuous data set. The extrapolation assumed that specific rates of the last analyzed time interval were maintained until new data became available. NH_4^+-uptake was compensated for by supplying amounts equal to the calculated consumption by a continuous feed. CO_2 was fed only during PEM operation, in equal volumes to oxygen consumption, to minimize pressure fluctuations and prevent the risk of limitations. This CO_2 feeding approach would align with a PQ_X value of 1, as described by:

$$q_{\mathrm{f,CO2}} = \frac{q_{\mathrm{H2}}}{\nu_{\mathrm{H2}} \cdot \mathrm{PQ_X}} := \frac{q_{\mathrm{H2}}}{\nu_{\mathrm{H2}}} \qquad \text{Equation 24}$$

The light intensity was increased during the cultivations proportionally to the biomass concentration to maintain the cells' light absorption as constant as possible, with the target specific light supply rate $spI_{h\nu,\mathrm{target}}$.

A fundamental description of the mathematical model for PBR automation and its underlying mechanisms is provided below. The change in active biomass concentration c_{actX} due to proliferation by cell division is conventionally described by the specific growth rate μ:

$$\frac{\mathrm{d}\, c_{\mathrm{actX}}}{\mathrm{d}\, t} = \mu \cdot c_{\mathrm{actX}} \qquad \text{Equation 25}$$

Integration of Equation 25 and resolution of the resultant logarithmic expression for c_{actX} yields the widely recognized formula for exponential growth:

$$c_{actX,tn+1} = c_{actX,tn} \cdot e^{\mu \cdot (t_{n+1} - t_n)} \qquad \text{Equation 26}$$

Given that the initial biomass concentration $c_{actX,tn}$ at the time t_n was determined from measurements, the specific growth rate μ remained the only parameter to be derived. In the automated control system, μ was primarily calculated based on hydrogen flow data, with an alternative approach utilizing OD measurements where needed. To approximate μ, Equation 25 was transformed into discrete terms and reorganizing, utilizing the volumetric productivity P_V from Equation 23 and expecting the sole formation of active biomass:

$$\mu = \frac{\frac{\Delta c_{actX}}{\Delta t}}{c_{actX}} = \frac{P_V}{c_{actX}} \qquad \text{Equation 27}$$

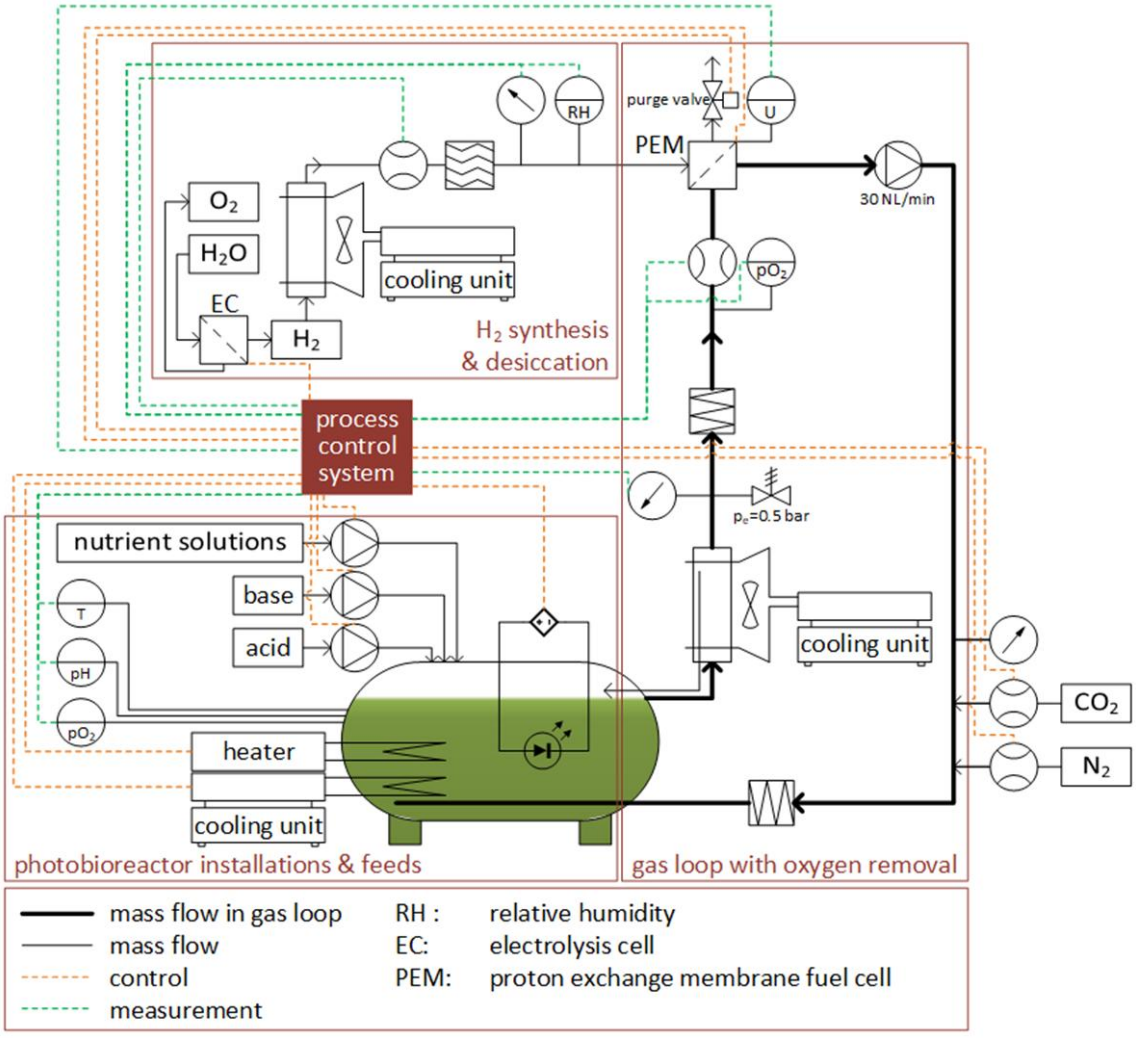

Figure 39: Process flow diagram of the compact photobioreactor including gas separation. Further installations non-essential for the automation and gas loop are neglected for visibility: spectral sensor, online transmission, off-gas measurement, manually controlled valves for gas feeds to circumvent back flow, separated nutrient solutions (summarized in figure), sampling port, ports for manual additions of e.g. antifoam agent, power supply units, balances to check nutrient feed, resistor, safety mechanisms as hardware.

The alternative calculation of the biomass concentration from offline OD measurements, with an experimentally determined correlation, was primarily executed when lacking hydrogen-based data, particularly at the onset of the cultivation. Using the OD values, the specific growth rate was either manually set or determined from two consecutive samplings. The OD measurements were also used to correct deviations of the OD-correlated c_{actX} from predictions, e.g. due to initially long calculation periods of H_2-flow. Negative deviations – indicating less growth than expected – resulted in maintaining constant light intensity while pausing nutrient and CO_2 feeds until the biomass formation caught up. Underestimations of growth might have caused light limitations, but stepwise increases may cause undesired metabolic effects due to acclimation. To cope with both, light was increased intermediately as if the underpredicted c_X was true but assuming μ being 50 % above the regular rate until the actual c_X was reached, in other terms, as long as $spI_{hν} < 50\ \mu mol \cdot g^{-1} \cdot s^{-1}$. The estimation of c_{actX} was directly used for the light control as the light supply was maintained proportional to the biomass.

$$I_{hυ,0} = \frac{spI_{hν,target} \cdot c_{actX} \cdot V_{PBR}}{A_{PBR}} \qquad \text{Equation 28}$$

During the growth phase, the incident light intensity $I_{hν,0}$ was controlled based on $spI_{hν,target}$ and the estimated c_{actX}, whereas decreases in light intensity and stepwise increases were both prohibited. Mismatches of the estimated and measured biomass concentration were originating from either manual inputs or inaccuracies in parameter estimation like the biomass composition and, thus, PQ and $\alpha_{k,H2}$. Overestimations in growth resulted in $spI_{hν} > spI_{hν,target}$ and were compensated by maintaining the incident light intensity constant until $spI_{hν} = spI_{hν,target}$. While underestimations caused $spI_{hν} < spI_{hν,target}$ and required the light intensity to catch up with c_{actX}. The catch up was performed by an increase of the light gradient over proportional to biomass growth restricted to 1.5·μ fictional biomass increase to get back to the target light supply rate.

Based on the actual light supply and the specific growth rate, the photoconversion efficiency (*PCE*) on available photons was approximated to allow the near-online evaluation of the photosynthetic performance as:

$$PCE = \frac{\mu \cdot \Delta H_c{}^0}{spI_{hν} \cdot E_{ph}} \qquad \text{Equation 29.}$$

High *PCE* values indicate healthy cellular growth and a vital culture, which are crucial for maintaining productivity during the growth phase and ensuring comparability between different cultivations, particularly at the onset of nutrient limitation. The approximation used an average value for the energy content of photons in the spectral range of 400 nm to 700 nm, $E_{ph} = 210.5\ kJ \cdot mol^{-1}$ [109] and a typical value for the heat of combustion of biomass $\Delta H_c{}^0$ = 20.0

to 23.0 kJ·g^{-1} [110]. The actual heat of combustion of the biomass depends on its composition and may deviate between 17.41 for starch and 39.51 kJ·g^{-1} for TAG according to Table 2 (chapter 1.5) which is, among others, determined by the nutrient availability during biomass growth.

The theoretical concentration of available nitrogen was calculated based on the elemental balance of autotrophic biomass formation on NH_4^+ feed ($q_{f,N}$) with the feed concentration $c_{N\text{-}feed}$. The NH_4^+-concentration in the cptPBR ($c_{N,tn}$) resulted from NH_4^+-feeding that either remained in the reactor volume (V_{PBR}) or was taken up into the cells and immediately incorporated into the biomass building the elemental fraction $e_{N,X}$:

$$c_{N,tn+1} = c_{N,tn} - e_{N,X} \cdot \left(c_{actX,tn+1} - c_{actX,tn}\right) + q_{f,N,tn} \cdot c_{N,feed} \cdot \frac{t_{n+1} - t_n}{V_{PBR}} \qquad \text{Equation 30}$$

The required feed to fully compensate the nitrogen incorporated into the biomass is thus given by:

$$q_{f,N,tn+1} = \frac{e_{N,X} \cdot \left(c_{actX,tn+1} - c_{actX,tn}\right)}{c_{N,feed}} \cdot \frac{V_{PBR}}{t_{n+1} - t_n} \qquad \text{Equation 31}$$

The NH_4^+-feed (Equation 31) and the light intensity (Equation 28) as the most relevant parameters for the intended kinetic studies were automated through implementation in LabView 2018. The custom controllers in LabView were written in three dynamically interacting MathScript codes at a parameter set interval of 1 s. The scripts first performed the calculation of the biomass concentration according to automated criteria and manual settings and forwarded this information to other calculation to maintain optimal cultivation conditions. More information on the scripts and the code used during the proof-of-concept was provided in A2.

3.2.5 Proof of concept - automated cultivation with closed gas loop in the cptPBR

The improved cptPBR design, together with the newly designed closed gas loop, which included oxygen removal by the PEM and the related automation of the cptPBR, formed the overall system. As a proof-of-concept for this system, a detailed analysis of the estimated biomass formation from one cultivation was conducted to define the limits for reliable operation and provide the basis for the following discussion of the setup.

The setup for the proof-of-concept was designed and parameters were estimated to test the entire cultivation setup and control, with particular focus on the nitrogen feed. Nutrients, except NH_4^+, were supplied in excess, while CO_2 and light limitation were avoided. This combination was achieved through the application of high $\alpha_{k,H2}$ and low PQ and $e_{N,X}$ using the calculation scheme for automation described in chapter 3.2.4 and the MathScript code in the appendix A2.

The factor $\alpha_{k,H2}$ linked biomass formation to the PEM's hydrogen consumption (Equation 21.1). An underprediction of $\alpha_{k,H2}$ would have led to an underestimation of biomass growth, resulting in nitrogen and light limitations. The underprediction would not directly affect CO_2 supply due to its dependence on hydrogen flow measurement (Equation 24). Overprediction of $\alpha_{k,H2}$, and thus biomass growth, was considered more acceptable for light control as long as not drifting into the light inhibition range to enable high productivities in this testing. Key components of the correlation factor $\alpha_{k,H2}$ included M_X and PQ_X, which were closely related to the reaction stoichiometry.

Active biomass would grow with a PQ_X of 1.22 according to the given data examples in chapter 3.2.3 (Table 4). Following the described control scheme, $PQ_X = 1$ equated the CO_2 feed to O_2 consumption, as described in Equation 24. This oversupply of CO_2 (up to 22 %), based on the assumption of active biomass formation with the mentioned composition, was intended to confidently prevent CO_2 limitation. Uncertainties regarding biomass composition under scarce nitrogen feeding were acknowledged, but no change in productivity was expected due to the surplus of CO_2. The insensitivity of growth to the applied CO_2 conditions was supported by preliminary experiments showing no significant differences in productivity between cultivations with 1 % and 2 % CO_2. These findings aligned with previous studies at our institute, which observed similar results between 1 kPa and 5 kPa for another *C. vulgaris* strain [111].

The following settings were only used for controlling purposes in the scripts for operational reasons that will be described below. The biologically appropriate parameters were used to evaluate cultivation data. Setting PQ_X to 1 in the control algorithms ensured CO_2-replete conditions and excluded CO_2 as a parameter to be considered for growth kinetics. The only remaining parameters influencing biomass growth were, then, light and nitrogen. To maintain the focus on nitrogen and prevent interacting kinetic effects, light supply was intended to be in the range of the ideal light supply rate in this cptPBR (50-70 $\mu mol \cdot g^{-1} \cdot s^{-1}$) by a formally high $\alpha_{X,H2}$, which was mainly caused by the low PQ_X. In addition, the M_X was set to 23.7 $g \cdot mol^{-1}$ to account for uncertainties in biomass composition, the presumed molecular weight represented a compromise between starch-rich and active biomass formation.

$$\alpha_{X,H2} = \frac{M_X}{V_m \cdot \nu_{H2} \cdot PQ_X} = \frac{23.7 \frac{g}{mol}}{22.4 \frac{L}{mol} \cdot 2 \cdot 1} = 0.53 \frac{g}{L} \qquad \text{Equation 32}$$

Uncertainty regarding the biomass composition arose due to scarce nitrogen supply during the growth phase, despite the intention to avoid nitrogen limitation. Conditions near nitrogen

limitation or kinetic constraints in NH_4^+-uptake may have initially promoted starch accumulation, followed by its subsequent conversion into active biomass under partial respiration. On a net balance, this process led to the intended overprediction of growth, as the PQ of 1 primarily reflected starch formation. The overprediction effectively prevented CO_2 and light limitation, even when the biomass composition was only roughly estimated prior to cultivation.

To ensure no excess of nitrogen supply during biomass growth, the overprediction of growth was counteracted by reducing the assumed nitrogen content in active biomass. This reduction was formalized as $e_{N,X} = 0.07$ in Equation 31. Enforcing this $e_{N,X}$ through controlled feeding enabled the growth of viable and reproducible biomass compositions [74] and ensured immediate uptake of the NH_4^+- feed. A higher $e_{N,X}$, such as 0.09, aligned with the approximated active biomass composition $CH_{2.08}O_{0.40}N_{0.15}P_{0.01}$ (Table 1, chapter 1.5; Equation 20), which considered only the most abundant five elements and excluded ash. In practice, $e_{N,X}$ reached 0.09 when only active biomass was formed, as described by the mentioned composition. This formation was associated with maximum overprediction of growth due to deviations between theoretical and real PQ.

Maintaining automated control of NH_4^+- feed within this physiological range of $e_{N,X}$ ensured the potential for an immediate onset of nitrogen limitation upon demand, albeit at the cost of some storage compound formation during the growth phase. The actual nitrogen demand was unlikely to exceed the nitrogen feed, as the feed calculation was based on c_{actX}, with slight overprediction to circumvent light and CO_2 limitations.

The near-online estimation of c_X, being error-prone to a certain extent, propagated uncertainties into the calculated $e_{N,X}$ during the cultivation. Both were closely related to biomass composition, so the estimation most precisely monitored growth under replete conditions. Since biomass composition influenced the monitored c_X, reassessment of PQ and the c_X became a mandatory part of post-cultivation data evaluation. Given the dependence of process control on near real-time c_X, recalibration of the factor $\alpha_{k,H2}$ was crucial due to its sensitivity to the photosynthetic reaction stoichiometry in the generated biomass.

3.2.6 Limits of PEM operation & corrective calculations during data assessment

In the presented cultivation setup (3.2.2), the calculation of the biomass concentration from the PEM's H_2 consumption was based on strict stoichiometry using defined coefficients (as described in 3.2.3, Table 4). This relationship between biomass formation and H_2 flow only held if both water and biomass formation remained within the system boundaries, meaning that

all measured H_2 was consumed by the PEM. Changes in environmental conditions, particularly those that opened the system boundaries, limited the applicability of the H_2 measurements for the estimation of biomass growth. Such conditions could relate to temperature fluctuations or the efficiency of current capture, but the primary factors were the availability or loss of the substrate H_2, the hydration state of the PEM stack and changes in the pO_2 inside the system boundaries.

Gradients and changes in pO_2 were predominantly influenced by the photosynthetic activity and PEM operation together with the gas transfer between liquid and gas phases. The system's delay in the pO_2 change within the medium in response to the changes in pO_2 in the gas loop due to PEM activity was only 0.02 to 0.04 h (red arrows in Figure 40), demonstrating sufficient gas transfer under the applied operation conditions relative to the typical duration of evaluation intervals (1-2 h). However, the periodic PEM operation caused repetitive changes in pO_2. The

gradient from the liquid to the gas phase served as the driving force for the removal of photosynthetically produced O_2 from the culture via the gas phase. This gradient increased to the pO_2 in the gas loop being up to 6 % below the pO_2 in the medium due to higher oxygen removal rates at high microalgal productivities.

The only source of oxygen within the closed system was the photosynthetic production by the microalgae (algae), while the PEM served as the only effective sink for excess oxygen. The medium (med) and the gas phase (gas) could be interpreted as temporary storage compartments for oxygen. This leads to the following balance of reaction and uptake rates of oxygen ($r_{O2,i}$):

$$\sum (r_{\mathrm{O2,algae}} + r_{\mathrm{O2,PEM}} + r_{\mathrm{O2,gas}} + r_{\mathrm{O2,med}}) = 0 \qquad \text{Equation 33}$$

These oxygen rates can be visualized as time differentials of pO_2 values, as shown in Figure 40**.** The figure provides a clear graphical interpretation of the system dynamics and highlights a typical evaluation interval under periodic PEM operation.

Corrective calculations during data evaluation accounted for the differences (violet arrows) and temporal shifts (red arrows in Figure 40) in pO_2 between measurement positions. The pO_2 in the medium served as the control reference, while the pO_2 in the gas phase was measured near the PEM as a secondary effect without active control. The pO_2 change over one evaluation period in the gas phase ($r_{O2,gas}$ in Figure 40) was included in the corrective calculations to compensate for the effects of non-ideal gas-liquid mixing and the formation of oxygen

gradients. As shown in Figure 40, ΔpO_2 increased by 0.4 % within one evaluation period as a consequence of increased photosynthetic activity.

The rate of oxygen change in the medium $r_{O2,med}$ was neglected, as the maximum solubility of oxygen in water (8 mg·L^{-1} at 27 °C) corresponded to only 3.2 mL of dissolved oxygen in the entire cptPBR medium within the control interval of 17 % to 19 % pO_2. The rate of oxygen consumption by the PEM was determined more accurately by measuring the H_2 flow rather than using pO_2, as the H_2 measurement was less dependent on pressure and gas volume.

While the corrective calculations and assumptions enabled consistent evaluation of oxygen gradients, the operation of the PEM itself imposed additional limitations on the system. To ensure long-term PEM performance, appropriate membrane hydration was required. During cultivation, the PEM tended to overhydrate due to water formation and humidified gas flows in the cathode chamber. Excess water was removed by purging with dried H_2, achieved by opening

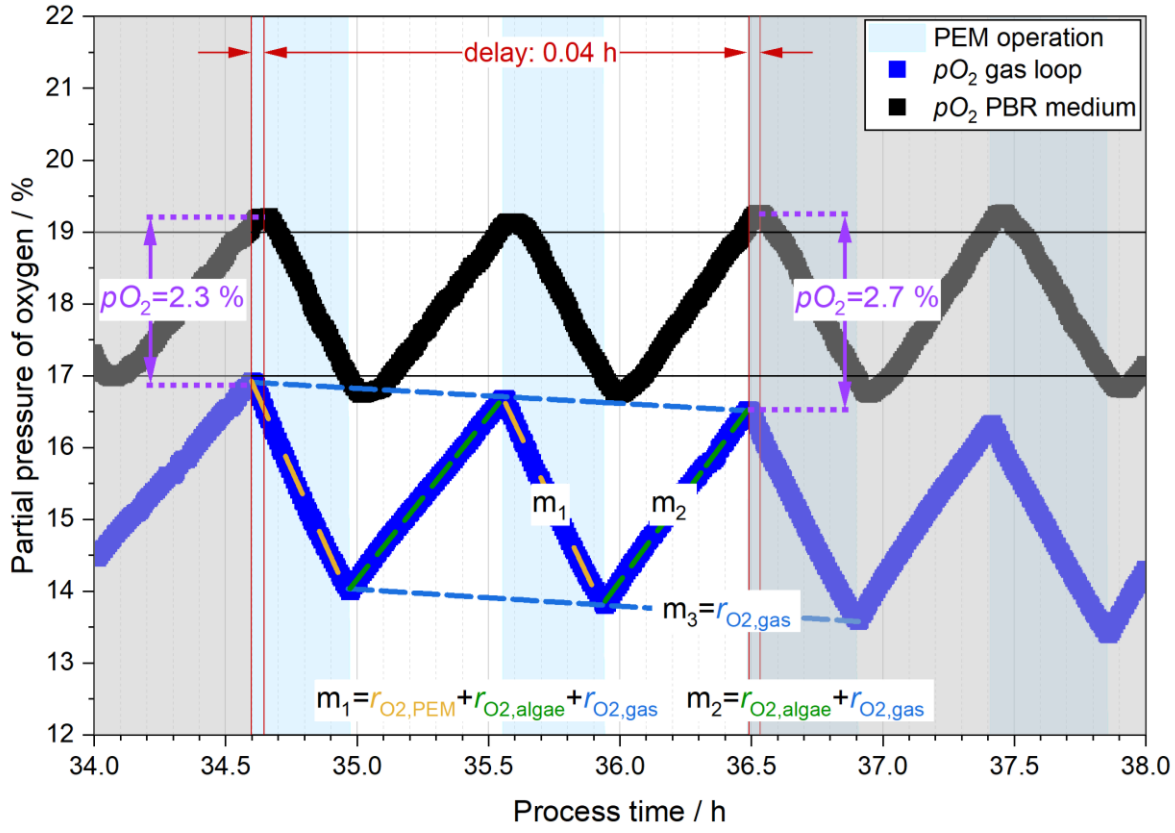

Figure 40: Partial pressure of oxygen (pO_2) in the gas loop before the PEM (blue) and in the cptPBR medium (black) during periodic PEM operation. The figure illustrates the cyclic pattern of oxygen dynamics under controlled operation, with PEM operation periods highlighted in light blue and intervals without PEM operation showing increasing pO_2 values. Violet arrows indicate the increasing differences in ΔpO_2 (2.3 % to 2.7 %) between the gas loop and the medium, while red arrows show the consistent temporal delay of 0.04 h between measurement positions during the displayed cultivation period. The slopes m_1, m_2 and m_3 from linear fits are predominantly determined by the PEM activity, the photosynthetic oxygen production and the downward drift of the pO_2 in the gas loop, respectively, as indicated by color. The time delay between the medium and gas phase (0.04 h) remained consistent during this cultivation period but may vary over longer time intervals.

the purge valve. However, opening the purge valve decoupled the measured H_2 flow from the actual H_2 consumption by the PEM. The decoupling of the H_2 measurement from the consumption crossed a system boundary and prohibited accurate biomass calculation due to overestimation.

Purging was initiated either at predefined time intervals or when the PEM voltage dropped below the operational limit $U < 6.5$ V, as specified by the manufacturer. To enable the estimation of biomass formation during purging, the correlation of the measured PEM voltage and the H_2 consumption was evaluated. The fundamental physical processes within the PEM stack, particularly those associated with purging and varying hydration states, were investigated to identify suitable data clusters and potential correlations under defined physical states, enabling approximation of H_2 consumption during purging from the PEM voltage. Two fundamentally different effects during purging and PEM operation were distinguished: The first was the physical changes directly caused by opening the purge valve and the other was related to the physical state of the PEM that triggers purging.

Opening the purge valve caused the pressure within the PEM to drop to ambient pressure in the anode chamber. The open valve allowed a portion of the supplied hydrogen to bypass the electrochemical reaction and flush through the system rather than forming water in the cptPBR gas loop. Consequently, the measured H_2 flow could exceed the maximum reaction rate of the PEM. The maximum H_2 reaction rate could still be achieved if a sufficiently high flow ensured adequate H_2 supply to the membrane. Effective access of H_2 to the catalyst layer of the membrane required favorable conditions, especially at ambient pressure.

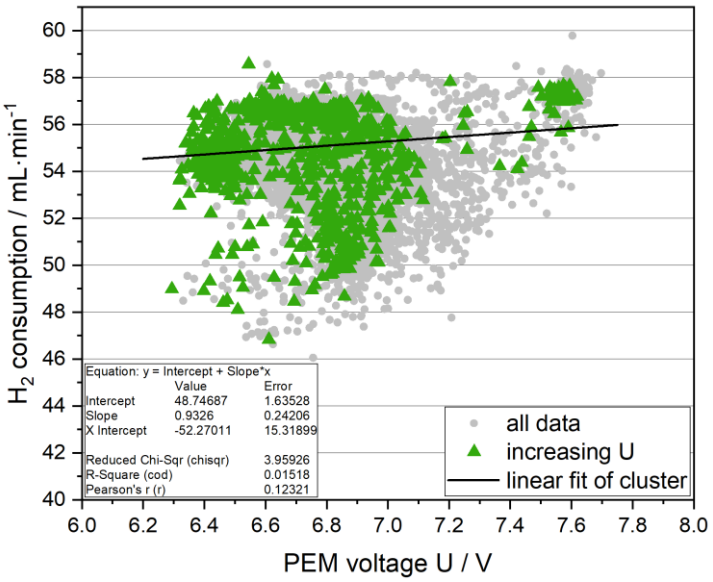

Figure 41: Correlation of measured H_2 flow to PEM voltage. Data were filtered for periods of steadily increasing voltage with the purge valve closed and excluding switching processes to cluster appropriate hydration states of the PEM membrane. Scatter was primarily attributed to temperature and pressure fluctuations.

In the proof-of-concept cultivation, the entire dataset during PEM operation (grey circles in Figure 41 to Figure 43) was evaluated, and data were clustered based on phases of increasing PEM voltage with the purge valve closed to identify favorable conditions. Appropriate

hydration, together with sufficient H_2 availability, led to a weak positive linear correlation between the H_2 flow and the PEM voltage ($r = 0.123$, $p < 0.001$, $n = 965$; Figure 41). This linear correlation resulted from the uniform spatial distribution of the water-forming reaction, which in turn enabled a uniform current distribution across the PEM stack. However, this correlation occurred only under favorable PEM conditions.

Purging during cultivation predominantly occurred under unfavorable conditions, as voltage drops triggered purging to recover the PEM from flooding. Although the voltage provided some insight into PEM performance, it did not directly reflect the true reaction rate, even under constant resistive load. Excess hydration blocked or restricted the H_2 flow through the channels on the anode side of the membrane, leading to locally reduced reaction rates due to the limited accessibility of the catalytic layer and, consequently, non-uniform current distribution across the PEM stack. This non-uniform current chemically decoupled the voltage from the reaction rate and thus from the H_2 consumption, emphasizing that a high measured voltage was necessary but not sufficient to reflect effective PEM performance.

Over-humidified PEM cells may still locally develop the expected voltages, while the current density varies throughout the PEM stack cross-section, resulting in an overall reduction in the reaction rate. Initial stages of overhydration potentially resulted in short-term voltage increases while overall H_2 consumption decreased. In contrast, rapid voltage drops were observed only when PEM performance was already drastically impaired. Although experimental data filtered for short-term dropping and fluctuating voltage with the purge valve closed demonstrated a lack of significant linear correlation ($r = -0.018$, $p = 0.195$, $n = 5238$; Figure 42), the slightly negative trend indicated a spatially non-uniform current distribution within the PEM stack due to uneven overhydration. Such local effects could transiently increase the measured voltage despite a reduced overall reaction rate, further emphasizing the complexity of

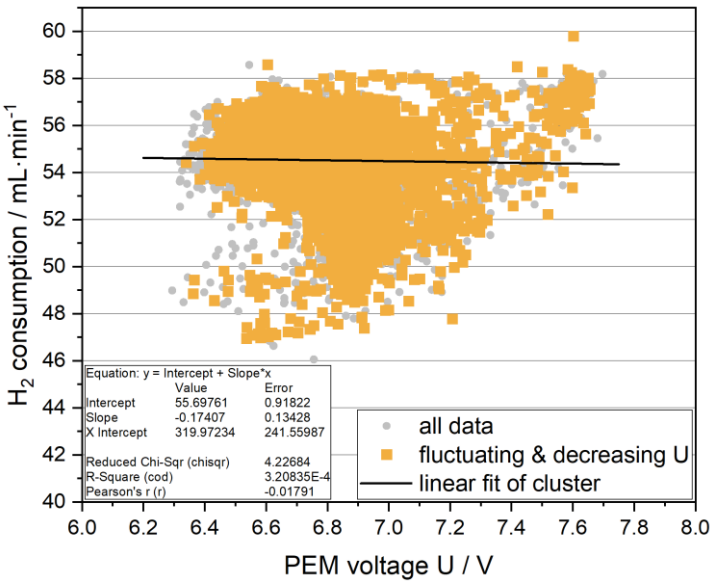

Figure 42: Correlation of measured H_2 flow to PEM voltage. Data were filtered (orange squares) for fluctuating and decreasing voltage with the purge valve closed and excluding switching processes to capture the onset of PEM membrane overhydration.

accurately assessing H_2 consumption under purging conditions. This decoupling of H_2 consumption and voltage necessitates reevaluation of the underlying mechanisms to develop correction strategies for approximating H_2 consumption during purging. The importance of these correction strategies increases with extended PEM operation periods, particularly during the later stages of cultivation.

Correction strategies for approximation of H_2 consumption during purging were based on the H_2 flow measurement, voltage and the PEM performance state. PEM performance during purging was assumed to resemble its performance between high frequent purge intervals triggered by voltage drops. Frequent purging indicated that overhydration was not sufficiently removed by single purging events for full recovery of PEM performance. To capture comparable PEM states to those during purging, data were clustered based on repetitive voltage drops below the critical voltage (< 6.5 V) within one minute before and after each data point, excluding switching processes. This cluster revealed a strong positive linear correlation between the H_2 flow and the PEM voltage ($r = 0.735$, $p < 0.001$, $n = 151$; Figure 43).

This correlation is considered to predominantly reflect the limited availability of H_2 at the active layer of the membrane, as overhydration progressed to suppress voltage increases. Extrapolation of this linear correlation to lower voltages enables the approximation of biomass formation during purging based on the measured voltage. The assumption of a continued linear correlation is justified by the expectation that the distribution of excess water restricting H_2 access to the active layer varied less across the PEM stack. Once hydration predominantly caused voltage drops, the local formation of direct current pathways was prevented by spatial disruptions due to water blockage. This absence of locally higher currents – and their associated high local voltages under constant resistance – allowed the PEM voltage to be reliably linked again to H_2 consumption. In

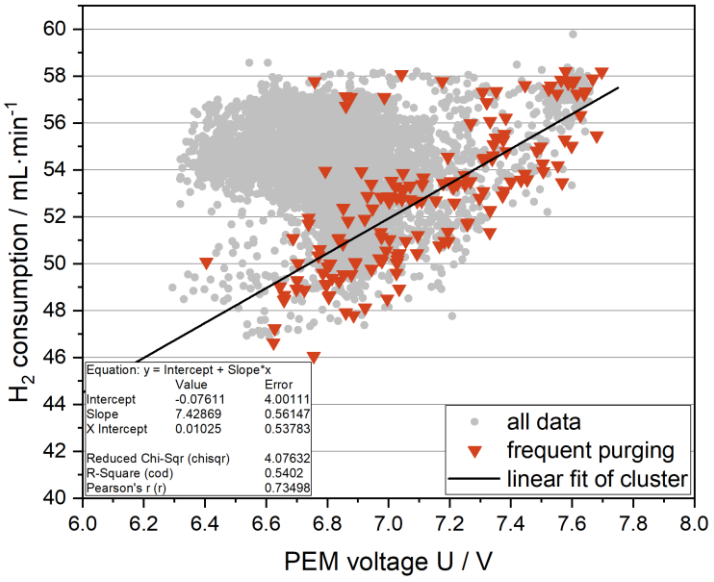

Figure 43: Correlation of measured H_2 flow to PEM voltage. Data were filtered for instances when purging occurred within one minute before and after each respective data point with the purge valve closed, excluding switching processes, to capture PEM membrane hydration states similar to those that trigger purging.

this later stage of overhydration, the disturbance present in the intermediate state, where voltage and H_2 consumption were impaired by uneven water distribution, was no longer present. Since purging was triggered by voltage drops due to overhydration, the correlation of voltage and H_2 consumption (Figure 43) was extrapolated and restricted to zero, yielding a value of 7.418 $V \cdot (mL \cdot min^{-1})^{-1}$, which was then used to approximate the H_2 consumption during purging.

3.2.7 Proof of concept cultivation – assumptions and biological boundaries

In the final data evaluation, the H_2 consumption rates were derived from H_2 measurements as described in chapter 3.2.3 to 3.2.6 including all mentioned corrections and constraints. The consumption rates were then stoichiometrically converted to biomass productivities to, finally, determine biomass concentrations continuously throughout cultivation. These biomass concentrations were compared with (interpolated) offline data from dry weight measurements to assess the suitability of the H_2-based method for automated control and metabolic studies.

The conversion from H_2 volume to biomass used the correlation factor $\alpha_{k,H2} = 0.42\ g \cdot L^{-1}$ determined for active biomass based on literature data (see section 3.2.3). Due to low biomass concentration at inoculation, the initial cultivation period was outside operational limits. In addition, the first H_2 consumption peak was excluded from the analysis, as it primarily reflected the oxygen introduced during inoculation rather than photosynthetic activity.

Prior to the completion of two evaluable PEM operation cycles, the system was operated using manual inputs. Data evaluation and the control algorithm based on H_2 consumption started after process time (PT) = 16.18 h. Two evaluable PEM operation cycles, during which oxygen was depleted to $pO_2 < 17$ % in the cptPBR, were completed within 5.42 h. The resulting average delay between measurement and its application for control adjustments was 4.04 h, based on the time of data acquisition and the duration the calculated values were applied in automated control. For automated control, the data were extrapolated to the current cultivation time under the assumption of a constant specific growth rate, as illustrated in Figure 44, acknowledging that the time shift may introduce inaccuracies.

These inaccuracies in data extrapolation originated from the delay between measurement and process adjustment, which particularly impacted cultivation at low biomass concentrations and thus low volumetric productivities. The robustness of the cultivation toward automated parameter adjustments determined the maximum acceptable delay and, in turn, defined the lower operational limit from a biological point of view in terms of biomass productivity.

The lowest suitable productivity was determined based on the cultivation data by evaluating the potential under- and overestimations in dependence on the evaluation time interval and the specific growth rate. To prohibit rare cases of huge overestimations due to system errors, the specific growth rate was kept at a physiological value via capping the maximum flow. In practice, the worst-case scenario would then either be expecting no growth during one evaluation interval while growth occurs at μ_{max}, or vice versa. These worst-case scenarios correspond to a 20 % underestimation and a 20 % overestimation, respectively, at the observed maximum specific growth rate μ_{max} = 2.81 day^{-1}, which corresponds to an evaluation period of 1.56 h. This limit was first reached at PT = 33.70 h, with c_X = 0.11 g·L^{-1} and P_V = 0.32 g·L^{-1}·day^{-1}, establishing the lower operational boundary under the tested conditions in the described setup.

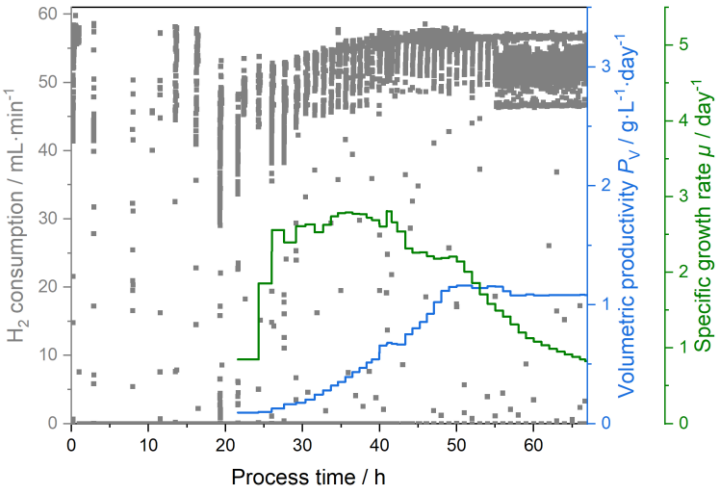

Figure 44: H_2 consumption (grey, left axis) and H_2-derived volumetric biomass productivity P_V (blue, right axis) and specific growth rate μ (green, right axis) during cultivation. The first cycle was excluded, as it mainly reflected oxygen from the inoculum, while P_V and μ are shown following the completion of the two subsequent evaluable PEM operation cycles based on depletion below pO_2 = 17 % in the culture.

More realistically, changes in the calculated specific growth rate from one evaluation interval to the next are typically lower, as observed during this cultivation, where the maximum change was 36 % of μ_{max}. The resulting over- and underpredictions based on changes in μ, with respect to the defined operational boundary, remained within a 10 % control error margin, which is commonly accepted in biological systems. This stability was attributed to the physiological inertia of microalgae in responding to environmental conditions, with the exception of CO_2 and light. Both of these growth parameters were controlled to avoid limitations, enabling testing the system across a broad range of volumetric productivities and growth rates. The upper operational limit was determined to be 1.15 g·L^{-1}·day^{-1}, constrained by the maximum oxygen removal rate of the PEM. Above this productivity, the pO_2 rose steadily above the upper defined limit of 19 % in the medium disturbing the stoichiometric relation of H_2 flow and biomass formation.

The H_2-based biomass concentrations within the operational boundaries are shown in Figure 45. Although these concentrations exhibit trends similar to those determined gravimetrically, their suitability for automated control and metabolic analysis required evaluation using statistical methods.

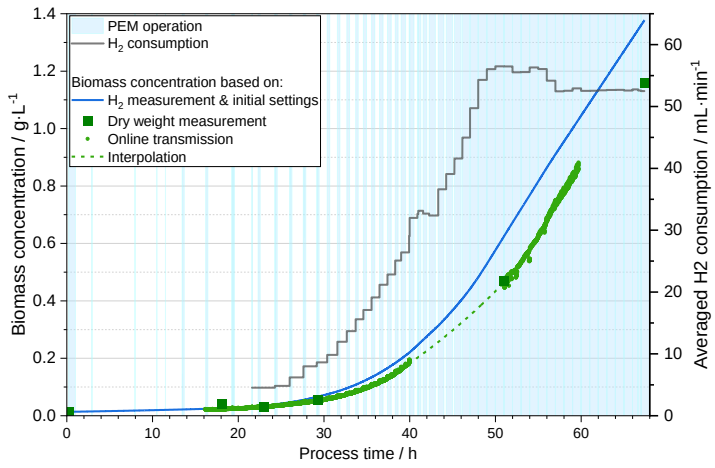

Figure 45: Biomass concentrations in an automated cultivation with control based on the H_2 consumption. The biomass concentrations were derived from H_2 measurement (blue) and gravimetrical method (green squares) interpolated by online transmission measurement in an external culture loop (green dots) and exponential fit (dashed line). The PEM was consistently operated with 15 Ω resistance to demonstrate the development of operation periods.

Ideally, biomass concentrations determined from different methods would be identical at each respective process time. In other words, a linear correlation between the H_2-derived biomass concentrations and those determined gravimetrically would result in a slope of 1 with the intercept equaling zero.

To increase the resolution of the dry weight dataset, offline measurements were interpolated using online transmission data acquired from a flow-through cuvette integrated into an external loop with continuous culture circulation. For this purpose, an external loop equipped with an online transmission measurement was installed during the proof-of-concept cultivation to ensure reliable interpolation using empirical correlations of the biomass concentration:

$$c_X = \frac{1}{(OT - B)\cdot A} \qquad \text{Equation 34}$$

The calibration constants A and B were determined from the inverse linear correlation between online transmission and biomass concentrations from dry weight and optical density offline measurements for two different light regimes (low for PT < 41 h: A = 210.44, B: -0.0926; high for PT > 51 h: A = 451.22, B = 0.3088). It should be noted that these calibration values were not long-term stable, requiring periodic recalibration, and were therefore not suitable to support automation.

Correlating the combined dataset of dry weight measurements and interpolated online transmission data with H_2-derived biomass concentrations revealed a strong positive correlation (Figure 46, $r = 0.998$, $p < 0.001$, $n = 5979$). This demonstrates that the H_2-derived biomass concentrations closely track the trends identified in offline measurements and interpolated

online transmission data. However, the observed slope of 0.796 indicates a systematic deviation within the system, corresponding to a 20.4 % overestimation when using the initially estimated parameters.

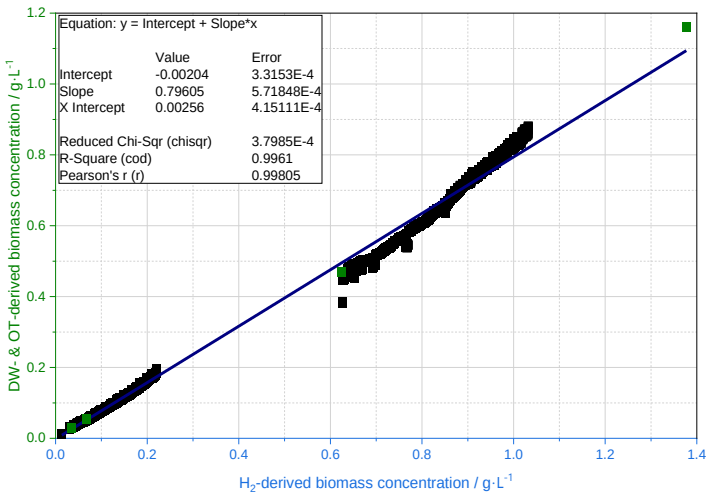

Figure 46: Biomass concentrations derived from H_2 measurements (blue) plotted against those determined gravimetrically (green squares) and by online transmission measurements. Linear fitting of the datasets was used to evaluate their correlation and to assess the resulting suitability for automation and metabolic analysis.

The systematic nature of the deviation was proportional to biomass formation and PEM activity. System tightness of the gas loop and the cptPBR was validated via GC measurements before the cultivation (see Figure 12 in chapter 2.5). The relative deviation suggests that the cause may lie in discrepancies between the measured H_2 flow and the actual H_2 consumption by the PEM or in biomass composition. Potential reasons include calibration inaccuracies due to fluctuations in moisture content between 0 % and 6 %, minor leakages, or an overestimation of $\alpha_{k,H2}$. To address the observed difference in slope, $\alpha_{k,H2}$ was adjusted by a 10 % reduction to 0.38 in subsequent cultivations, and this adjustment was also implemented in the MathScripts used for control (appendix A2). This adjustment remained within the range of biomass compositions consistent with active biomass growth and provided an acceptable level of deviation ($Ø(\text{rel. error}^2) \leq 0.005$). The reduced deviation enabled the use of H_2 derived biomass concentrations for online control, particularly over shorter cultivation periods or when supported by periodic offline sampling and subsequent data adjustment.

For monitoring trends in biomass growth, H_2 consumption was considered a valid proxy for near-online estimation. Comparability of absolute biomass concentrations across different cultivations required supplemental offline measurements due to the above-mentioned parameter uncertainties. Even without supplemental data, the system was regarded as suitable for assessing growth trends, as microalgal cultivations generally behave as slowly responding systems. The H_2-based trend estimation therefore qualified for automated control of microalgal cultivations and also for the central research aim of ^{13}C-labeled biomass production in the closed system with full $^{13}CO_2$ retention. The combination of automation with periodic offline sampling added considerable value for data interpolation and metabolic analysis. Metabolic

changes became apparent when highly similar initial conditions shifted toward conditions in which biomass compositions differed in photosynthetic quotient (see also Table 4 in chapter 3.2.3). Changes in conditions were indicated earlier by the near-online calculation of production rates than by optical systems or offline measurements, supporting prompt process decisions during cultivation, and ensuring reproducible conditions as the basis for feeding-related studies in chapter 3.4.

3.3 Discussion of cptPBR design, gas separation design and automation approach

The previous chapters described the development of the compact photobioreactor (cptPBR, chapter 3.1), including its closed gas loop and automation strategy (chapter 3.2.4). The system was validated for proton exchange membrane fuel cell (PEM)-based oxygen removal with full CO_2 retention and for monitoring trends in biomass formation. This chapter discusses the design decisions, limitations, and practical implications of this system in context, outlining their interactions and potential future adaptions to enhance its applicability.

The cptPBR design with internal illumination enabled a consistent light supply while maintaining a compact structure. The light sources covered approximately one third of the light emitting diode (LED) bar surface with spot-wise illumination. Experiencing consistent light conditions was essential for microalgae to promote homogeneous biomass formation [112]. The transitions between light zones were accelerated by improving radial flow dynamics. While improving flow characteristics was critical to overcome the light gradients between the LED bars, the consistency of the illumination on the LED bars could be further improved in future applications. Implementing LED bars with more spots would reduce inhomogeneities in light intensity on the surface of the glass tubes housing the LEDs. Over the past decade, improved LED efficiency and, consequently, lower cooling demand combined with price reductions made these adjustments feasible for future applications.

Besides supporting light zone transfer, improving flow dynamics within the cptPBR played a critical role in gas transfer and management. Effective gas transfer was primarily required to allow for stable cultivation at high productivity and growth rates, while it also enabled the system to remove oxygen efficiently from the gas phase.

The gassing geometry in the cptPBR was broadened by using four parallel gassing tubes instead of a single tube. The spatial distribution of gassing pores prevented coalescence, supporting efficient gas transfer. While gassing through membranes might have further accelerated gas exchange, it would reduce mixing due to lower local flow rates at the same total gassing flow. Gas transfer and mixing were prioritized radially to address light gradients and prevent nutrient

and biomass gradients over the cross-section. Longitudinal mixing was not a design focus, as both illumination and gassing were applied evenly along the length of the cptPBR. Longitudinal gradients in gas composition were not expected, as the gas phase was continuously circulated through the closed gas loop.

Gas separation approaches, including membrane and adsorption systems, were evaluated, but would lead to inevitable CO_2 losses, making them unsuitable for the targeted closed-system operation required for autotrophic ^{13}C labeling. Pure oxygen-conducting ceramic membranes could, in principle, remove oxygen while retaining CO_2, but they require high operating temperatures (800-1,300 °C) [113]. In comparison, the calm operating conditions and controllability of the PEM system were preferable for maintaining stable and safe processes.

The integration of the PEM enabled selective oxygen removal in a closed gas loop while providing consistent cultivation conditions. The closed gas loop and selective oxygen removal were particularly essential for ^{13}C labeling cultivation, as the oxygen removal via PEM allowed the system to maintain stable cultivation conditions without opening the gas cycle and losing CO_2. The PEM system demonstrated rapid responsiveness, with switching delays in partial pressure of oxygen (pO_2) between gas loop and medium of only 0.02-0.04 hours, indicating effective gas transfer and minimal system inertia for pO_2 regulation.

Within this closed-loop system, the approximation of growth based on oxygen production proved to be a practical method for monitoring cultivation trends. This approach was valuable for assessing overall system behavior. Detailed evaluation of autotrophic growth required the context of light gradients and investigation of light kinetics to differentiate the effects of light, CO_2, and nutrient availability. Light and nutrient conditions were addressed in more detail later in this work to maintain the focus on closed-system operation and the automation method.

Automation in bioreactors is commonly based on optical biomass measurements such as transmission based on light scattering within a certain optical path. However, these optical methods are often unreliable under changing conditions due to the varying optical properties of biomass, which differ with growth conditions and accumulation of storage compounds. In the internal illuminated cptPBR, this issue is further complicated by the presence of multiple light sources and stray light. An additional external loop for online transmission monitoring was investigated and gained supportive information for interpolation of the biomass concentration in the proof-of-concept cultivation. Transmission could reduce the dependence on offline samples and assumptions of biomass compositions when carefully calibrated. But the online transmission proved unreliable due to fluctuations in the closed system, primarily due to

pressure fluctuations from the pulsed vacuum pump used for gassing and bubble formation in the tube. The unreliability and the noise in data prevented automated control based on online transmission in this system, so it was only used to gain supporting information for metabolic studies. Control was based on oxygen removal by the PEM representing photosynthetic activity.

The stable operation of the PEM-controlled system in the proof-of-concept cultivation allowed the system to maintain high specific growth rates of 2.0 day^{-1} to 2.8 day^{-1} for approximately one day. This maximum specific growth rate reached almost two-thirds that reported for the same strain under heterotrophic conditions with glucose (4.3 day^{-1}) [81]. The closeness indicated sufficient light supply and gas exchange that enabled high productivities. After 51.5 h, growth started to become light limited as the light intensity was not further increased proportionally to the biomass concentration as the maximum oxygen removal rate of the PEM was reached.

The reduced biomass specific light supply rate avoided unintentional pO_2 increase. Increasing pO_2 at high productivity despite maximum oxygen removal of the PEM demands a more powerful PEM and a scale-up in hydrogen supply. Higher O_2 removal rates are especially needed when using the cptPBR as a production system and scaling the process to either a larger or multiple photobioreactors as well as using the cptPBR at its full capacity. The lower operation boundary could be addressed by adjusting the oxygen depletion boundaries. This reduction required lower volumetric productivity while maintaining acceptable control delays, but this would increase noise relative to the depletion target and reduce accuracy. Another inaccuracy in growth monitoring and control via PEM consumption was the extrapolation of hydrogen flow measurements to zero voltage during purging. While extrapolating the voltage to zero is logical and supported by experimental observations, this approach has not been validated in practice to avoid potential damage to the PEM system. Direct outflow measurements could improve monitoring accuracy, but remain challenging due to humidity, especially during purging operations. As long as the PEM is kept in good condition, purging rarely occurs and the aforementioned potential inaccuracies hardly influence the system control output.

In conclusion, the cptPBR with PEM operation in the closed gas loop allowed precise monitoring of cultivation trends and proved its functionality for automated control. The system supported stable, reproducible, and automated operation of the cptPBR while ensuring full CO_2 retention and achieving high growth rates. The reproducibility was especially valuable to ensure comparable initial conditions and, subsequently, conduct kinetic studies on starch accumulation via systematic micro-feeding variation (chapter 3.4). Studying the kinetics of starch accumulation in microalgae aimed to maximize carbon partitioning toward starch. This

supported the central research objective of cost-effective ^{13}C-labeled glucose, which is mostly determined by $^{13}CO_2$ utilization efficiency.

3.4 Micro-feeding – keeping metabolic efficiency while preventing balanced growth

Maximizing the efficiency of photosynthetic ^{13}C fixation from $^{13}CO_2$ and storage as starch with subsequent hydrolysis to glucose follows the research aim of economically feasible ^{13}C-labeled glucose production. Enhancing starch accumulation is commonly induced by nutrient depletion at the cost of metabolic activity, and thus, productivity loss. To prevent this loss, sub-stoichiometric feeding of the nitrogen source, further referred to as micro-feeding, was identified as a promising strategy. The micro-feed rates were varied systematically to determine the nitrogen feed required to maintain photosynthetic activity while maximizing starch accumulation.

This metabolic study on nutrient limitation required precise evaluation of biomass formation and reproducible conditions prior to limitation, which was ensured by the reactor design with automated control (chapter 3.1-3.3). Initially, ammonium was supplied in proportion to the biomass formed within the compact photobioreactor (cptPBR). The resulting balanced growth was characterized by reproduction of active biomass with a stable macromolecular composition. The balanced growth phase maintained the ammonium (NH_4^+) concentration near zero (zero N conditions). A feeding strategy was developed to allow for these balanced growth conditions while accounting for the mixing time in the cptPBR and kinetic limitations. Zero N conditions ensured immediate nutrient limitation upon stopping or reducing the feed. Consequently, the nutrient limitation induced storage compound accumulation. Here, micro-feeding refers to a controlled, limited nutrient supply that sustained high metabolic activity without promoting further active biomass formation.

3.4.1 Zero N conditions – estimation of boundaries to avoid nutrient limitation

Balanced growth feeding is a straightforward concept when biomass concentration and productivity are continuously monitored, as enabled by the proton exchange membrane fuel cell (PEM). A logical strategy would be to inoculate the cptPBR under zero N conditions and supply NH_4^+ in proportion to the biomass formation. However, targeting a cellular nitrogen quota ($e_{N,X}$) below its maximum value ($e_{N,X,max}$) through balanced feeding carries a critical risk due to mixing delays: NH_4^+ may not reach all cptPBR sections, particularly at low feed flows.

At lower feed rates, mixing becomes increasingly important to ensure nutrient access for all cells. A combination of low feed flows, long mixing times, and high cellular nutrient uptake posed a risk of local nutrient depletion. Preliminary experiments revealed no measurable growth

during two days of balanced NH_4^+ feeding under zero N conditions. However, growth was induced within hours after injecting an NH_4^+ pulse into the cptPBR. This indicated that insufficient nutrient distribution caused nutrient limitation despite a stoichiometrically balanced NH_4^+ supply. These findings highlighted the need to define a minimum feed flow threshold that ensured NH_4^+ availability throughout the cptPBR. This threshold could be estimated based on the expected nitrogen uptake by microalgae and the mixing time, which together determine the spatial decline in NH_4^+ concentration along the cptPBR.

The nitrogen uptake rate was determined from a batch cultivation with ammonium runout in the cptPBR (Figure 47). The culture was initially supplied with ammonium at a concentration of $c_{N,0}$ = 23.8 mg·L^{-1} and depleted NH_4^+ below the measurement limit after 51.35 h. For the batch cultivation, the $e_{N,X}$ was derived from the quota of depleted nitrogen (Δc_N) and grown biomass concentration (Δc_X) as $e_{N,X}$ = 8.7 % (w/w) over the growth phase under replete conditions. This value aligned well with the maximum nitrogen content of 9 % observed by others for growth of *C. vulgaris* on nitrate [114] and the assumed active biomass composition with $e_{N,X}$ = 9.2 % in this dissertation (Table 1, chapter 1.5). The maximum nitrogen uptake rate ($r_{N,max}$) was then determined from $e_{N,X}$ and the μ_{max} during nitrogen replete conditions:

$$r_{N,max} = \mu_{max} \cdot \frac{\Delta c_N}{\Delta c_X} \qquad \text{Equation 35}$$

$r_{N,max}$ = −11.6 mg$_N$·g$_X^{-1}$·h^{-1} was derived from the fitted biomass concentration (Equation 13 in chapter 2.6), yielding μ_{max} = 3.2 day^{-1} before N depletion in Figure 47.

Combining $r_{N,max}$ with the biomass concentration defined the maximum decline in NH_4^+ concentration due to the microalgal uptake in batch cultivations. In addition to this biological activity, experimental setups that included feeding needed to consider potential gradients due to mixing delays.

Mixing times were experimentally determined using time constants derived from pH shifts and optical measurements (chapter 2.4). For nutrient supply considerations, the goal was not complete equilibration, but rather sufficient nutrient supply across all sections of the cptPBR. Optical mixing times, which reflected the initial distribution dynamics, were therefore considered more relevant for the following analysis.

Integrated optical mixing times along the cptPBR length exceeded the radial mixing times by a factor of 20 using broad gassing geometries. Thus, the nutrient distribution in the cptPBR was primarily limited by longitudinal mixing, while instantaneous homogenization over the cross-section was assumed. The longitudinal nutrient distribution was approximated using a plug-

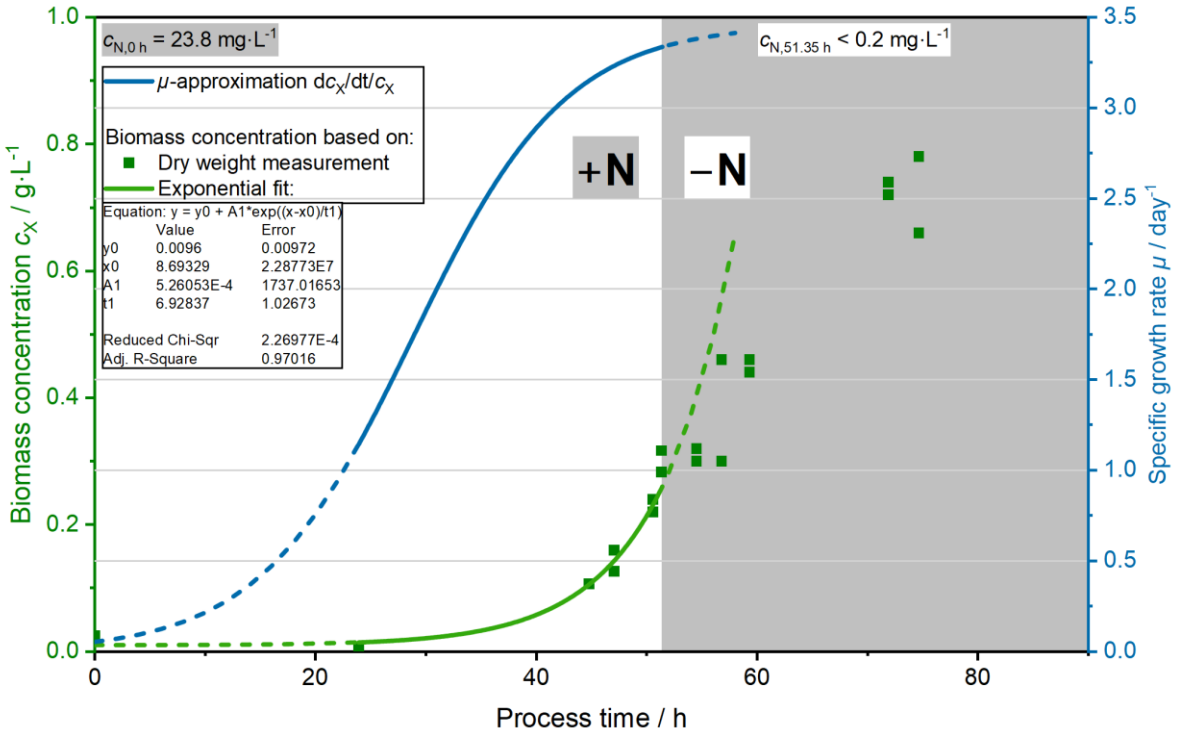

Figure 47: Fitted biomass concentrations (c_X) and derived specific growth rate throughout the nitrogen replete (+N) cultivation phase. The solid line represents the fitted data section as the initial $c_{X,0}$ = 0.03 g·L^{-1} was estimated based on optical density measurement and nutrient depletion (–N) was confirmed by reflectometer measurement after 51.35 h at c_X = 0.30 g·L^{-1}. Dashed lines represent extrapolation of fits and the estimation of how growth would have continued without N depletion. The deviation from measured c_X illustrates the decline in photosynthetic performance due to nitrogen limitation.

flow-like model that incorporated microalgal movement in the reverse direction of the nutrient flow in each section.

The initial ammonium concentration in the cptPBR was estimated by integrating the feed flow over the optical mixing time of the first section ($\Delta t_{mix,1}$):

$$c_{N,1} = q_{feed} \cdot c_{N,feed} \cdot \Delta t_{mix,1} \cdot \left(V_{PBR} \cdot \frac{\Delta z_1}{z} \right)^{-1} \qquad \text{Equation 36}$$

This initial concentration resulted from the nutrient feed flow (q_{feed}), the concentration of the nutrient feed $c_{N,feed}$, and the volume of the first section derived from the total liquid volume of the reactor V_{PBR}, the cptPBR length z_{PBR}, and the length of the first section $\Delta z_{PBR,1}$. The simplified model assumed that this initial concentration in the first section remained constant, as the automated cultivation control kept q_{feed} constant over time periods that greatly exceeded optical mixing times. A stationary state was presumed due to continuous nutrient uptake and balanced feeding, which prevented any ammonium accumulation in the cptPBR.

The initial ammonium concentration in the first section declined along the cptPBR length as a result of dilution and nutrient uptake. While the uptake rate had been determined earlier in this section, the dilution in the respective sections was related to the mixing times. To visualize this

effect, the flow dynamics supporting longitudinal nutrient transport were represented schematically in Figure 48. The local forward flow effectively transporting nutrients ($q_{\mathrm{forward,j}}$) was approximated from spatially resolved longitudinal mixing times, adjusted for broadening of the mixing profile according to Equation 17 in chapter 3.1.4.1.

$$q_{\mathrm{forward,j}} = \frac{\mathrm{V_{PBR}} \cdot \Delta \mathrm{z_j}}{\Delta t_{\mathrm{mix,j}} \cdot \mathrm{z}} \qquad \text{Equation 37}$$

This flow was assigned to section j of the cptPBR and referred to the transport of liquid occurring within the local mixing time difference $\Delta t_{\mathrm{mix,j}}$ between adjacent sections. As the mixing time was determined by pH induced color change, it reflected the propagation of nutrients through the cptPBR and therefore the flow on a net balance.

The dilution of the nutrient was determined from the ratio of liquid flow into and out of the respective section to the physical decline of the nutrient concentration throughout the cptPBR:

$$c_{\mathrm{N,j}} = \frac{q_{\mathrm{forward,j-1}}}{q_{\mathrm{forward,j}}} \cdot c_{\mathrm{N,j-1}} \qquad \text{Equation 38}$$

This concentration gradient was steepened by the microalgal ammonium uptake to the effective concentrations ($c_{\mathrm{N,eff,j}}$) throughout the cptPBR

$$c_{\mathrm{N,eff,j}} = c_{\mathrm{N,j}} - r_{\mathrm{N,max}} \cdot c_{\mathrm{X}} \cdot \Delta t_{\mathrm{mix,j}} \qquad \text{Equation 39}$$

with $r_{\mathrm{N,max}}$ from Equation 35 and the biomass concentration c_{X}. This effective concentration could theoretically drop below zero at some position along the cptPBR length, as illustrated by the example data in Figure 49, when compared to dilution-only conditions. The theoretically negative concentrations indicated local ammonium depletion. Biomass located upstream of the longitudinal position of ammonium depletion experienced ammonium-replete conditions. The cells downstream from this point were potentially nutrient limited. The fraction of biomass was assumed to equal the volumetric fraction presuming homogeneous biomass distribution in the entire cptPBR.

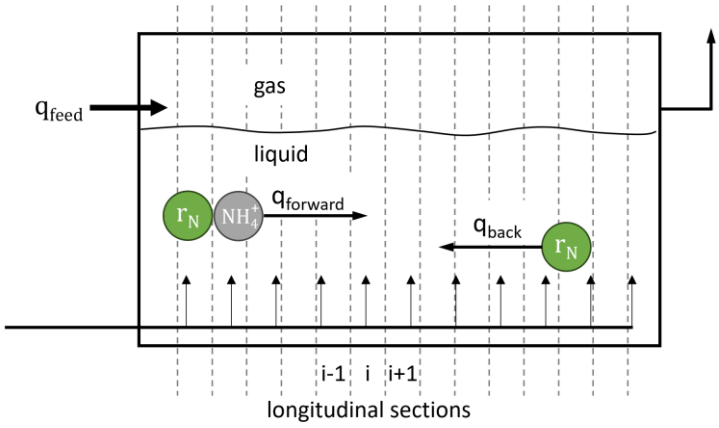

Figure 48: Schematic representation of longitudinal flow dynamics in the cptPBR. The nutrient feed (q_{feed}) entered from the top and distributed ammonium (NH_4^+) along the reactor length through a net forward flow (q_{forward}). Microalgal nutrient uptake (r_N) reduced NH_4^+ concentrations, while reverse flow (q_{back}) induced movement of microalgae and increased the fraction of cells exposed to NH_4^+-replete sections. Dashed lines indicate the structure of cptPBR sections.

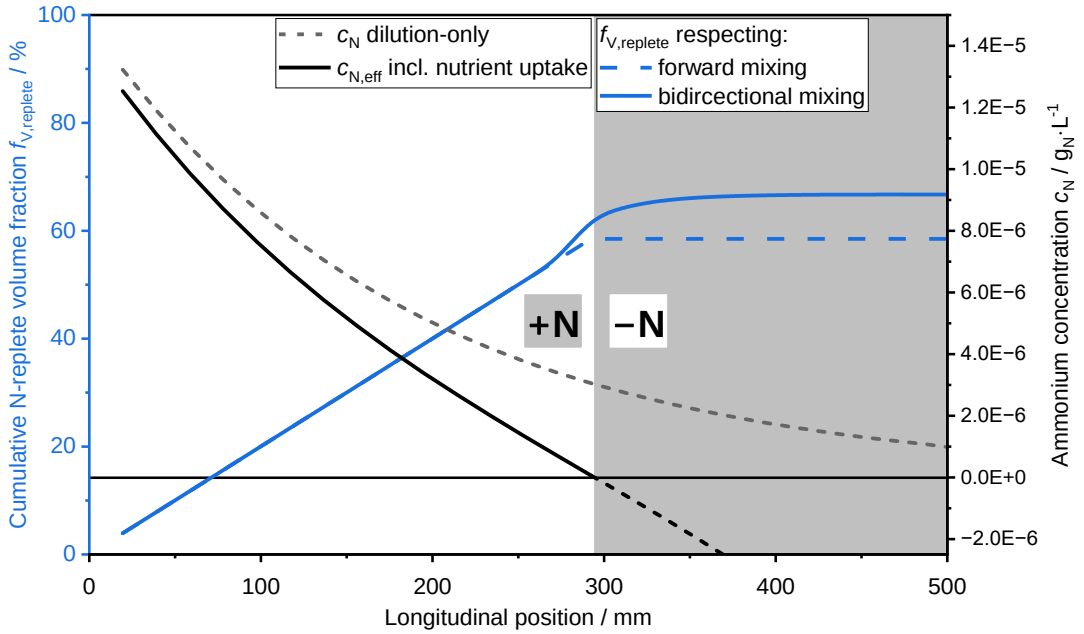

Figure 49: Simulation results of the plug-flow-like model incorporating microalgal movement in the reverse direction of the nutrient flow, with c_X = 0.1 g·L^{-1} and μ = 0.5 day^{-1}. The NH_4^+ concentrations along the photobioreactor length were calculated based on dilution only (dashed grey line) and microalgal nutrient uptake combined with dilution (solid black line). The resulting effective NH_4^+ concentrations $c_{N,eff}$ were used to calculate the cumulative volume fraction of NH_4^+-replete zones $f_{V,replete}$ for two mixing assumptions: forward mixing transporting NH_4^+ (dashed blue line) and bidirectional mixing including microalgal movement (solid blue line). The shaded area indicates the longitudinal region with predicted ammonium depletion.

The estimation of the actual fraction of biomass that experienced ammonium depletion needed to consider reverse mixing. The net forward flow from Equation 37 included potential back-flow of the injected compound, in this case ammonium, and therefore potentially underestimated the actual forward flow. The reverse flow ($q_{back,j}$) needed to at minimum equal the net forward flow in each section of the cptPBR in absolute terms, as a constant liquid level in the cptPBR was inherent to the cultivation mode.

$$q_{back,j} \geq -q_{forward,j} \qquad \text{Equation 40}$$

The potential underestimation of forward flow circumvented overprediction of the movement of microalgae backwards in the cptPBR. The movement of microalgae did not affect the biomass concentration as this was assumed to be homogeneously distributed in the cptPBR and move with liquid volume. Microalgal mixing was evaluated solely to estimate the fraction of cells that experienced ammonium-replete conditions despite the predicted concentration gradient.

Microalgae either experienced ammonium-replete conditions due to their initial presence in cptPBR sections containing sufficient ammonium (dashed blue line) or indirectly via back-mixing from deplete to replete zones (difference to the solid blue line in Figure 49). This upstream movement of microalgae was modeled using a multiplicative approach, cascading the

probability of transfer from each deplete section toward replete zones. Each deplete section was assumed to contain a volumetric fraction that included microalgae exposed to replete conditions within the respective mixing time according to the probability:

$$P_{\mathrm{replete,j}} = \begin{cases} 1, & \text{for } j < j_{\mathrm{deplete}} \\ \prod_{j_{\mathrm{deplete}}}^{n} \left(\frac{q_{\mathrm{back,j}}}{q_{\mathrm{back,j}} - q_{\mathrm{forward,j}}} \right), & \text{for } j \geq j_{\mathrm{deplete}} \end{cases} \qquad \text{Equation 41}$$

$$f_{\mathrm{V,replete,j}} = \mathrm{P}_{\mathrm{replete,j}} \cdot \frac{\Delta \mathrm{z_j}}{\mathrm{z}} \qquad \text{Equation 42}$$

with the first section with $c_{\mathrm{N,eff}} \leq 0$ (Equation 39) being j_{deplete} and the number of sections in the cptPBR n. The probability $P_{\mathrm{replete,j}}$ of each section j combined with its length, defined the replete volumetric fraction originating from the respective section:

The total volume fraction of the cptPBR expected to be sufficiently supplied with ammonium was obtained by summing the replete fractions of all sections:

$$f_{\mathrm{V,replete}} = \sum_{j=1}^{n} f_{\mathrm{V,replete,j}} \qquad \text{Equation 43}$$

Under the simulated conditions with a low specific growth rate of 0.5 day^{-1}, only two thirds of the microalgae experienced ammonium-replete conditions (Figure 49). This value exceeded the 60 % replete volumetric fraction from the spatial concentration profile due to the inclusion of back-mixing into the definition of $P_{\mathrm{replete,j}}$ (Equation 41). During a cultivation, such uneven ammonium supply could severely limit microalgal growth.

Balanced feeding ensured that the ammonium supply was strictly stoichiometric with biomass formation, while nutrient uptake was modeled as a function of the existing biomass only (Equation 39). As a result, the biomass concentration scaled the steepness of the ammonium gradient along the cptPBR but did not influence the volumetric fraction that experienced replete conditions $f_{\mathrm{V,replete}}$. The specific growth rate alone determined the required threshold for balanced feeding, as it directly affected the feed flow but not the ammonium uptake rate over time intervals as short as mixing times.

The relationship between the specific growth rate and the replete volume fraction is illustrated in Figure 50. Simulations showed that 80 % of the culture volume was supplied with ammonium at μ = 1.1 day^{-1}, marking the threshold at which balanced feeding became feasible. Theoretically, this threshold was independent of the biomass concentration (c_{X}). In practice, however, higher c_{X} increased the absolute feed flow, which enhanced longitudinal nutrient transport due

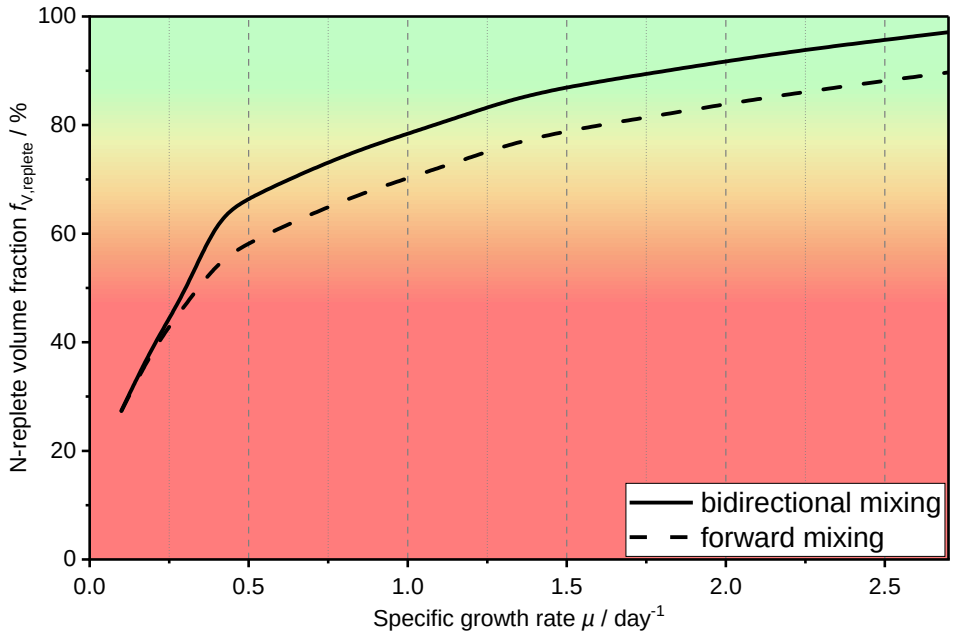

Figure 50: Simulated replete volume fraction ($f_{V,replete}$) as a function of specific growth rate (μ) under forward (dashed line) and bidirectional (solid line) mixing, based on the plug-flow-like model. The green region above 80 % repletion indicates conditions compatible with balanced ammonium supply for $\mu \geq 1.1$ day^{-1} when bidirectional mixing is accounted for in the model.

to the shift from dripping to spraying through the injection needle. The shift to spraying likely lowered the effective threshold at higher c_X. Nevertheless, such flow-induced effects were beyond the scope of this simplified model intended to provide a robust estimate of a practically relevant operating limit.

Specific growth rates (μ) below the threshold of 1.1 day^{-1} were particularly observed shortly after inoculation, as cells acclimated from preculture conditions. During this early cultivation phase, avoiding local nutrient depletion and ensuring nutrient availability throughout the cptPBR for all microalgal cells were essential to increase μ. Applying higher feed flows as a precaution would conflict with balanced feeding and risk uncontrolled nitrogen accumulation in the liquid phase and heterogeneously within the biomass. An initial batch phase ensured homogeneous NH_4^+ uptake and allowed a smooth transition to feeding once μ had increased sufficiently.

3.4.2 Balanced growth feeding – strategy to achieve zero N conditions

Balanced feeding involved the strict stoichiometric supply of ammonium in proportion to biomass formation, enforcing a defined elemental nitrogen quota. This approach risked local ammonium depletion under the applied conditions when $\mu < 1.1$ day^{-1} as discussed in chapter 3.4.2. To achieve zero N conditions without inducing nutrient limitation or compromising photosynthetic performance, the cptPBR was initially operated in batch mode and gradually transitioned to balanced feeding as cultivation progressed.

The primary challenge of the transition and balanced feeding was to precisely match the nutrient supply to biomass growth to avoid any transient limitations. A smooth transition from batch to balanced feeding was essential, as an abrupt switch could cause growth limitations, especially when considering delays in process monitoring. A mismatch between feeding and growth could limit actual growth, which would in turn reduce the next monitored value, leading the control system to further reduce the feed supply. This feedback loop could lead to severe process instability, with an increased risk at low biomass concentrations and low NH_4^+ feed rates, where the acceptable margin of error was narrow.

A feeding strategy was developed to enable a smooth transition from the initial batch phase to balanced feeding while sustaining high specific growth rates under NH_4^+ concentrations near zero. Theoretically, maintaining a minimal NH_4^+ concentration prevented kinetic limitation in nitrogen uptake that might otherwise constrain growth during the balanced growth phase. This minimum concentration was estimated using the half saturation constant (K_S value), defined as the concentration at which nutrient uptake reaches half its maximum. Reported K_S values for NH_4^+ range from 10^{-8} to 10^{-6} $g_{N\text{-}NH4+}\cdot L^{-1}$ for various microalgae [115–117]. These values demonstrate the high NH_4^+ affinity of microalgae and explain why any available NH_4^+ tends to be fully consumed unless supplied in excess [118]. A theoretical minimum ammonium concentration of $c_{N,min,theo} = 8.4\cdot10^{-4}$ $g_{N\text{-}NH4+}\cdot L^{-1}$ was assumed to ensure high uptake rates and incorporated into the feed profile.

The strategy to achieve balanced feeding at zero N conditions was implemented in three phases (Figure 51). The first phase was a batch operation without nutrient addition, during which the NH_4^+ concentration declined according to:

$$c_{N,i} = c_{N,i-1} - \left(c_{X,i} - c_{X,i-1}\right) \cdot e_{N,X} \qquad \text{Equation 44}$$

where *i* denotes the process time step. The NH_4^+ depletion was simulated as NH_4^+ uptake associated with biomass growth based on a defined nitrogen quota ($e_{N,X}$). The resulting concentration decline in pure batch mode (dotted black line) was compared to the process with a transition to feeding (solid black line in Figure 51).

Feeding in phase II was gradually increased to ensure a smooth transition from batch operation to balanced feeding, which avoided ammonium limitation:

$$q_{feed,i} = \frac{c_{N,min,theo}}{c_{N,i}} \cdot \frac{\left(c_{X,i} - c_{X,i-1}\right) \cdot e_{N,X}}{\left(t_i - t_{i-1}\right)} \cdot \frac{V_{PBR}}{c_{N,feed}} \qquad \text{Equation 45}$$

This expression incorporated the ratio between the minimum and actual NH_4^+ concentration to modulate the feed rate and enable a gradual onset. Phase II was initiated when the NH_4^+ concentration had declined to 50 % of $c_{N,0}$ based on the calculated uptake from biomass growth. Starting at this point left sufficient nitrogen in the system to prevent abrupt depletion during feeding onset. This smooth transition in phase II also tolerated deviations in $e_{N,X}$ during phase I without negatively affecting the photosynthetic performance, as the defined $e_{N,X}$ was only enforced toward the end of phase II.

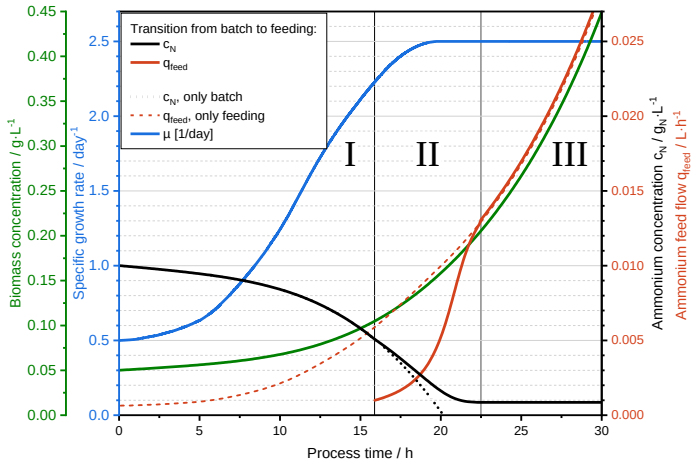

Figure 51: Simulated transition (phase II) from batch mode (phase I) to balanced feeding (phase III) in a microalgal process (solid lines), with feeding starting at 16.0 h and c_N = 0.005 $g_N \cdot L^{-1}$ using a feed solution with $c_{N,feed}$ = 4 $g_N \cdot L^{-1}$ and $e_{N,X}$ = 9 %. The transition to balanced feeding was completed after 22.5 h, reaching and theoretically maintaining a minimum residual ammonium concentration of $c_N = 8.4 \cdot 10^{-4}$ $g_N \cdot L^{-1}$ in the cptPBR. For comparison, the ammonium depletion in a batch-operated process (dotted line) and the feed flow with balanced feeding from the beginning of the process (PT = 0; dashed line) serve as reference cases.

The transition to feeding (phase II) was completed when c_N theoretically approached $c_{N,min,theo}$ and practically reached zero, at which point the first term in Equation 45 became equal to one. Balanced feeding in phase III was then continued to produce microalgal biomass with a constant macromolecular composition, while avoiding any NH_4^+ accumulation in the cptPBR. This balanced feeding at zero N enabled immediate nitrogen limitation upon reducing the feed rate.

3.4.3 Concept of micro-feeding and experimental design

Nitrogen limitation was applied to channel the photosynthetically fixed carbon toward the accumulation of storage compounds instead of active biomass formation. However, photosynthetic efficiency may rapidly decline in the absence of nitrogen, as nitrogen is essential for cellular maintenance processes such as protein turnover and repair. To avoid energy-intensive intracellular recycling of nitrogen-containing compounds, the demand could be met extracellularly. This approach is further referred to as micro-feeding – a controlled minimal nitrogen supply, designed to sustain metabolic activity while preventing cell division.

Fundamental for the application of micro-feeding in phase IV was the defined initial situation prior to nutrient limitation: The balanced feeding strategy (chapter 3.4.2) resulted in a nitrogen quota of $e_{N,X}$ = 9 % at the end of phase III. This quota was sufficient to sustain active growth but was assumed to avoid accumulating nitrogen reserves within the biomass or in the medium.

These controlled initial conditions from phase I to III ensured a consistent physiological starting point across different experiments. This consistency allowed the subsequent feed rate in phase IV to directly provoke a measurable physiological response.

The testing of various feed rates in phase IV aimed to identify the optimum feed to maintain highly efficient photosynthetic accumulation of storage compounds. The metabolic response to nitrogen feed reduction in phase IV was monitored via oxygen evolution using the PEM system integrated into the closed gas loop and the online transmission supplemented by manual offline sampling. The PEM system provided a semi-continuous approximation of the net photosynthetic oxygen production.

This measurable oxygen formation provided a reliable indication of photosynthetic efficiency as it fundamentally depended on two parameters: the yield of the respective compound k on photons ($Y_{k,ph}$) and its photosynthetic quotient (PQ_k). Assuming identical efficiency in light utilization for the production of triacylglycerol (TAG), active biomass (actX) and starch (STA) the smallest amount of product would be formed in the case of TAG, since $Y_{TAG,ph} < Y_{actX,ph} < Y_{STA,ph}$. However, TAG biosynthesis also requires the most intense respiration due to the high degree of reduction, carbon content, and energy density as discussed in chapter 1.5, which reduces the CO_2 fixation on the net balance as reflected by its high PQ value. In contrast, starch formation requires no reductive equivalents, as its degree of reduction is close to zero. The inverse correlation between $Y_{k,ph}$ and PQ_k of the aforementioned compounds results in only minor effects on the net photosynthetic oxygen evolution, assuming constant photoconversion efficiency and light conditions. This insensitivity to biomass composition enables a robust estimation of the photosynthetic efficiency from the oxygen evolution in response to different feeding rates.

Phase IV was initiated by reducing the nutrient feed to a defined percentage of the rate applied at the end of phase III. Until the end of phase III, the incident light intensity $I_{hv,0}$ had been increased proportionally to the biomass in the cptPBR and was then maintained constant during phase IV. This resulted in a constant specific light supply across all experiments relative to the active biomass, assuming that the formation of the active biomass was effectively suppressed by the feed setting. In phase IV, the nitrogen supply was the only varied parameter between experiments. Feed levels were set to approximately 100 %, 12 %, 6 %, or 1 % of the final balanced rate used in phase III, as the lower rates were considered most appropriate to promote the accumulation of storage compounds rather than active biomass formation. The tested feed

levels served to identify a suitable micro-feeding range that supported storage compound formation without continuing active biomass growth.

3.4.4 Application of balanced feed approach as starting condition for micro-feeding

The micro-feeding experiments were conducted in phase IV after constraining $e_{N,X}$ to a defined range using the balanced feeding approach at zero N conditions in the medium (chapter 3.4.2), either immediately after inoculation or following a repeated batch. The repeated batch was performed either by diluting previously nitrogen-limited cultures and resupplying them with ammonium according to their mass balance, or by dilution to achieve targeted biomass concentrations at the onset of phase IV. To verify that the automated strategy yielded physiologically comparable replicates at the end of phase III in all growth phase replicates, growth behavior and biomass-specific offline measurements were evaluated.

Biomass was characterized by the (wavelength-dependent) absorption cross-section ($\sigma_{X,abs(,\lambda)}$) and the STA content. The parameter $\sigma_{X,abs}$ served as an indicator of the state of active biomass, while STA quantified the storage compound accumulation, as the cultivated microalgal strain *C. vulgaris* H14 primarily accumulated starch under nitrogen starvation. The first sampling for these indicators coincided with the switch from phase III to phase IV and cultures were named according to the percentage of feed reduction in phase IV.

To assess the comparability of physiological states, $\sigma_{X,abs}$ was determined from transmission measurements using the integrating sphere in the spectrophotometer. Across all four cultivations at the onset of phase IV, $\sigma_{X,abs}$ deviated by up to 14.7 % from the mean value of 0.122 $m^2 \cdot g^{-1}$. The maximum deviation occurred in Lim12 and coincided with the lowest absolute value (Lim12: 0.104, Lim100: 0.131, Lim6: 0.126, and Lim1: 0.125 $m^2 \cdot g^{-1}$). To enable direct comparison of spectral shapes independent of absolute scaling, each spectrum (Figure 52 a) was normalized to its respective maximum $\sigma_{X,abs,\lambda,norm}$ (Figure 52 b). This procedure compensated for differences in amplitude and focused on shape-related features that were related to pigment content and thus reflected active biomass composition. As expected from its lowest $\sigma_{X,abs}$, Lim12 required the largest normalization factor, $(\max(\sigma_{X,abs,\lambda}))^{-1}$ = 3.46 $g \cdot m^{-2}$. When expressed relative to Lim12, the normalization factors for Lim100, Lim6, and Lim1 corresponded to −16.8 %, −10.9 %, and −11.7 %, respectively.

While Lim12 required the highest relative scaling, its spectral shape exhibited only minor differences compared to those of Lim1 and Lim6 according to Cohen's classification of ANOVA results. Two-factor ANOVA on the raw $\sigma_{X,abs,\lambda}$ yielded $F = 102.25$, $p < 6.4 \cdot 10^{-39}$, generalized eta squared (ges) = 0.0066, and a mild but significant deviation from sphericity in

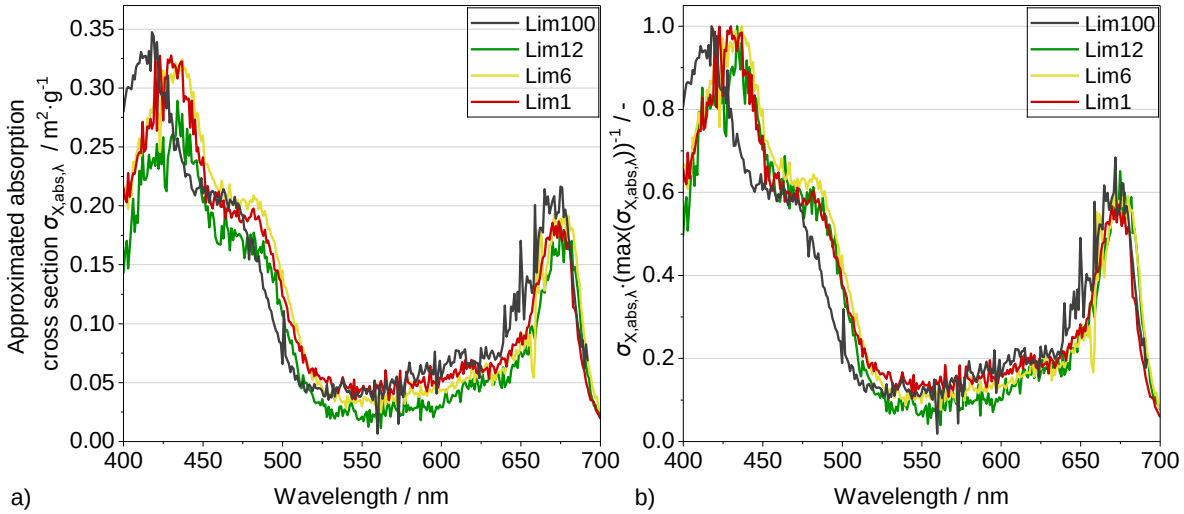

Figure 52: Wavelength-dependent absorption cross-section of the microalgal culture $\sigma_{X,abs,\lambda}$ by measurement with the integrating sphere (a) and the normalization to its maximum (b) for slope comparison. Samples were taken for the cultivations Lim100, Lim12, Lim6, and Lim1 and the end of the growth phase (PT = 0 h) coinciding with the onset of phase IV.

the Mauchly test ($W = 0.947$, $p < 3.3 \cdot 10^{-4}$, W close to 1 indicates sphericity, lower values indicate violation). This agreed with their consistent $e_{N,X}$ of 9 %, STA of 22 % ± 1 % (w/w). In contrast, inclusion of the Lim100 spectrum measured at the onset of phase IV revealed larger amplitude and shape deviations ($F = 26.80$, $p < 1.4 \cdot 10^{-16}$, and $ges = 0.0074$) with extreme and highly significant violation of sphericity ($W = 0.136$, $p < 5.5 \cdot 10^{-126}$), indicating a distinct physiological state associated with the lower $e_{N,X}$ = 7 %. The $\sigma_{X,abs,\lambda}$ differences observed in the three other cultures most likely resulted from amplitude scaling or baseline offset rather than from fundamental changes in pigment composition, which was assumed to serve as a proxy for active biomass. These minor deviations were primarily ascribed to measurement noise, baseline drift, or inherent methodological variation in dry weight measurement. Overall, the data suggested that pigment composition and absorption behavior remained largely conserved under balanced feed conditions when targeting identical $e_{N,X}$.

At −15 h before the onset of phase IV, the initial c_X deviated by 6.3 % from their mean among Lim1, Lim6, and Lim12, all targeting $e_{N,X}$ = 9 %. Throughout the growth phase, the maximum relative deviation of these three cultivations from their mean $c_X(t)$ remained below 11.8 %. While absolute concentration differences could mask growth trends, normalization effectively highlighted their similarity (Figure 53 b). A two-factor ANOVA on normalized c_X confirmed only small differences between the three cultivations ($ges = 0.037$), despite being statistically significant, whereas inclusion of Lim100, with lower $e_{N,X}$ = 7 %, increased the effect size substantially ($ges = 0.12$), confirming a distinct growth trajectory. The normalization thus emphasized analogous growth patterns among the three cultivations with $e_{N,X}$ = 9 % under balanced feed conditions.

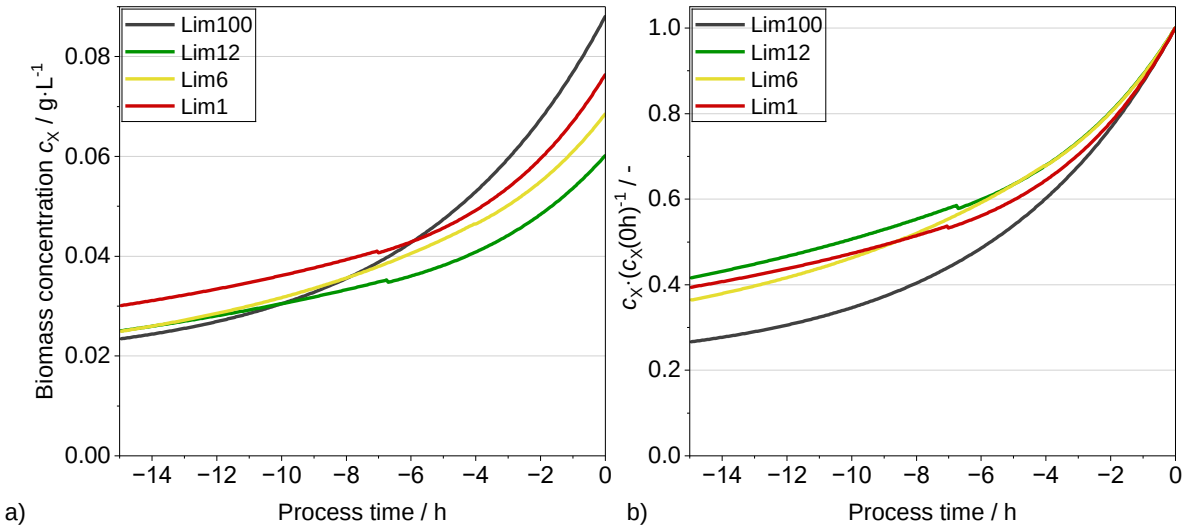

Figure 53: Biomass concentration (c_X) throughout the growth phase of the cultivations Lim100, Lim12, Lim6, and Lim1. The initial and final values were each determined from dry weight measurements. The c_X derived from H_2-measurement was aligned accordingly and fitted for visual smoothening and further data processing (a). To allow for better comparability of slopes, growth curves were normalized to c_X at the end of the growth phase (PT = 0 h) coinciding with the onset of phase IV.

Biomass was solely photosynthetically produced, so growth was further evaluated in relation to light conditions. At similar c_X values, as given here the biomass-specific light supply rate ($spI_{h\nu}$) provided a reasonable first estimate for photosynthesis responding to:

$$spI_{h\nu} = \frac{I_{h\nu,0} \cdot A_{PBR}}{c_X \cdot V_{PBR}} \qquad \text{Equation 46}$$

While $spI_{h\nu}$ was in the narrow range of 45 to 65 µmol·m^{-2}·s^{-1} (Figure 54 b) due to inherent inaccuracies of the H_2 based control strategy, the specific growth rate (μ) showed an increase over the process time (Figure 54 a). The increasing µ may be caused by acclimation or recovery

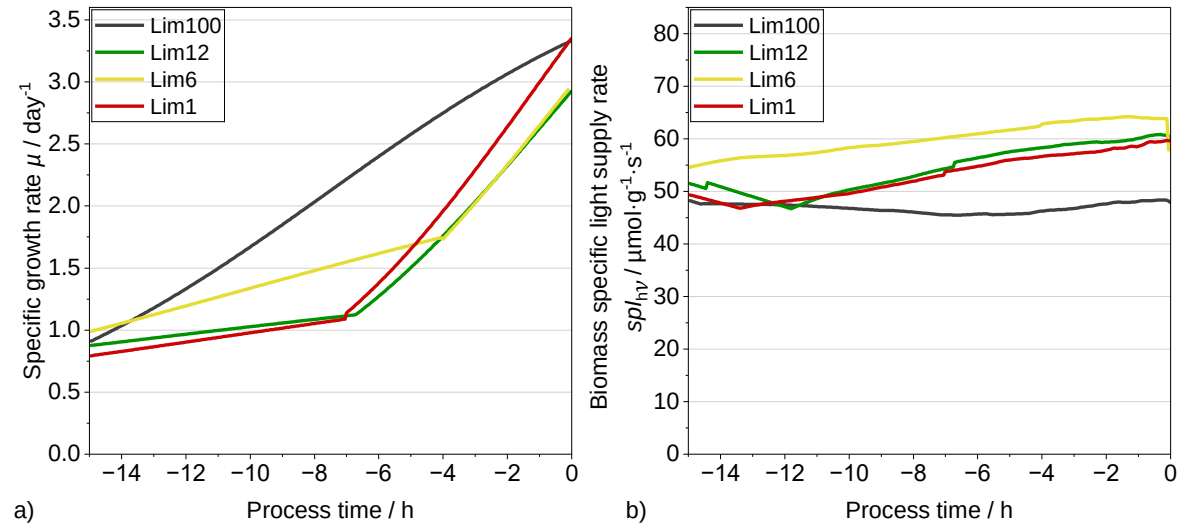

Figure 54: Specific growth rate (μ, a) as the biomass-specific time derivative of biomass concentration (Equation 13) and the biomass-specific light supply rate ($spI_{h\nu}$) over the process time during the growth phase. Data was based on H_2 measurement after alignment with dry weight measurements and incident light intensities supplied to the photobioreactor.

processes or slightly increasing $spI_{h\nu}$ over process time. Whereas these effects were indistinguishable in the present data set, the similarity of the behavior was the main focus here to allow for comparable cultivation states and the end of the growth phase coinciding with the switch to the application of various feeding rates (phase IV).

Despite other effects over process time, the average increase of μ with $spI_{h\nu}$ was significant (Figure 55 a, ANCOVA: multiple $R^2 = 0.786$, $F = 438.5$, $p < 2.3 \cdot 10^{-16}$). Lim1, Lim6, and Lim12 followed nearly parallel trajectories for µ against $spI_{h\nu}$, with minor statistically significant slope differences compared to Lim12 (Lim6 0.043, $p < 4.7 \cdot 10^{-4}$; Lim1 0.070, $p < 2.5 \cdot 10^{-13}$), not proving causality, but underlining comparability at photoconversion efficiencies of PCE > 5.6 % when approaching PT = 0 h. Lim100 deviated more strongly and significantly with a less obvious trajectory with $spI_{h\nu}$ (Lim100 0.177, $p < 6.0 \cdot 10^{-12}$). Independent from process time related effect, the shifts and differences in shape were assumed to originate from its 2 % lower $e_{N,X}$ compared to the other three replicates with $e_{N,X}$ values in a narrow range of 0.5 %.

As a consequence of the apparent deviation in growth relative to nitrogen quota, the growth response was related to the nitrogen-specific light supply rate ($N\text{-}spI_{h\nu}$) according to Equation 47:

$$N - spI_{h\nu} = \frac{I_{h\nu,0} \cdot A_{PBR}}{c_X \cdot e_{N,X} \cdot V_{PBR}} \qquad \text{Equation 47}$$

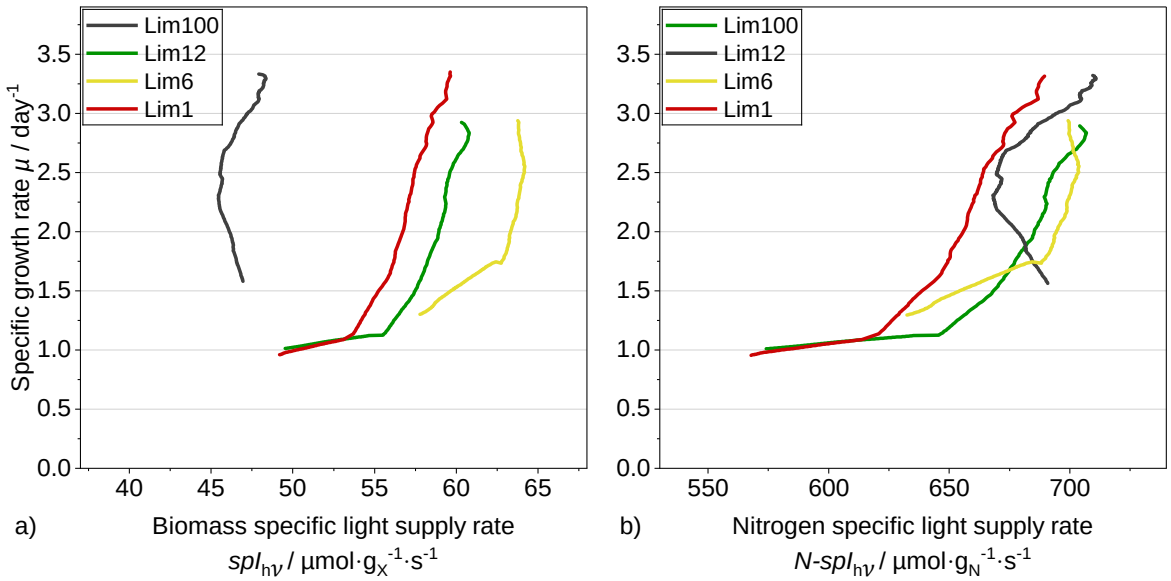

Figure 55: Specific growth rate (µ, a) versus the biomass-specific light supply rate ($spI_{h\nu}$, a) and versus the nitrogen-specific light supply rate ($N\text{-}spI_{h\nu}$, b), respectively. Data for PT < -10.6 h was neglected compared to Figure 54 due to insufficient PEM cycles for high time resolved measurement.

Correlating μ with *N-spI*$_{hν}$, rather than with *spI*$_{hν}$, brought all cultivations into closer alignment (Figure 55 b) and reduced the ANCOVA estimates to 5 % to 11 % (interaction slopes against *N-spI*$_{hν}$ relative to Lim12: Lim100 0.0093, $p < 1.5 \cdot 10^{-7}$; Lim6 0.0047, $p < 2.1 \cdot 10^{-5}$; Lim1 0.0061, $p < 1.1 \cdot 10^{-13}$). This substantial reduction in deviation assigned the small deviations in growth behavior primarily to $e_{N,X}$, fundamentally supported by the larger deviation of Lim100, as it was in the same range but deviated in shape. The N-specificity supported that an adequate range for the targeted $e_{N,X}$ was selected with no evidence for non-functional N-storage formation during the growth phase. Storage would have been indicated for no increase of μ as response to higher $e_{N,X}$ as this allows the production of additional active biomass constituents.

In summary, examining μ as a function of biomass-specific photon light supply rate produced a consistent picture: Lim1, Lim6, and Lim12 followed near-identical trends. Accounting for nitrogen-specific light supply further aligned Lim100 within the same physiological range, indicating that all N-feed supported active biomass formation. Minor deviations were explainable by slightly lower nitrogen content and initial local light distribution effects. Collectively, the findings confirm that Lim1, Lim6, and Lim12 entered phase IV in a highly comparable physiological state in terms of growth behavior, active biomass, pigment profile, nitrogen quota, and starch content, ensuring that any physiological effects observed in the subsequent phase could be ascribed to the change in ammonium feed.

3.4.5 Experimental exploration of micro-feeding rates

This micro-feeding approach aimed to identify a feed rate that suppressed active biomass formation while maintaining photosynthetic performance for starch accumulation. Different ammonium feed rates were applied in phase IV, after comparable starting conditions had been established at the end of the growth phase replicates. These feed rates were reduced relative to the final balanced feed rate and then kept constant throughout phase IV. Immediate physiological changes were expected, since the synthesis of nitrogen-containing compounds (proteins, nucleic acids and pigments) was limited by feed reduction as no non-functional reserves of nitrogen were expected in the biomass.

Physiological changes and photosynthetic efficiencies were investigated through frequent offline sampling every 2 h over the duration of phase IV (6 h). Offline measurements included dry weight determination, starch measurement and the absorption cross-section. These data were complemented by biomass concentration estimated from H_2 measurements and online transmission. Based on these values, active biomass formation and accumulated starch were distinguished and the photosynthetic productivity and efficiency were evaluated.

The only operational changes from phase III to phase IV were keeping the light supply constant from the end of phase III (Lim100: 125.2 µmol·m^{-2}·s^{-1}, 50.6 µmol·g^{-1}·s^{-1}; Lim12: 107.7 µmol·m^{-2}·s^{-1}, 62.2 µmol·g^{-1}·s^{-1}; Lim6: 117.6 µmol·m^{-2}·s^{-1}, 59.4 µmol·g^{-1}·s^{-1}; Lim1: 127.8 µmol·m^{-2}·s^{-1}, 58.7 µmol·g^{-1}·s^{-1}) and the reduction of feed rates. The applied feeding rates $q_{feed,Ph4}$ expressed relative to the final balanced growth feeding rate of phase III at PT = 0 h were 100.0 %, 11.7 %, 6.3 % and 0.8 % for Lim100, Lim12, Lim6 and Lim1, respectively. The focus was on the lower feeding rates, which were assumed to effectively prevent active biomass formation.

Biomass formation in phase IV was evaluated using four offline dry-weight (*DW*) samples and complemented by *DW*-calibrated H_2-based and online transmission (*OT*) measurements (Figure 56). Where available, *OT* data agreed with the *DW* trends, while the H_2-based c_X approximation deviated. For Lim100, the steeper H_2-based slope relative to *DW* likely reflected slight systematic miscalibration, as it aligned with the upper *DW* values. Chapter 3.4.3 showed that the H_2 measurement was proportional to oxygen production and therefore insensitive to biomass composition under constant illumination, but sensitive to energetic efficiency.

Across all feed rates, the mean increase of the biomass concentration (c_X) was nearly linear. In Lim6 and Lim1, deviations from H_2-based c_X to *DW*-derived c_X were considered physiologically meaningful due to their variation throughout phase IV. In Lim6, the *DW* slope exceeded the H_2-based c_X slope. This relation reflected considerably lower carbon specific release of oxygen to the gas phase than during balanced growth, which was an intrinsic property of the H_2-based method compared to *DW* measurement under STA accumulation. In Lim1, the decline in the H_2-based slope of c_X after 5 h indicated reduced photosynthetic efficiency. This reduction may have been caused either by

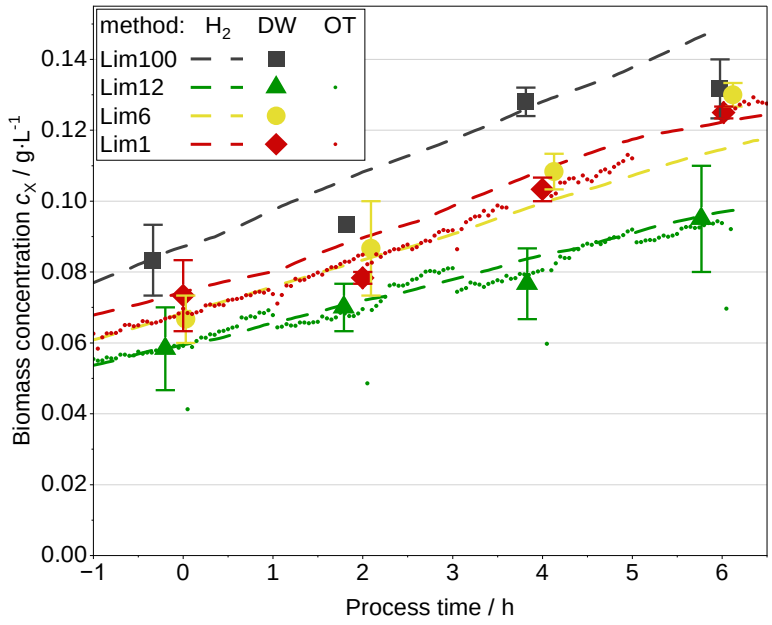

Figure 56: Biomass concentration (c_X) throughout phase IV with various feed rates for Lim100, Lim12, Lim6, and Lim1. Symbols denote dry weight (*DW*) concentrations with error bars for replicate measurements. The c_X estimates from the H_2-based method (dashed line) and, where available, *OT*-measurements (dots) were calibrated to the dry weight concentrations across the entire cultivation, including the growth phase.

lower primary carbon fixation as glyceraldehyde-3-phosphate in the Calvin-Benson cycle [80] or by increased respiration consuming oxygen to meet cellular energy demand for maintenance, recycling and repair mechanisms. To further interpret the physiological changes, starch contents were analyzed.

The reference cultivation Lim100 slightly increased in STA content within the 6 h period of phase IV (4 %, Figure 57). This increase was attributed to progressive limitation under constant feeding with c_X(6 h) at 160 % of c_X(0 h). For all reduced-feed cultivations, STA content approached values close to its maximum of 36 % within 4 h, corresponding to a total STA increase of 13 to 15 %.

In agreement with the steeper *DW*-derived versus H_2-based c_X curve, STA initially increased nearly linearly in Lim6, matching the slope in Lim1. In contrast, Lim12 initially matched Lim100 in STA slope, but between 2 and 4 h after feed reduction switched to the slope observed in Lim6 and Lim1. So, Lim12 showed a delay in STA increase, whereas Lim6 and Lim1 increased immediately. The applied N-supply in Lim12 was too high to immediately induce starch accumulation, while it was low enough in Lim6 and Lim1.

Physiological differences between Lim6 and Lim1 were visible in the $\sigma_{X,abs,\lambda}$ throughout phase IV (Figure 58). In Lim1, the relative amplitude of chlorophyll peaks at ~435 nm and ~680 nm dropped temporarily from 1.8 (t_1 = 0 h) to 1.5 (t_1 = 2 h) and then recovered to 1.8. In contrast, all other $\sigma_{X,abs,\lambda}$ developed steadily in amplitude and shape, while the average amplitude behaved inversely to STA. The decreasing $\sigma_{X,abs,\lambda}$ in the first 2 h of phase IV, followed by constant $\sigma_{X,abs,\lambda}$ and STA at 4 h and 6 h, supported summarizing various cellular compounds as actX and distinguish them from STA for further analysis.

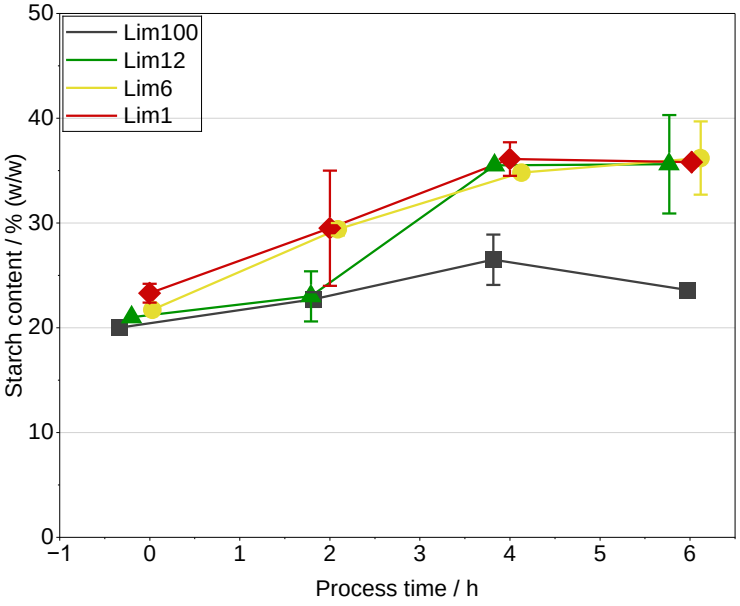

Figure 57: Starch content throughout phase IV with various feed rates for Lim100, Lim12, Lim6, and Lim1. Symbols denote STA with error bars for replicate measurements, and lines only for visualization of different cultivations.

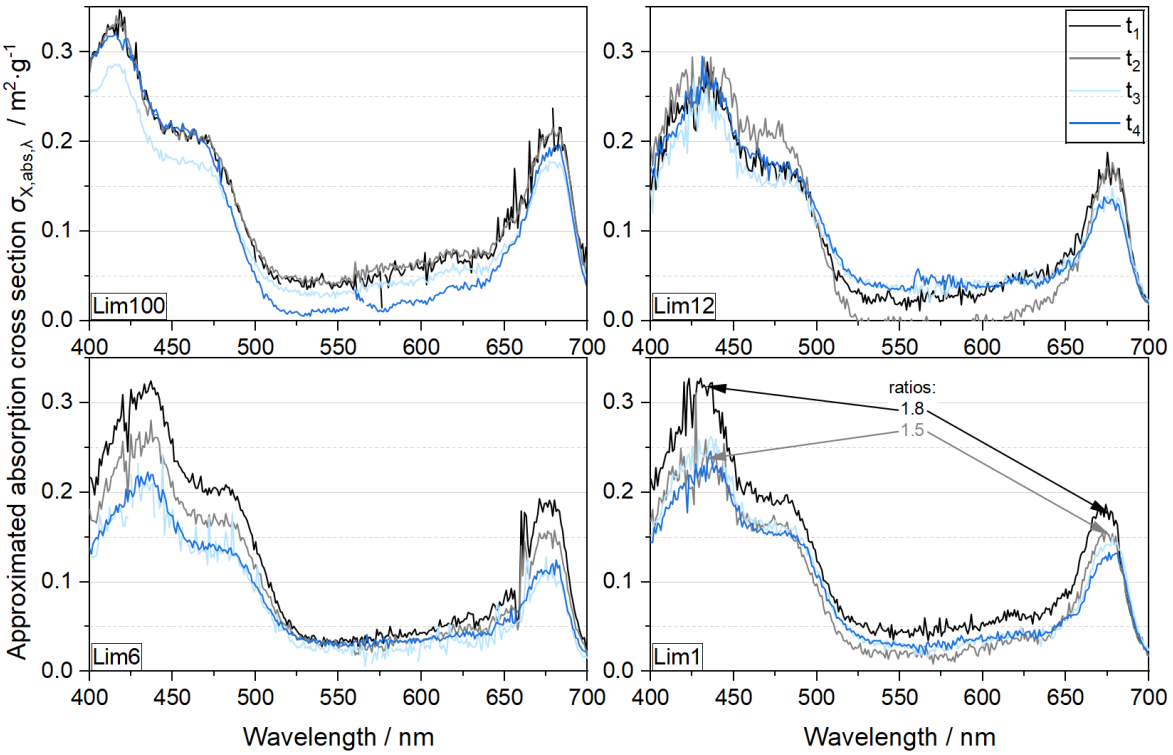

Figure 58: Wavelength-dependent absorption cross-section ($\sigma_{X,abs,\lambda}$) based on integrating sphere measurement. The spectra were plotted throughout phase IV for Lim100, Lim12, Lim6 and Lim1 with t_1, t_2, t_3 and t_4 corresponding to approximately PT = 0 h, 2 h, 4 h and 6 h, respectively.

The photoconversion efficiency (*PCE*) was analyzed to identify feed rates and related physiological changes that suppressed actX formation, while maintaining high efficiency for starch accumulation. Evaluating *PCE* required to distinguish actX and STA in absolute terms (Figure 59), since their different energy densities needed to be accounted for in the *PCE* calculation.

The trends expected from the peak ratios were also observed in the absolute concentrations through Lim6 and Lim1: In Lim1, the increase in STA fraction was primarily driven by starch accumulation and even enhanced by a small actX degradation (– 0.7 %). Compared to that, in Lim6, STA and actX were produced simultaneously throughout phase IV, with STA following the inverse trend to $\sigma_{X,abs,\lambda}$. The simultaneous production of starch and actX with similar partitioning was also observed for Lim1 between PT = 2 and 6 h, but this could not compensate for the lower initial efficiency in the balance over phase IV (Lim1: 5.3 % vs. Lim6: 7.6 %). The substantially lower PCE observed in the first sampling interval of Lim1 in phase IV demonstrated initial nutrient limitation.

Lim6 was the most consistent in biomass formation, with stable efficiencies of both actX (PCE_{actX} = 4.0 %) and starch (PCE_{STA} = 3.1 %) across phase IV on supplied photons. The reference cultivation Lim100 showed the same average PCE_{actX} (4.0 %), while PCE_{STA}

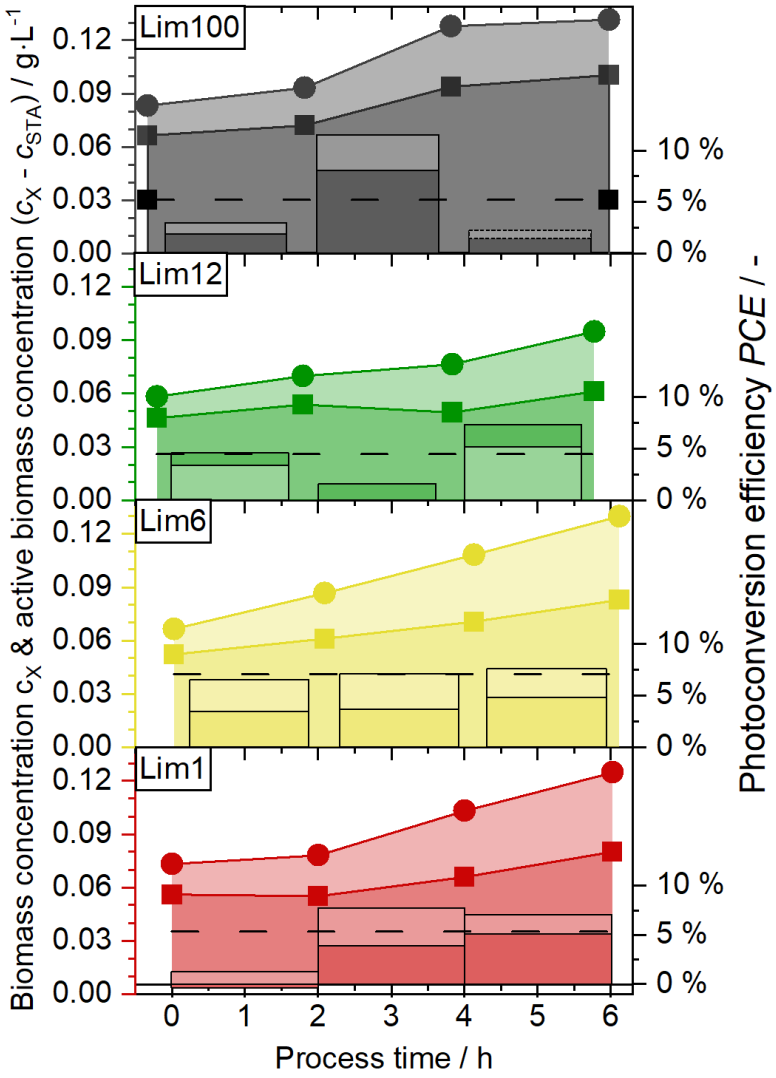

Figure 59: Biomass concentrations (c_X) and photoconversion efficiencies (*PCE*) throughout phase IV for Lim100, Lim12, Lim6 and Lim1. Circles denote c_X and squares indicate active biomass concentration with the lighter areas in between representing the starch content recalculated as concentration in the cptPBR. Dashed lines represent the average *PCE* throughout the respective cultivation, whereas solid lines were added for visualization only. The darker section of the columns displays the PCE to active biomass and the lighter section the *PCE* to STA, summing up to the total *PCE*. Note: In Lim100, the STA content was reduced from PT = 4 h to PT = 6 h, lowering the overall *PCE*. The *PCE* was calculated based on the mass balance and E_{photon} = 210.5 kJ·mol^{-1}, ΔH_c^0(STA) = 17.41 kJ·g^{-1}, and ΔH_c^0(actX) = 23.55 kJ·g^{-1}.

averaged only 1.2 %. This pointed to a potential metabolic limitation of active biomass formation around 4.0 % *PCE* under the applied conditions.

Beyond the highest total *PCE* over phase IV, the consistency of Lim6 demonstrated high physiological activity and a healthy state, despite substantial starch accumulation. *PCE* in Lim12 was initially lower, but rose in the last sampling interval to values comparable to Lim6, including similar actX/STA partitioning. This again underscored that nitrogen supply in Lim12 was too high to immediately induce efficient STA accumulation. To further assess the impact of preexisting nitrogen and acclimation on the metabolism under reduced feed rates, theoretical

$e_{N,X}$ was calculated according to Equation 48 and analyzed. Complete ammonium consumption during constant feeds was experimentally validated for all samples.

$$e_{N,X,i} = \frac{c_{X,ph4,0} \cdot e_{N,X,ph4,0} + q_{feed,Ph4} \cdot (PT_i - PT_{ph4,0}) \cdot c_{N,feed} \cdot \frac{1}{V_{PBR}}}{c_{X,i}} \quad \text{Equation 48}$$

The impact of the preexisting nitrogen quota and the acclimation to that quota became apparent when comparing the slopes of $e_{N,X}$ across the four cultivations (Figure 60). Across cultivations with various feed rates, $e_{N,X}$ values converged to a narrow range at PT = 2 h and 4 h. Growth in Lim100 appeared to adapt to the nitrogen supply, maintaining $e_{N,X}$ close to 7 % – the quota applied during balanced feeding – without considerable starch accumulation. Instead, PCE dropped in Lim100 while $e_{N,X}$ remained stable. Reasons for the stable $e_{N,X}$ may be related to cellular regulation after acclimation to comparatively low $e_{N,X}$ in the growth phase and average *PCE* = 5.2 %. Effective starch accumulation was here not induced, whereas nitrogen depletion without feeding was reported to respond by transcriptional changes within 12 minutes regulating biosynthesis down and nitrogen-scavenging modules up [119].

In contrast, the $e_{N,X}$ of the reduced-feed cultivations steadily decreased almost in parallel over process time. The $e_{N,X}$ decrease to below 6 % occurred at a rate of 0.6 %/h. This analogous behavior across feed rates indicated intrinsic cellular limitations to the rate of $e_{N,X}$ decline. The rate may reflect time constants of cellular reorganization, recycling, or repair needed for efficient nitrogen use or for the capacity of building starch storage.

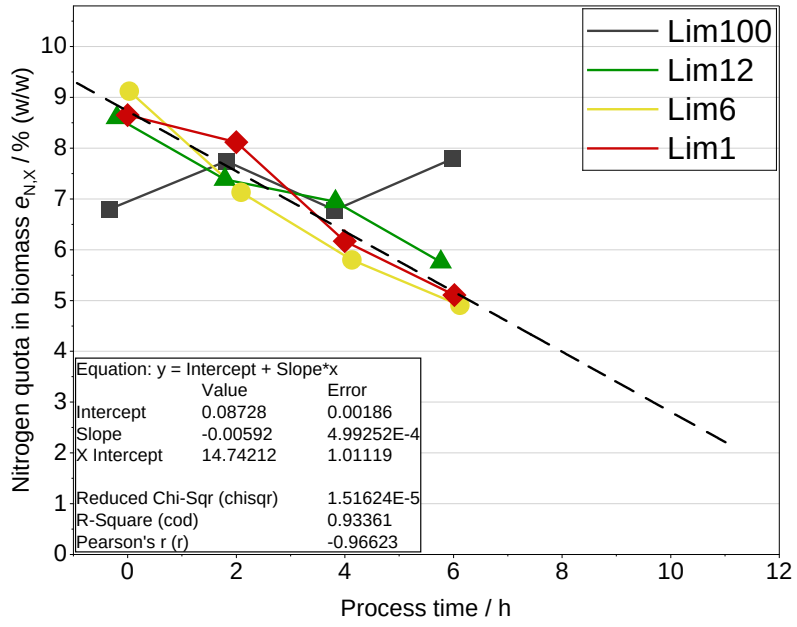

Figure 60: Nitrogen quota in the biomass ($e_{N,X}$) throughout phase IV with various feed rates in Lim100, Lim12, Lim6, and Lim1. Symbols denote $e_{N,X}$ calculated according to Equation 48, the dashed line represents the linear fit through $e_{N,X}$ of Lim12, Lim6 and Lim1 with extrapolation to the $e_{N,X}$ limit of cellular survival. Solid lines are only for visualization of different cultivations.

In summary, all of the applied feed rates suppressed active biomass formation, but none directed all photosynthetic capacity to starch accumulation. Instead, a steady decrease in nitrogen quota and an increase in

starch content were achieved in all reduced feed cultivations. Starch accumulation at maximum total *PCE* was achieved in Lim6. Compared to that, nitrogen deficiency in Lim1 initially caused a *PCE* drop below 1.3 %, while Lim12 first maintained replete growth instead of the intended starch accumulation. Concluding from these observations, among these experiments the best feed rate for maintaining maximum photosynthetic efficiency was applied in Lim6. The ideal rate would be expected above 0.8 % of the balanced feed to sustain maximum *PCE*, but not exceeding 6.3 %. A feed rate below this upper limit may further enhance carbon partitioning toward STA accumulation. These results provide an experimental basis to subsequently evaluate the success of micro-feeding in comparison to a nitrogen runout experiment and the discussion of underlying metabolic effects.

3.4.6 Discussion of metabolic response to micro-feeding versus nitrogen runout

Classical approaches to achieve starch accumulation involve primarily nutrient runout cultivations [120]. The microalgae in nitrogen runouts (N-runouts) commonly compromise cell growth for storage compound accumulation [77]. The efficiency of biomass formation declines as the $e_{N,X}$ decreases due to depletion of the nitrogen source in the medium [120,121]. In contrast, micro-feeding aimed at maintaining photosynthetic performance for starch accumulation, while suppressing active biomass formation despite the decline in $e_{N,X}$. A suitable measure to assess the effect of micro-feeding is the comparison of the growth behavior at different $e_{N,X}$.

The effect of micro-feeding on growth relative to $e_{N,X}$ was evaluated in comparison to an N-runout phase of a batch cultivation with the same microalgal strain under similar process conditions (Figure 61). The theoretical $e_{N,X}$ in the nitrogen runout was derived on a mass balance, and thus included ammonium available in the medium. Therefore, the theoretical value may have initially combined effects of ammonium uptake kinetics from the medium with intracellular nitrogen kinetics reflected by $e_{N,X}$. True $e_{N,X}$ values were only experimentally validated after 51 h due to the sampling interval, but high feed rates in other cultivations revealed temporary $e_{N,X}$ up to 17.9 %. To compensate for biomass, increase after nitrogen depletion in the runout, the light supply was manually increased according to offline optical density measurements and expected growth. Throughout the phase of nitrogen depletion, the specific light supply rate mainly ranged from $spI_{h\nu}$ = 50 to 63 µmol·g_X^{-1}·s^{-1}, which matched the automatically controlled level of $spI_{h\nu}$ = 60 ± 2 µmol·g_X^{-1}·s^{-1} maintained before micro-feeding.

The described setup provided a reference to compare the metabolic behavior under micro-feeding with the classical nitrogen runout focusing on the growth response relative to the

nitrogen quota. Each μ was calculated over an interval and related to the mean calculated $e_{N,X}$ during the respective interval (Figure 62). In the N-runout, μ responded to $e_{N,X}$ in agreement with the Droop model (Equation 49), which commonly serves to express microalgal growth dependent on the intracellular nitrogen quota [122].

$$\mu = \mu_{max}\left(1 - \frac{e_{N,X,0}}{e_{N,X}}\right) \qquad \text{Equation 49}$$

The parameters estimated by minimizing standard error of estimate (SEE) to 0.224 (R^2 = 0.966) were highly consistent with experimentally obtained values. Under replete conditions, μ_{max} = 4.5 day^{-1} was the maximum across all performed cultivations in this dissertation. The subsistence quota estimated from the N-runout, $e_{N,X,0}$ = 3.4 % (Q_0), lay at the transition between growth and biomass degradation.

In contrast, micro-feeding seems to disrupt the dependence of μ on $e_{N,X}$. For closer comparison, only μ values linked to $e_{N,X}$ were considered. Transient decreases in μ could not be attributed to $e_{N,X}$, because μ subsequently recovered while $e_{N,X}$ continued to decline. These temporary lower μ values most likely indicated insufficient intracellular nitrogen supply to sustain high growth rates. Concluding, biomass growth responds with higher growth rates not only to $e_{N,X}$ and ammonium concentrations according to Droop [122] and Monod [123], respectively, but most likely also responds to freshly taken up ammonium.

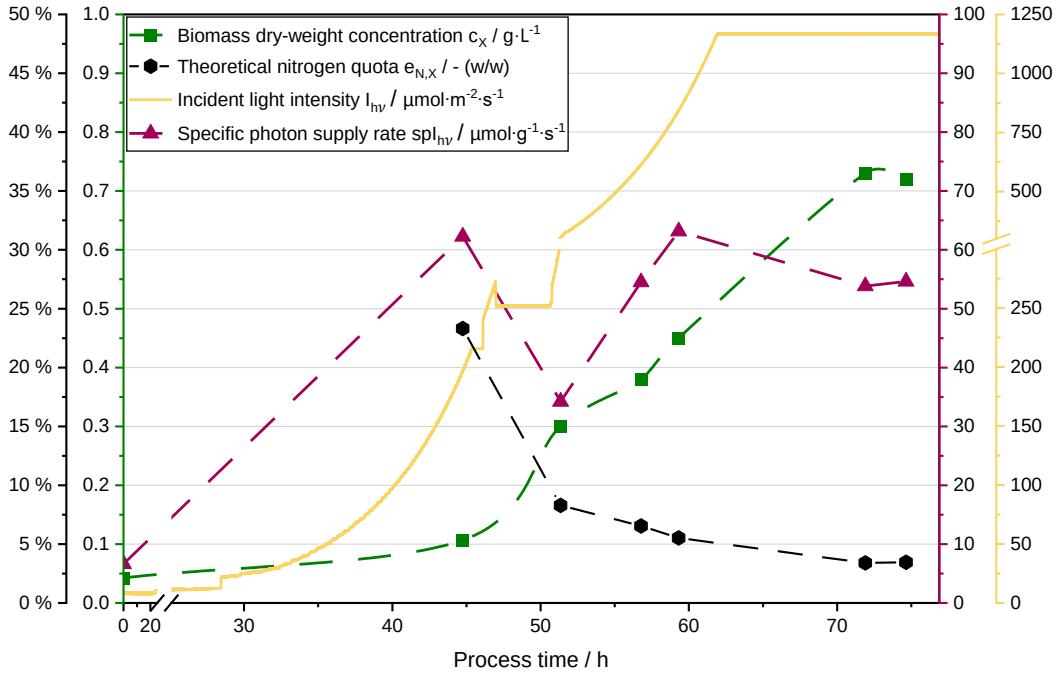

Figure 61: Biomass concentrations (c_X) based on dry-weight measurement, theoretical nitrogen quota ($e_{N,X}$), incident light intensity (I_{hv}) and specific light supply rate (spI_{hv}) throughout a nitrogen runout cultivation. Nitrogen depletion in the medium was experimentally validated at 51 h with the theoretical $e_{N,X}$ being based on the nitrogen and biomass mass balance implying full uptake. Solid line represents recorded data, while the dashed lines serve as visual guides.

A mechanistic explanation may lie in intracellular availability: nitrogen previously incorporated into the biomass requires recycling or degradation prior to reuse. These processes underlie certain time constants and regulation, whereas ammonium freshly taken up during micro-feeding can be used immediately.

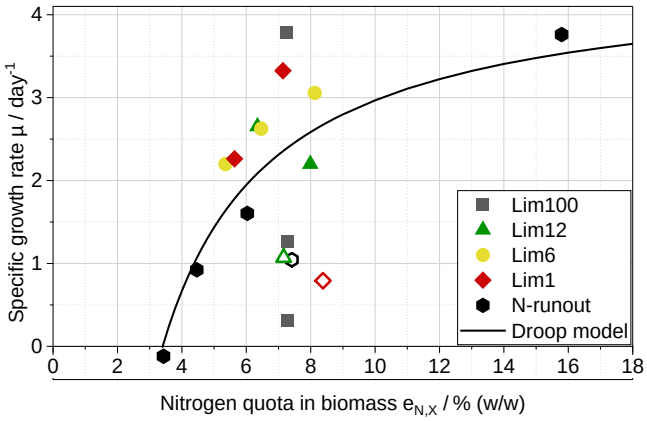

Figure 62: Specific growth rate plotted versus nitrogen quota in the biomass ($e_{N,X}$) during phase IV of Lim100, Lim12, Lim6, and Lim1 and during a nitrogen runout cultivation. Symbols denote μ over one time interval based on dry-weight concentrations plotted against the mean value of $e_{N,X}$ calculated according to Equation 48. Open symbols indicate temporary decreases in μ with subsequent recovery, for the N-runout due to temporarily lower light supply. The line represents the Droop model with $e_{N,X,0}$ = 3.4 % (commonly Q_0) and μ_{max} = 4.5 day^{-1}.

Comparing the relationship between μ and $e_{N,X}$ under micro-feeding and N-runout revealed two main features: A similar trend but weaker dependence was observed for the majority of micro-feeding data. This trend of data points corresponding to maximum photoconversion efficiency (mainly Lim6) followed the same slope, but was shifted upward by 0.5 ± 0.1 day^{-1}. This upward shift may imply an additional respiratory demand during N-runout compared to micro-feeding. An amount of primary fixed carbon equivalent to supporting 0.5 day^{-1} of growth appears to be respired to restore intracellular nitrogen availability for maintenance, turnover, repair, or cellular reorganization. The effect was likely underestimated due to the incident light intensity being maintained in micro-feeding, so the specific light supply decreased with $e_{N,X}$, but *PCE* was maintained. The evaluation was here only carried out based on a biomass balance, as commonly performed for the Droop model and already showed enhanced efficiency by micro-feeding compared to N-runout.

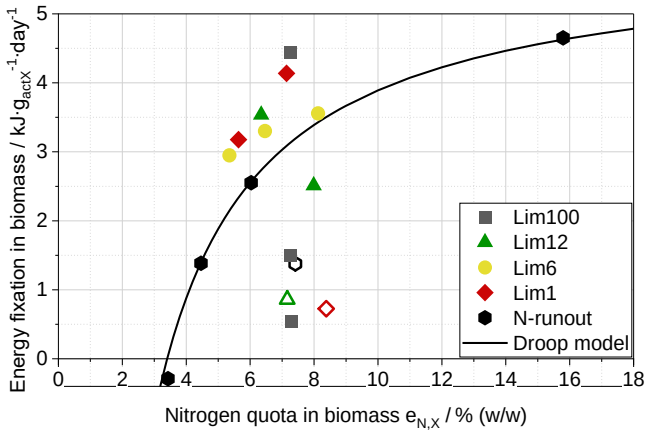

Figure 63: The active biomass (actX)-specific rate of energy fixation into biomass plotted versus mean nitrogen quota in the biomass ($e_{N,X}$) during phase IV of Lim100, Lim12, Lim6, and Lim1 and during a nitrogen runout cultivation, analogously to Figure 62. The line represents the adapted Droop model with $e_{N,X,0}$ = 3.4 % (commonly Q_0) and the maximum rate of energy fixation fitted as 5.9 kJ·g$_{actX}^{-1}$·day^{-1}.

Analogous evaluation in terms of absolute energy fixation relative to actX is appropriate to compare the metabolic activity of the producing cellular fraction,

excluding storage (Figure 63). Fixed energy was calculated by converting actX-specific productivity via the heat of combustion.

The relationship between energy fixation and $e_{N,X}$ yielded an even better agreement with a Droop-like correlation for N-runout data (SEE = 0.110, R^2 = 0.987), which is attributed to the physiological plausibility. The comparison with micro-feeding data shows larger deviations in slope. The increasing deviation with declining $e_{N,X}$ supports that micro-feeding is particularly valuable for sustaining photosynthetic performance as nitrogen depletion progresses. Nevertheless, starch has only been hypothesized as the rapid response to limitation in studies with *Chlorella zofingiensis*, whereas lipids provide long-term storage [124]. Considering this temporal course, immediate starch accumulation at high rates is particularly beneficial to achieve high starch productivities, because shorter time frames avoid respiration and intracellular conversion.

Quantifying the achievements of the micro-feeding approach, starch accumulation increased while photosynthetic performance remained high compared with both balanced growth conditions and N-runout. The effective feed range was narrowed to > 0.8 % to 6.3 %, with the percentage referring to the balanced feed rate that sustained $\mu = 3\ day^{-1}$ at 60±2 $\mu mol \cdot g_X^{-1} \cdot s^{-1}$ and $e_{N,X}$ = 9 % prior to feed reduction. Under these conditions, maximum partitioning to starch reached 47 to 49 % of the heat of combustion of synthesized total biomass at high *PCE*, whereas the maximum was 32 % during N-runout under similar process conditions using the same microalgal strain.

Exploring the lower boundary of the suggested feed range, Lim1 revealed characteristic signs of nitrogen limitation. *PCE* was initially low, then recovered to high values, but a decline in the H_2-based slope of c_X indicated another reduction in *PCE* towards the end of phase IV. Taken together with the transiently high *PCE* observed in between, these findings suggest that the feed in Lim1 improved photosynthetic performance compared to no feeding, but remained insufficient to sustain *PCE* at a high level. Substantial decreases in *PCE* under nitrogen limitation are commonly attributed to the loss of functional photosystem II reaction centers [121]. In Lim1, such loss was evident initially but later no longer apparent, most likely due to micro-feeding in combination with intracellular recycling and repair. Nevertheless, micro-feeding at such low rates still introduces temporary inefficiencies and poses the risk that even minor changes in conditions render the supply insufficient to maintain a metabolically active and healthy state with consistently high *PCE* over several hours.

Appropriate specific nitrogen supply rates for efficient and immediate STA accumulation were initially $7.3 \cdot 10^{-4}$ $g_N \cdot g_X^{-1} \cdot h^{-1}$ and declined to $4.5 \cdot 10^{-4}$ $g_N \cdot g_X^{-1} \cdot h^{-1}$ in Lim6, or, when expressed relative to active biomass (actX), from $9.4 \cdot 10^{-4}$ to $6.9 \cdot 10^{-4}$ $g_N \cdot g_{actX}^{-1} \cdot h^{-1}$. The lower values may represent a reasonable estimate to further direct primary fixed carbon towards STA. Nevertheless, Lim1 demonstrated that the cellular metabolism can adapt to feed rates as low as $8.7 \cdot 10^{-5}$ $g_N \cdot g_X^{-1} \cdot h^{-1}$ ($1.2 \cdot 10^{-4}$ $g_N \cdot g_{actX}^{-1} \cdot h^{-1}$) after an initial decrease in photoconversion efficiency at $9.3 \cdot 10^{-5}$ $g_N \cdot g_X^{-1} \cdot h^{-1}$ ($1.2 \cdot 10^{-4}$ $g_N \cdot g_{actX}^{-1} \cdot h^{-1}$). The recovery of high *PCE* was probably the result of combined effects of feeding and endogenous nitrogen [116], together with chlorophyll degradation for nutrient recycling under depletion [124]. This interpretation is consistent with the initial decline of actX and changes in chlorophyll peak ratios. These mechanisms enabled recovery of high *PCE* during phase IV but also demonstrated that high *PCE* values at certain feed rates did not automatically ensure immediate STA accumulation and efficiency. Still, the lowest rate observed in Lim6, $4.5 \cdot 10^{-4}$ $g_N \cdot g_X^{-1} \cdot h^{-1}$, may serve as a useful starting point for future investigations into optimal feed rates based on this micro-feeding study. While the optimum rate itself has not yet been identified, and a clear definition of how it should be determined for transferability remains to be established, the positive effects of micro-feeding were clearly demonstrated.

Uncertainties remain in transferring the findings on improved accumulation behavior and modeling implications to other microalgae and conditions. Such transfer requires causal attribution of improvements, which in turn demands distinguishing the interplay among light conditions, growth rates, nitrogen availability, and nitrogen quota. Ammonium uptake limitations apparently occur in the lower micromolar concentration range, whereas colimitation of nutrient effects with light may mask distinct kinetic responses [123]. Since the relationship between μ and $e_{N,X}$ was decoupled by micro-feeding, the kinetics of freshly taken-up ammonium need to be investigated. Developing a modeling approach based on uptake rate at zero nitrogen concentration, rather than on nitrogen quota or medium concentration, requires distinguishing nutrient from light kinetics. This separation was especially challenging in the applied photobioreactor with internal multidirectional illumination.

The response to light in the presented analysis was considered only in terms of incident specific light supply, as also applied in [68], and thus served as a first estimate. The benefit of the micro-feeding strategy was likely underestimated due to constant light supply in contrast to the N-runout. An increase in light supply proportional to active biomass concentration could likely have induced starch accumulation to levels comparable to those during the N-runout (45 % at

$e_{N,X}$ = 3.4 %). Such a light increase was not implemented to avoid the risk of photoinhibition in the case of effectively suppressed active biomass formation. Within the tested micro-feeding range, photoconversion efficiency remained constant despite $e_{N,X}$ degradation, supporting that declines in μ were mainly driven by light conditions.

The estimation of the actual influence of the light conditions was essential to causally relate adaptations of the micro-feed rate and to further optimize the cultivation strategy, which aimed for profitability of phototrophic ^{13}C-labeled glucose production as the main objective in this dissertation. Particularly under multidirectional illumination as in the cptPBR used for the micro-feeding experiments, scattering fundamentally impacted the light distribution, turning the assumption of full light integration and the simplest light models inapplicable. Distinguishing light and nutrient-related effects (chapter 3.6) thus required the determination of light kinetics (chapter 3.5), starting with simulation of light distribution in the cptPBR and subsequent integration of local growth rates over the reactor volume. This approach allows light effects to be distinguished from nutrient effects, in contrast to the full light integration applied so far, which cannot provide reliable correlations across biomass concentration. The light distribution model in turn depends on characterization of absorption cross-sections and scattering phase function, since the multidirectional illumination of the system excludes any simplification that would neglect scattering phenomena.

3.5 Retrieving light kinetics in a complex photobioreactor geometry

The identified feed profiles derived in chapter 3.4 seemed to promote maximal ^{13}C fixation into starch and thereby supported the central research aim of the economic feasibility of ^{13}C-labeled glucose production. To verify whether the micro-feed rates were indeed primarily governed by nutrient availability rather than light limitations, the light kinetics of the compact photobioreactor (cptPBR) had to be quantified.

The investigation of light kinetics with mechanistic relevance requires knowledge of the light distribution in the cptPBR. The light sources were oriented in three directions around each light bar (120° shifted) during the micro-feeding study in the cptPBR. In addition, the illumination was spotwise as visible in the empty cptPBR (Figure 64), whereas the spots appeared blurred in the cptPBR containing a microalgal culture (Figure 65). The blurred appearance of the light emitting diode (LED) spots indicates predominantly forward scattering within the suspension.

Figure 64: Empty cptPBR containing 37 light bars, with 72 LED spots per bar.

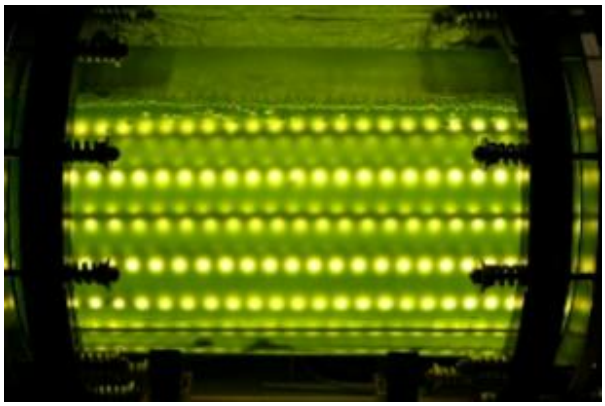

Figure 65: cptPBR during cultivation with *C. vulgaris* H 14 (c_X = 0.3 g/L).

In simplified modeling, this forward scattering is often combined with absorption into a single attenuation coefficient. Applying the attenuation coefficient in analogy to the Lambert-Beer law may serve as a first approximation of light gradients in straight PBR geometries. However, the simplified approach is not applicable to multidimensional light sources [125] as scattered light from neighboring sections cannot counterbalance. Under these complex light conditions, more precise optical parameters and mechanisms are required to adequately simulate light distribution, especially the scattering phase function.

3.5.1 Measuring device for the determination of the scattering phase function

Scattering phase functions of dry samples are conventionally determined using goniometers equipped with fixed sensors and a movable light source [126]. Adaptations of goniometer setups allow measurements in liquids and simplified data processing [62,63]. These approaches, however, still require costly instrumentation to achieve high-resolution, including precise alignment of light sources, optical fibers, and sensors. The high costs limit the practical applicability of such methods but can be reduced by employing a simplified setup based on the same optical principles.

A new measuring device for determining the phase function in suspensions was designed and constructed within this project (Figure 66 and Figure 67). The accuracy and resolution were lower compared to high-end goniometers. The chosen increment of the polar scattering angle represented a compromise between accuracy of the scattering phase function and experimental effort. Measurements at $\Delta\theta = 10°$ increments provided a higher angular resolution than that typically used in the discretized radiative transfer models, for example in applications of the lattice Boltzmann method [54,127]. This resolution was considered sufficient for reliable application in light modeling of microalgal suspensions in photobioreactors, while keeping complexity and computational effort manageable.

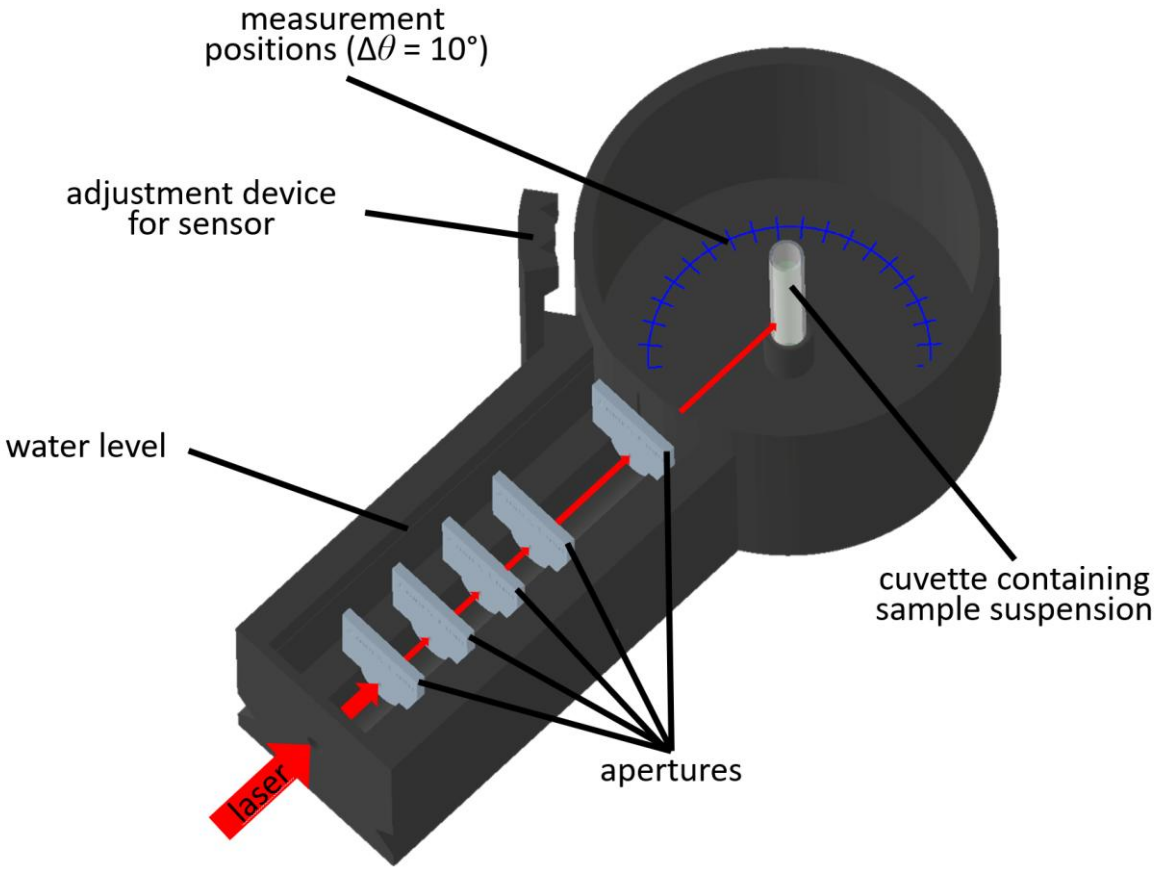

Figure 66: Technical drawing of the measuring device for determining the scattering phase function, with indication of the laser beam also shown in the photograph in Figure 67b.

Angular measurements were performed equidistantly (40 mm) using a movable planar sensor facing the cuvette, while the light sources of selected wavelengths (violet: 404 nm, blue: 446 nm, green: 522 nm, red: 659 nm, Figure 68) remained fixed. The beam was guided through ultrapure water, with stray light eliminated by successive apertures, without requiring mirrors. To minimize boundary effects, air was excluded by immersing the optical path in water. As a result, only water and quartz glass were present in the laser path, with refractive indices of n_{water} = 1.33-1.34 and n_{quartz} = 1.46-1.47 within the photosynthetically active radiation range. During the measurements, the cell was kept closed to avoid perturbations by stray light. The

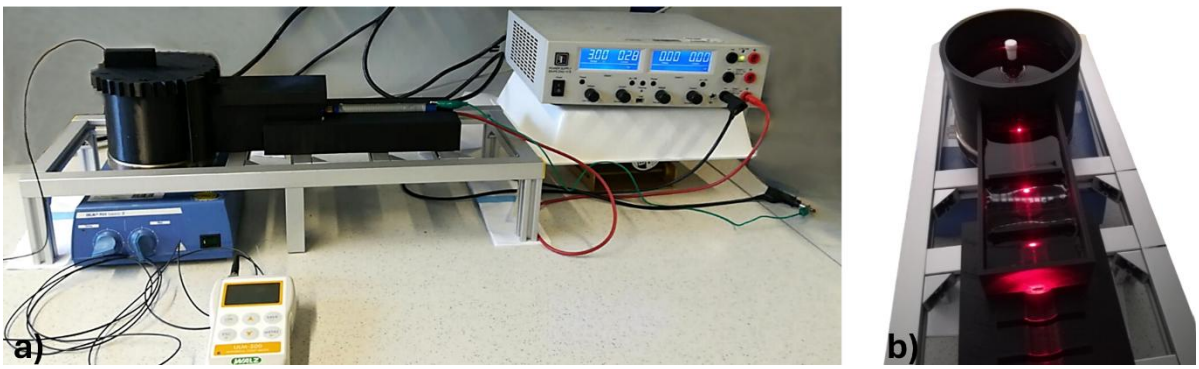

Figure 67: Photograph of the closed measuring device: (a) closed setup including electricity supply, laser, stirrer, and light meter connected to the sensor, and (b) open setup with the 659 nm (red) laser beam visible.

sample was held in a cylindrical quartz cuvette and stirred continuously to prevent sedimentation. High dilution of the suspension (OD_{750nm} = 0.1 to 0.4) ensured domination of single scattering events, as required for reliable determination of the phase function.

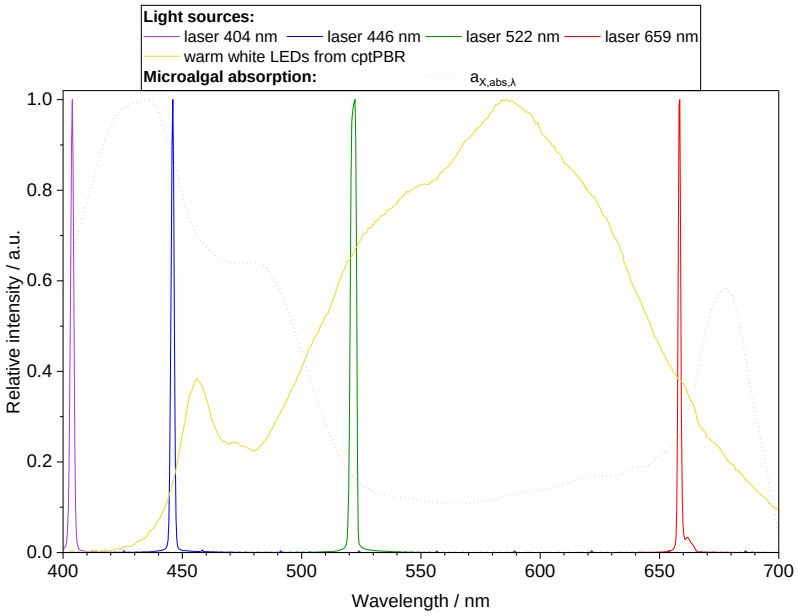

Figure 68: Measured emission spectra of applied light sources in the measuring device (lasers at 404, 446, 522, and 659 nm) and in the compact photobioreactor (warm white LEDs), compared with the normalized absorption cross-section of *Chlorella vulgaris* ($\sigma_{x,abs,\lambda}$).

Further technical specifications are provided in chapter 2.8 (Materials and Methods), while this section focuses on the rationale and practical performance of the developed measuring device.

3.5.2 Experimental determination of scattering cross-section and data processing

The wavelength-dependent absorption and scattering cross-sections ($\sigma_{X,abs,\lambda}$ and $\sigma_{X,sca,\lambda}$) were determined from angular light intensities recorded in the measuring device, supplemented by photometric measurements as described in this chapter.

The angular information on scattering was provided by the measuring device. Light intensities were measured at every angular position ($\Delta\theta$ = 10°) from 0° to 170° on one half circle and 0° to 160° on the opposite side to provide a technical replicate. Each position represented a three-dimensional ring-shaped area on a sphere, referred to as detector bin. Normalization of the measured intensities to the respective area, considering the angular increment, was performed by multiplying with the discretized solid angle weights (Equation 50, unit: sr).

$$\Delta\Omega_\theta = 2\pi \cdot \left(\cos\left(\theta - \frac{\Delta\theta}{2}\right) - \cos\left(\theta + \frac{\Delta\theta}{2}\right)\right) \qquad \text{Equation 50}$$

The resulting angular scattering intensities were normalized to the maximum measurement for comparability of each respective wavelength. This scattering distribution was statistically

analyzed across the used wavelengths and samples to yield scattering phase functions ($p(\theta)$, Figure 69) suitable as modeling inputs.

The normalized scattering phase function showed dominant forward scattering (Figure 69), which was fitted by the Henyey-Greenstein function [128] using the asymmetry parameter g to represent forward scattering [129].

ANOVA showed that wavelength-dependent differences reached significance at 10°, 20°, 40°, 160° and 170°. The Akaike Information Criterion was lower for per-curve fits compared to a common fit ($\Delta AIC = -24.67$). Nevertheless, the deviations in forward scattering remained negligible compared to the measurement accuracy ($p < 0.05$). Fitting all mean angular measurements jointly between 10° and 150° yielded $g = 0.88$. Curve-specific values ranged from 0.85 to 0.97, with a maximum relative deviation in slope below 3.3 %.

The low deviations confirmed that a common function adequately described the forward and side scattering range. In contrast, substantial deviations appeared in the backscattering region (≥ 160°). Per-curve fits outperformed the common model even though the magnitude of backscattering remained consistent across samples. Across wavelengths and angles, the determined backscattering relative to the total scattering cross-section ranged from 0 % to 7.2 % in single measurements. More precise determination of backscattering was not possible in the designed setup, while the absence of measurable backscattering in the blue and red spectral ranges was likely related to the limited sensitivity of the light sensor compared to the incident laser intensity. The measured data showed no clear angular dependency in backscattering, instead indicating isotropic backscattering behavior. Consequently, the initial description of the backscattering range was based on the measured intensities ($I_{MC,\lambda,\theta}$), while more precise evaluation was performed on modeling basis in chapter 3.5.4. Forward and side scattering were approximated by the Henyey-Greenstein fit as defined by Equation 51.

$$p(\theta, g, \lambda) = \begin{cases} \frac{1-g^2}{(1+g^2-2g\cos\theta)^{\frac{3}{2}}} & \text{for} \quad 1° < \theta < 160° \\ \frac{\Delta\theta}{180°-160°} \cdot \sum_{\theta=160°}^{170°} \left(\Delta\Omega_\theta \cdot \frac{I_{MC,\lambda,\theta}}{I_{MC,\lambda,max}} \right) & \text{for } 160° < \theta \leq 180° \end{cases} \qquad \text{Equation 51}$$

The output of this composite phase function using $g = 0.88$ is illustrated in Figure 69 (solid lines). According to this description, the scattering phase function $p(\theta)$ was only wavelength dependent in back scattering, while one identical function was applied to forward ≥ 1° and side scattering.

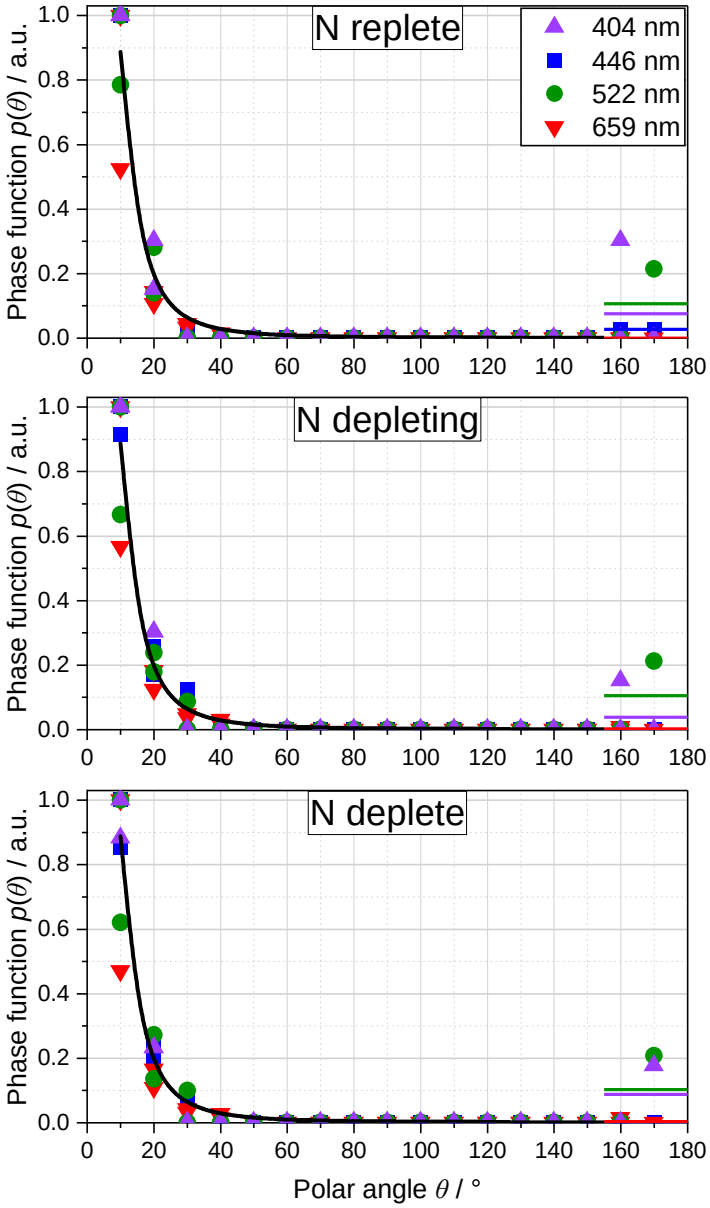

Figure 69: Measurements of the scattering phase function after weighing according to Equation 50 at illumination of 404, 446, 522, and 659 nm using three *Chlorella vulgaris* samples cultivated under different nutrient conditions. Solid black lines represent the common Henyey-Greenstein fit [128] with g = 0.88.

The phase function was related to biomass by the photometric determination of the total scattering cross-section $\sigma_{X,sca,\lambda}$, which was estimated according to Equation 52, analogously to the absorption cross-section ($\sigma_{X,abs,\lambda}$, Equation 14).

$$\sigma_{X,sca,\lambda} = -\log_{10} T \frac{\ln(10)}{z_{cuvette} \cdot c_{X,sample}} = -\frac{\ln(T)}{z \cdot c_{X,sample}} \qquad \text{Equation 52}$$

The difference between $\sigma_{X,abs,\lambda}$ and $\sigma_{X,sca,\lambda}$ determination was that $\sigma_{X,sca,\lambda}$ was obtained without the integrating sphere in the photometer. Both quantities included the ln(10) factor, originating from the base-10 definition of absorbance and its conversion into natural logarithmic form to express as cross-sections. The measured transmission (T) through the cuvette with the light path $z_{cuvette}$ = 2 mm at biomass concentrations of c_X < 0.1 g·L^{-1} was primarily influenced by

scattering, since $\sigma_{X,sca,\lambda}$ exceeded $\sigma_{X,abs,\lambda}$ by a factor of 68 at 446 nm and up to 420 at 522 nm. Therefore, the absorption was neglected in the estimation of $\sigma_{X,sca,\lambda}$ (Figure 70), which included scattering over all scattering angles except for the acceptance angle of the photometer. The photometrically determined $\sigma_{X,sca,\lambda}$ was recorded for the full PAR range. For the photosynthetically active radiation, $\sigma_{X,sca,\lambda}$ was within a narrow range across wavelength for each physiological state of the measured cultures (rel. SD = 2.5 %). This was in agreement with the Mie theory, assuming that scattering becomes flat for particles largely bigger than the wavelength [130]. Compared to that the individual samples of different physiological states deviated more (rel. SD = 8.6 %). This spectral shape, distinct from $\sigma_{X,abs,\lambda}$, underlined the negligible influence of $\sigma_{X,abs,\lambda}$ on $\sigma_{X,sca,\lambda}$.

The parameter $\sigma_{X,sca,\lambda}$ represented the biomass-specific fraction of light expected to be deflected beyond the photometer's acceptance angle, which is not specified by the manufacturer and was

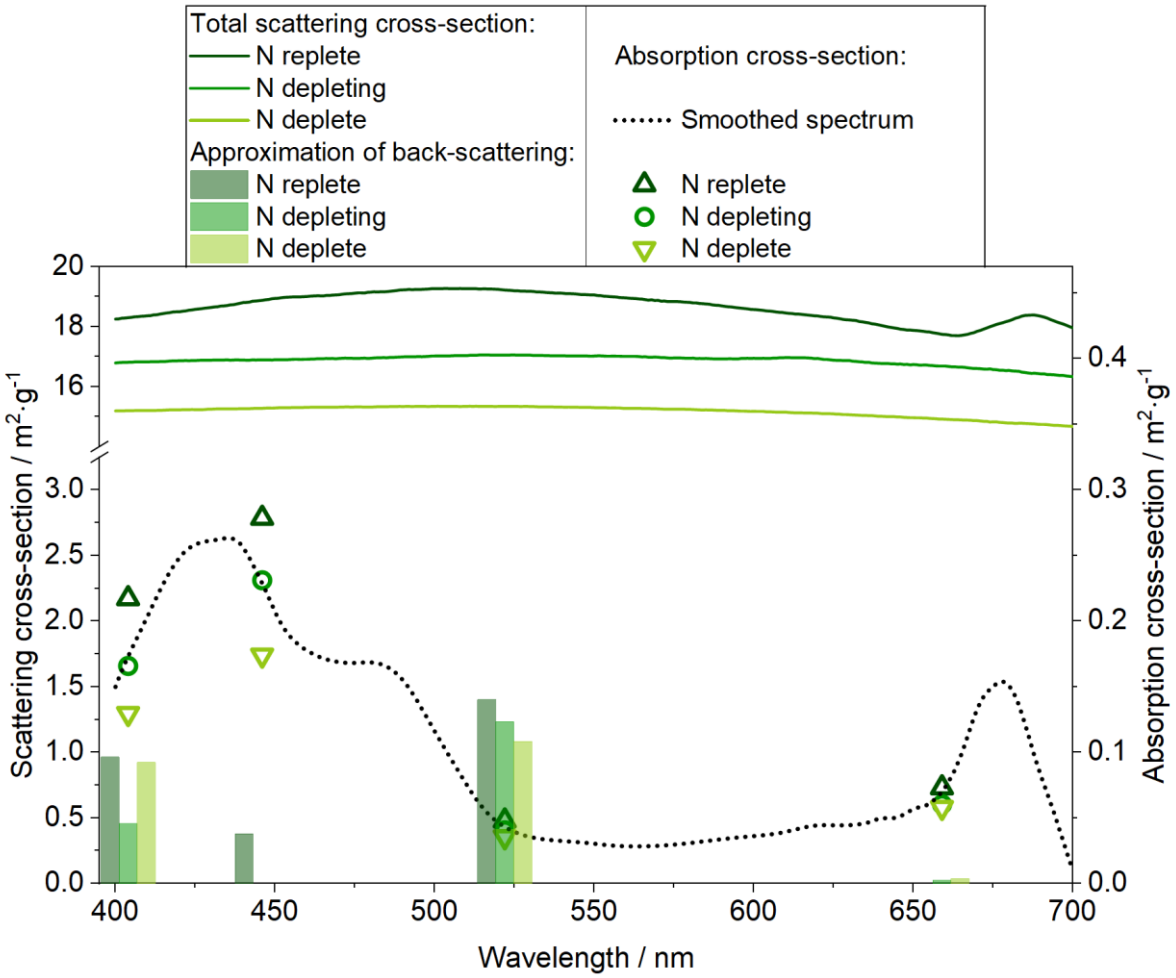

Figure 70: Wavelength-dependent scattering cross-sections ($\sigma_{X,sca,\lambda}$, solid lines) and absorption cross-sections ($\sigma_{X,abs,\lambda}$, symbols) with a smoothed absorption spectrum (dotted line) used to approximate $\sigma_{X,sca,\lambda}$. Bars indicate the approximated backscattering fraction from measurements at 160° and 170° according to Equation 51. Data are shown for *Chlorella vulgaris* under N-replete, N-depleting, and N-depleted conditions.

therefore assumed to be about ±1°. Equation 51 was applied under the assumption that $\sigma_{X,sca,\lambda}$ corresponded only to scattering at angles ≥ 1° (Figure 70). This assumption was considered acceptable for modeling, as a directional change of 1° in a single scattering event results in only a 0.015 % light path prolongation.

Conversely, backscattering led to an apparent overestimation of $\sigma_{X,abs,\lambda}$ in the photometric measurement. The correction of $\sigma_{X,abs,\lambda}$ for backscattering would demand highly accurate data on the acceptance angle of the photometer and the corresponding measurement in the measuring device. As the accuracy is insufficient for this purpose, no correction for backscattering was applied. The curve of $\sigma_{X,abs,\lambda}$ was smoothed for modeling (dotted line in Figure 70) and normalized to the average measured $\sigma_{X,abs,\lambda}$ resulting in $\sigma_{X,abs,\lambda}^{norm}$.

In summary, the combination of absorption, scattering cross-sections, and phase function data provided a coherent description of the optical properties of *Chlorella vulgaris* suspensions at different physiological states. These datasets served directly as the input for the light simulation setup described in the following section.

3.5.3 Modeling light distribution & fitting backscattering of microalgal suspensions

Modeling the light distribution in the photobioreactor required a consistent description of the optical properties of the culture. The methods applied in chapter 3.5.2 provided the relevant parameters by distinguishing spectral and angular dependencies for specific conditions in direct relation to the respective biomass concentration. This minimalistic approach retained only mechanistically meaningful parameters for simulation in Matlab R2025b and allowed clear identification of the effects of single parameters on light distribution and resulting effects on light kinetics.

Absorption was modeled using a normalized spectral shape ($\sigma_{X,abs,\lambda}^{norm}$), shown as the dotted line in Figure 70. Condition-specific differences were introduced by scaling with the corresponding mean absorption cross-section $\sigma_{X,abs}(i)$, giving

$$\sigma_{X,abs,\lambda}(i) = \sigma_{X,abs,\lambda}^{norm}(i) \cdot \sigma_{X,abs}, \text{ with } \frac{1}{N_\lambda}\sum_{\lambda=400\,nm}^{700\,nm}\sigma_{X,abs,\lambda}^{norm} = 1. \qquad \text{Equation 53}$$

In this formulation, the spectral shape remained invariant while the magnitude reflected the physiological state of the culture. The assumption of consistent shape was supported by experimental observations under comparable light conditions where the cells maintained the ability to achieve or rapidly recover high photosynthetic performance.

The scattering behavior was represented by a wavelength-invariant angular probability distribution and scaled by the wavelength-dependent scattering cross-section $\sigma_{X,sca,\lambda}$. For all evaluated conditions and wavelengths, the range 1° to 160° was represented by a single, wavelength-invariant Henyey-Greenstein fit, while angles < 1° were treated as straight transmission without scattering and therefore excluded from the mean free path calculation. The backscattering region (160° to 180°) was, in a first attempt, taken from averaged measurements in this angular range at discrete wavelengths giving the possibility for spectral interpolation. Backscattering characteristics were further evaluated in chapter 3.5.4 using the model described here.

Independent of the description of backscattering itself, the combined distribution of scattering for each wavelength was normalized to:

$$\int_{1^\circ}^{180^\circ} p(\theta, \lambda, i)\mathrm{d}\theta = 1 \qquad \text{Equation 54.}$$

The angular resolution was limited to 10° increments, with the exception of < 1° treated as straight transmission without scattering. This classification minimized the extrapolation of the measured distribution. The phase function was fully defined by the polar angle θ from 1° to 180°, while the probability of scattering into the third dimension was assumed to be uniform across all increments of the azimuthal angle ϕ around the incident light direction.

The probability of an optical event – either scattering or absorption – primarily depended on the optical cross-sections. The cross-sections were translated to bulk optical properties of the culture by multiplication with the biomass concentration $c_X(i)$, which yielded the coefficients for the calculation of the free optical path. For that purpose, the biomass concentration linked the specific properties on a per-mass basis to the light-path scale in the culture, defined as the absorption coefficient ($\alpha_{abs,\lambda}$, Equation 55) and scattering coefficient ($\alpha_{sca,\lambda}$, Equation 56) under the respective conditions (i) with units of inverse length (m^{-1}).

$$\alpha_{\mathrm{abs},\lambda}(i) = \sigma_{\mathrm{X,abs},\lambda}(i) \cdot c_{\mathrm{X}}(i) \qquad \text{Equation 55}$$

$$\alpha_{\mathrm{sca},\lambda}(i) = \sigma_{\mathrm{X,sca},\lambda}(i) \cdot c_{\mathrm{X}}(i) \qquad \text{Equation 56}$$

$$\alpha_{\mathrm{ext},\lambda}(i) = \alpha_{\mathrm{abs},\lambda}(i) + \alpha_{\mathrm{sca},\lambda}(i) \qquad \text{Equation 57}$$

The extinction coefficient $\alpha_{ext,\lambda}$ quantified the probability of photon absorption or scattering relative to the path length in the culture. The distance between two optical events along the light path

$$\Delta s = -\frac{\ln \xi}{\alpha_{\mathrm{ext},\lambda}(i)} \qquad \text{Equation 58}$$

was drawn from a cumulative distribution of the exponential free-path probability with ξ uniformly distributed in (0,1). The interaction type after Δs was selected according to relative probabilities for absorption (P_{abs}) and scattering (P_{sca}) as derived from the optical coefficients (Equation 59 to Equation 61).

$$P_{\mathrm{abs}} = \frac{\alpha_{\mathrm{abs},\lambda}(i)}{\alpha_{\mathrm{ext},\lambda}(i)} \quad \text{Equation 59}$$

$$P_{\mathrm{sca}} = \frac{\alpha_{\mathrm{sca},\lambda}(i)}{\alpha_{\mathrm{ext},\lambda}(i)} \quad \text{Equation 60}$$

$$P_{\mathrm{abs}} + P_{\mathrm{sca}} = 1 \quad \text{Equation 61}$$

Consequently, every photon was either scattered or absorbed after completing the light path Δs (Equation 58). At the culture scale, scattering steepens the light gradient compared to absorption-only behavior, because photons are redistributed in both forward and backward directions. This redistribution increases the effective path length relative to the incident direction of the light source.

This light distribution was modeled by a Monte Carlo approach in which the occurrence of optical events on light rays was governed by the optical free path probability distribution. The selection between absorption and scattering was drawn stochastically according to their respective probabilities, while the polar scattering angle was further randomized according to the phase function. Scattering was treated three-dimensionally by combining the polar angle with a uniformly distributed azimuthal angle. Light rays were tracked until absorption or escape from the microalgal suspension at the system boundaries. The number of light rays (N_{ray}) passing a geometrically defined voxel was proportional to the local light intensity ($I_{hv}(x,y,z)$). Light intensities in the investigated suspension were then projected to a 2D-plane using the factor k_{laser}, the counted light rays per voxel and the voxel area (A_{voxel}).

$$\mathrm{I_{hv}}(x,y,z) = \frac{k_{\mathrm{laser}} \cdot N_{\mathrm{ray}}}{\mathrm{A_{voxel}}}, \text{ with } k_{\mathrm{laser}} = \frac{I_{\mathrm{hv}}(0,0,0) \cdot \pi \cdot \left(\frac{\mathrm{d_{sensor}}}{2}\right)^2}{N_{\mathrm{ray}}} \quad \text{Equation 62}$$

The proportionality factor k_{laser} (unit: µmol·s^{-1}·ray^{-1}) was based on the incident light intensity $I_{hv}(0,0,0)$ of the light source and the mean projected area of the sensor, here calculated from its diameter (d_{sensor}) or the illumination area (A_{PBR}) for $A_{PBR} > A_{sensor}$.

The light intensity distribution in Equation 62 described the local conditions, while the number of absorbed light rays ($N_{ray,abs}$) was tracked analogously. The light intensity diminished due to absorption as described by Equation 63, with the photon absorbance rate $r_{hv,abs}$ based on absorbed light rays being defined in Equation 64.

$$I_{\mathrm{hv,abs}}(x,y,z) = \frac{k_{\mathrm{laser}} \cdot N_{\mathrm{ray,abs}}}{A_{\mathrm{voxel}}} \quad \text{Equation 63}$$

$$r_{\mathrm{hv,abs}}(x,y,z) = \frac{k_{\mathrm{laser}} \cdot N_{\mathrm{ray,abs}}}{c_X \cdot V_{\mathrm{voxel}}} \quad \text{Equation 64}$$

Simulated photons that hit or surpassed the boundaries were terminated (vanishing photons), without considering refraction or reflection.

With these parameters and model mechanisms, the culture-specific contributions to radiative transfer were functionally defined. In summary, scattering was treated in three dimensions: the polar angle θ drawn from incrementally defined $p(\theta,\lambda,i)$ with < 1° being treated as straight transmission and the azimuthal angle ϕ drawn uniformly over 0° to 360°. Each simulated light ray was defined by the states x, y, z, θ, ϕ and λ. Nevertheless, backscattering as part of $p(\theta,\lambda,i)$ demanded further investigation. To approximate backscattering behavior, spatially resolved measurements were carried out in a test setup containing diluted microalgal suspension.

3.5.4 Test setup for improvement of backscattering model

The measured scattering phase function of the microalgal suspension showed no significant differences between wavelengths for forward and side scattering beyond measuring accuracy (chapter 3.5.2). For the red and blue wavelength ranges, the measurements yielded no interpretable results for backscattering. Backscattering was therefore estimated by an alternative approach. Simulation results of the light model described in chapter 3.5.3 were aligned with the experimentally measured light distribution in a test setup by isotropic variation of backscattering from 160° to 180°.

In the test setup, light intensities were measured in a vessel illuminated from below by a red laser (678 nm, beam diameter = 2 mm) along the vertical axis. A monochromatic setup was chosen for simplicity, as detectable backscattering intensities were confined to a narrow spectral range. Measurements were taken from above at horizontal offsets of 5, 10 and 15 mm (± 1 mm) from the center of the laser beam and at vertical increments of 10 mm (± 1 mm). For light measurement, a submersible sensor equipped with a 3.7 mm white plastic diffusing sphere was used.

To account for the experimental conditions, simulations used vertical incident light (z_0 = 0 mm, θ_0 = 0°, ϕ_0 = 0°, λ = 678 nm). Homogeneous incident light was applied for the entire area of the laser beam by random variation of x_0 and y_0 according to

$$x_0 = (2u_1 - 1) \cdot \frac{\mathrm{d}_{laser}}{2};\ y_0 = (2u_2 - 1) \cdot \frac{\mathrm{d}_{laser}}{2} \quad \text{Equation 65}$$

with a laser diameter (d_{laser}) of 2 mm. The parameters u_1 and u_2 were uniformly distributed random numbers in the interval (0,1) under the necessary condition of $x_0^2 + y_0^2 \leq (0.5 \cdot d_{laser})^2$, ensuring that random positions remain within the cylindrical beam.

New positions of optical events were calculated geometrically with the direction vector ($\hat{v}$) as

$$P' = (x', y', z') = (x, y, z) + \Delta s \cdot \hat{v} \qquad \text{Equation 66}$$

with the unit direction vector $\hat{v} = (\sin\theta\cos\phi\,, \sin\theta\sin\phi\,, \cos\theta)$ and the free path length Δs from Equation 58. Positions outside boundaries were flagged as lost rays and crossing the system boundary was tracked spatially.

System boundaries of simulation were artificially set at 100 mm along the mean incident light direction, and 30 mm sideways, which was outside the visually detectable scale as photographically displayed in Figure 71 b and c. A low biomass concentration of 17.8 g·m^{-3} during the measurements combined with the high light intensity of the laser maximized the resolution of measurement per biomass to minimize the impact of the sensor size.

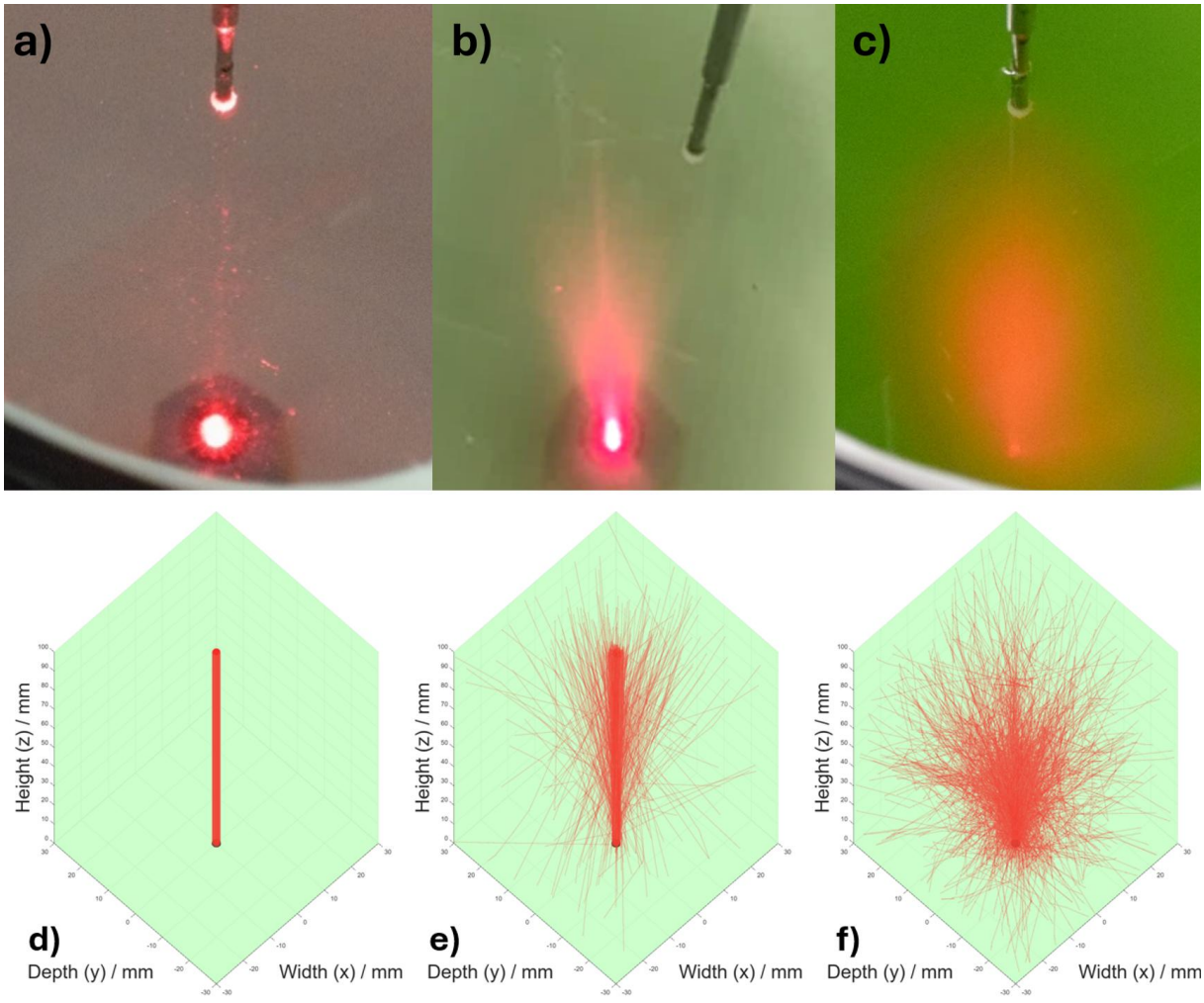

Figure 71: Photograph of red laser and simulation results with isotropic backscattering of 7 % in the test setup in a) and d) in deionized water and at biomass concentrations of b) and e) 1.5 g·m^{-3}, and c) and f) 17.8 g·m^{-3}, respectively.

For the evaluation of simulation results compared to experimentally measured light intensities at 17.8 $g \cdot m^{-3}$, the evaluated height was reduced to 50 mm. Most light absorption events occurred below 50 mm and only some rays were scattered above. Using these boundaries, the effect of backscattering on the simulation results was evaluated.

In previous measurements of the phase function (chapter 3.5.2), up to 7.3 % average backscattering was shown for green and 6.1% for violet lasers. In contrast, no backscattering for the red laser and little to no backscattering for the blue laser were detected in the measuring device. The lacking backscattering in the blue wavelength range between violet and green wavelength contradicted expectations due to the wavelength dependency of the scattering mechanism. This was likely caused by limited accuracy of measurements relative to incident laser intensities. Similar underprediction was assumed to have been occurring in the red range. Backscattering was thus treated as a fitting parameter and wavelength dependency was neglected.

Simulations used backscattering levels from the measured value of 0 % in the red range as expressed by Equation 51 in chapter 3.5.2 to up to 25 % isotropic backscattering (Figure 72). The upper range was set to cover the full plausible range of backscattering also under consideration of the unmeasurable 180° scattering due to incident light collision. 25 % of backscattering was simulated to visualize the continuation of the trend in fit quality at higher backscattering levels.

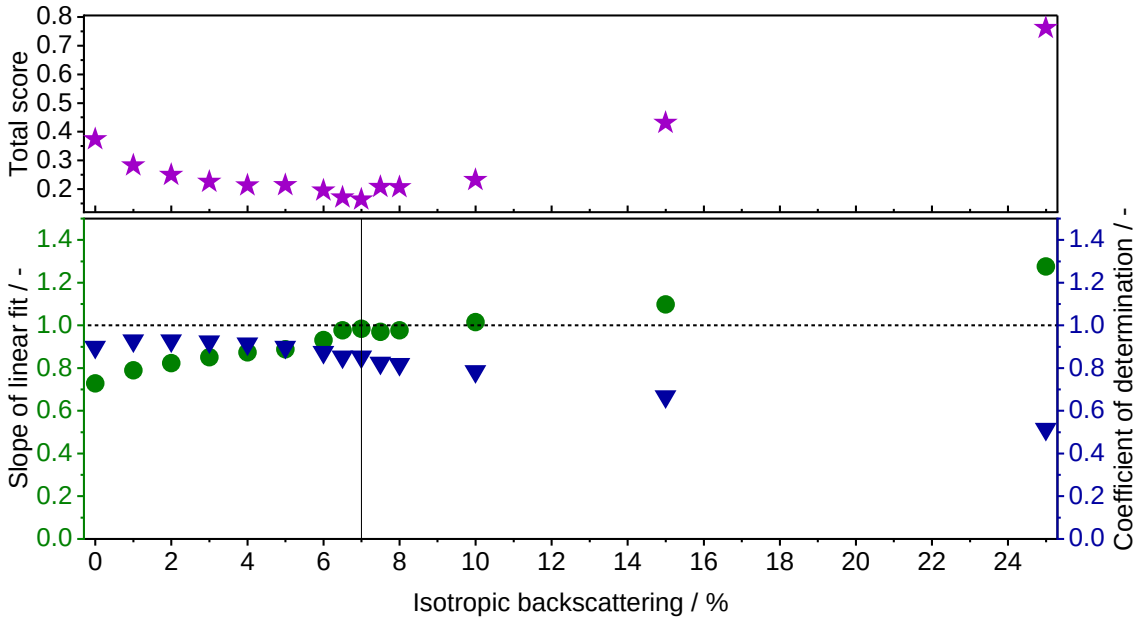

Figure 72: Slope of linear fit forced through the origin, coefficient of determination (R^2) and combined scores from regression of simulated versus experimental light intensities plotted against total isotropic backscattering. The dotted line marks the ideal slope (m = 1) and R^2 = 1. The combined score represents the sum of deviations from these ideal values. The score minimum (solid line) indicates 7 % backscattering as the best-fitting simulation result. N_{ray} = 40,000, cubic voxel length = 3.7 mm.

The fitting objective was to approach the ideal correlation of simulated to measured light intensities at side-shifts of $x = 5$, 10 and 15 mm by variation of backscattering. Linear regressions of the simulated versus the experimental light intensities were forced to zero intercept, giving the correlation factor. The modeling objective was to achieve a 1:1 relationship between simulated and measured light intensities and the regression of different backscattering levels were evaluated accordingly. Isotropic backscattering was chosen as the fitting parameter, since no trend within the backscattering angular range was seen in the measured data.

To quantitatively balance between the slope and fit quality the total score (S) defined in Equation 67 was minimized as plotted in the upper section in Figure 72.

$$S = |m_0 - 1| + 1 - \mathrm{R}_0^2 \qquad \text{Equation 67}$$

Regression forced through the origin systematically underestimated slopes at low backscattering levels (Figure 72 lower section), confirming an underestimation of scattering in the initial phase function (Equation 51 in chapter 3.5.2). The improvement of fit quality, in the range of 6.5 to 8 % backscattering compared to lower levels was primarily assigned to better agreement at x-shifts at and close to z = 0, with the minimum at 7 % in the range of experimental data for violet and green light as indicated by the vertical line in Figure 72.

Best agreement was found between 6.5 % and 8 % backscattering, with the minimum combined score at 7 % (Figure 70), which is consistent with results for violet and green light. The correlation factor improved from 0.728 (R^2 = 0.899) without backscattering to 0.983 (R^2 = 0.853) at 7 % backscattering. This backscattering was implemented isotropically over the angular range of 160° to 180° in the updated phase function:

$$p(\theta, g, \lambda) = \begin{cases} \frac{1-g^2}{(1+g^2-2g\cos\theta)^{3/2}} & \text{for } 1° < \theta < 160° \\ 0.023 & \theta \epsilon \{160°, 170°, 180°\} \end{cases} \qquad \text{Equation 68}$$

Using the phase function described in Equation 68, the light distribution was simulated and presented in Figure 73 together with measured light intensities at the respective positions. At sensor-sized voxels (3.7 mm), the trends of measured and simulated light intensities roughly match (Figure 73a). Higher-resolution simulations (1 mm voxels) reveal that deviations vanish when accounting for spatial accuracy of $\Delta x,z = \pm 1$ mm (Figure 73b), which was inherent to the preliminary test setup.

Considering these spatial deviations likely explains the full discrepancy between experiment and simulation, resulting in a close match and confirming the general validity of the applied scattering model and phase function. The validity is especially strengthened by the choice of

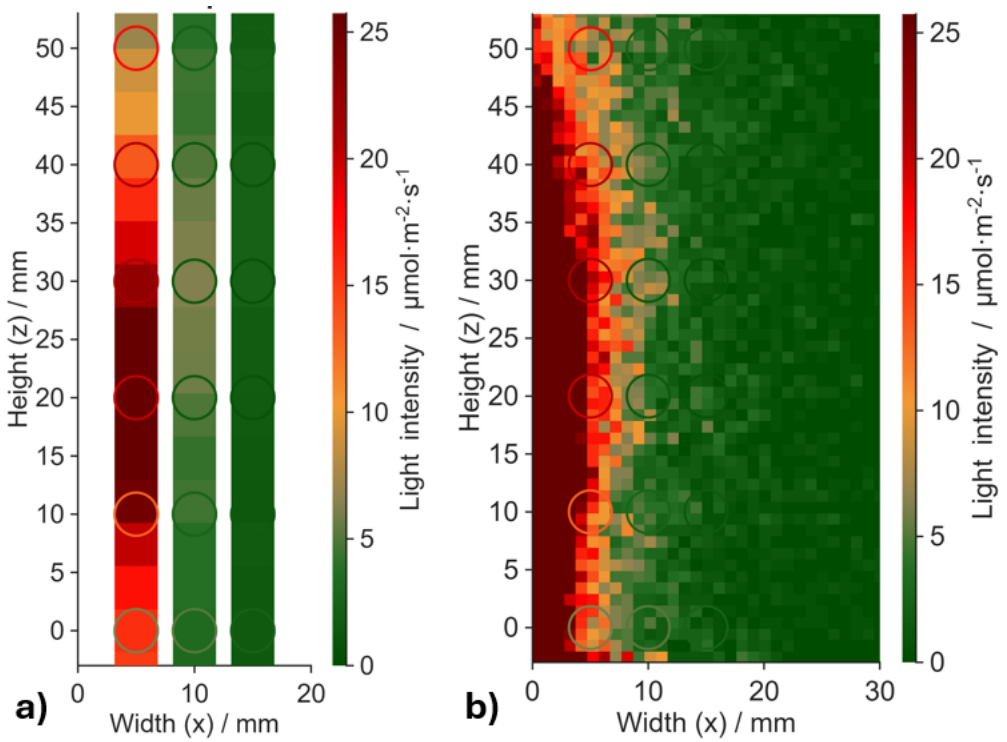

Figure 73: Light simulation results with a laser beam from below (0 | 0) at c_X = 17.8 g·m^{-3} and 7 % isotropic backscattering from 160° to 180°. N_{ray} = 40,000. Circles indicate sensor position and size. Cubic voxel length = a) 3.7 mm and b) 1 mm.

measurement positions in the lateral region, where the light pattern is predominantly determined by side and backscattering. Equation 68 was therefore adopted for further light simulations across conditions and wavelengths, while absorption and scattering cross-sections remained wavelength-dependent.

3.5.5 Model adaptation to light sources of the cptPBR

Modeling light distribution was performed as described in chapter 3.5.3 and applied in the test setup (chapter 3.5.4), including wavelength dependency and backscattering (Equation 68). Simulations were first carried out for a single LED spot in the glass tube to specify the incident photon distribution at the suspension boundary. The simulated light distribution was validated experimentally using artificially defined outer boundaries first. In the next step, the single LED distribution was overlaid to yield the light distribution of one of the PBR's repetitive longitudinal sections. Reactor walls and installations were introduced as additional boundaries, which terminated crossing light rays. Together, these steps provided a representation of the full cptPBR light model.

Simulation boundaries were chosen to minimize their impact on light distribution. Their placement was guided by experimental observations and by the final simulation geometry, in which installations physically limited photon propagation. In the cptPBR, the distance between neighboring glass tubes serving as light sources was 23-25 mm. This spacing corresponded to

observed flattening of light gradients between 20 and 30 mm, even in diluted cultures (Figure 74). Consequently, artificial boundaries were placed at a radial distance of 30 mm from the glass tube containing the LED bar. The longitudinal center-to-center distance between neighboring LED spots was ~19.5 mm, which was used as lateral boundary to account for additive light contribution of neighboring spots in the final light simulation.

Figure 74: Photograph of LED spots of one light bar in a glass tube from the cptPBR in microalgal suspension (c_X = 26.5 g·m^{-3}) with approximate cm/mm scale.

A single LED spot was simulated to specify the incident light ray distribution on the glass tube as modeling input. The angular emission pattern of the LED spot was used to describe the initial light ray distribution in air before refraction at the glass surface. The LED spots closely resembled Lambertian emitters according to the manufacturer's data sheet. The polar angle-dependent light intensity of the LED was therefore described by

$$I_{h\nu}(\theta) = I_0 \cdot \cos\theta \qquad \text{Equation 69}$$

where $I_{h\nu}(\theta)$ was the light intensity at the polar angle θ relative to the maximum intensity $I_{h\nu}(0°)$ at orthogonal emission (0°).

To obtain the corresponding light ray probability distribution, $p_{LED}(\theta)$, Equation 69 was weighted by the differential solid angle ($d\Omega_\theta$) to reflect the angular variation of the represented spherical surface area, and subsequently normalized.

$$p_{LED}(\theta) = \frac{I_0 \cdot \cos\theta \cdot d\Omega_\theta}{\int_{0°}^{90°} I_0 \cdot \cos\theta \cdot d\Omega_\theta \, d\theta} = \sin(2\theta) \quad \text{with } d\Omega_\theta = 2\pi \cdot \sin\theta \, d\theta \qquad \text{Equation 70}$$

This relation was assumed to apply uniformly across the emitting surface of each LED spot (diameter 4.3 mm) with the selection of the position analogously applied to Equation 65. The θ was combined with a uniformly distributed azimuthal angle (ϕ) to account for rotational symmetry. The light distribution from the LED spot was then described by the unity vector, earlier introduced in Equation 66, and here reshaped for the different phases:

$$\hat{v}_{\text{air}} = \begin{pmatrix} \sin\theta\cos\phi \\ \sin\theta\sin\phi \\ \cos\theta \end{pmatrix}, \quad \|\hat{v}_{\text{air}}\| = 1 \qquad \text{Equation 71}$$

$$x^2 + z^2 = r^2_{\text{glass,inner}} \qquad \text{Equation 72}$$

To describe the following refraction at the glass tube in physical terms, the origin of the *x*-*z* plane was defined at the center of the glass tube, with the y-axis in longitudinal direction of the cptPBR to remain consistent with the light simulation in the test setup. Assuming the simulated LED spot pointed upward, the emitting surface was located at z = 4.85 mm, with the inner radius of the glass tube ($r_{\text{glass,inner}}$) measuring 6.2 mm and the glass thickness t_{glass} = 1.8 mm. The inner shape of the glass tube in the *x*,*z*-plane was described by the circle equation along y leading to a cylinder description.

To determine the light path to the intersection with the inner glass tube, x and z were substituted by $x = x_0 + \Delta s_{\text{air}} \cdot \hat{v}_{\text{air,x}}$ and $z = z_0 + \Delta s_{air} \cdot \hat{v}_{air,z}$, respectively, with respect to their initial position (x_0, z_0) and the traveled distance through air (Δs_{air}). The substitution yielded a quadratic equation, which resulted in two solutions for Δs_{air}

$$\Delta s_{air,1,2} = \frac{-B \pm \sqrt{B^2 - 4AC}}{2A} \qquad \text{Equation 73}$$

with $A = \hat{v}_{\text{air,x}}{}^2 + \hat{v}_{\text{air,z}}{}^2$, $B = 2 \cdot \left(x_0 \cdot \hat{v}_{\text{air,x}} + z_0 \cdot \hat{v}_{\text{air,z}}\right)$ and $C = x_0^2 + z_0^2 - r^2_{\text{glass,inner}}$, of which the positive Δs_{air} is selected as it represents the intersection in the forward light ray direction.

Analogously to the computation of other optical event positions (compare Equation 66), the position of intersection (P_{inner}) was then given by Δs_{air}, the initial position and $\hat{v}_{\text{air}}$. At this position, the light ray was refracted described by changes in the angles θ and ϕ.

At P_{inner}, the refraction was described by Snell's law in vector format using radial unit normal ($\hat{n}_{\text{rad,inner}}$), which represented the outward-facing surface normal from the air phase. The angle θ at which the light ray approached the inner surface of the glass tube relative to $\hat{n}_{rad,inner}$ was described by:

$$\cos\theta = \hat{v}_{\text{air}} \cdot \hat{n}_{\text{rad,inner}} \qquad \text{Equation 74}$$

The refracted ray was then propagated through the glass in the direction defined by the incident θ and the ratio of refractive indices $\eta = n_{\text{air}} \cdot n_{\text{glass}}{}^{-1}$.

$$\hat{v}_{\text{glass}} = \eta \cdot \hat{v}_{\text{air}} - \left(\eta \cdot \cos\theta - \sqrt{1 - \eta^2 \cdot (1 - \cos^2\theta)}\right) \cdot \hat{n}_{\text{rad,inner}} \qquad \text{Equation 75}$$

After normalization to unit length $\|\hat{v}_{\text{glass}}\| = 1$, the direction vector was converted into the angular representation consistent with the defined model coordinates, yielding the updated polar and azimuthal angles after refraction at the inner glass surface.

$$\theta = \arccos \hat{v}_{\text{glass,y}}\,, \quad \phi = \text{atan}^2\left(\hat{v}_{\text{glass,z}}, \hat{v}_{\text{glass,x}}\right) \in [0°, 360°] \qquad \text{Equation 76}$$

From the position and direction vector at the inner surface of the glass tube, the calculations from Equation 72 to Equation 76 were repeated analogously with $r_{glass,outer}$ = 8.0 mm and $\eta = n_{glass} \cdot n_{water}^{-1}$ to define the position and angle at the outer surface of the glass tube. At the outer surface, the light rays reached the microalgal suspension.

Further light simulation was carried out using the Monte Carlo approach described in chapter 3.5.3 with the phase function from Equation 68 to account for backscattering. Only light distributions from a single LED under varying conditions were simulated, applying single wavelength in separate rays and binning subsequently. Installations were introduced by post-simulation data processing through termination of crossing light rays. The contributions of multiple LEDs were obtained by geometrical overlays of individual LED simulations, yielding the full light distribution in the cptPBR.

3.5.6 Model validation with experimental data based on single LED of the cptPBR

The cptPBR light model relied on simulating light rays from a single LED, followed by binning and overlaying. The dependence on this single LED highlighted the importance of evaluating the modeling accuracy. Comparative measurements were carried out with a single glass tube containing a light bar in a microalgal suspension placed outside the cptPBR to minimize interference from neighboring PBR installations.

Single-LED simulation based on the Monte Carlo approach was performed in a wavelength-dependent manner with respect to the LED emission, and experimentally determined scattering and absorption cross-sections using the model described in chapter 3.5.5. Each light ray emitted by the LED was assigned a wavelength between 400 and 700 nm according to a probability distribution sampled from the LED emission spectrum (Figure 68).

Light rays in the suspension were binned irrespective of their wavelength to enable conversion into measurable light intensities. Binning tiles of 1 x 1 mm^2 were oriented radially, perpendicular to the radius of the glass tube to emphasize the predominant light direction by counting the crossing light rays. Light intensities were calibrated based on ray count and measured light intensities on a glass tube surface, yielding the following calibration coefficient k_{LED} (unit: $\mu mol \cdot s^{-1} \cdot ray^{-1}$):

$$k_{\mathrm{LED}} = \frac{I_{\mathrm{h\nu,0,avg}}(I_{\mathrm{LED}}) \cdot \mathrm{A}_{\mathrm{glass\ tube}}}{\#LED_{\mathrm{glass\ tube}} \cdot N_{\mathrm{ray}}}$$ Equation 77

with $k_{\mathrm{Ih}\nu}$ = 0.0257 A·(µmol·m^{-2}·s^{-1})$^{-1}$ linking the average light intensity on the glass tube to the applied current (I_{LED}, chapter 2.6). The illumination area $\mathrm{A}_{\mathrm{glass\ tube}}$ was normalized to the number of LEDs ($\#LED_{\mathrm{glass\ tube}}$) per glass tube because measurements were averaged across the entire glass tube, accounting for inherent interference from neighboring LEDs.

For single LED measurements, interference from neighboring LEDs was minimized by covering the glass tube as illustrated in Figure 75. The cover left a translucent window of approximately ± 30° for light propagation into the liquid. The measurements were carried out with a planar light sensor of 3 mm in diameter oriented towards the center of the glass tube. This measurement setup was closely reproduced by the described ray-tracing simulation.

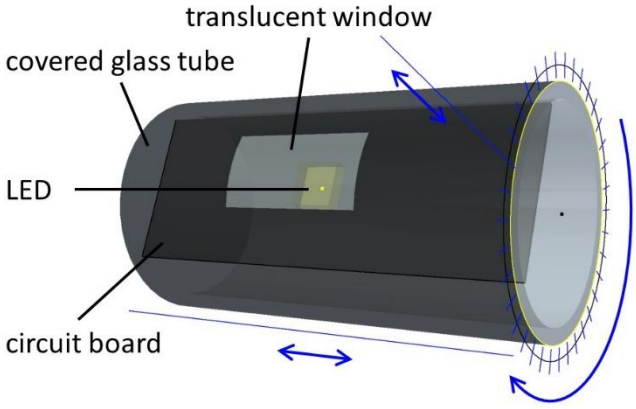

Figure 75: Illustration of the measurement setup for single LED on a light bar within a glass tube adapted from [41]. Blue lines and arrows indicate the performed shifts of the sensor in longitudinal direction, distance and angle (Δ = 10°).

The applied averaged light intensity for all single LED measurements was 38.9 µmol·m^{-2}·s^{-1} (I_{LED} = 1 A). With constant light intensity, the biomass concentration was varied ($c_{\mathrm{X,I}}$ = 0.00, $c_{\mathrm{X,II}}$ = 30.43, $c_{\mathrm{X,III}}$ = 84.49 g·m^{-3}) to assess model performance at different specific light supply rates ($spI_{\mathrm{h}\nu,\mathrm{I}}$ = ∞, $spI_{\mathrm{h}\nu,\mathrm{II}}$ = 49.4, $spI_{\mathrm{h}\nu,\mathrm{III}}$ = 15.51 µmol·g^{-1}·s^{-1}). These $spI_{\mathrm{h}\nu}$ covered most of the relevant range in the micro-feeding experiments (chapter 3.4) for which the light simulation was performed to distinguish nutrient and light kinetics.

Simulation results for a single LED were obtained from 1,000,000 light rays to generate smooth distribution patterns and represent the light spectra. The LED emission spectrum (black line in Figure 76) was closely reproduced by all simulated light rays (blue histogram). High numbers of light rays enabled the approximation of spectra also in PBR sections distant from the LED (red histogram and line in Figure 76) to resolve wavelength-dependent effects.

More distant PBR sections generally exhibited lower light intensities and a modified spectrum caused by wavelength-specific absorption along the light path before reaching the respective section. With increasing distance from the light source, less absorption of green and yellow

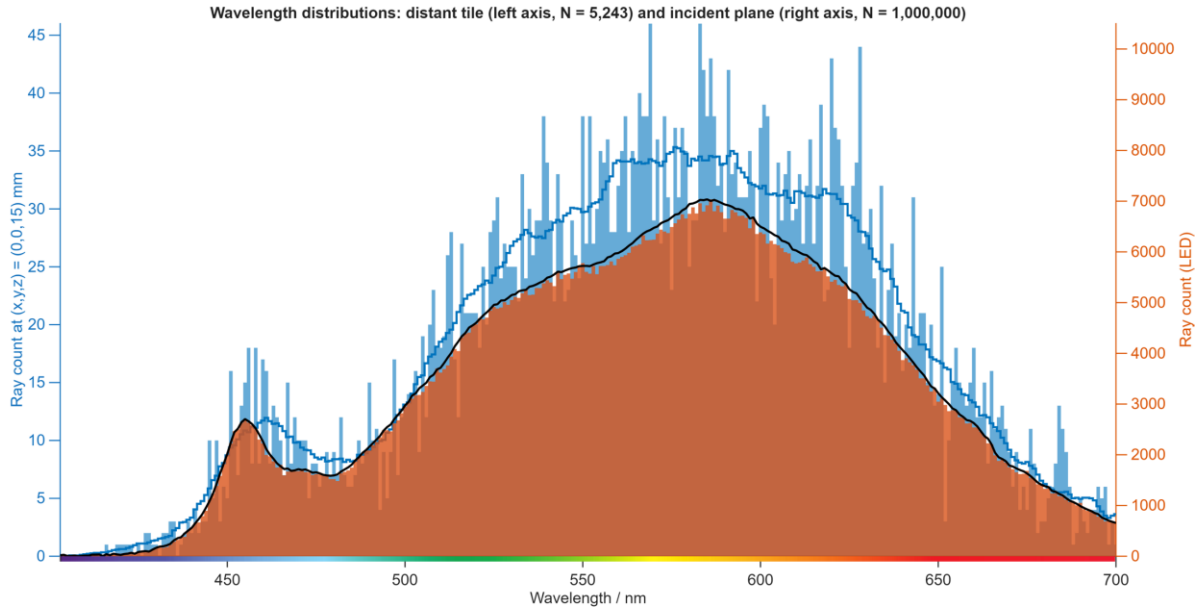

Figure 76: Simulated LED emission spectrum (orange histogram) with the measured spectrum from which the emitted rays were sampled (black line). The simulated spectrum in a PBR region distant from the LED (blue histogram) was smoothed (dashed blue line, average of $\Delta\lambda = 11$) and scaled to match the blue spectrum for comparison. Biomass concentration $c_{X,II} = 30.43\ g \cdot m^{-3}$, with $N_{ray} = 1{,}000{,}000$ for high-resolution spectral evaluation.

wavelengths relative to blue and red light – commonly known as the green gap – led to a higher remaining proportion of green and yellow light. This spectral selectivity resulted in steeper absorption than light-intensity gradients in the PBR. In other words, this results in lower light availability to the microalgal cells and consequently a higher extent of light-limited regions than would have been expected by a wavelength-independent model at the same light intensity.

Using the wavelength-dependent model and integrating the light intensity over the wavelength gave the light distribution shown two-dimensionally through the center of the LED in Figure 77. Measurements were taken with a planar sensor with positions marked by black lines, closely mimicked by the simulated bent tiles. Simulation results were acquired with the measured absorption cross-section $\sigma_{X,abs} = 0.227\ m^2 \cdot g^{-1}$ projected to wavelength dependency by multiplication with the normalized spectrum as described earlier, in chapter 3.5.3 by Equation 53 and the scattering cross-section as measured wavelength-dependent, $\sigma_{X,sca} = 13.3\ m^2 \cdot g^{-1}$.

For comparison of experimental and simulated data, three neighboring simulated tiles of 1 mm x 1 mm were averaged and correlated to the measured light intensities at the matching position. The longitudinal direction (y-direction) was neglected for simplification justified by the light-emitting diameter of the LED exceeding the sensor size, which rendered deviations along the y-direction negligible.

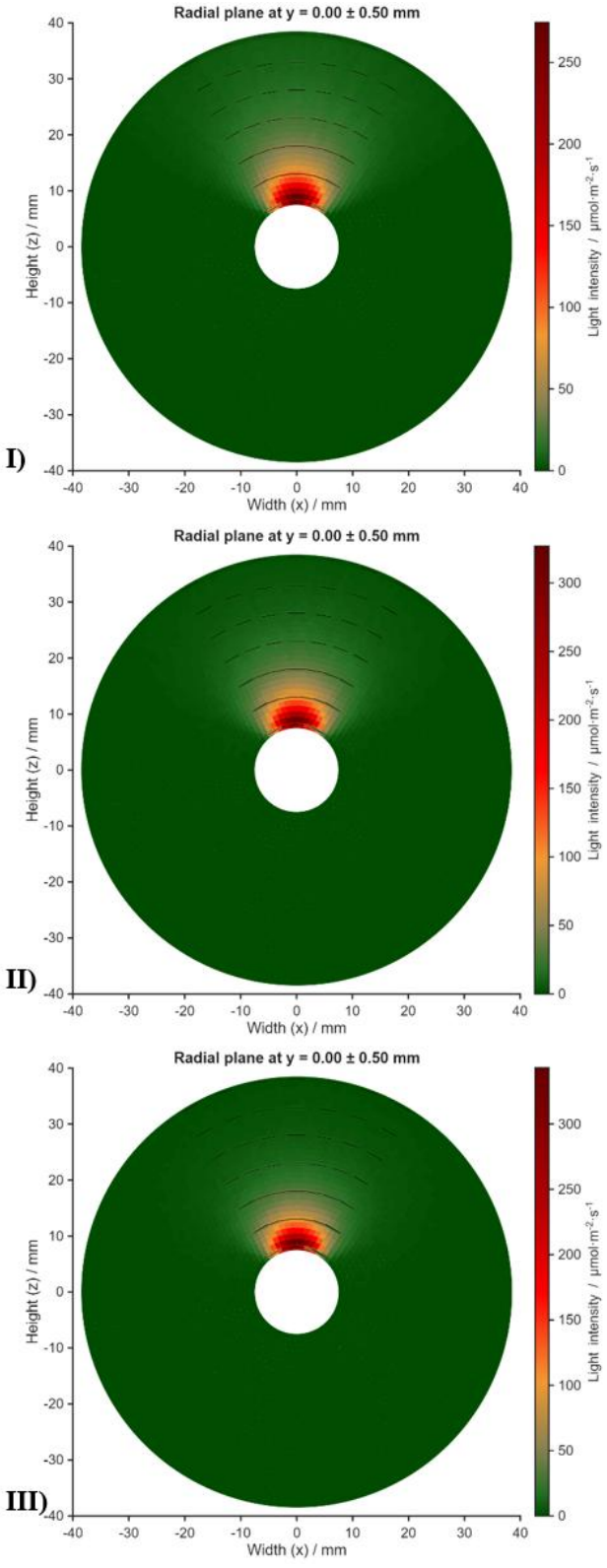

Figure 77: Light simulation results in microalgal suspensions with illumination from a single LED in a glass tube at I) $c_{X,I}$ = 0.00, II) $c_{X,II}$ = 30.43 and III) $c_{X,III}$ = 84.49 g·m^{-3}. Black lines indicate sensor position and size surrounded by a bar with the measured value according to the color scale. White disk illustrates the glass tube housing the LED. N_{ray} = 1,000,000. Radial tiles on the cylinder surface measured 1 x 1 mm^2.

The simulation results showed good agreement with the measured data as illustrated by the cross-section through the center of one LED spot in Figure 77. The correlation factors of measured ($I_{h\nu,meas}$) to simulated light intensities ($I_{h\nu,sim}$) were $I_{h\nu,sim}$ equaling to I) $0.829 \cdot I_{h\nu,meas}$ ($R^2 = 0.991$) at $c_{X,I}$ = 0.00 g·m^{-3}, II) $1.078 \cdot I_{h\nu,meas}$ ($R^2 = 0.977$) at $c_{X,II}$ = 30.43 g·m^{-3}, and III) $1.025 \cdot I_{h\nu,meas}$ ($R^2 = 0.957$) at $c_{X,III}$ = 84.49 g·m^{-3}.

The lower accuracy in water was primarily attributed to measurements taken near the glass tube surface and interpreted as interference of neighboring LEDs. Measuring with a planar sensor on a cylindrical surface allowed photons from other LEDs to pass through the translucent window at flat angles to the *y*-axis, increasing the light intensity compared to an isolated LED. These effects were reduced at higher biomass concentrations due to increased absorption and scattering along the light path from other LEDs before reaching the measurement position. This assumption was supported by the correlation improving to $I_{h\nu,sim} = 0.917 \cdot I_{h\nu,meas}$ ($R^2 = 0.987$) by excluding the measurements on the LED glass surface at $\pm$ 20°.

The resulting range of simulation accuracy within $\pm$ 10 % deviation sufficiently validated the model,

especially given the theoretical implementation of the light source and simplicity of mechanisms and parameter estimation. These results confirmed the single LED spot as a reliable basis for light modeling of the entire PBR to retrace light kinetics.

3.5.7 From single LED simulation to light distribution of the entire cptPBR

The single-LED simulation was overlaid geometrically to compute the light distribution in the entire cptPBR. The procedure was executed in multiple steps including replication of the single LED, trimming to a repetitive longitudinal section, replication to 37 light bars, and light extinction by PBR installations (Figure 78 and Figure 79).

Details on ray tracing from the single LED into the suspension (Figure 78a), on the computation of the light distribution (Figure 78b), and on the calculation of absorbance rates in the suspension were provided in chapters 3.5.3, 3.5.5, and 3.5.6. The single-LED light distribution was simulated and validated on tiles concentric with the LED bar. These results were replicated around the single LED's glass tube to represent neighboring LED spots. Neighboring spots

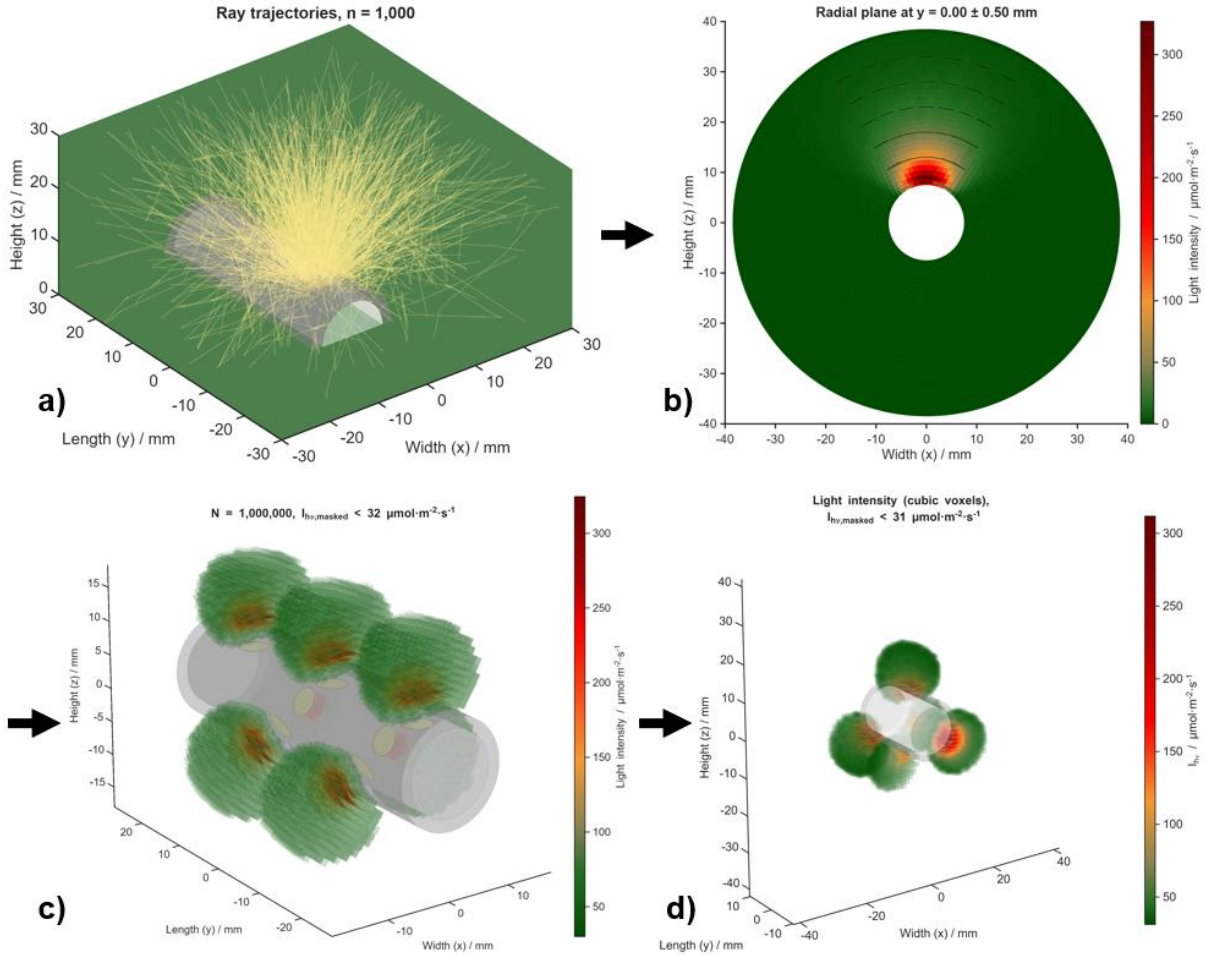

Figure 78: Workflow from the single-LED simulation to the repetitive light bar section. (a) Single-LED Ray tracing from LED through glass tube into the suspension. (b) Binning to cylindrical tiles. (c) Radial and longitudinal replication to 7 LED spots. (d) Conversion of tile intensities to cubic voxels and trimming to longitudinal section (± 10 mm). Simulation settings: N_{ray} = 1,000,000 for one LED. Simulation example: c_X = 30.43 g·m^{-3} and $I_{h\nu,0}$ = 38.9 µmol·m^{-2}·s^{-1}.

were shifted radially (120° turn) and longitudinally (~19.5 mm shift), which yielded the 7-LED simulation result (Figure 78c).

Voxels instead of tiles were needed to count absorbed rays and relate absorption spatially to light intensity. To overlay multiple LED bars, the tile data were mapped onto a Cartesian grid. Each tile's light intensity was distributed to the eight neighboring voxels using volume-weighted trilinear interpolation, with the location assigned to the tile's center. The weighted sum defined each voxel's light intensity (Figure 78d). This grid enabled precise trimming of the light distribution to a repetitive longitudinal section within ± 10 mm of the initial single-LED's center (Figure 78d).

In contrast to the longitudinal case, the cross-section required an additional overlay step to reconstruct the placement of light bars and interfering installations such as gassing tubes, cooling bars, and heating bars at the voxel size's accuracy. The overlay respected these boundaries by occluding voxels at installations or outside the vessel and by applying line-of-sight (LoS) shading. LoS was applied from each light bar center to every voxel within a simulated light path of 30 mm from the glass surface for each LED spot. If a line to a voxel intersected an installation, that bar's contribution was set to zero (Figure 79).

This simplified LoS shading ignored finite emitter area, partial shading, and reflections, which can under- or overestimate light intensities near obstacles, but kept the model tractable. Attenuation was strong as shown by the data example: after 10 mm only ~10 % of the incident intensity remained, and after 15 mm ~0.5 %. Installations rarely lay within these distances; therefore, LoS-related bias was not expected to substantially affect the simulated fields of light intensity or specific absorbance rate.

The resulting 3D distributions of light intensity $I_{h\nu}$ and specific absorbance rate $r_{h\nu,abs}$ represented the entire PBR because the 20 mm longitudinal section (4 % of the length) was repetitive in the cptPBR. Extrapolation to the full cptPBR length of 500 mm gave 27.5 L total voxel volume, agreeing with the average working volume. Both distributions were plotted in the cross-section (Figure 79), with $r_{h\nu,abs}$ simulated according to Equation 64. The simulation assumed equal orientation of all 37 light bars to display the longitudinal effects. The first longitudinal position (Figure 79a) crossed the center of the upward pointing LED. To illustrate the 3D pattern, b) and c) represented maximum longitudinal distance to any LED spot and maximum longitudinal distance between two neighboring upper spots, respectively.

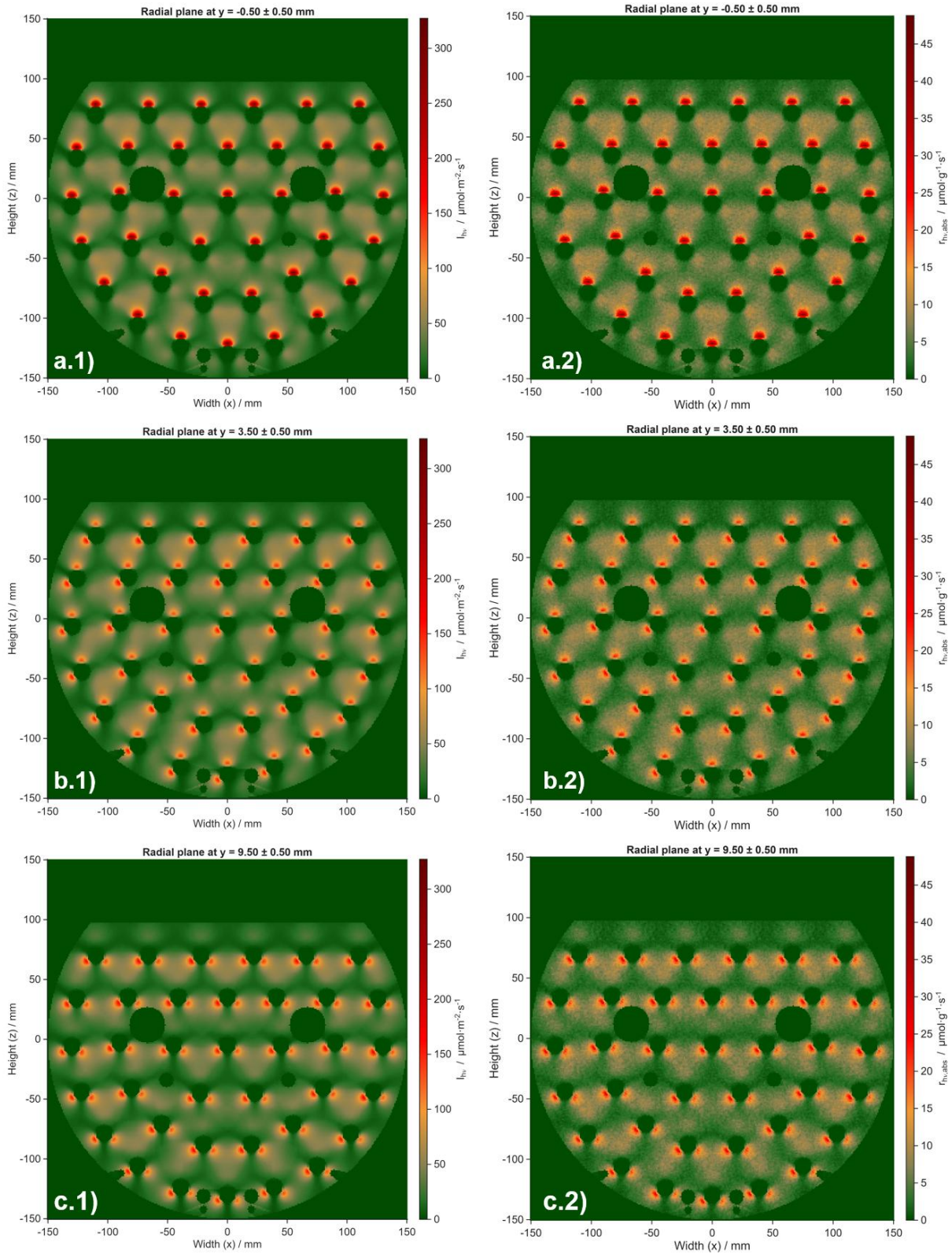

Figure 79: Replication of 37 light bars in the cross section of the cptPBR and resulting distributions of (1) light intensity and (2) specific absorbance rate. (a) Center of upward-pointing LEDs. (b) Maximum distance to any LED spot. (c) Midway between two upward LEDs. Simulation settings identical to Figure 78.

Despite the lower resolution of $r_{h\nu,abs}$ (Figure 79.1) compared to $I_{h\nu}$ (Figure 79.2), both distributions appeared similar due to their stoichiometric coupling via the absorption cross-section $\sigma_{X,abs}$ (see Equation 1 in chapter 1.3). However, wavelength-dependency of simulations

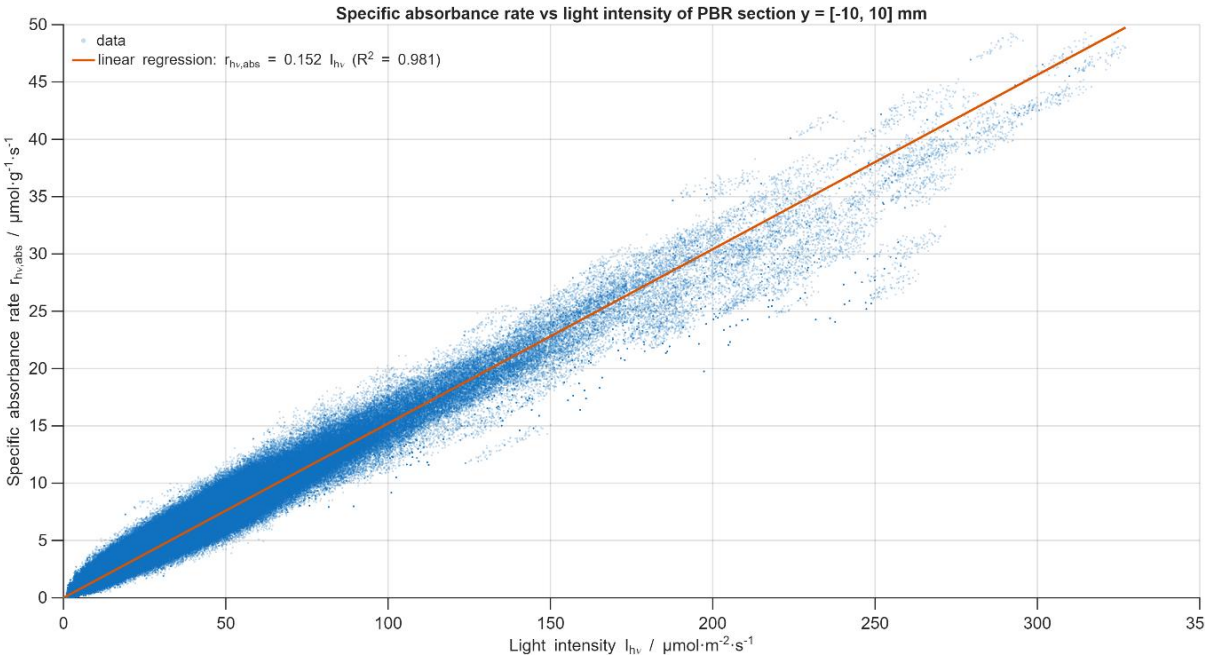

Figure 80: Specific absorbance rate versus light intensity of all voxels including linear regression. Simulation settings identical to Figure 78.

weakened this relation and reduced the effective ratio from the applied average $\sigma_{X,abs}$ = 0.227 to 0.152 m^2·g^{-1} when relating $r_{hν,abs}$ to $I_{hν}$ on a wavelength-independent basis (Figure 80).

Ratios < 0.14 m^2·g^{-1} occurred mainly at the largest distances to the light sources due to reduced absorption at high green-yellow light proportions. This observation highlighted the importance of using $r_{hν,abs}$ rather than $I_{hν}$ to investigate light kinetics.

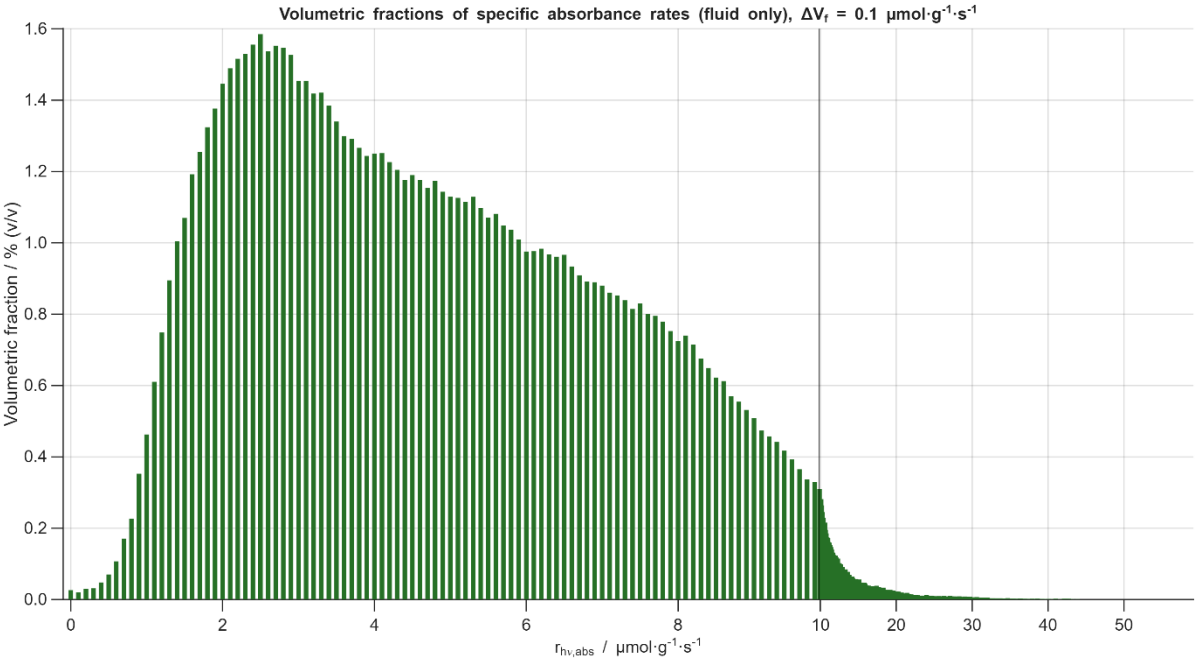

Figure 81: Volume-fraction histogram of specific absorbance rates, bin width 0.1 µmol·g^{-1}·s^{-1}. Simulation settings identical to Figure 78.

The volumetrically resolved specific absorbance rate (Figure 81) as derived based on the measurements and simulation throughout chapter 3.5 formed the basis for evaluating light kinetics. The light kinetics were explored to distinguish nutrient- and light-related effects during the micro-feeding experiments, guiding the direction of further optimization of this strategy with the aim of efficient ^{13}C utilization in ^{13}C labeled glucose production.

3.6 Reevaluation of micro-feeding with respect to light kinetics

Micro-feeding was designed to maintain photosynthetic performance while selectively directing carbon towards starch. Active biomass formation was suppressed but not fully prevented. Further adaptation of the feed strategy should aim to suppress active biomass formation more in favor of maximum carbon partitioning into starch, thereby supporting the central goal of ^{13}C-efficient isotopically labeled glucose production. The application of micro-feed rates decoupled the specific biomass accumulation rate (r_X) from intracellular nitrogen quota and ammonium concentration, which complicated causal attribution of changes in r_X to feed rates or unintentionally to light. As with ammonium (NH_4^+) feed, the incident light intensity was kept constant throughout micro-feeding, which may have introduced additional limitations. The reevaluation of micro-feeding (chapter 3.4) in the context of light kinetics aimed to distinguish between light-driven and nutrient-driven growth responses to guide the direction of future micro-feeding adaptations.

Light kinetics throughout the micro-feeding phase as derived by measurements and modeling as described in chapter 3.5 could indicate whether metabolic limitations restricted the potential biomass accumulation rate [26] and whether photosynthetic efficiency was maintained. Reductions in the maximum growth efficiency ($y_{X,ph,max}$) or the maximum specific biomass accumulation rate $r_{X,max}$ indicate limitations beyond light, here insufficient nutrient supply. Conversely, if these parameters remained stable while the measured specific growth rate (μ) declined, no metabolic constraints in addition to light emerged, indicating light availability was the dominant limitation.

The light kinetics were derived from the volumetric distribution of local specific photon absorbance rates ($r_{h\nu,abs}$) in the compact photobioreactor (cptPBR), provided by the light distribution model (see example in Figure 81, chapter 3.5). The simulated absorption data reflected the effect of local light intensities leading to local biomass growth rates, which were then volumetrically integrated over the cptPBR.

The simulated $r_{h\nu,abs}$ values from the voxels were clustered into K discrete levels ($r_{h\nu,abs,i}$) with volumetric fractions f_i. For each cluster, the growth model applied the piecewise saturation function in analogy to Pirt's law:

$$r_{X,i}(r_{h\nu,abs,i}) = \min(y_{X,ph,max} \cdot r_{h\nu,abs,i} - r_{X,m}, r_{X,max}). \quad \text{Equation 78}$$

while the kinetic parameters $y_{X,ph,max}$, $r_{X,max}$, and the maintenance rate ($r_{X,m}$) were fitted to let the volumetrically weighted sum r_X match the experimentally based μ.

$$r_X = \sum_{i=1}^{K} f_i \cdot r_{X,i}(r_{h\nu,abs,i}) \quad \text{Equation 79}$$

The fitting was a relative least-squares regression on the piecewise linear saturation model with absorbance rate-weighted volumetric averaging. Hard parameter bounds were applied as $y_{X,ph,max} > 0$, $r_{X,max} > 0$, and $r_{X,m} < 0$.

For better comparability, the experimental μ values were energetically normalized before parameter fitting by correcting the biomass concentrations used in μ calculation for the starch content (x_{STA}). Corrected dry-weight concentrations (c_X^{corr}) reflected the hypothetical scenario where only active biomass was formed, based on the theoretical biomass yield on photons $Y_{k,ph}$ (chapter 1.5, Table 4).

$$c_X^{corr} = c_X \cdot \left(1 - x_{STA}\left(1 - \frac{Y_{actX,ph}}{Y_{STA,ph}}\right)\right) \quad \text{Equation 80}$$

The recalculated μ based on Equation 80 was the fitting target of r_X (Equation 79) for each sampling point of the micro-feeding cultivations (Lim12, Lim6 and Lim1).

Similar metabolic performance at the onset of the micro-feeding phases across cultivations were already assumed based on the growth behavior, and measured parameters and similar conditions (chapter 3.4.4). The light distribution model supported the successful equalization of the light conditions at deviating biomass concentration by the adapted specific light supply. Comparing the fitted photosynthesis irradiance response curves in Figure 82a validated very similar light kinetics and photosynthetic activity prior to feed reduction.

The fitted kinetic parameters at t_0 were determined to $r_{X,max}$ = 3 day^{-1}, $r_{X,m}$ = 0.26 day^{-1}, and $y_{X,ph,max}$ of 3.6-3.7 g·mol^{-1}. The fitted photon-yield $y_{X,ph,max}$ was higher than physiologically expected (≤ 1.5 g·mol^{-1}, chapter 1.5, Table 4). This overestimation likely arose from simplifications in the light model. About 20 % of the supplied light was not absorbed but lost at simulated boundaries under the applied conditions. Light at boundaries was partly reflected

back into the culture, so neglecting the reflection reduced $r_{h\nu,abs}$ compared to the experimental absorbance utilized for growth, leading to a seemingly increased yield on photons.

The bigger effect contributing to overestimation of $y_{X,ph,max}$ presumably originated from the implicit light-integration approach in the applied light model. Light integration was implicitly restricted to the 1 mm voxel resolution and did not account for local flow dynamics. This underrepresentation of light integration led to overemphasized differences in local growth. In reality, small light-saturated regions near LED spots supply light not only to cells in one local volume fraction but also to passing cells, reducing heat dissipation and effectively diminishing the experienced light gradients. As a result, comparatively low local $r_{h\nu,abs}$ values were assigned to high r_X by the kinetics fit, which led to an overestimation of $y_{X,ph,max}$ and to $r_{X,max}$ values approaching the experimental μ initially. The true $r_{h\nu,abs}$ values, especially near high-light regions, would be higher when accounting for the light trajectories experienced by microalgal cells due to mixing.

Coupling of mixing and light simulation could enable explicit treatment of light integration, for example within a Lattice-Boltzmann framework, but was not feasible in this simplified model.

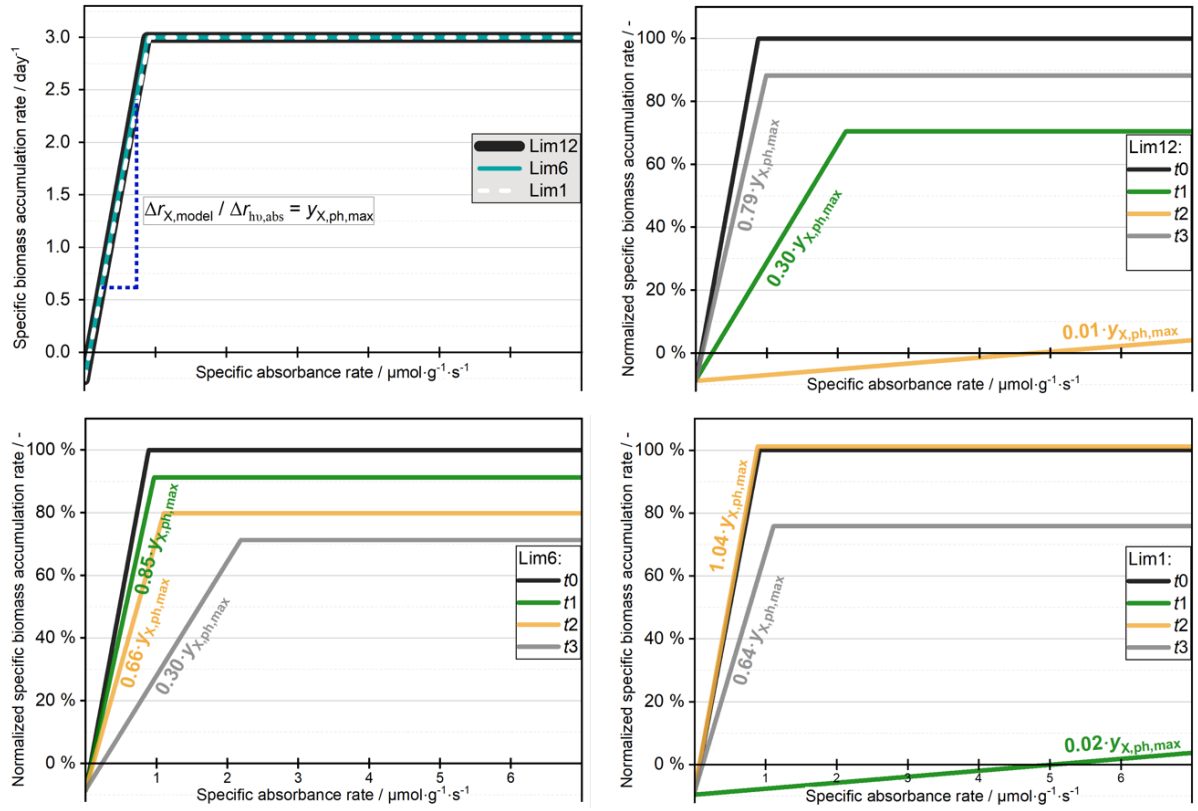

Figure 82: Trends of photosynthesis irradiance response curves for the micro-feeding experiments with reduced feeds. (a) Initial states before feed reduction at t0. (b-c) Samples along the phase with reduced feeds each normalized to the initial values (t_0) of the respective cultivation.

Trends throughout the cultivation were still assumed to represent metabolic effects due to systematic deviation under consistent flow dynamics and similar light patterns.

To allow direct comparison of response dynamics $r_X(r_{hv,abs,i})$ was normalized to the onset of feed reduction (start of phase IV) for each cultivation. The normalization reference was the light saturation onset, which was defined as $y_{X,ph,max} \cdot r_{hv,abs} - r_{X,m} = r_{X,max}$ using the corresponding $r_{X,max}$ and $r_{hv,abs}$.

The development of light kinetics throughout the three sampling points (t_1-t_3) during the cultivation phase with reduced feeds showed substantially different trends (Figure 82). Chapter 3.4.5 showed that Lim6 exhibited the most consistent photoconversion efficiency on incident light, starch formation and active biomass accumulation. The efficiency of biomass on absorbed photons was likewise consistent (Figure 82c), correlating inversely with the starch content for t_0 to t_2. This trend predominantly represented the higher absorption due to increasing active biomass concentration in the cptPBR, with partially light saturation occurring.

After the maximum starch fraction at t_2 in Lim6, the efficiency subsequently declined to 30 % of its maximum, suggesting that either cellular limitations had been reached or that the feed had become insufficient to maintain high efficiency over ≥ 6 h. This reduction in efficiency was already indicated by the slow decrease in the H_2-based biomass estimate between t_2 and t_3 (Figure 56 in chapter 3.4.5), and would probably have substantially affected the biomass concentration shortly after t_3.

The formation of higher starch fractions in biomass during a nitrogen runout experiment with the same microalgal strain and PBR made inherent cellular limitations unlikely. The feed was presumably insufficient at t_3. Biomass growth throughout Lim6 effectively reduced the specific feed from initially $7.3 \cdot 10^{-4}$ $g_N \cdot g_X^{-1} \cdot h^{-1}$ by 38 % to $4.5 \cdot 10^{-4}$ $g_N \cdot g_X^{-1} \cdot h^{-1}$.

Maintaining high photosynthetic efficiency at reduced feed rates is apparently also a matter of acclimation to the nitrogen conditions within the scope of hours as Lim1 and Lim12 demonstrated. Biomass accumulation was temporarily impaired from light supply in Lim1 (t_1) and Lim12 (t_2). In both cultivations, hardly any biomass formed transiently, indicating intracellular limitations. Limitations potentially include adaptations in the cellular metabolism such as mobilization of nitrogen resources and induction of pathways for that to enable repair mechanisms. However, both cultures Lim12 (t_3) and Lim1 (t_2) recovered to 79 % and 104 % of maximum efficiency, respectively, within the next sampling interval of 2 h, indicating either colimitations or light limitations Lim1.

These recoveries to efficient light use were observed at specific feed rates of $6.6 \cdot 10^{-5}$ $g_N \cdot g_X^{-1} \cdot h^{-1}$ in Lim12 and $8.7 \cdot 10^{-5}$ $g_N \cdot g_X^{-1} \cdot h^{-1}$ in Lim1, while an effective specific feed of $4.5 \cdot 10^{-4}$ $g_N \cdot g_X^{-1} \cdot h^{-1}$ in Lim6 was insufficient to maintain high photosynthetic efficiency after 6 h. The lower feed rates may effectively induce starch accumulation but can cause efficiency loss and even active biomass degradation when applied immediately after balanced feeding. $7.3 \cdot 10^{-4}$ $g_N \cdot g_X^{-1} \cdot h^{-1}$ was initially sufficient to maintain efficiency but incompletely suppressed active biomass formation.

In conclusion, efficient starch accumulation at effective suppression of active biomass formation was not achievable applying any of the tested stable feed rates. The ideal feed rate for *C. vulgaris* H14 in the used PBR setup will be higher than $9.3 \cdot 10^{-5}$ $g_N \cdot g_X^{-1} \cdot h^{-1}$ (Lim1 t_0) due to initial productivity loss but below $7.3 \cdot 10^{-4}$ $g_N \cdot g_X^{-1} \cdot h^{-1}$ (Lim6 t_0) after acclimation to the applied balanced feeding strategy. These feed rates periodically maintained photosynthetic activity and efficient ^{13}C incorporation into starch, both required to satisfy the main research objective. Lower values in this range offer the chance of more effective suppression of active biomass formation, while risking productivity loss. Feed rates will need to be gradually increased over time – at least as long as active biomass continues to be produced to maintain photosynthetic performance. Freely allocated nitrogen is required for protein and pigment turnover to prevent accumulation of severe damage associated with efficiency losses. Even without active biomass formation, cells might face increasing difficulties with repair mechanisms over time, which could be mitigated by slightly increasing the feed rate.

4 Conclusion

The present thesis aimed for a microalgal production system that allowed high productivities, reproducibility, and maximum purity for an economically feasible production of ^{13}C-labeled biomass. To achieve this central objective a photobioreactor concept was established that combined compactness, internal illumination, and closed-loop oxygen removal with automated monitoring. The design enabled full CO_2 retention and systematic kinetic studies with microalgae under precisely defined process conditions to improve profitability by partitioning the costly ^{13}C toward starch, which can be extracted and hydrolyzed to very high value ^{13}C-labeled glucose.

The compact reactor footprint was realized by a high internal illumination surface, controlled mixing, and advanced gas management. The design included 37 horizontal glass tubes providing a total illuminated surface area of 0.909 m^2, and a surface-to-volume ratio of 33.7 m^{-1}, comparable to other photobioreactor systems. The three-directionally oriented LEDs, with ~19.5 mm longitudinal spacing, were helically distributed to reduce the effective distance. Together with circulation advanced through modeling and experiments, this setup enabled high specific growth rates that approached the theoretical kinetic limits for photoautotrophic microalgae. The structural compactness thus did not come at the expense of metabolic performance. However, light homogeneity was limited by the geometry of the LED arrangement, since only approximately one third of the glass tube surface emitted light directly, leading to light gradients in all dimensions. The importance of such intrinsic gradients becomes increasingly critical at higher biomass concentrations, with increasing heterogeneity due to scattering. Future technical iterations should therefore apply more uniform LED coverage to prevent light inhibition zones at higher biomass concentrations, while reducing the dependence on dynamic mixing to compensate for structural non-uniformity.

The integration of a closed gas loop with a proton exchange membrane fuel cell (PEM) for selective oxygen removal marked a key innovation in this work, especially valuable for the central goal of isotopically labeling biomass using $^{13}CO_2$. Unlike stripping-based concepts that couple O_2 removal with CO_2 loss, the PEM setup retained CO_2 while converting O_2 stoichiometrically into water, ensuring a cost-effective production process for ^{13}C labeling. The PEM-based oxygen removal system further allowed stable operation with quasi-synchronous dynamics between the gas loop and the liquid phase, with a measured response delay of only 0.02-0.04 h. The system maintained pO_2 levels between 17 % and 19 %, a range suitable for active photoautotrophic growth, and enabled oxygen removal capacities equivalent to biomass

productivities up to 1.15 $g \cdot L^{-1} \cdot day^{-1}$. The hydrogen consumption rate could be stoichiometrically related to biomass-specific oxygen evolution, providing a process variable for metabolic monitoring and automated feedback. This demonstrated that a gas loop originally designed for isotope retention could simultaneously function as a metabolic control tool. Specific growth rates of 2.0-2.8 day^{-1} under photoautotrophic conditions were sustained until the PEM oxygen removal limit was reached. This rate equaled nearly two-thirds of the microalgal strain's maximum heterotrophic rate on glucose (4.3 day^{-1}), confirming favorable growth conditions in the designed system that made it a suitable production system for ^{13}C-labeled biomass.

The cultivation system including the closed gas loop, however, revealed operational boundaries during periods of excess humidity. The PEM membrane in the gas loop overhydrated, causing voltage drops and temporary decoupling of hydrogen uptake from oxygen removal. Under such conditions, correlation between hydrogen consumption and biomass accumulation declined ($r = 0.735$), compared to near-perfect agreement under stable hydration ($r = 0.998$, $p < 0.001$). Since hydrogen-based oxygen removal provided accurate monitoring only under proper hydration, PEM hydration itself became a critical process parameter. This suggests that future system adaptations could incorporate moisture management strategies, such as automated purging with dry hydrogen or integration of active load control to maintain PEM operation in the upper voltage range and prevent performance impairment, in the case of monitoring and automation being desired. Such strategies would extend the operational robustness and elevate PEM-based monitoring from a proof of concept to a reliable process analytical tool.

Beyond the photobioreactor and gas loop design making the ^{13}C-labeled microalgal biomass production on $^{13}CO_2$ economically feasible, profitability of the process could be improved by maximal partitioning of ^{13}C toward starch. Commonly nutrient depletion is applied to induce starch accumulation. A conventional nitrogen runout experiment, thus, served as the reference experiment, which typically exhibited transient growth even after nitrogen depletion, reflecting mobilization of intracellular nitrogen reserves.

The new concept of micro-feeding aimed to supply minimal feed rates sufficient to sustain photosynthetic performance while suppressing further active biomass growth, leading to a higher proportion of the highest value product in the production process. The micro-feeding strategy required to prevent the build-up of nitrogen reserves – both intracellular and dissolved in the suspension – by applying balanced feeding prior to feed reduction to minimize intracellular nitrogen recovery processes. The maximum experimentally determined nitrogen

uptake rate of 11.6 $mg_N \cdot g_X^{-1} \cdot h^{-1}$, combined with mixing data, defined a minimum feed rate threshold to prevent local depletion during balanced feeding. To address this threshold, feeding began after an initial batch depletion phase, then gradually increased until being stoichiometric with biomass accumulation, while maintaining theoretical minimum concentrations around $8.4 \cdot 10^{-4}$ $gN \cdot L^{-1}$. The smooth feed rate adjustment avoided premature limitation while ensuring consistent starting conditions for micro-feeding.

Micro-feeding was applied at 60 $\mu mol \cdot g_X^{-1} \cdot s^{-1}$ with feed rates of 0.8-11.7 % compared to balanced feeding assuming $\mu = 3\ day^{-1}$. Across these conditions, the nitrogen quota declined at a constant rate of 0.6 $\% \cdot h^{-1}$, indicating a limiting reorganization dynamic. Photoconversion efficiency (*PCE*) reached a maximum of 7.6 % at 6.3 % of the balanced feed rate (%-feed), with 47-49 % of fixed energy partitioned to starch compared to only 32 % under classical runout. At 0.8 %-feed and 11.7 %-feed, *PCE* temporarily collapsed below 1.3 % and 1.6 %, respectively before recovering, while *PCE* remained high at 6.3 %-feed. These findings highlighted that acclimation substantially impacted the growth response and biomass accumulation. The resulting window for efficient starch accumulation with suppressed active biomass growth was between $9.3 \cdot 10^{-5}$ and $7.3 \cdot 10^{-4}$ $gN \cdot gX^{-1} \cdot h^{-1}$, below which the total biomass formation declined markedly. Comparison with nitrogen runout confirmed that micro-feeding decoupled growth from Droop-type dependencies: at identical intracellular nitrogen quota, specific growth rates were 0.5 day^{-1} higher under micro-feeding. The specific growth rate increase by micro-feeding indicated that immediate assimilation of external ammonium reduces metabolic demand compared to relying on intracellular recycling. The application of micro-feeding in appropriate feed rates thus promises higher biomass productivity, which is generally valuable for ^{13}C-labeled biomass production. However, under the observed constant rate of decline in starch content, the proportion of ^{13}C fixation into starch, so the efficiency of $^{13}CO_2$ did not change across the applied feed rates. To further improve profitability of the process by increased efficiency of ^{13}C partitioning toward starch, mechanistic understanding of reactor performance was required to ensure that observed effects were predominantly nutrient-related and not a result of light limitation.

For exploring potential light limitation, the light distribution in the culture was determined by light modeling. To adequately simulate multidirectional light propagation, scattering and absorption were characterized separately. Measurements from integrating sphere photometry and a custom-designed scattering cell quantified that, at $c_X < 0.1\ g \cdot L^{-1}$, the total scattering cross-section exceeded the absorption cross-section by factors of 68 (446 nm) to 420 (522 nm).

The custom scattering cell designed within this thesis used four laser wavelengths (404, 446, 522, 659 nm) and 10° angular resolution to determine phase functions without costly goniometers. Across nitrogen regimes, asymmetry factors of $g = 0.88$ demonstrated strong forward-scattering, with relative backscattering intensities of 0-7.2 %. The backscattering coefficient was more precisely estimated by calibrating Monte Carlo ray-tracing results against laser-illuminated microalgal suspension measurements. Agreement was best when 7 % isotropic backscattering was assumed yielding a regression slope of 0.98 with $R^2 = 0.85$. This confirmed the adequacy of the modeling approach while also indicating that calibration effort could be reduced by higher measurement sensitivity or more powerful lasers in future studies.

Fitted optical coefficients and phase functions were used to simulate the light propagation and absorption in the microalgal suspension. Simulations of a single LED as a Lambertian emitter through a glass tube showed strong agreement with measured light intensities across biomass concentrations. The yielded slopes were 0.829, 1.078, and 1.025 at 0.00, 30.43, and 84.49 $g \cdot m^{-3}$, respectively, with R^2 values of 0.991, 0.977, and 0.957, which confirmed the suitability of the measuring device and modeling approach to represent the light distribution of the light emitting diodes (LEDs) in the compact photobioreactor geometry. To extend the single-LED model to the entire reactor cross-section, volumetric interpolation into voxels and replication of LED spots were performed, yielding three-dimensional maps of absorbance rate distributions. Predicting the light distribution and absorbance rates in the compact, internally illuminated photobioreactor provided light kinetics for the sampling points throughout the micro-feeding phases.

The light kinetics confirmed the reproducibility of starting conditions prior to feed reduction besides the online adaptation of only the incident light intensity proportional to biomass growth. Most changes in photosynthetic performance could not be causally linked to the light supply, given the markedness of changes at the constant incident light intensity, so were assigned to the nutrient feeds and previous acclimation. Potential light limitations only emerged shortly after transient productivity loss in Lim1, which was not critical with respect to the research aims as the initial productivity loss excluded the respective feed rate from the production process due to concerns of process robustness.

Taken together, this dissertation defined both the capabilities and limitations of the newly developed compact photobioreactor design, as well as its application scope. The experimental results demonstrated that compactness did not preclude high-performance cultivation, provided that illumination, mixing, and gas management were carefully engineered. The closed-loop

oxygen removal via PEM ensured CO_2 retention complementing the photobioreactor to a suitable system for the intended ^{13}C-labeled biomass production, and further enabling growth monitoring and automation.

Oxygen evolution monitoring was particularly valuable in the closed, aerated photoautotrophic system, as O_2 deviations emerged earlier than measurable biomass changes. In future, the system may be applied by operating individual units fully closed across day-night transitions or stress events to trigger early feed or illumination adaptation, which could also control parallel open units. The closed gas loop system may thus advance from use in a single cultivation platform to an actively regulating component within a photobioreactor network.

Micro-feeding was evaluated as a promising strategy to not only induce starch accumulation but also suppress active biomass formation and partition more fixed carbon toward starch than in conventional runout experiments. The experimental results showed that nitrogen micro-feeding decoupled growth from classical quota models and redirected energy into storage compounds. Refinement of this strategy offers great potential to improve the starch accumulation efficiency on the supplied $^{13}CO_2$, leading to increased profitability of the overall production process of ^{13}C-glucose. Optimization of the micro-feeding approach may allow switching from active biomass growth to starch accumulation, using CO_2 in the growth phase and $^{13}CO_2$ only during starch accumulation to further reduce the demand for $^{13}CO_2$, and improve profitability.

References

[1] McCue MD. Tracking the oxidative and nonoxidative fates of isotopically labeled nutrients in animals. BioScience 2011;61(3):217–30.

[2] Zhang H, Li X, Martin DB, Aebersold R. Identification and quantification of N-linked glycoproteins using hydrazide chemistry, stable isotope labeling and mass spectrometry. Nature biotechnology 2003;21(6):660–6.

[3] Spellman DS, Deinhardt K, Darie CC, Chao MV, Neubert TA. Stable isotopic labeling by amino acids in cultured primary neurons: application to brain-derived neurotrophic factor-dependent phosphotyrosine-associated signaling. Molecular & Cellular Proteomics 2008;7(6):1067–76.

[4] Grankvist N, Watrous JD, Lagerborg KA, Lyutvinskiy Y, Jain M, Nilsson R. Profiling the metabolism of human cells by deep 13C labeling. Cell chemical biology 2018;25(11):1419-1427. e4.

[5] Zachleder V, Vítová M, Hlavová M, Moudříková Š, Mojzeš P, Heumann H et al. Stable isotope compounds-production, detection, and application. Biotechnology advances 2018;36(3):784–97.

[6] Des Rosiers C, Lloyd S, Comte B, Chatham JC. A critical perspective of the use of 13C-isotopomer analysis by GCMS and NMR as applied to cardiac metabolism. Metabolic engineering 2004;6(1):44–58.

[7] Long CP, Au J, Gonzalez JE, Antoniewicz MR. 13C metabolic flux analysis of microbial and mammalian systems is enhanced with GC-MS measurements of glycogen and RNA labeling. Metabolic engineering 2016;38:65–72.

[8] Tang YJ, Martin HG, Myers S, Rodriguez S, Baidoo EEK, Keasling JD. Advances in analysis of microbial metabolic fluxes via 13C isotopic labeling. Mass spectrometry reviews 2009;28(2):362–75.

[9] Wu L, Mashego MR, van Dam JC, Proell AM, Vinke JL, Ras C et al. Quantitative analysis of the microbial metabolome by isotope dilution mass spectrometry using uniformly 13C-labeled cell extracts as internal standards. Analytical Biochemistry 2005;336(2):164–71.

[10] Geiger T, Wisniewski JR, Cox J, Zanivan S, Kruger M, Ishihama Y et al. Use of stable isotope labeling by amino acids in cell culture as a spike-in standard in quantitative proteomics. Nature protocols 2011;6(2):147–57.

[11] Bruheim P, Kvitvang HFN, Villas-Boas SG. Stable isotope coded derivatizing reagents as internal standards in metabolite profiling. Journal of Chromatography A 2013;1296:196–203.

[12] Gaffney TE, Hammar CG, Holmstedt B, McMahon RE. Ion specific detection of internal standards labeled with stable isotopes. Analytical Chemistry 1971;43(3):307–10.

[13] Dethloff F, Bueschl C, Heumann H, Schuhmacher R, Turck CW. Partially 13C-labeled mouse tissue as reference for LC-MS based untargeted metabolomics. Analytical Biochemistry 2018;556:63–9.

[14] Rauniyar N, McClatchy DB, Yates JR. Stable isotope labeling of mammals (SILAM) for in vivo quantitative proteomic analysis. Methods 2013;61(3):260–8.

[15] Verde Arregoitia LD, D'Elía G. Classifying rodent diets for comparative research. Mammal Review 2021;51(1):51–65.

[16] Ble-Castillo JL, Aparicio-Trapala MA, Juárez-Rojop IE, Torres-Lopez JE, Mendez JD, Aguilar-Mariscal H et al. Differential effects of high-carbohydrate and high-fat diet composition on metabolic control and insulin resistance in normal rats. International journal of environmental research and public health 2012;9(5):1663–76.

[17] Grusak MA. Intrinsic stable isotope labeling of plants for nutritional investigations in humans. The Journal of Nutritional Biochemistry 1997;8(4):164–71.

[18] Soong JL, Reuss D, Pinney C, Boyack T, Haddix ML, Stewart CE et al. Design and operation of a continuous 13C and 15N labeling chamber for uniform or differential, metabolic and structural, plant isotope labeling. Journal of visualized experiments JoVE 2014(83):e51117.

[19] Xu X, Gu X, Wang Z, Shatner W, Wang Z. Progress, challenges and solutions of research on photosynthetic carbon sequestration efficiency of microalgae. Renewable and Sustainable Energy Reviews 2019;110:65–82.

[20] Satyanarayana KG, Mariano AB, Vargas JVC. A review on microalgae, a versatile source for sustainable energy and materials. Int J Energy Res 2011;35(4):291–311.

[21] Mello-Sampayo C de, Corvo ML, Mendes R, Duarte D, Lucas J, Pinto R et al. Insights on the safety of carotenogenic Chlorella vulgaris in rodents. Algal Research 2013;2(4):409–15.

[22] Nagarajan D, Varjani S, Lee D-J, Chang J-S. Sustainable aquaculture and animal feed from microalgae – Nutritive value and techno-functional components. Renewable and Sustainable Energy Reviews 2021;150:111549.

[23] Safi C, Zebib B, Merah O, Pontalier P-Y, Vaca-Garcia C. Morphology, composition, production, processing and applications of Chlorella vulgaris: A review. Renewable and Sustainable Energy Reviews 2014;35:265–78.

[24] Metting FB. Biodiversity and application of microalgae. Journal of industrial microbiology 1996;17:477–89.

[25] Ru ITK, Sung YY, Jusoh M, Wahid MEA, Nagappan T. Chlorella vulgaris: A perspective on its potential for combining high biomass with high value bioproducts. Applied Phycology 2020;1(1):2–11.

[26] Schediwy K, Trautmann A, Steinweg C, Posten C. Microalgal kinetics—a guideline for photobioreactor design and process development. Engineering in Life Sciences 2019;19(12):830–43.

[27] Coronado-Reyes JA, Salazar-Torres JA, Juarez-Campos B, Gonzalez-Hernandez JC. Chlorella vulgaris, a microalgae important to be used in Biotechnology: a review. Food Science and Technology 2020;42.

[28] Andrade CJ de, Andrade LM de. An overview on the application of genus Chlorella in biotechnological processes. J. Adv. Res. Biotechnol 2017;2:1–9.

[29] Liu J, Chen F. Biology and Industrial Applications of Chlorella: Advances and Prospects. Advances in biochemical engineering/biotechnology 2016;153:1–35.

[30] Ahmad MT, Shariff M, Md. Yusoff F, Goh YM, Banerjee S. Applications of microalga Chlorella vulgaris in aquaculture. Reviews in Aquaculture 2020;12(1):328–46.

[31] Nelson N, Ben-Shem A. The complex architecture of oxygenic photosynthesis. Nature Reviews Molecular Cell Biology 2004;5(12):971–82.

[32] Allen JF. Photosynthesis of ATP—Electrons, Proton Pumps, Rotors, and Poise. Cell 2002;110(3):273–6.

[33] Sun H, Zhao W, Mao X, Li Y, Wu T, Chen F. High-value biomass from microalgae production platforms: strategies and progress based on carbon metabolism and energy conversion. Biotechnology for Biofuels 2018;11(1):227.

[34] Tena FO, Bickel V, Steinweg C, Posten C. Continuous microalgae cultivation for wastewater treatment–Development of a process strategy during day and night. Science of The Total Environment 2024;912:169082.

[35] Perez-Garcia O, Bashan Y. Microalgal heterotrophic and mixotrophic culturing for bio-refining: from metabolic routes to techno-economics. Algal Biorefineries: Volume 2: Products and Refinery Design 2015:61–131.

[36] Lowrey J, Brooks MS, McGinn PJ. Heterotrophic and mixotrophic cultivation of microalgae for biodiesel production in agricultural wastewaters and associated challenges—a critical review. Journal of applied phycology 2015;27:1485–98.

[37] Xu L, Weathers PJ, Xiong X-R, Liu C-Z. Microalgal bioreactors: challenges and opportunities. Engineering in Life Sciences 2009;9(3):178–89.

[38] Weinold M, Kolesnikov S, Anadon LD. Quantifying the impact of performance improvements and cost reductions from 20 years of light-emitting diode manufacturing. Light-Emitting Devices, Materials, and Applications XXV 2021:76–82.

[39] Eilertsen HC, Strømholt J, Bergum J-S, Eriksen GK, Ingebrigtsen R. Mass Cultivation of Microalgae: II. A Large Species Pulsing Blue Light Concept. BioTech 2023;12(2):40.

[40] Jacobi A, Steinweg C, Sastre RR, Posten C. Advanced photobioreactor LED illumination system: scale-down approach to study microalgal growth kinetics. Engineering in Life Sciences 2012;12(6):621–30.

[41] Mink A, Schediwy K, Posten C, Nirschl H, Simonis S, Krause MJ. Comprehensive computational model for coupled fluid flow, mass transfer, and light supply in tubular photobioreactors equipped with glass sponges. Energies 2022;15(20):7671.

[42] Pruvost J, Legrand J, Legentilhomme P, Muller-Feuga A. Simulation of microalgae growth in limiting light conditions: flow effect. AIChE Journal 2002;48(5):1109–20.

[43] Bernard O. Hurdles and challenges for modelling and control of microalgae for CO2 mitigation and biofuel production. Journal of Process Control 2011;21(10):1378–89.

[44] Huesemann MH, van Wagenen J, Miller T, Chavis A, Hobbs S, Crowe B. A screening model to predict microalgae biomass growth in photobioreactors and raceway ponds. Biotechnology and bioengineering 2013;110(6):1583–94.

[45] Blanken W, Postma PR, Winter L de, Wijffels RH, Janssen M. Predicting microalgae growth. Algal Research 2016;14:28–38.

[46] Yeh Y-C, Haasdonk B, Schmid-Staiger U, Stier M, Tovar GEM. A novel model extended from the Bouguer-Lambert-Beer law can describe the non-linear absorbance of potassium dichromate solutions and microalgae suspensions. Frontiers in Bioengineering and Biotechnology 2023;11:1116735.

[47] Fernández FA, Camacho FG, Pérez JS, Sevilla JF, Grima EM. A model for light distribution and average solar irradiance inside outdoor tubular photobioreactors for the microalgal mass culture. Biotechnology and bioengineering 1997;55(5):701–14.

[48] Wágner DS, Valverde-Pérez B, Plósz BG. Light attenuation in photobioreactors and algal pigmentation under different growth conditions – Model identification and complexity assessment. Algal Research 2018;35:488–99.

[49] Naderi G, Znad H, Tade MO. Investigating and modelling of light intensity distribution inside algal photobioreactor. Chemical Engineering and Processing: Process Intensification 2017;122:530–7.

[50] Gaigalas AK, He H-J, Wang L. Measurement of Absorption and Scattering With an Integrating Sphere Detector: Application to Microalgae. Journal of Research of the National Institute of Standards and Technology 2009;114(2):69–81.

[51] Kong B, Vigil RD. Simulation of photosynthetically active radiation distribution in algal photobioreactors using a multidimensional spectral radiation model. Bioresource Technology 2014;158:141–8.

[52] Csőgör Z, Herrenbauer M, Schmidt K, Posten C. Light distribution in a novel photobioreactor–modelling for optimization. Journal of applied phycology 2001;13:325–33.

[53] Laifa R, Morchain J, Barna L, Guiraud P. A numerical framework to predict the performances of a tubular photobioreactor from operating and sunlight conditions. Algal Research 2021;60:102550.

[54] Mink A, Thäter G, Nirschl H, Krause MJ. A 3D lattice Boltzmann method for light simulation in participating media. Journal of Computational Science 2016;17:431–7.

[55] Krause MJ, Kummerländer A, Avis SJ, Kusumaatmaja H, Dapelo D, Klemens F et al. OpenLB—Open source lattice Boltzmann code. Computers & Mathematics with Applications 2021;81:258–88.

[56] Konzen, Pedro Henrique de Almeida, Guidi, Leonardo Fernandes and Thomas Richter. Quasi-random discrete ordinates method to radiative transfer equation with linear anisotropic scattering 2023:109–19.

[57] Marken E, Ssebiyonga N, Lotsberg JK, Stamnes JJ, Hamre B, Frette Ø et al. Measurement and modeling of volume scattering functions for phytoplankton from norwegian coastal waters. 0022-2402 2017.

[58] Gu W, Theau E, Anderson AW, Fletcher DF, Kavanagh JM, McClure DD. A modelling workflow for quantification of photobioreactor performance. Chemical Engineering Journal 2023;477:147032.

[59] Dauchet J, Blanco S, Cornet J-F, El Hafi M, Eymet V, Fournier R. The practice of recent radiative transfer Monte Carlo advances and its contribution to the field of

microorganisms cultivation in photobioreactors. Journal of Quantitative Spectroscopy and Radiative Transfer 2013;128:52–9.

[60] Kandilian R, Soulies A, Pruvost J, Rousseau B, Legrand J, Pilon L. Simple method for measuring the spectral absorption cross-section of microalgae. Chemical Engineering Science 2016;146:357–68.

[61] Castillo LA, Valadés-Pelayo PJ, Avila-Paredes HJ, Cabello JJ, Balbuena A. Methodology for the fast direct estimation of spectral radiative transport properties in microalgae photobioreactors. Chemical Engineering Journal 2023;458:141462.

[62] Nothelfer S, Foschum F, Kienle A. Goniometer for determination of the spectrally resolved scattering phase function of suspended particles. Review of Scientific Instruments 2019;90(8).

[63] Foschum F, Kienle A. Optimized goniometer for determination of the scattering phase function of suspended particles: simulations and measurements. Journal of biomedical optics 2013;18(8):85002.

[64] Strümpfer J, Schulten K. Excited state dynamics in photosynthetic reaction center and light harvesting complex 1. The Journal of chemical physics 2012;137(6).

[65] Sforza E, Urbani S, Bertucco A. Evaluation of maintenance energy requirements in the cultivation of Scenedesmus obliquus: effect of light intensity and regime. Journal of applied phycology 2015;27:1453–62.

[66] Pulz O, Scheibenbogen K. Photobioreactors: design and performance with respect to light energy input. Bioprocess and algae reactor technology, apoptosis 2006:123–52.

[67] Ortiz Tena F, Bickel V, Steinweg C, Posten C. Continuous microalgae cultivation for wastewater treatment – Development of a process strategy during day and night. Science of The Total Environment 2024;912:169082.

[68] Zijffers J-WF, Schippers KJ, Zheng K, Janssen M, Tramper J, Wijffels RH. Maximum photosynthetic yield of green microalgae in photobioreactors. Marine biotechnology 2010;12:708–18.

[69] Raven JA, Beardall J. Dark respiration and organic carbon loss. The physiology of microalgae 2016:129–40.

[70] Kliphuis AMJ, Janssen M, van den End EJ, Martens DE, Wijffels RH. Light respiration in Chlorella sorokiniana. Journal of applied phycology 2011;23:935–47.

[71] Stockar U von, Liu J-S. Does microbial life always feed on negative entropy? Thermodynamic analysis of microbial growth. Biochimica et Biophysica Acta (BBA) - Bioenergetics 1999;1412(3):191–211.

[72] Breuer G, Martens DE, Draaisma RB, Wijffels RH, Lamers PP. Photosynthetic efficiency and carbon partitioning in nitrogen-starved Scenedesmus obliquus. Algal Research 2015;9:254–62.

[73] Johnson X, Alric J. Central carbon metabolism and electron transport in Chlamydomonas reinhardtii: metabolic constraints for carbon partitioning between oil and starch. Eukaryotic cell 2013;12(6):776–93.

[74] Mandalam RK, Palsson B. Elemental balancing of biomass and medium composition enhances growth capacity in high-densityChlorella vulgaris cultures. Biotechnol. Bioeng. 1998;59(5):605–11.

[75] Kabo GJ, Voitkevich OV, Blokhin AV, Kohut SV, Stepurko EN, Paulechka YU. Thermodynamic properties of starch and glucose. The Journal of Chemical Thermodynamics 2013;59:87–93.

[76] Freedman B, Bagby MO. Heats of combustion of fatty esters and triglycerides. Journal of the American Oil Chemists' Society 1989;66(11):1601–5.

[77] dos Santos RR, Kunigami CN, Gomes Aranda DA, Luz Lapa Teixeira, Cláudia Maria. Assessment of triacylglycerol content in Chlorella vulgaris cultivated in a two-stage process. Biomass and Bioenergy 2016;92:55–60.

[78] Breuer G, Lamers PP, Martens DE, Draaisma RB, Wijffels RH. The impact of nitrogen starvation on the dynamics of triacylglycerol accumulation in nine microalgae strains. Bioresource Technology 2012;124:217–26.

[79] Shen P-L, Wang H-T, Pan Y-F, Meng Y-Y, Wu P-C, Xue S. Identification of Characteristic Fatty Acids to Quantify Triacylglycerols in Microalgae. Frontiers in Plant Science 2016;7:162.

[80] Alishah Aratboni H, Rafiei N, Garcia-Granados R, Alemzadeh A, Morones-Ramírez JR. Biomass and lipid induction strategies in microalgae for biofuel production and other applications. Microbial Cell Factories 2019;18:1–17.

[81] Doucha J, Lívanský K. Production of high-density Chlorella culture grown in fermenters. Journal of applied phycology 2012;24:35–43.

[82] Gorman DS, Levine RP. Cytochrome f and plastocyanin: their sequence in the photosynthetic electron transport chain of Chlamydomonas reinhardi. Proceedings of the National Academy of Sciences 1965;54(6):1665–9.

[83] Sager R, Granick S. Nutritional studies with Chlamydomonas reinhardi. Annals of the New York Academy of Sciences 1953;56(5):831–8.

[84] Hutner SH, Provasoli L, Schatz A, Haskins CP. Some Approaches to the Study of the Role of Metals in the Metabolism of Microorganisms. Proceedings of the American Philosophical Society 1950;94(2):152–70.

[85] Cheng M, Yan X, Cui Y, Han M, Wang X, Wang J et al. An eco-friendly film of pH-responsive indicators for smart packaging. Journal of Food Engineering 2022;321:110943.

[86] Rusishvili M, Grisanti L, Laporte S, Micciarelli M, Rosa M, Robbins RJ et al. Unraveling the molecular mechanisms of color expression in anthocyanins. Physical Chemistry Chemical Physics 2019;21(17):8757–66.

[87] Fernandes B, Dragone G, Abreu AP, Geada P, Teixeira J, Vicente A. Starch determination in Chlorella vulgaris—a comparison between acid and enzymatic methods. Journal of applied phycology 2012;24:1203–8.

[88] Blanken W, Cuaresma M, Wijffels RH, Janssen M. Cultivation of microalgae on artificial light comes at a cost. Algal Research 2013;2(4):333–40.

[89] Heining M, Buchholz R. Photobioreactors with internal illumination - A survey and comparison. Biotechnology journal 2015;10(8):1131–7.

[90] Jacobi A, Bucharsky EC, Schell, KG, Habisreuther P, Oberacker R, Hoffmann MJ et al. The application of transparent glass sponge for improvement of light distribution in photobioreactors. J. Bioprocess. Biotech 2012;2(01):1–8.

[91] Prieto DM, Devesa-Rey R, Rubinos DA, Diaz-Fierros F, Barral MT. Biofilm formation on river sediments under different light intensities and nutrient inputs: a flume mesocosm study. Environmental Engineering Science 2016;33(4):250–60.

[92] Xue S, Zhang Q, Wu X, Yan C, Cong W. A novel photobioreactor structure using optical fibers as inner light source to fulfill flashing light effects of microalgae. Bioresource Technology 2013;138:141–7.

[93] Posten C. Design principles of photo-bioreactors for cultivation of microalgae. Engineering in Life Sciences 2009;9(3):165–77.

[94] Degen J, Uebele A, Retze A, Schmid-Staiger U, Trösch W. A novel airlift photobioreactor with baffles for improved light utilization through the flashing light effect. Journal of Biotechnology 2001;92(2):89–94.

[95] Terry KL. Photosynthesis in modulated light: quantitative dependence of photosynthetic enhancement on flashing rate. Biotechnology and bioengineering 1986;28(7):988–95.

[96] Wang L, Wang Q, Zhao R, Tao Y, Ying K, Mao X. Novel flat-plate photobioreactor with inclined baffles and internal structure optimization to improve light regime performance. ACS Sustainable Chemistry & Engineering 2021;9(4):1550–8.

[97] Vejrazka C, Janssen M, Streefland M, Wijffels RH. Photosynthetic efficiency of Chlamydomonas reinhardtii in attenuated, flashing light. Biotechnology and bioengineering 2012;109(10):2567–74.

[98] Sánchez-Luna L, Converti A, Tonini G, Sato S, Carvalho JC. Continuous and pulse feedings of urea as a nitrogen source in fed-batch cultivation of Spirulina platensis. Aquacultural Engineering 2004;31:237–45.

[99] Rai U, Deshar G, Rai B, Bhattarai K, Dhakal RP, Rai SK. Isolation and Culture Condition Optimization of Chlorella vulgaris. Nepal Journal of Science and Technology 2014;14(2):43–8.

[100] Coronado-Reyes JA, Acosta-Ramírez E, Martínez-Olguín MV, González-Hernández JC. Antioxidant activity and kinetic characterization of chlorella vulgaris growth under flask-level photoheterotrophic growth conditions. Molecules (Basel, Switzerland) 2022;27(19):6346.

[101] Ndiaye M, Gadoin E, Gentric C. CO2 gas–liquid mass transfer and kLa estimation: Numerical investigation in the context of airlift photobioreactor scale-up. Chemical Engineering research and design 2018;133:90–102.

[102] Uyar B, Ali MD, Uyar GEO. Design parameters comparison of bubble column, airlift and stirred tank photobioreactors for microalgae production. Bioprocess and Biosystems Engineering 2024;47(2):195–209.

[103] Gao X, Kong B, Vigil RD. Characteristic time scales of mixing, mass transfer and biomass growth in a Taylor vortex algal photobioreactor. Bioresource Technology 2015;198:283–91.

[104] Xing W, Yin M, Lv Q, Hu Y, Liu C, Zhang J. Oxygen solubility, diffusion coefficient, and solution viscosity. In: Rotating electrode methods and oxygen reduction electrocatalysts: Elsevier; 2014, p. 1–31.

[105] Cadogan SP, Maitland GC, Trusler JM. Diffusion coefficients of CO2 and N2 in water at temperatures between 298.15 K and 423.15 K at pressures up to 45 MPa. Journal of Chemical & Engineering Data 2014;59(2):519–25.

[106] Wu Z, Tan P, Chen B, Cai W, Chen M, Xu X et al. Dynamic modeling and operation strategy of an NG-fueled SOFC-WGS-TSA-PEMFC hybrid energy conversion system for fuel cell vehicle by using MATLAB/SIMULINK. Energy 2019;175:567–79.

[107] Kong B, Vigil RD. Light-limited continuous culture of Chlorella vulgaris in a Taylor vortex reactor. Environmental Progress & Sustainable Energy 2013;32(4):884–90.

[108] Laws EA. Photosynthetic quotients, new production and net community production in the open ocean. Deep Sea Research Part A. Oceanographic Research Papers 1991;38(1):143–67.

[109] Dillschneider R, Steinweg C, Rosello-Sastre R, Posten C. Biofuels from microalgae: photoconversion efficiency during lipid accumulation. Bioresource Technology 2013;142:647–54.

[110] Tredici MR. Photobiology of microalgae mass cultures: understanding the tools for the next green revolution. Biofuels 2010;1(1):143–62.

[111] Trautmann AM. Prozessstrategien zur Beeinflussung der makromolekularen Zellzusammensetzung photoautotropher Mikroorganismen bei Kultivierungen im Labor- und Pilotmaßstab: Karlsruhe; 2018.

[112] Perner-Nochta I, Posten C. Simulations of light intensity variation in photobioreactors. Journal of Biotechnology 2007;131(3):276–85.

[113] Ahmad FN, Sazali N, Shalbi S, Ngadiman NHA, Othman MHD. Oxygen separation process using ceramic-based membrane: A review. Journal of Advanced Research in Fluid Mechanics and Thermal Sciences 2019;62(1):1–9.

[114] Griffiths MJ, van Hille RP, Harrison STL. The effect of nitrogen limitation on lipid productivity and cell composition in Chlorella vulgaris. Applied microbiology and biotechnology 2014;98(5):2345–56.

[115] Caperon J, Meyer J (eds.). Nitrogen-limited growth of marine phytoplankton—II. Uptake kinetics and their role in nutrient limited growth of phytoplankton: Elsevier; 1972.

[116] Hu Z, Duan S, Xu N, Mulholland MR. Growth and nitrogen uptake kinetics in cultured Prorocentrum donghaiense. PloS one 2014;9(4):e94030.

[117] Mairet F, Bernard O, Lacour T, Sciandra A. Modelling microalgae growth in nitrogen limited photobiorector for estimating biomass, carbohydrate and neutral lipid productivities. IFAC Proceedings Volumes 2011;44(1):10591–6.

[118] Tam N, Wong YS. Effect of ammonia concentrations on growth of Chlorella vulgaris and nitrogen removal from media. Bioresource Technology 1996;57(1):45–50.

[119] Schmollinger S, Mühlhaus T, Boyle NR, Blaby IK, Casero D, Mettler T et al. Nitrogen-sparing mechanisms in Chlamydomonas affect the transcriptome, the proteome, and photosynthetic metabolism. The Plant Cell 2014;26(4):1410–35.

[120] Dragone G, Fernandes BD, Abreu AP, Vicente AA, Teixeira JA. Nutrient limitation as a strategy for increasing starch accumulation in microalgae. Applied energy 2011;88(10):3331–5.

[121] Kolber Z, Zehr J, Falkowski P. Effects of growth irradiance and nitrogen limitation on photosynthetic energy conversion in photosystem II. Plant physiology 1988;88(3):923–9.

[122] Lemesle V, Mailleret L. A mechanistic investigation of the algae growth “Droop” model. Acta biotheoretica 2008;56(1-2):87–102.

[123] Liu F, Gaul L, Giometto A, Wu M. A high throughput array microhabitat platform reveals how light and nitrogen colimit the growth of algal cells. Scientific Reports 2024;14(1):9860.

[124] Zhu S, Huang W, Xu J, Wang Z, Xu J, Yuan Z. Metabolic changes of starch and lipid triggered by nitrogen starvation in the microalga Chlorella zofingiensis. Bioresource Technology 2014;152:292–8.

[125] Luzi G, McHardy C. Modeling and simulation of photobioreactors with computational fluid dynamics—a comprehensive review. Energies 2022;15(11):3966.

[126] Lequime M, Zerrad M, Deumié C, Amra C. A goniometric light scattering instrument with high-resolution imaging. Optics Communications 2009;282(7):1265–73.

[127] McHardy C, Horneber T, Rauh C. New lattice Boltzmann method for the simulation of three-dimensional radiation transfer in turbid media. Optics express 2016;24(15):16999–7017.

[128] Henyey LG, Greenstein JL. Diffuse radiation in the galaxy. Astrophysical Journal, vol. 93, p. 70-83 (1941). 1941;93:70–83.

[129] Song Y, Nakath D, She M, Köser K. Optical imaging and image restoration techniques for deep ocean mapping: a comprehensive survey. PFG–Journal of Photogrammetry, Remote Sensing and Geoinformation Science 2022;90(3):243–67.

[130] Ehlers K, Moosmüller H. Small and large particle limits of the asymmetry parameter for homogeneous, spherical particles. Aerosol Science and Technology 2023;57(5):425–33.

Appendix

A1 Supervised student projects

Holger Dittmann:

Einfluss verschiedener Kultivierungsparameter auf das Sedimentations- und Flockungsverhalten von *Chlorella vulgaris*, Bachelor Thesis (2017)

Manuel Walter:

Charakterisierung von Licht und Durchmischung im Algfine-Photobioreaktor unter Verwendung verschiedener Begasungsrohre, Bachelor Thesis (2017)

Manuel Müller: Optimierung der Lichtbedingungen in der Wachstumsphase von *Chlorella vulgaris* H14 in Batch-Kultivierungen, Bachelor Thesis (2017)

Tim Ballweg: Optimierung der Stärkeproduktion in Kultivierungen von *Chlorella vulgaris* H14, Bachelor Thesis (2017)

Alejandro Aurelio Castillo Salvador:

Design of a measuring cell for the characterization of wavelength specific scattering and absorption coefficients, Bachelor Thesis (2018)

Nikolaos Nissiotis:

Optimierung der Wachstumsphase von *Chlorella vulgaris* H14 durch Nährstoff-Fütterung; Bachelor Thesis (2018)

David S. García:

Optimization of the starch accumulation in *Chlorella vulgaris* H14 by nutrient depletion and micro-feeding. Master Thesis (2018)

Paulius Trumpickas: Optimisation of illumination and growth medium properties in cultivations of *Chlorella vulgaris* H14, Internship (2018)

Marcel Klingler:

Einfluss von Photoadaption auf die Lichtkinetik in Batch-Kultivierungen, Bachelor Thesis (2019)

Julia Schmidt:

Automation of a photobioreactor with closed gas loop, Bachelor Thesis (2019)

Vera J. Schnepp:

Untersuchung der Photokonversionseffizienz in Abhängigkeit der Nährstoffaufnahmerate, Bachelor Thesis (2019)

A2 MathScript codes for process control

The automated control was executed through implementation in LabView 2018, utilizing three interplaying custom controllers written in MathScript codes. The scripts interact dynamically to maintain optimal cultivation conditions. The main tasks of the scripts are summarized below, and the code used during the proof-of-concept is provided.

The first MathScript, ‘transmission_OD’, only performed calculation tasks and adapted the intensity of the light source for the online transmission measurement to calculate an online OD based on calibration settings from the user interface. Photoconversion efficiency was calculated as a measure of the system’s performance. The script calculated the biomass concentration from offline OD measurements and forwarded this biomass concentration to other controllers for further processing.

The MathScript 'nutrients_H2' calculated biomass concentration, specific growth rate and N-NH_4^+-concentration from the measured H_2 flow or, alternatively, from offline OD measurements as manual input parameters analogously to the calculation in ‘transmission_OD’. The calculated values were forwarded to the ‘light_BSZ’ controller and used directly to control NH_4^+- feed and CO_2 feed. The feed calculations were substantially governed by the cultivation strategy, particularly, the cultivation phase (see chapter 3.4).

The MathScript ‘light_BSZ’ controlled the light intensity in the PBR proportional to biomass concentration, as calculated in the ‘nutrients_H2’ controller. Exceptions were applied for cultivation phase IV/4, where the light intensity remained constant. Minimum currents were set to avoid light limitation after inoculation or dilution in repeated batch. Additionally, this script restricted light intensity decreases or stepwise increases and ensured long-term stability of the PEM by purging and regulating H_2 pressure through electrolysis control.

```
Name= 'transmission_OD';
%% setting input variables for the MathScript 'nutrients_H2'
%   from manual input parameters, measurements and other controllers
OT_high_low_in=Doi1         % intensity setting of the led for online transmission high/low
OT_LED=Ai2                  % measured online transmission (OT)
buttonpressed=Aoi3          % count of the number of OD measurements
cX_H2_in=Vii1               % biomass concentration calculated from H2 flow and initial inputs
rX_H2_in=Vii2               % growth rate used for calculation, based on H2 flow
cX_OD_in=Vii3               % biomass concentration calculated from offline OD-measurement
rX_OD_in=Vii4               % growth rate used for calculation, based on either OD
PFDout=Vii5                 % PFD-setting from 'light_BSZ'
currentODin=Vii6            % offline OD value of the most recent measurement
lasttime=Vii7               % process time at the last run of this MathScript
switch_cX=Vii8              % regulates, if control is based in cX calculations from H2 flow (1) or OD (2)
sampletime=Vii9             % process time of the most recent sampling for OD measurement
cX_sample_in=Vii10          % biomass concentration from most recent offline OD measurement
%   manually adjustable variables
value_A=A                   % variable for OT to OD calibration at low intensity, OT_high_low_in=0
value_B=B                   % variable for OT to OD calibration at low intensity, OT_high_low_in=0
value_C=C                   % variable for OT to OD calibration at high intensity, OT_high_low_in=1
value_D=D                   % variable for OT to OD calibration at high intensity, OT_high_low_in=1
switchhighlow=E             % switching led to high/low (1: low, 2: high, 3: hourly change)
offlineOD=F                 % input for od from a sample
offline_time=G              % time the sample was taken
OD_to_BTM=H                 % calibration factor of OD to BTM used for calculation of biomass concentration
```

```
rX_man=I                    % manual setting of growth rate to overwrite rX_OD
%  unused variables in this MathScript, but definition of output required for functionality
Aoo2=Aoi2;
Aoo3=Aoi3;
Aoo4=Aoi4;
Aoo5=Aoi5;
Vio8=Vii8;
Vio1=Vii1;
Vio2=Vii2;
Vio11=Vii11;
Vio12=Vii12;
Vio13=Vii13;
Doo2=Doi2;
ArrayOUT=ArrayIN;

%% setting mode of cX calculation being based on either H2 flow or OD measurement
if switch_cX==1             % set control to be based on H2 flow
    cX_used=cX_H2_in
    rX_used=rX_H2_in
else
    cX_used=cX_OD_in        % set control to be based on offline OD measurement
    rX_used=rX_OD_in
end

%% Calculation of biomass concentration from online transmission (OT) measurement
%  with calibration values from user interface for low (OT_high_low_in=0) and
%  high intensity (OT_high_low_in=1) with OD=(1/OT-B)/A and OD=(1/OT-D)/C
%  in the transition phase between low and high, calibration values switched hourly
if OT_high_low_in==1
    OD_from_OT=(1/OT_LED-value_D)/value_C
elseif OT_high_low_in==0
    OD_from_OT=(1/OT_LED-value_B)/value_A
end
if switchhighlow==1
    OT_high_low_out=0
elseif switchhighlow==2
    OT_high_low_out=1
elseif switchhighlow==3
    ODPT=PT
    while ODPT>2
        ODPT=ODPT-2
    end
    if ODPT >1
        OT_high_low_out=1
    else
        OT_high_low_out=0
    end
end

%% calculation of specific light supply rate setting, unit: µmol/g/s
%  with V_PBR=27 L, illumination area: 0.02458*37 m^2
light_to_DW=PFDout*0.02458*37/(cX_used*27)

%% calculation of the photoconversion efficiency (PCE)
%  with PCE=(µ*deltaH_X*100%)/(Light/BTM*E_photon*(3600*24 s/d))
PCE=(rX_used*20*100)/(light_to_DW*0.0002105*3600*24)
lasttime=PT

%% implementation of the manual input from offline OD measurement
%  biomass concentration is calculated thruogh OD->BTM conversion factor
%  sampling time is saved to allow calculating the cX using rX calculated
%  from the last two OD measurements or from the manual rX setting/reset
%  in the user interface until calculation mode is changed to H2
Button1Name='enter new OD'
if Button1i==1 & buttonpressed==0 & (offlineOD>currentODin | offlineOD<currentODin) &
(offline_time>sampletime | offline_time<sampletime)
    rX_OD_out=rX_man
    currentODout=offlineOD
    cX_sample_out=OD_to_BTM*currentODout
    cX_OD_out=cX_sample_out*exp(rX_OD_out*(PT-offline_time)/24)
    sampletime=offline_time
    buttonpressed=buttonpressed+1
    Button1o=0
elseif Button1i==1 & (offlineOD>currentODin | offlineOD<currentODin) & (offline_time>sampletime |
offline_time<sampletime)
    rX=(log(offlineOD/currentODin)/((offline_time-sampletime)/24))
    if is_inf(rX)==1 | is_nan(rX)==1
        rX_OD_out=rX_man
    else
        rX_OD_out=(log(offlineOD/currentODin)/((offline_time-sampletime)/24))
    end
    currentODout=offlineOD
    cX_sample_out=OD_to_BTM*currentODout
    cX_OD_out=cX_sample_out*exp(rX_OD_out*(PT-offline_time)/24)
    sampletime=offline_time
    buttonpressed=buttonpressed+1
    Button1o=0
else
```

```
    if Button1i==1
        Button1o=0
    else
        Button1o=Button1i
    end
    rX_OD_out=rX_OD_in
    cX_OD_out=cX_sample_in*exp(rX_OD_out*(PT-sampletime)/24)
    cX_sample_out=cX_sample_in
    currentODout=currentODin
end
Button2Name='set µ to I'
if Button2i==1
    rX_OD_out=rX_man
end
Button2o=Button2i

%% redefining output variables used in calculation
Aio1=Vii13;   % pH value averaged over 30 min outside MathScrpts to be forwarded to 'nutrients_H2'
Doo1=OT_high_low_out
Aoo1=light_to_DW
Aoo2=PCE
Aoo3=buttonpressed
Vio6=currentODout
Vio3=cX_OD_out
Vio4=rX_OD_out
Vio5=PFDout
Vio7=lasttime
Vio9=sampletime
Vio10=cX_sample_out
Vio11=cX_used
wo=OD_from_OT
xo=light_to_DW
yo=cX_OD_out
zo=rX_OD_out

Name= 'nutrients_H2';
%% setting input variables for the MathScript 'nutrients_H2'
%   from manual input parameters, measurements and other controllers
flowH2in=Ai1                % H2 flow measured
pH=Ai2                      % pH value measurement averaged over 30 minutes forwarded from 'transmission_OD'
pO2=Ai3           % pO2 measured in the PBR
exp_feed=Aoi1       % feed flow proportional to biomass, if biomass growth was exponential
feed_NH4=Aoi3               % nitrogen feed as NH4+ solution
pO2max=Aoi5         % upper boundary of pO2 from light_BSZ
BSZon=Doi1          % state of the PEM (ON/OFF)
averagingtime=Vii1      % averaging time for avg H2 flow (time of two PEM on/off cycles)
flowH2avg_in=Vii2           % capped and nonnegative H2 flow for further calculations
cX_H2_in=Vii3       % biomass concentration calculated from H2 flow and initial inputs
rX_H2_in=Vii4               % growth rate used for calculation, based on H2 flow
enter_phase_4=Vii5      % saves whether phase 4 (nitrogen depletion phase)
comp_feed_out=Vii6      % calculated feed deficit in phase 4
switch_cX=Vii7              % regulates, if control is based in cX calculations from H2 flow (1) or OD (2)
rX_OD_in=Vii8               % growth rate used for calculation, based on either OD
cN_in=Vii9          % nitrogen concentration in medium dissolved as NH4+
cN_backup=Vii10       % nitrogen concentration in medium
lasttime=Vii11;       % process time at the last run of 'transmission_OD'
cX_OD_in=Vii12        % biomass concentration calculated from offline OD-measurement
PFD=Vii13                   % incident Photon Flux Density the culture is exposed to
endtime_phase_4=Wi          % process time when compensation feed was started after limitation in phase 4
cX_Phase4=Xi        % biomass concentration starting phase 4
starttime_Phase4=Yi     % process time starting phase 4
%   manually adjustable variables
flowH2reset=A               % resets the average H2 flow an expected value to allow initial calculations
feed_Phase4=B       % stable NH4+ feeding rate feed rate in cultivation phase 4
manual_Phase=C        % entering/exiting cultivation phase 4 (nitrogen depletion phase)
manualCO2=D         % setting a manual CO2 flow, used for initial CO2 equilibration
minCO2_controlling=E        % turning on/off min CO2 control
cN_0=F            % nitrogen concentration in medium dissolved as NH4+ at begin of cultivation
cN_feed=H          % nitrogen concentration dissolved as NH4+ in the nitrogen feed solution
cN_reset=I          % reset cN in the PBR based on measurement or calculation for manual pulse feed
%   unused variables in this MathScript, but definition of output required for functionality
Aoo4=Aoi4;
Aoo5=Aoi5;
Doo1=Doi1;
Doo2=Doi2;
Vio7=Vii7;
Vio8=Vii8;
Vio12=Vii12;
Vio13=Vii13;

%% setting mode of cX calculation being based on either H2 flow or OD measurement
if switch_cX==1             % set control to be based on H2 flow
    cX_used=cX_H2_in
    rX_used=rX_H2_in
else
    cX_used=cX_OD_in        % set control to be based on offline OD measurement
    rX_used=rX_OD_in
end
```

```
%% H2 flow calculation after data cleansing
%  initializing vectors for assessment of indices of PEM adjustment
BSZoffIndexVector=0;
BSZonIndexVector=0;
%  save indices of PEM switching (ON/OFF) derived from ArrayIN (measured PEM voltage) to
%  BSZonIndexVector and BSZoffIndexVector after eliminating insufficient voltage buildup
for i=6:1:(length(ArrayIN)-6)
    if ArrayIN(i)==0 & ArrayIN(i+1)>0 & ArrayIN(i+2)>0 & ArrayIN(i+3)>0 & ArrayIN(i+4)>0 & ArrayIN(i+5)>0
     if BSZoffIndexVector(1)==0 && BSZoffIndexVector(end)==0
        BSZoffIndexVector=i;
     else
       BSZoffIndexVector=[BSZoffIndexVector;i];
     end
  end
    if ArrayIN(i+1)==0 & ArrayIN(i+2)==0 & ArrayIN(i+3)==0 & ArrayIN(i+4)==0 & ArrayIN(i+5)==0 &
    ArrayIN(i)>0
     if BSZonIndexVector(1)==0 && BSZonIndexVector(end)==0
       BSZonIndexVector=i;
     else
       BSZonIndexVector=[BSZonIndexVector;i];
     end
  end
    if ArrayIN==0 | (length(BSZonIndexVector)>2 & length(BSZoffIndexVector)>2)
  break;                  % stops the for loop as only two ON/OFF periods are required for calculation
    end
end
%  averaging the H2 flow during PEM operation over the last complete operation period
%  to allow for capping the H2 flow with the latest performance data of the PEM
%  (if PEM ON: from 2nd last PEM start to last off, if PEM on: last operation period)
if ArrayIN(1)>0 & length(BSZonIndexVector)>=2 & BSZoffIndexVector(1)>0
    flowH2avgON=mean(ArrayIN((BSZoffIndexVector(1)+1):(BSZonIndexVector(2))))
elseif ArrayIN(1)==0 & BSZonIndexVector(1)>0 & BSZoffIndexVector(1)>0
    flowH2avgON=mean(ArrayIN((BSZoffIndexVector(1)+1):(BSZonIndexVector(1))))
else
    flowH2avgON=50      % preset: 50 L/min (previous tests), if insufficient operation periods
end
if is_nan(flowH2avgON)==1
    flowH2avgON=50
end
%  data cleansing of hydrogen flow:
%  - reject negative H2 flows and PEM off periods
%  - cap flow above max depletion by PEM to allow reasonable calculations while purging the PEM
if flowH2in<0 | BSZon==0
    flowH2in=0
end
if flowH2in>60
    flowH2in=flowH2avgON
end
%  ensuring one value per second in ArrayOUT to use index as seconds in further calculations
if (floor(PT*3600)>floor(lasttime*3600))
    ArrayOUT(1:10000)=[flowH2in,ArrayIN(1:9999)]
else
    ArrayOUT=ArrayIN
end
%  calculation of the mean of H2flow in the detected interval of ON,OFF,ON,OFF PEM phases or
%  if no H2avg can be obtained yet, preset value is applied
if length(BSZonIndexVector)>=2 & BSZonIndexVector~=0
  StartH2avgIndex=BSZonIndexVector(1)+1;
  if length(BSZonIndexVector)==2
    StoppH2avgIndex=BSZonIndexVector(2);
  else
    StoppH2avgIndex=BSZonIndexVector(3);
  end
  averagingtime_seconds_out=StoppH2avgIndex-StartH2avgIndex;
    flowH2avg=mean(ArrayIN(StartH2avgIndex:StoppH2avgIndex))
else
    averagingtime_seconds_out=0;
    StartH2avgIndex=0;
    StoppH2avgIndex=0;
    flowH2avg=flowH2reset
end
averagingtime=averagingtime_seconds_out/3600 % unit conversion to h

%% reset of averaged H2 flow and biomass concentration based on data manually adjusted on the user surface
Button1Name='Reset avgH2,avgtime,cX(H2)';
if Button1i==1
    ArrayOUT(1:10000)=0
    cX_H2_in=cX_OD_in
    averagingtime=0
    Button1o=0
else
    Button1o=Button1i
end

%% calculation of the biomass concentration
%  being initially defined by the offline OD value
```

```
if PT==0
    cX_H2_in=cX_OD_in
end

%   calculation of the biomass concentration based on biomass formation since the last run of the MathScript
%   alpha correlates generated biomass to cosumed H2 volume, V_PBR=27 L, other numbers for unit conversion
alpha=0.53 % unit: gX/L_H2,for biomass with partial STA accumulation, low PQ
delta_cX_per_day=flowH2avg*alpha*24*60/(1000*27)
rX_H2_out=flowH2avg*alpha*24*60/1000/(cX_H2_in*27);
if is_nan(rX_H2_out)==1
    cX_H2_in=cX_OD_in
end
cX_H2_out=cX_H2_in*exp(rX_H2_out*(PT-lasttime)/24)
%   setting CO2 flow proportional to PEM's oxygen consumption (0.5*H2flow) for least pressure fluctuation
if BSZon==1
    flowCO2out=0.5*flowH2in
else
    flowCO2out=0
end

%   CO2-feed adjustments as:
%   - pH regulation backup
%   - deadlock prevention before PEM-operation:
%   CO2 feed for PCE=1% for active biomass composition for 27 L culture, 02458*37 m^2 illumination area
%   molar volume of CO2 as ideal gas 22.4 L/mol for 3 min every hour, if manual activation through user
%   interface
%   155 mL/min at pH>7.6, setting highest flow of installed mass flow control to reduce pH
%   with delta_cX_per_day=(PCE*deltaHx*(3600*24)s/day*PFD*A_illuminated)/(V_algfine*deltaE_ph*100%)
if pH>7.6
    flowCO2out=155
end
%   manual CO2 feed to set conditions for repeated batch
if manualCO2>(-1)
    flowCO2out=manualCO2    % the desired CO2 flow can be set in D on the user interface
end
minimal_delta_cX=(1*0.0002105*3600*24*PFD*0.02458*37)/(27*20*100)
pPT=PT
while pPT>1.05
    pPT=pPT-1
end
if minCO2_controlling==1 & (delta_cX_per_day<minimal_delta_cX) & pPT>1
    flowCO2out=minimal_delta_cX*22.4*1000*27/(23.7*60)
end
% reset opportunity for NH4+ concentration to measured value by user interface
comp_feed_AO=0
Button2Name='reset cN to I'
if Button2i==1
    cN_in=cN_reset
    Button2o=0
else
    Button2o=Button2i
end

%% nitrogen concentration and feeding medium using eN,X=0.0695 during different phases of cultivation
% calculation of nitrogen concentration in medium as N in NH4+ and feed of NH4+ solution
% Phase 3: during growth proportional feed
cN_out=cN_in-(cX_used-(cX_used/(exp(rX_used*(PT-lasttime)/24))))*0.0695+feed_NH4*cN_feed/(27*1000)*(PT-
lasttime)

% if errors occur and cN is computed as NAN, use backup
if is_nan(cN_out)==1 | is_inf(cN_out)==1
    if is_nan(cN_backup)==1 | is_inf(cN_backup)==1
        cN_out=I
    else
        cN_out=cN_backup
    end
else
    cN_backup=cN_out
end
enter_phase_4=0             % status of phase 4, when active reset to 1
compensationtime=0.8        % duration of feeding the NH4+ to restore N in biomass after phase 4, unit: h

% Phase 1 (no feed)
if cN_in>=0.5*cN_0 & manual_Phase < 3
    cNneeded=0
    starttime_Phase4=0
    comp_feed_out=0
    feed_NH4=cNneeded*27/(cN_feed*(PT-lasttime))*1000

% Phase 2 (feed slows down nitrogen runout for smooth transition to 3)
% theoretical minimum concentration to avoid limitations: cN=0.00084 g/L
elseif cN_in>=0.00084 & manual_Phase < 3
    cNneeded=(cX_used-(cX_used/(exp(rX_used*(PT-lasttime)/24))))*0.0695*0.00084/cN_in
    starttime_Phase4=0
    comp_feed_out=0
    feed_NH4=cNneeded*27/(cN_feed*(PT-lasttime))*1000
% Phase 4 (constant feed according to manual setting on user interface)
elseif manual_Phase==4
```

```
    enter_phase_4=1
    if starttime_Phase4==0
        starttime_Phase4=PT
        cX_Phase4=cX_used
    end
    endtime_phase_4=PT
    feed_NH4=feed_Phase4
    comp_feed_out=(((cX_used-cX_Phase4)*27*0.0695/(cN_feed))*1000-feed_NH4*(PT-
    starttime_Phase4))/compensationtime
% Compensation phase (4->3)
elseif manual_Phase==3 & (endtime_phase_4+compensationtime)>PT
    feed_NH4=0
    cNneeded=0
    starttime_Phase4=0
    comp_feed_AO=comp_feed_out
% Phase 3 (feeding proportional to biomass)
else
    cNneeded=(cX_used*exp(rX_used*(PT-lasttime)/24)-cX_used)*0.0695
    feed_NH4=(cX_used*exp(rX_used*(1/3600)/24)-cX_used)*0.0695*27*1000/(cN_feed*(1/3600))
    starttime_Phase4=0
    comp_feed_out=0
end
% feed calculation as if we were in Phase 3, only for comparision and data evaluation
exp_feed=(cX_used*exp(rX_used*(PT-lasttime)/24)-cX_used)*0.0695*27*1000/(cN_feed*(PT-lasttime))
% circumvent negative feed upon previous biomass overprediction, so theoretical degradation
if feed_NH4<0
    feed_NH4=0
end

%% redefining output variables used in calculation
Aoo1=exp_feed
Aoo2=flowCO2out
Aoo3=feed_NH4
Aoo4=comp_feed_AO
Vio1=averagingtime
Vio2=flowH2avg
Vio3=cX_H2_out
Vio4=rX_H2_out
Vio5=enter_phase_4
Vio6=comp_feed_out
Vio9=cN_out
Vio10=cN_backup
Vio11=PT
wo=endtime_phase_4
xo=cX_Phase4
yo=starttime_Phase4
zo=comp_feed_out

Name= 'light_BSZ';
%% setting input variables for the MathScript 'nutrients_H2'
%   from manual input parameters, measurements and other controllers
BSZin=Doi1                  % PEM status: on/off
purgevalve_in=Doi2          % status of purge valve: open/close
voltageBSZin=Ai1            % PEM voltage measured
pO2 =Ai2                    % pO2 measured in the PBR
rf_in=Ai3                   % residual humidity of the H2 flow measured before PEM
currentLEDin=Aoi2           % LED current setting, sum of 3 devices (2 automated, 1 manually adjusted)
pO2_min=A                   % pO2 at which the PEM will be turned off
pO2_max=B                   % pO2 at which the PEM will be turned on
switch_cX=C                 % regulates, if control is based in cX calculations from H2 flow (1) or OD (2)
light_to_DW=D               % specific light supply rate setting, unit: µmol/g/s
phase_4_entered=Vii2        % checks whether phase 4 is entered (given by 'nutrients_H2')
cX_OD_in=Vii3               % biomass concentration calculated from offline OD-measurement
rX_OD_in=Vii4               % growth rate used for calculation, based on OD
cX_H2_in=Vii5               % biomass concentration calculated from H2 flow and initial inputs
rX_H2_in=Vii6               % growth rate used for calculation, based on H2 flow
BSZpressure=Vii9            % pressure measured before PEM in the H2 gas line, funneled in virtual variable
PFDin=Vii10                 % PFD proportional to currentLEDin calibration factor 0.0257 A/(µmol/m^2/s)
purgealwayson=G             % set in G on the user interface, 1 = open the purge valve of the PEM's H2 line
dilution_on=H               % default: no decrease in PFD allowed, 4 = lowering light intensity allowed
mincurrent=E                % minimum current setting PFD to avoid light limitation for <<cX, 0,26 A
manualcurrent=F             % current of 3rd device for LEDs, which is not automated but manually set

% unused variables in this MathScript, but definition of output required for functionality
Aoo3=Aoi3;
Aoo5=Aoi5;
Vio1=Vii1;
Vio2=Vii2;
Vio3=Vii3
Vio4=Vii4
Vio5=Vii5
Vio6=Vii6
Vio11=Vii11
Vio12=Vii12
Vio13=Vii13;
ArrayOUT=ArrayIN;
Button1Name='Not in use';
Button1o=Button1i;
```

```
Button2Name='N/A';
Button2o=Button2i;

%% control of PEM operation dependent on pO2
%   PEM off, if PEM on and pO2 < pO2_min; PEM stays on, if PEM on and pO2 >= pO2_min
if BSZin==1 & pO2 <pO2_min
    BSZout=0
elseif BSZin==1 & pO2 >=pO2_min
    BSZout=1
end
%   PEM on, if PEM off and pO2 > pO2_max; PEM stays off, if PEM off and pO2 =< pO2_max
if BSZin==0 & pO2 >pO2_max
    BSZout=1
elseif BSZin==0 & pO2 <=pO2_max
    BSZout=0
end

%% control of electrolysis cell operation dependent on PEM operation and H2 pressure before PEM
if BSZout==1 & BSZpressure<450
    currentEZout=4
else
    currentEZout=0
end

%% adaptions of PEM control and purging for safety and durability of equipment
%   protection of PEM for failures in voltage buildup
if BSZin==1 & voltageBSZin<6.5
    BSZout=0
end

%% control of purging with H2: purge valve open (=1) and electrolysis cell on (=4), if:
%   - PEM voltage < 7.0 V
%   - humidity of H2 > 15 %
%   - last purging was longer ago than 5 h, purge for 10 s (=0.003 h)
%   - releasing remaining pressure after PEM operation
%   - continuous purging to remove water from PEM manually activated through user interface
%   purge valve closed in all other cases
pPT=PT
while pPT>5.003
    pPT=pPT-5
end
if BSZout==1 & voltageBSZin<7.0
    purgevalve=1
    currentEZout=4
elseif rf_in>15
    purgevalve=1
    currentEZout=4
elseif pPT>5
    BSZout=0
    purgevalve=1
    currentEZout=4
else
    purgevalve=0
end
if BSZout==0 & BSZpressure>0
purgevalve=1
end
if purgealwayson==1
    purgevalve=1
    currentEZout=4
end

%% setting mode of cX calculation being based on either H2 flow or OD measurement
if switch_cX==1             % set control to be based on H2 flow
    cX_used=cX_H2_in
    rX_used=rX_H2_in
else
    cX_used=cX_OD_in        % set control to be based on offline OD measurement
    rX_used=rX_OD_in
end

%% control of current for light control
%   currentneeded: the sum of all power devices for light supply
%   calibration factor 0.0257 A/(µmol/m^2/s), V_PBR=27 L, illumination area: 0.02458*37 m^2
currentneeded=light_to_DW*0.0257*27*cX_used/(0.02458*37);
%   adjustments of currentneeded compared to the current calculated proportional to cX
%   - circumvent decrease in light intensity
%   - turn light on at start of cultivation using mincurrent, default: 0,26 A, ~10 µmol/m^2/s
%   - avoid stepwise increase of light intensity in case of underprediction by H2 compared to
%   offline OD measurement by limiting the increase to 1.5*rX
if currentneeded<PFDin*0.0257
    currentneeded=PFDin*0.0257
elseif currentneeded<mincurrent
    currentneeded=mincurrent
end
if PT~=0 & currentneeded>PFDin*0.0257*exp(rX_used/24*(PT-Yi)*1.5)
    currentneeded=PFDin*0.0257*exp(rX_used/24*(PT-Yi)*1.5)
end
```

```
% adjustments of automated light control to setting of manual 3rd power device (each 10 A)
automaticcurrent=currentneeded-manualcurrent
if automaticcurrent>20
    automaticcurrent=20
    currentneeded=automaticcurrent+manualcurrent;
end
currentLEDout=automaticcurrent
PFDout=currentneeded/0.0257;
%   adjustments of light control for cultivation phase 4 and dilution for repeated batch
%   - phase 4: the light intensity is kept constant
%   - dilution_on=4: only exception for decreasing the light intensity
if phase_4_entered==1
    if switch_cX==2
        currentLEDout=currentLEDin
        PFDout=PFDin
    end
    if dilution_on==4
        if (light_to_DW*0.0257*28*cX_used/(0.02458*37))>0.26
            Aoo2=light_to_DW*0.0257*28*cX_used/(0.02458*37)
        else
            Aoo2=0.26
        end
        PFDout=Aoo2/0.0257;
    end
end

%% redefining output variables used in calculation
Doo1=BSZout
Aoo1=currentEZout
Aoo4=pO2_max
Doo2=purgevalve
Vio7=switch_cX
Aoo2=currentLEDout
Vio8=switch_cX
Vio9=BSZpressure
Vio10=PFDout
wo=currentLEDout
xo=PFDout
yo=PT
zo=voltageBSZin
```

A3 Online transmission in the compact photobioreactor

Automation was initially intended to build upon the online transmission. The biomass concentration in the compact photobioreactor and the transmission of the culture in the external loop correlated reciprocally linear in the first data set. The linearity could not be confirmed for combined data sets recorded in different cultivations. Longer periods of cultivation e.g. varying light or nutrient conditions associated with different physiological states of the cells demanded recalibrations. The measuring signal was also fluctuating on a longer time scale. This lack of reliability in the correlation of online transmission and biomass concentration banned the online transmission from the automation of photobioreactor control.

The online transmission was still used to justify the slope of growth curves in between sampling. Cultivations with the closed gas loop were conducted without the online transmission. Safe operation of the online transmission was hardly possible due to the oscillating pressure generated by the pump for gas circulation.